Universitat de les Illes Balears

TESI DOCTORAL

TOPOGRAPHICALLY INDUCED FLOWS AND NOCTURNAL COOLING IN THE ATMOSPHERIC BOUNDARY LAYER

Tesi presentada per Daniel Martínez Villagrasa, al Departament de Física de la Universitat de les Illes Balears, per optar al grau de Doctor en Física

Daniel Martínez Villagrasa

Palma, 19 d'abril del 2011

TOPOGRAPHICALLY INDUCED FLOWS AND NOCTURNAL COOLING IN THE ATMOSPHERIC BOUNDARY LAYER

Daniel Martínez Villagrasa
Grup de Meteorologia, Departament de Física
Universitat de les Illes Balears (UIB)

PhD Thesis

Director: Dr. Joan Cuxart Rodamilans

Copyleft 2011, Daniel Martínez Villagrasa
Universitat de les Illes Balears
Palma

This document was typeset with LaTeX 2$_\varepsilon$

Cover shows the formation of a cold pool with fog at the bottom of an imaginary valley designed by the author, entitled *A tribute to Max*.

Joan Cuxart Rodamilans, Professor de la Universitat de les Illes Balears,

FA CONSTAR

que aquesta tesi doctoral ha estat realitzada pel Sr. *Daniel Martínez Villagrasa* sota la seva direcció al Departament de Física de la Universitat de les Illes Balears (UIB) i, per a donar-ne constància, firma la mateixa.

Palma, 19 d'abril del 2011

Joan Cuxart Rodamilans
Director

Daniel Martínez Villagrasa
Doctorand

Als meus pares,
a la Laia i a l'Aina

"El plaer coincideix amb el fet de conèixer. Perquè no es gaudeix després d'haver après, sinó que gaudir i aprendre es donen al mateix temps" — Epicur (341–270 aC)

Acknowledgments

Heus aquí una tesi. Tot i que aquestes línies apareixen a l'inici, acostumen a ser de les darreres coses que s'escriuen, quan la feina exposada en les properes seccions ja ha estat acabada, escrita i (mai prou) revisada. El meu cas no n'és una excepció. Ara, mentre fullejo mentalment les pàgines, un torrent de cares i noms m'envaeixen el pensament. Pertanyen a les persones que m'heu estat acompanyant aquests anys. Ha arribat el moment d'agrair-vos-ho.

Vull començar pel meu director de tesi perquè sense el seu suport aquest treball no hauria vist mai la llum. Joan, em vas fer confiança ja fa una pila d'anys, des d'aquella entrevista al bar de la Facultat de Física de la UB. El teu tracte proper i afable m'ha permès aprendre una manera de fer recerca en la que em sento molt còmode. Sobretot, per la llibertat que m'has donat per a concentrar-me en allò que creia important, per deixar-me fer, i per la teva habilitat d'aprofitar les virtuts dels teus col·laboradors en lloc d'exigir-nos les que no tenim. També voldria destacar les jornades intenses de reunions, dinars i passejades pel campus quan la feina ho ha requerit. I les converses que, tot sovint, transcendien l'àmbit estricte de la Capa Límit Atmosfèrica. Per tot això, gràcies.

Faig extensives aquestes paraules a la Maria Antònia, companya de feina des del primer dia i responsable de córrer les simulacions mesoscalars d'aquesta tesi. Gràcies per trobar sempre un moment per resoldre'm els dubtes (innumerables pel que fa al Meso-NH!) i per la teva immensa capacitat de feina, que encara ara em meravella.

I would like to acknowledge Jens Bange and Aline van den Kroonenberg for their warm hospitality during my several visits to the Technical University of Braunschweig and for showing me the mysteries of airborne meteorological data and the operation of UAVs. Similarly, my acknowledgements to Dave Whiteman,

who gave me the opportunity to visit his research group at the University of Utah and learning a lot about Mountain Meteorology. It has been a pleasure to share discussions and field work with him and the rest of researchers, Sebastian Hoch, Manuela Lehner, and also Meinolf Kossmann, who joined all of us in the amazing trip to the Meteor Crater.

Besides, I also acknowledge Dave Fitzjarrald and Larry Mahrt for the time they spent with us and the discussions during their respective visits to our group. Larry, thank you for inviting me to the Oregon State University and for the time that you dedicated to me, discussing about meteorology and showing me Corvallis and its surroundings. I would like to acknowledge all the co-authors of the articles presented in this thesis for improving the texts substantially.

Gràcies a la Maria Rosa Soler, la meva professora de Micrometeorologia a la UB, per posar-me en contacte amb en Joan quan li vaig mostrar el meu interès per a iniciar una tesi doctoral.

M'agradaria agrair l'ajuda d'en Damià durant tot aquest temps per a tirar endavant un projecte tan complex com el de fer volar el Carolo. Gràcies pel teu suport i entusiasme i per posar-nos en contacte amb l'Hugo García, el *Messi* dels pilots d'aeromodelisme. També voldria mencionar en Raúl pel seu suport tècnic en aquest camp i a l'Armand per facilitar-nos la logística a Lleida. El treball experimental no s'hauria pogut dur a terme sense la vostra col·laboració. Gràcies també a en Felipe per les seves idees tan resolutives per resoldre aspectes tècnics que a mi m'haurien ocupat setmanes de treball per a fer-ho la meitat de bé. I a la Guida per l'optimisme que desprens i per millorar l'estació EMBAT. També a en Toni Capó pel cop de mà ofert durant la construcció de les primeres estacions. Vull donar les gràcies a en Xavi per ajudar-me en la maquetació de la tesi i a l'Alejandro per aquells consells de darrera hora tan imprescindibles perquè la impressió surti correctament.

Gràcies a tots els membres del Grup de Meteorologia per la seva acollida i el bon ambient creat. Ha estat un plaer compartir espai, coneixements i bons moments amb tots vosaltres. En especial, amb en Toni i en Lluís, amb qui comparteixo una bonica amistat. A en Lluís també li vull agrair les *classes particulars* de GNUplot, shell, fortran o LaTeX que organitzava cada cop que tenia un dubte, així com totes les fideuades que he gaudit a casa seva, símbol d'una època. Acompanyat de tots vosaltres va ser fàcil atenuar l'enyorança de la família i amics que en un principi deixava a Barcelona.

El temps, però, m'ha demostrat que la mar no suposa distància suficient per allunyar-me dels bons amics. Roger, gràcies per acompanyar-me sense importar on ens trobàvem l'un i l'altre. Ajuntant aquest treball i el teu, potser sí que al final n'acabarem escrivint un anomenat *Filosofísica*. Al Funo, al Sandro i a la resta

de físics us vull agrair que em feu sentir com si no hagués marxat mai de casa cada cop que ens veiem. Espero que mai no us canseu de demanar-me quan torno d'una vegada per totes a Barcelona.

Marta, gràcies pel suport incondicional durant tot el llarg (i variable) camí que hem traçat junts. Per fer-me costat en els moments dolents i per l'alegria que sempre em transmets. Però sobretot, gràcies per explorar amb mi en què consisteix l'esdevenir.

M'agradaria també dedicar unes paraules a tota la gent que he conegut a Mallorca i que han fet que pagui la pena viure-hi. En particular, en Xavi, testimoni de totes les coses importants que m'han passat a l'illa. Gràcies pels moments de pis brindats, per les disquisicions filosòfiques i per convertir el nostre cau en una veritable llar. De l'Isma en vull destacar la seva generositat i que sempre tingui temps per dedicar-me quan el necessito. Gràcies per compartir amb mi la vostra visió del món.

Sònia, gràcies per mostrar-me Mallorca amb els teus ulls i per fer-me sentir un privilegiat per viure en aquest racó de món. Al teu costat he après (i el que em queda per aprendre) que s'ha de viure amb passió i que la vida no la podem passar fent qualsevol cosa.

A la Camino vull dir-li que ha estat un immens plaer conèixer-la en el darrer tram d'elaboració d'aquesta tesi. Gràcies per entendre les neures habituals d'aquest període i per cuidar-me tant els darrers mesos.

Finalment, per la seva especial importància, vull donar les gràcies a la meva família. Òscar, Àlex, gràcies pel caliu que m'heu donat durant tots aquests anys. Sense el vostre suport hauria estat molt difícil centrar-me en els estudis, arribar a la universitat i, finalment, presentar aquesta tesi. Estic content que aquest caliu s'hagi traslladat també a les vostres respectives llars. Gràcies Núria i Mònica per haver-ho fet possible. A la meva mare li vull agrair el seu recolzament incondicional i la confiança que sempre m'ha transmès . Educar-nos en la llibertat ha estat el regal més important que m'has fet mai. Gràcies per escoltar-me i per les converses que hem tingut durant tos aquests anys. M'agradaria acabar aquestes línies amb un record al meu pare, a qui encara li continuo dedicant totes les coses importants que faig a la vida.

Daniel Martínez Villagrasa
Palma, abril del 2011

Resum

La Capa Límit Atmosfèrica (CLA) normalment es defineix com la part inferior de l'atmosfera que es troba directament influenciada per la superfície terrestre. Tots els processos d'intercanvi d'energia, massa o moment entre la superfície i l'atmosfera tenen lloc a través d'aquesta capa d'aire. Per això és tant important analitzar els processos físics que hi tenen lloc.

La interacció entre la CLA i la superfície de la Terra és molt complexa. Quan la situació sinòptica ve marcada per forts gradients de pressió, els vents intensos que es generen a gran escala provoquen forts moviments turbulents a prop del terra degut al fregament de l'aire amb la superfície terrestre. Com a resultat, s'obté una capa límit molt barrejada que emmascara les peculiaritats locals i els processos físics es troben fortament condicionats per la dinàmica de gran escala. En canvi, sota la influència d'un anticicló, els moviments horitzontals d'escala regional són molt febles i la dinàmica de la CLA es veu condicionada per fenòmens que responen a escales inferiors, des de la mesoscala fins a l'escala local i turbulenta. En aquests casos, el cicle diürn de la CLA és més marcat, en especial damunt dels continents.

Durant el dia, l'escalfament del terra es transmet a l'atmosfera a través de la convecció, provocant forts moviments verticals que contribueixen a redistribuir l'excés d'energia aportat pel Sol. Aquest mecanisme també contribueix a una barreja i homogeneïtzació de la CLA d'una manera similar a la del cas amb forts vents. Durant aquesta fase la capa límit es coneix com a Capa Límit Convectiva (CLC) o de barreja. A partir del vespre, l'aportació d'energia, i per tant la convecció, desapareixen amb la posta de Sol, iniciant-se un procés de refredament radiatiu del terra. L'aire en contacte amb el sòl també es refreda, formant una inversió de temperatura que anirà guanyant altura a mesura que

avanci la nit. Aquest règim, en què la CLA rep el nom de Capa Límit Estable (CLE), està caracteritzat per una turbulència més feble que no pas durant el dia, amb menys capacitat per barrejar l'aire. En aquestes condicions, quan la turbulència perd capacitat per homogeneïtzar la capa límit, l'heterogeneïtat de la superfície es tradueix en gradients horitzontals de pressió i temperatura a la part baixa de l'atmosfera, induint moviments d'aire que tendeixin a reduir-los. A la CLE damunt de terreny complex, doncs, són aquestes circulacions les que en molts casos dominen els intercanvis d'energia, massa i moment entre la superfície i l'atmosfera.

La presència de muntanyes, valls, pendents, llacs o boscos contribueix a una distribució heterogènia de la temperatura damunt la superfície, generant estructures coherents com corrents de gravetat, vents de pendent o de vall, per citar uns exemples. Aquesta tesi es concentra en l'estudi de les circulacions de vent nocturnes en condicions atmosfèriques estables o de bon temps, tot analitzant el paper de l'orografia en la seva generació i organització a escala de conca. També analitza com interaccionen els diversos corrents entre ells i amb els vents d'escala major, així com en els patrons de temperatura que es formen damunt del terreny complex.

L'estudi s'ha realitzat per a quatre localitzacions diferents a latituds mitjanes. Cada localització conté una o vàries conques hidrogràfiques ben definides que organitzen els corrents nocturns a nivell de mesoscala. Aquests indrets són l'illa de Mallorca, la conca del Duero i la vall de l'Ebre, ambdues d'escala similar, i finalment un cràter de mida molt més reduïda situat a l'altiplà del Colorado, Arizona. Per als tres primers indrets, s'ha estudiat la dinàmica dels corrents locals a múltiples escales, tot identificant les configuracions orogràfiques que els determinen i l'escala més gran que s'ha de tenir en compte. Al cràter s'hi ha analitzat els canvis que experimenta el corrent de pendent damunt de la vessant interior del cràter durant la transició dia-nit.

Les eines utilitzades per a elaborar l'anàlisi exposada han estat variades. Per una banda, s'ha procurat fer ús de totes les dades experimentals disponibles, des de dades d'estacions meteorològiques fins a imatges de satèl·lit. Per als casos del cràter i la vall de l'Ebre, també s'han utilitzat dades de campanyes experimentals dissenyades específicament. En el cas de la conca del Duero i l'illa de Mallorca, les observacions s'han complementat amb dues simulacions de mesoscala d'alta resolució per a nits seleccionades. Aquestes simulacions tenen suficient resolució vertical i horitzontal per generar corrents de pendent (o vents catabàtics) a diversos indrets del domini. Les sortides del model s'han utilitzat per a analitzar les principals característiques de dos d'aquests corrents, posant-les en relació amb les d'altres vents catabàtics mesurats o simulats a diferents llocs.

Amb l'estudi de les circulacions induïdes per l'orografia a diferents indrets, aquesta tesi vol contribuir en la identificació d'aquelles característiques comunes en la interacció entre la CLE i el terreny complex.

Contents

Titlepage **i**

Acknowledgments **ix**

Contents **xvii**

1 Introduction **1**

1.1 The stable boundary layer over complex terrain 2
1.2 Nocturnal cooling 4
1.2.1 Radiative energy budget 4
1.2.2 Surface energy budget 6
1.2.3 The buildup of the nocturnal surface inversion 8
1.2.4 Cold-air pooling 10
1.3 Thermally driven flows 13
1.3.1 Valley winds 16
1.3.2 Slope flows 19
1.3.3 Thermally driven winds in basins 24
1.4 The study of the thermally driven flows and nocturnal cooling . . 24
1.5 Motivation and outline of thesis 28
1.5.1 Outline of the thesis 32

2 Nocturnal meso-beta basin and katabatic flows on a midlatitude island 35

2.1 Introduction 36
2.2 The interaction of the island with the general flow 39
2.3 Circulation in the mesobeta Palma basin 45

2.4 Features of a katabatic flow over a gentle slope 48
2.5 Conclusions 59

3 Heterogeneous nocturnal cooling in a large basin under very stable conditions 61

3.1 Introduction 62
3.2 Tools 65
3.3 Description of the night 66
3.4 Spatial distribution and time evolution of surface temperature . . 70
3.4.1 Mean nocturnal temperature 71
3.4.2 Basin-averaged deviation 73
3.4.3 Local spatial deviation 75
3.5 Simulated within-basin flow heterogeneities 75
3.6 Conclusions 80

4 Assessment of the hydraulic slope flow approach using a mesoscale model 83

4.1 Introduction 84
4.2 Description of the flow 86
4.3 The hydraulic slope flow approach 92
4.4 Application of the simplified model 95
4.5 The katabatic wind as seen by the two-layer approach 97
4.6 Analysis of the closure of the two-layer budget equations 100
4.7 Conclusions 103

5 The upslope-dowslope flow transition on a basin sidewall 105

5.1 Introduction 106
5.2 Background 106
5.3 Meteor Crater topography and meteorological data 109
5.4 Case study of 20 October 2006 111
5.5 The upslope-downslope flow transition 114
5.5.1 Smoke dispersion 114
5.5.2 Results from the meteorological towers 115
5.5.3 Evolution as seen by the wavelet transform 119
5.6 Discussion 123
5.7 Conclusions 128

6 Conditioned climatology for stably stratified nights in the Lleida area 131

6.1 Introduction 132
6.2 Climatology and location 134

6.3 Characteristics of the temporal series . . . 136
6.4 Selection of stable nights . . . 139
6.5 Study of the selected nights . . . 143
6.5.1 Wind roses and nightly evolution . . . 143
6.5.2 Temperature, speed and humidity evolution . . . 146
6.6 Conclusions . . . 149

7 Meso-beta basin flows in the eastern Ebro river basin 151

7.1 Introduction . . . 152
7.2 Observational tools . . . 155
7.3 Scintec's WindRASS . . . 158
7.4 Within-basin boundary-layer flows . . . 161
7.4.1 Weak westerly flows . . . 161
7.4.2 Thermal within-basin flows . . . 163
7.4.3 Winter circulation and radiation Fog . . . 167
7.5 Summary . . . 169

8 General Conclusions 171

9 List of publications 179

List of Tables 181

List of Figures 183

Chapter 1

Introduction

The atmospheric boundary layer (ABL) is usually defined as the region of the atmosphere directly influenced by the surface, in which turbulence plays a central role. Due to this influence, particularly over land, the ABL experiences a diurnal cycle which is especially notorious under cloudless conditions and weak mean flow. Over heterogeneous surfaces, the induced horizontal gradients in the air near the surface generate terrain flows that contribute significantly to the ABL evolution.

In daytime with clear skies, the solar radiative surface heating generates vigorous turbulence that mixes the air uniformly in the vertical, forming a deep *mixed layer* that can reach a depth of more than a thousand metres in the afternoon. Turbulence is driven by convective motions due to the thermal instability (buoyant turbulence), which can be enhanced by the wind shear present at the upper part of the layer (mechanical turbulence). This region is also usually referred as the *convective boundary layer* (CBL). With the arrival of the sunset, the incoming shortwave radiative energy decreases and, consequently, the surface experiences a cooling process that cuts off the convective motions, with a progressive decay of the ABL turbulence. The radiative surface and air cooling generate an inversion of temperature that grows upwards throughout the night, forming a *stably stratified boundary layer* (SBL). Under this regime, the turbulence is weak and mixes less than in the unstable case. Therefore, its depth is reduced to tens or few hundreds metres, even smaller under very stable conditions. In case of windy conditions or a sky completely overcast, the surface thermal forcing is minimised, generating the classical *neutral ABL* in which buoyancy is a minor factor and turbulence is mechanically generated by wind shear.

The diurnal cycle described here considers an ABL over flat and homogeneous terrain, where the relevant forcings come from the surface and its interaction with the free atmosphere, located at the upper boundary. However, non-uniform surfaces predominate over land. Sloping terrain, mountains, valleys and basins of a large variety of scales, different soil uses and surface covers, lakes,... all these irregularities add complexity to the ABL meteorology. Terrain induced circulations contribute significantly to the vertical and horizontal exchange of mass, temperature and moisture. Therefore, new tools are needed and are becoming available to address the ABL structure over heterogeneous terrain, arising as one of the main issues during last 20 years.

The works presented in the following chapters of this thesis deal with some of the phenomena generated by these terrain irregularities and their influence on the SBL evolution. In the present chapter, Section 1.1 describes the main characteristics of the SBL regime over complex terrain. Section 1.2 presents the basic mechanisms related to the surface and air nocturnal cooling, while the principles involved in the generation of thermally driven currents are described in Section 1.3. An overview of the previous studies related with these topics is exposed in Section 1.4 and, finally, motivation and outline of the thesis can be found in Section 1.5.

1.1 The stable boundary layer over complex terrain

The SBL or *nocturnal boundary layer* (NBL) is characterised by the buildup of a stable layer close to the ground due to the surface radiative cooling. The largest stability concentrates near the ground and decreases with height until reaching near-neutral conditions, which indicates the top of the temperature inversion. The NBL is classically defined in terms of the turbulence structure, as for the rest of the ABL regimes, considering it as the shallow part of the atmosphere above which the mean shear stress and turbulent heat flux are negligibly small (Garratt, 1992). With this definition, the NBL height is typically found below the temperature inversion level, known as the *inversion layer*. Several works (Cuxart and Jiménez, 2007; Mahrt, 1999) have reported the existence of elevated turbulence disconnected from the surface influence under certain circumstancies. For this case, the definition of the NBL height in terms of turbulence is more difficult.

After sunset in a flat and homogeneous terrain, the increasing stability within the inversion layer reduces the influence of the frictional drag and winds can

accelerate aloft, producing a supergeostrophic current known as the *low-level jet* (LLJ). This jet is the response of the atmosphere to the necessary re-adjustment of the flow between the negligible speed on the ground and the geostrophic flow in the free atmosphere when convection ceases, describing an inertial oscillation that can persist for much of the night (Blackadar, 1957). The wind shear associated to this current generates turbulence which, in turn, is partially suppressed by the temperature inversion. As a result, the turbulence evolution can differ significantly depending on the wind and thermal structure for each case.

When the geostrophic wind is important, the generated wind shear is strong enough to produce mechanical mixing through the SBL, connecting the surface with the air aloft. However, under a synoptical situation with weak pressure gradients, the strong surface cooling enhanced by clear skies and the presence of a weak geostrophic wind generates a deep temperature inversion above the ground, decoupling the surface layer from the air aloft. Under such situation, turbulence turns weak, sporadic and anisotropic due to the suppression of vertical motions. These turbulence characteristics difficult the study of the SBL since the classical concepts that describe the ABL are not longer valid under strong stability conditions (Cuxart et al., 2006). For example, the Kolmogorov theory for the energy dissipation or the similarity theory, both designed for an isotropic and homogeneous turbulence, may not be of application. Therefore, the SBL is often classified into two subcategories, the *very stable boundary layer* and the *weakly stable boundary layer*, and the classical boundary layer theory would only be applicable to the later subcategory, where the turbulence is more or less continuous and the surface cooling is relatively slow (Mahrt, 1998).

Under very stable cases, the sporadic turbulence, also known as *intermittency*, can be mechanically generated by the presence of a quasi-stationary LLJ. Intermittency can also be due to non-stationary motions on time scales just larger than turbulence but smaller than what is typically considered within the mesoscale category. These structures are sometimes referred to as *submeso* motions (Belušić and Mahrt, 2008) and include gravity waves, non-stationary drainage flows, microfronts and other more complex phenomena (Mahrt, 2008). These motions are characterised by their unpredictability and they have been of increasing interest during the last years because of their interaction with larger mesoscale structures (Mahrt et al., 2010).

Over complex terrain, where the surface is neither flat nor homogeneous, the SBL evolution is also affected by other local phenomena like low-level currents of a scale larger than submeso and cold air pooling in sheltered regions. Low-level currents can become turbulent depending on the thermal and wind structure and represent another source of mixing. Often, they take the form of a LLJ or interact with the LLJ generated from the geostrophic adjustment. Therefore, many times

the origin of the LLJ is controversial. A broad range of motions from micro- to meso- scales (including submeso) are generated due to the synoptic scale baroclinity, horizontal thermal differences caused by land surface heterogeneities or the presence of (even gentle) slopes. All these phenomena contribute to the exchange of mass, energy and momentum budgets and their effects are as important as turbulence.

The spatial variability of air temperature at night leads to spatial pressure differences that the atmosphere tends to compensate by means of horizontal motion, generating those low-level currents. Over complex terrain, cold air accumulates over low-lying areas, leading to the formation of a shallow SBL within the topographically-confined areas usually known as a *cold pool*.

In summary, the study of the SBL evolution at a given place requires to consider the local properties of terrain that generate those low-level currents and cold pools. The nocturnal air cooling is driven by the radiative and energy balances at the underlying surface, while the buildup of a stable layer is conditioned by the features of the local terrain. These basic mechanisms are therefore addressed in the next section.

1.2 Nocturnal cooling

1.2.1 Radiative energy budget

Ground represents the lower boundary condition of the ABL and is the major source or sink of energy to the system, described by the net all-wave radiation (Q^*) at the surface, which depends on the sum of the individual short- (K^*) and longwave (L^*) streams

$$Q^* = K^* + L^* = K\downarrow - K\uparrow + L\downarrow - L\uparrow \tag{1.1}$$

Equation 1.1 includes the important radiation budget components at an ideal site with a horizontal, homogeneous and extensive surface (Figure 1.1).

The evolution of the incoming shortwave radiation ($K\downarrow$) depends on the location of the Sun relative to the horizon and on the bulk atmosphere conditions, since clouds and other gases absorb part of the extraterrestrial radiation that reaches the top of the atmosphere. The solar radiation that arrives at the surface can be split in diffuse and direct-beam radiation. In the middle of a cloudless day the former hardly represents the 10%–15% of the total $K\downarrow$, depending on the

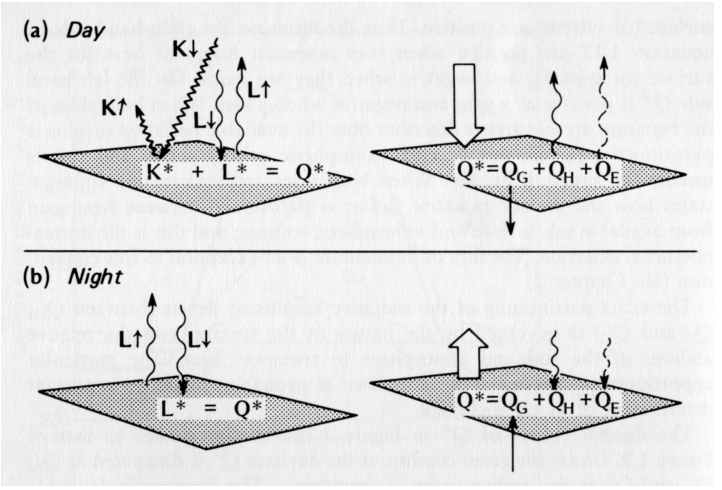

Figure 1.1: Schematic illustration of the fluxes involved in the radiation budget (left) and energy balance (right) for a flat and homogeneous surface, (a) by day and (b) at night, from Oke (1987).

amount of water vapour content (Oke, 1987). This proportion increases when the Sun is closer to the horizon due to the greater path length of the streams through the atmosphere. Part of the solar radiation that arrives at the surface is reflected again towards the atmosphere ($K\uparrow$) and the rest is absorbed. The amount of radiation reflected depends on the ground properties and is defined by the surface albedo α.

The incoming longwave radiation emitted by the atmosphere ($L\downarrow$) depends upon the bulk atmospheric properties (temperature and emissivity) and on the presence and type of clouds. Finally, the outgoing longwave radiation from the surface ($L\uparrow$) is similarly driven by its emissivity and temperature, but also includes the small amount of $L\downarrow$ reflected by the surface. Since temperature and emissivity at the surface are larger than their respective values from the bulk atmosphere, $L\uparrow$ is both greater and more variable than $L\downarrow$, resulting in a net longwave loss ($L^* < 0$).

The radiation energy budget (1.1) evolves throughout the day, with a common daytime radiative surplus due to a net shortwave gain that is above the net long-

wave loss. At night, the solar input disappears and the net radiation becomes negative as it only depends upon the longwave contribution.

The presence of clouds modifies substantially this common cycle and represents the major factor in reducing the diurnal surface radiation budget variation. On one side, clouds absorb and reflect from the top part of the $K\downarrow$ input, reducing up to the 90% of the reception in a cloudless day for the case of an overcast sky of low and thick clouds. Regarding the longwave radiation, clouds absorb the major part of the $L\uparrow$ emitted by the surface and re-emit it back, increasing substantially $L\downarrow$ and reducing the resulting L^*. Therefore, cloudy weather limits daytime surface heating and nocturnal cooling, reducing the diurnal temperature range.

The effects of topography on the radiation balance are numerous and very important. Terrain exposure (slope and aspect angles of the ground) and configuration of the surrounding topography, which determines the propagation of shadows, modify the direct-beam solar radiation. In case of depressions or valleys, $K\downarrow$ is reflected on the surrounding elevated terrain, increasing substantially the diffuse radiation at lower sites. The complex interaction between topography and the longwave radiation field becomes determinant at night, when the dominating term (the direct shortwave radiation) disappears. The portion of sky replaced by elevated terrain emits larger longwave radiation since these surfaces are warmer than the bulk atmosphere, enhancing the $L\downarrow$ at local depressions. Moreover, the accumulation of cold air over lower areas also controls the rate of surface cooling and, correspondingly, the longwave emission to the atmosphere $L\uparrow$ (Hoch and Whiteman, 2010).

1.2.2 Surface energy budget

The net radiation flux represents the basic input of the surface energy budget, in which the rest of the components react to any imbalance of Equation 1.1. The major components are represented by the convective (turbulence) exchange within the air in the form of either the sensible (Q_H) or latent (Q_E) heat fluxes, and conduction to or from the underlying soil (Q_G)

$$Q^* + Q_H + Q_E + Q_G = 0 \tag{1.2}$$

In this thesis the sign convention used considers that those fluxes directed toward the surface, whether from the atmosphere or soil, are positive. Equation 1.2 reduces the surface to a massless plane across which energy passes (Figure 1.1).

In many cases, specially regarding more realistic situations, it is convenient to consider the surface as a layer or volume capable to store energy. The term ΔQ_s is therefore added in order to account for the changes in the energy storage. These changes can be due to the physical heat storage by substances in the volume (*i.e.* plants or water), the biochemical energy storage driven by the photosynthesis or the absorption or release of heat by the plant biomass among other things.

ΔQ_s also accounts for the advection effects that occur when the input and output of the horizontal fluxes do not balance (Figure 1.2). In the ABL it is very common to consider the horizontal fluxes negligible relative to the vertical fluxes (Stull, 1988), being their variations in the horizontal even smaller. However, over heterogeneous terrain, the surface energy budget differs from one site to another. The presence of a horizontal airflow can carry upwind near-surface-air with different energy flux properties, altering the local atmospheric conditions and modifying the surface energy budget on the interested site. As seen above, since the SBL over complex terrain is prone to contain such horizontal flows, advection effects must be considered.

When the surface energy budget terms are measured from field experiments, it is common to fail in achieving closure. The error found tends to be larger than it is usually expected from the measurements of any individual term. Most of the imbalance can be attributed to the mechanisms included in ΔQ_s which cannot be measured easily and, in consequence, its origin is unknown. Nowadays, the imbalance term uses to represent a 10%–30% of the total (Oncley et al., 2007).

The role of any particular heat flux of Equation 1.2 to compensate for the radiative excess or deficit on the surface depends upon the surface characteristics, underlying soil properties and the state of the ABL. An irrigated agricultural field, for example, would favour the daytime dissipation of Q^* through the evaporation of soil moisture, increasing the amount of Q_E respect to the value of Q_H. During the first hours after sunrise, when convection is not very strong, the excess of net radiation is subtracted by conduction downwards to the soil, being Q_G the largest heat flux. At night, the stably stratified boundary layer tends to reduce the turbulent fluxes in the atmosphere, leading to the surface heat flux (Q_G) to play the major role in compensating for the radiative loss of energy. In this case, whenever the heat fluxes cannot compensate for the radiative losses, the temperature surface decreases and, consequently, Q^* is reduced until reaching the balance of Equation 1.2.

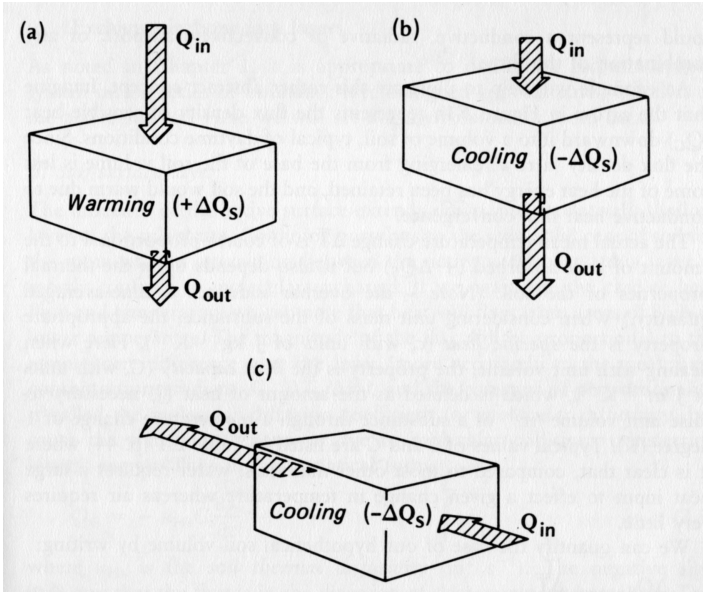

Figure 1.2: Schematic depiction of the relationship between energy storage ΔQ_s in a volume and (a) vertical flux convergence, (b) vertical flux divergence and (c) horizontal flux divergence, from Oke (1987).

1.2.3 The buildup of the nocturnal surface inversion

During clear nights, the surface cooling leads to a progressive buildup of a stably stratified layer sometimes referred as the nocturnal surface inversion. Its development is mainly due to the following processes (André and Mahrt, 1982). Firstly, a downward heat flux driven by any shear-generated turbulence transports heat to the underlying ground and, correspondingly, cooling propagates upwards. Secondly, clear-air radiative cooling due to emission by water vapour, carbon dioxide, ozone and aerosols also stratifies low-level air. Finally, horizontal advection, particularly enhanced over complex terrain by thermally driven flows, can modify the local depth of the inversion layer.

The interaction between the radiative and turbulent flux divergences is quite complex because they both modify and depend upon the thermal structure of the nocturnal surface inversion. Within the NBL, characterised by the presence

of turbulence, heat fluxes arise as the control mechanism for the air cooling close to the surface. Radiative flux divergence extends the inversion layer to levels well above the NBL. The stratification is weaker in the radiatively-cooled layer, giving a negative curvature of the profile of the potential temperature since the strongest cooling is developed close to the ground. When turbulence intensifies across the whole layer, negative curvature weakens due to the mixing process modifying, in turn, both flux divergences.

Thermal structure is also affected by low-level currents due to the horizontal advection of temperature, which can be very important even over almost homogeneous and gentle terrain (Sun et al., 2003; Ha and Mahrt, 2003; Mahrt et al., 2001). In addition, the presence of an elevated current at a height where the stratification is weak may lead to occasional turbulence transferred toward the surface in the form of downward bursts. The intermittent turbulence can mix the air and compensate for the divergence flux cooling (Mahrt, 1999).

In the early evening transition, when convection collapses, the cooling of the surface layer is primarily driven by the radiative flux divergence (Sun et al., 2003). The lack of turbulent mixing decouples the surface inversion layer from air aloft and the confined air cools very rapidly. Actually, the mean quantities during the first hours after sunset change at a rate much larger than they do subsequently until sunrise (Acevedo and Fitzjarrald, 2001). Besides, the small eddy sizes related with this period enhance the effects of surface heterogeneities in the SBL. Decay of turbulence depends on the local landscape configuration. Convection ceases faster in valleys, sinkholes, gullies and other small local depressions or regions sheltered by vegetation, whereas it typically persists on areas well exposed (Bodine et al., 2009). Following the early evening transition, thermally driven flows generated by those heterogeneities can produce the proper wind shear and, consequently, mix the air along the areas they cross. Depending on the flow structure, length scale and intensity, they can either enhance the low-air cooling by increasing the downward heat flux close to the surface, or warm the whole surface inversion layer through mixing with the air aloft. Moreover, the thermal structure is modified by horizontal advection, as discussed above.

In summary, heterogeneity leads to a spatial nighttime temperature distribution, which is enhanced by the presence of topographic depressions and other sheltered configurations. When the buildup of a stable layer remains undisturbed and confined within a stagnant area, it is commonly referred as a cold pool and it is described below.

1.2.4 Cold-air pooling

In complex terrain, the air close to the surface is cooled due to the radiative energy loss of the ground, becoming denser than the air at the same elevation but far from the surface influence. In consequence, the cold air generated over slopes and sidewalls sinks toward lower areas where the near-the-ground air is also cooling. This process leads into a buildup of a stable layer within sheltered regions where the air is unlikely to drain. These regions include basins, valleys and depressions of a wide range of scales (Whiteman, 2000), shallow gullies (Mahrt et al., 2001) or clearings within forests (Gustavsson et al., 1998).

The height of the inversion layer is conditioned by the ridge top of the topographical configuration, since temperature inversion is sheltered from the larger scale flows. Small valleys and basins generally contain an inversion top below the surrounding topography, which is well characterised by a temperature jump (Whiteman et al., 2001). This discontinuity separates the cold air confined within the small basin and the warm advection of the air above. Within the basin, potential temperature gradients are greater than isothermal, so that temperature increases with height and the inversions are relatively isolated from the winds aloft due to the temperature jump (Figure 1.3).

In contrast, as the basin becomes larger, the confining topography increasingly fails in protecting the basin atmosphere adequately from the synoptic-scale influences (Whiteman et al., 1999). In consequence, potential temperature gradients within the basin get relatively weaker and the basin atmosphere becomes more exposed to the synoptic flows and their accompanying temperature advection, specially at the upper part. Warm air advected above the cold pool becomes better mixed with the air below and the inversion losses its distinct height stability top that separates clearly both atmospheres (Figure 1.3).

When the external influences do not penetrate within the cold pool, either because the basin is small and well isolated or the larger-scale flows are very weak, the strong basin inversion protects the lower levels from the winds aloft. On the top, inversion strength is modulated by synoptic advection. Close to the surface, it is modified diurnally by the daytime growth of a shallow CBL containing upslope flows, and the nighttime buildup of a shallow stable sublayer containing downslope flows. These sub-layers follow the topography within the basin, forming over both horizontal and inclined slopes. Under such situation, weak currents are strongly influenced by submeso motions that make them non-stationary, complicating the analysis of exchange of momentum, energy and humidity between the surface and the boundary layer.

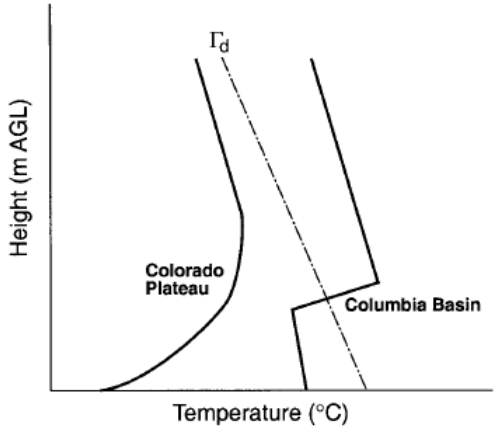

Figure 1.3: Schematic vertical temperature profiles in the Colorado plateau (considered a large basin in Whiteman et al., 1999) and Columbia basin (small basin). A cloudy cold pool is regularly formed in the Columbia basin, with the temperature profile following a moist-adiabatic lapse rate. The sharp temperature jump indicates the height of the basin rim. The dry-adiabatic lapse rate (Γ_d) is shown for comparison (from Whiteman et al., 2001).

Cold-air pooling also depends on the cooling rate, which is related with the volume of air enclosed by the valley or basin (Whiteman, 2000). Considering the same heat loss from two valleys, the one containing the smaller volume of air produces a larger cooling inside, leading to a larger temperature inversion. Thus, the shape of the valley also plays a role, with convex sidewalls tending to further enhance the cold pool formation compared to concave or V-shaped sidewalls (Whiteman, 1990). Similarly, the generated inversions are usually deeper than those formed over adjacent areas where the terrain is flat.

The buildup of the cold pool is usually studied by means of the volumetric atmospheric budgets of mass, heat, momentum and moisture (Whiteman, 1990) since they provide a more comprehensive idea of the cold pool evolution. This methodology also avoids the effects derived from the non-representativeness of a single surface site. De Wekker and Whiteman (2006) characterise the NBL

cooling in different valleys and basins and over plains by means of the volumetric atmospheric heat balance.

The influence of drainage currents to the cold pool formation is an issue discussed repeatedly. Thompson (1986) argued that the presence of drainage flows advecting cold air to the bottom is not necessary and that the colder air found inside valleys is primarily due to a decrease of the turbulent heat transfer in those sheltered locations. Moreover, Clements et al. (2003) concluded that downslope flows played a secondary role in the cold pool formation within a small basin, since they observed very shallow and weak drainage currents over the sidewalls. Indeed, in many cases, downslope flows are warmer than the cold pool formed at the foot of the slope. Under these circumstances, gravity currents detach from the surface and flows over the colder air, at the elevation where they are in buoyant balance with the environment, as observed by Heywood (1933) and Yoshino (1984).

Cold pools can be characterised as diurnal, forming during the evening or night and decaying following sunrise the next day, or as persistent, lasting longer than a normal nighttime temperature inversion. Persistent cold pools are temperature inversions that occur primarily in winter when the daily cycle of sensible heating and convection are insufficient, either because of cloudiness or seasonal reductions of sensible heat flux, to destroy the stable layer on a daily basis.

The presence of a cold pool leads to a very limited dispersion of the pollutants emitted inside, sometimes causing severe air pollution episodes. If the air within the cold pool is moist enough, low temperatures favour the radiation fog formation (Fitzjarrald and Lala, 1989) or other types of stratiform clouds. Similarly, dewfall (frostfall) occurs when the bare surface or leaves -for surfaces with vegetation- cool radiatively below the dewpoint (frostpoint) temperature of the adjacent air and water vapour condensates (sublimates) onto the surface (Whiteman et al., 2007). Indeed, all these phenomena are closely related, sometimes even coupled, and the interaction of factors involved make very difficult their prediction.

In the framework of the surface energy budget, dewfall and radiation fog play a relevant role. Dew deposition is tied to the rate of heat release, reducing the total nocturnal cooling respect to a night without dew. When the fog is formed, the active radiative surface is displaced upwards to the fog top and the underlying ground radiatively balances with the fog deck, cooling at the same rate. Although the radiation fog is not explicitly analysed in the present thesis, this phenomenon is an important subject related with the cold pool formation and for this reason the basic mechanisms are exposed below.

Radiation fog

Radiation fog takes place on cloudless nights with light winds. It is the result of a fine balance between radiative cooling and turbulent warming of the volume of air near the surface. The process is aided when the near-the-ground moist air is close to the saturation and the air aloft is dry. The moist air layer cools very rapid due to a strong radiative flux divergence. The lower boundary receives less longwave radiation from the underlying colder surface than the radiation emitted. At the upper boundary, moist air emits more than it receives from the dry air aloft due to a greater emissivity of moist air. The layer cools until its saturated dew-point and droplets of water start to form. Fog formation is aided by light winds that enhance the loss of sensible heat from the layer to the surface. If winds are too strong, however, turbulence mixes the moist layer with the dry air aloft and the process is finished.

When the fog is formed, the upper boundary emits very efficiently, increasing the cooling at this part and increasing its thickness. Radiation fogs can last for several days in winter since they are a phenomena related with the cold air pooling. They are normally eroded by convection or by a frontal passage that mixes the fog with drier air.

1.3 Thermally driven flows

The distribution of temperature over complex terrain gives rise to characteristic systems of air motion that dominate the atmospheric circulations especially under weak synoptic pressure gradients. Three types of diurnal wind systems are generally recognised in mountainous areas (Whiteman, 2000): slope, valley and mountain-plain winds (Figure 1.4). Each wind system works at their respective length scale, being the slope currents the smallest scale of the diurnal wind system.

The *slope wind* system is produced by buoyancy forces induced by temperature differences between the air adjacent to the slope and the ambient air outside the slope boundary layer. Slope winds blow parallel to the inclined surface and typically blow up the slope by day and down the slope by night. The *valley wind* system is produced by horizontal pressure gradients formed as a result of the thermal gradient developed along the valley axis or temperature differences between the air in the valley and the air at the same elevation over the adjacent plain. Valley winds blow up-valley in daytime and down-valley in nighttime,

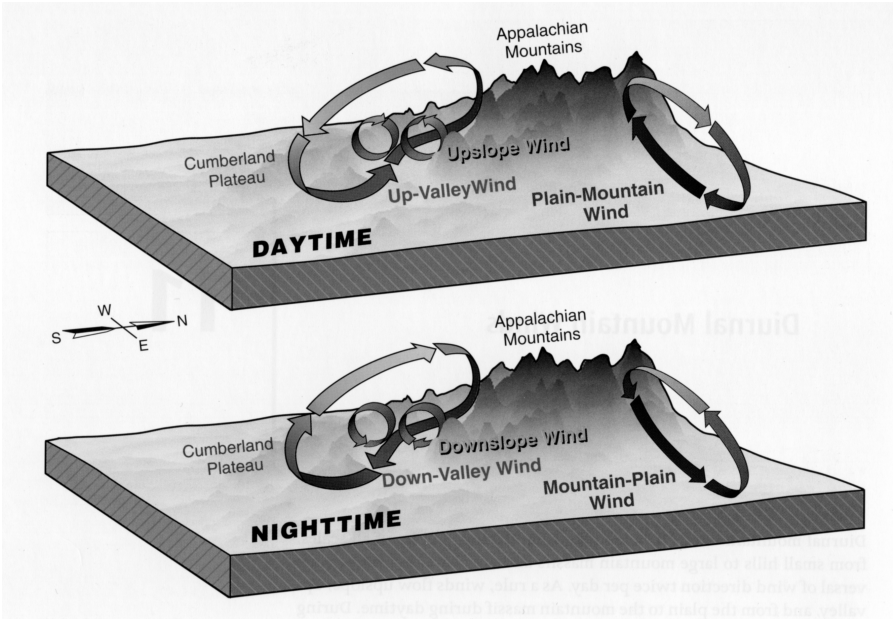

Figure 1.4: Diurnal mountain wind system in (a) daytime and (b) nighttime (from Whiteman, 2000).

although this cycle can be substantially delayed depending on the amount of air volume involved. The *mountain-plain wind* circulation is developed at a larger scale due to the horizontal temperature differences between the air over a mountain massif and the air over the surrounding plains. These winds are not confined by the topography and normally blow up the outer slopes of the mountain massif during the day and down the slopes at night.

There are two basic dynamic processes involved in the thermally driven wind systems (Barry, 2008). Firstly, an antitriptic wind component (friction balances pressure gradient) directed towards low pressure, when the Coriolis effect is small, and, secondly, a gravity wind component directed downslope, in the absence of any general pressure gradient. These circulations are closed by compensatory flows higher in the atmosphere. The same mechanism is common for the rest of thermally driven flows such as the sea and land breezes, the cross-valley wind system or other more complex mountain-valley winds. Cross-valley

winds result from horizontal temperature differences between the air over two opposite sidewalls that blow perpendicular to the valley axis and toward the more heated side (see Egger, 1990).

The study of the thermally driven flows is complicated because it is hard to observe any component of the diurnal wind system isolated from the influence of the others or without being affected by larger scale flows aloft, like those produced by regional pressure gradients. Besides, each wind system is modified by mechanical effects induced by the topography. In the latter category we can cite the effects of channelling of synoptic flows along the valley axis (Whiteman and Doran, 1993) that can overcome thermally driven winds developed within a valley. Mountains can also modify large-scale winds by blocking them or forcing them to be carried over or to be deviated and flow around, forced through gaps in the barrier. These effects depend on the topographic characteristics and properties of the approaching flow (velocity and stability) and can generate a wide range of phenomena -like mountain waves, eddies and vortexes in the lee side of the obstacle- that interact and modify the thermally driven winds (see Whiteman, 2000, for a complete review).

Under anticyclonic weather conditions, when large-scale flows are weak, the thermally driven wind system is prevalent over complex terrain, showing a regular diurnal evolution that can be simply described as follows. A daytime period characterised by the presence of winds flowing up the terrain and a super-adiabatic temperature profile close to the ground. Next, an evening transition phase in which an inversion of temperature builds up over the ground and low-level winds reverse into the nighttime winds flowing down the terrain. A stable nocturnal period with a ground-based temperature inversion well established and, finally, a morning transition period completes the cycle by destroying the inversion layer and winds reverse again to the daytime direction. This cycle is usually quite similar from day to day under the same fair weather conditions (Figure 1.5) and, therefore, represent a key feature of the climatology of complex terrain (Whiteman, 1990). However, the wind strength, onset times, depth and other characteristics of the thermally driven flows depend on the specific site, making difficult the generalisation of the local findings to the rest of the observed mountain wind systems.

Although thermally driven winds are subject to several influences, the usual procedure is to emphasise each component of the wind system and consider the rest of the interactions as modifying factors. For the rest of the section, we will analyse the main characteristics of the valley and slope winds.

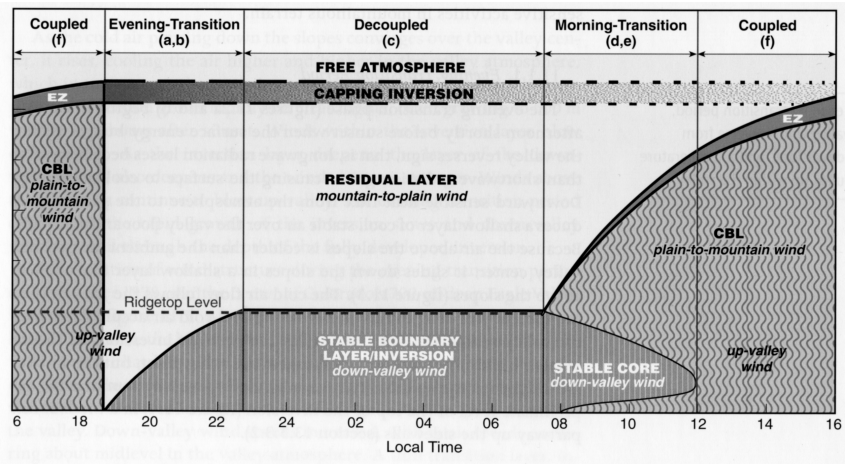

Figure 1.5: Diurnal cycle of the ABL in a valley considering valley and mountain-plain circulations (from Whiteman, 2000).

1.3.1 Valley winds

As seen in Section 1.2.4, in nighttime the air within a confined topography cools faster and reaches lower temperatures than over a clear plain. Similarly, volumetric-air temperatures are larger within a valley in daytime. The differing temperature ranges produce a diurnal cycle of pressure gradients that drive the valley wind system, providing down-valley currents at night (also known as *mountain winds*) and up-valley currents during daylight (sometimes referred as *valley winds*), as depicted in Figure 1.6. Typical pressure differences of several hPa in 100 km may be considered for deep valleys (Hawkes, 1947), while smaller gradients are expected for more shallow topographic configurations.

The size and shape of the valley determine the volume of air enclosed inside and, consequently, the temperature variation for a fixed change in heat. The type of surface, vegetation, among other things, modulates the rate of heat transferred into the atmosphere. Downslope flows also play a role in this process. In the evening transition, for example, sensible heat flux reverses on the valley sidewalls, in the shadowed parts first, and downslope flows develop. This motion transfers the cooling generated in the shallow slope layer to the valley atmosphere by means of compensatory rising and cooling motions. Thus, slope

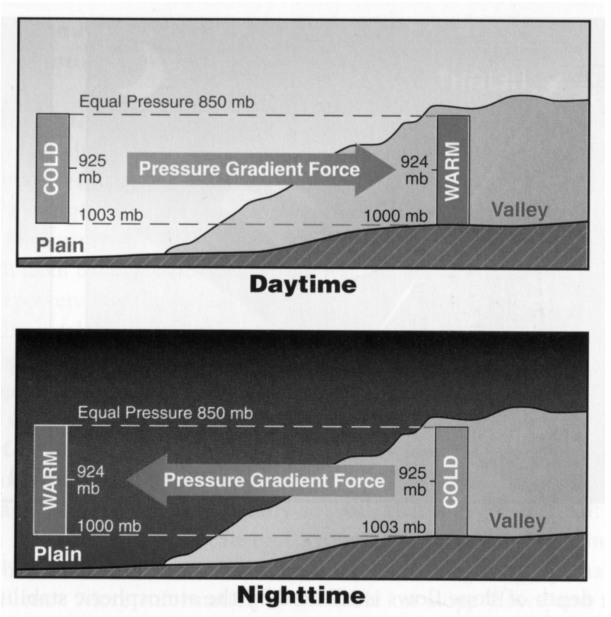

Figure 1.6: Illustration of the thermal forcing of valley-plain pressure gradients leading to the development of an along-valley wind system (from Whiteman, 2000).

winds normally appear well before the establishment of valley winds as they contribute to the initial cooling of the valley atmosphere. All these factors condition the temperature evolution within the valley and, in consequence, the onset and cessation times of the valley wind system.

Irregularities in the valley geometry can determine the local strength of along-valley pressure gradient (McKee and O'Neal, 1989). Widening and narrowing of valleys along their course can dominate this gradient, maximising the wind speed at a particular location. Similarly, the wind cycle within a smaller valley can be dominated by the valley wind system organised by a larger valley in which it resides (Davidson and Rao, 1963).

The along-valley winds are the lower branch of a closed circulation that is complemented by compensatory flows higher in the atmosphere. The development

of these circulations requires rising motions over the warm column and sinking motions above the cold column. The return flow normally forms above the valley and is not confined to a channel like valley winds. Thus, it is rarely observed since it is much weaker than the drainage current and weaker than the prevailing synoptic wind. The overall circulation can be determined by baroclinity and characterised by vorticity, after applying the Bjerknes theorem (see Chapter 7).

The key physical processes involved in the development of an along-valley wind system can be illustrated with a simplified set of Reynolds-averaged Navier-Stokes equations. This is done using an orthogonal coordinate system oriented along the valley axis (x), with y oriented on the cross-slope direction and z indicating the vertical coordinate. The down-valley momentum equation, the thermodynamic energy equation, the continuity equation and the equation of state are then written as (Whiteman, 1990)

$$\frac{\partial u}{\partial t} + u\frac{\partial u}{\partial x} + v\frac{\partial u}{\partial y} + w\frac{\partial u}{\partial z} = -\frac{1}{\rho_0}\frac{\partial p}{\partial x} + F \tag{1.3}$$

$$\frac{\partial \theta}{\partial t} + u\frac{\partial \theta}{\partial x} + v\frac{\partial \theta}{\partial y} + w\frac{\partial \theta}{\partial z} = -\frac{1}{\rho_0 C_p}\frac{\partial Q^*}{\partial z} - \frac{\partial \overline{u'\theta'}}{\partial x} - \frac{\partial \overline{v'\theta'}}{\partial y} - \frac{\partial \overline{w'\theta'}}{\partial z} \tag{1.4}$$

$$\frac{\partial u}{\partial x} + \frac{\partial v}{\partial y} + \frac{\partial w}{\partial z} = 0 \tag{1.5}$$

$$\frac{dp}{p} = -\frac{gdz}{RT} \tag{1.6}$$

where u, v and w are the velocity components in orthogonal directions x, y and z, respectively. F is friction, R is the gas constant, T is air temperature, ρ_0 is the air density, C_p is the specific heat of air at constant pressure p, Q^* is the all-wave net radiation flux and $\overline{u'\theta'}$, $\overline{v'\theta'}$ and $\overline{w'\theta'}$ represent the kinematic turbulent Reynolds fluxes of heat for the three directions. Dependent variables must be considered as averaged over an appropriated time scale, while overbars have been dropped except for the Reynolds terms. Coriolis force is considered negligible since valley motions are confined within the valley.

If the atmosphere is initially considered stationary, it is possible to give a simplified overview of the along-valley wind system evolution by considering two vertical cross-sections. The first one within the valley and the second one located down-valley, either over the adjacent plain or within the same valley but with a wider cross-section. During the evening transition, the two air masses will cool at a different rate by sensible and radiative flux divergence following Equation 1.4, depending on the properties of the valley at each cross-section,

as explained above. Integrating Equation 1.6 downward from a common pressure level on the top (well above the valley influence), it is possible to obtain the vertical pressure distribution for every column. The cooler column of air, located upvalley, will have a higher pressure at each height within the valley, developing an along-valley pressure gradient. Following Equation 1.3, this upvalley pressure gradient will generate a down-valley acceleration of the flow. The conservation of the atmospheric mass (Equation 1.5) will lead to a three dimensional movement. Once the current is activated, advection terms increase in Equations 1.3 and 1.4, redistributing the energy and momentum throughout the valley.

According to this simplified scheme, valley winds do not depend on the inclination of the underlying valley floor, since the main driven force is the horizontal pressure gradient. Actually, they have been observed in valleys where their floor is not tilted (Egger, 1990). Given an idealised valley with no large modifications along its axis concerning its topography or surface characteristics, down-valley winds accelerate and increase their depth along the valley. This along-valley divergence forces the warmer air aloft or the air from tributaries to re-fill the valley atmosphere. Such motions tend to balance the temperatures along the valley axis by advection, while sensible heat fluxes within the valley maintain the thermal differences. During evening and morning transitions, sensible heat flux reverses its sign, horizontal thermal gradients are not further maintained and valley winds gradually loss strength until reversing their direction.

1.3.2 Slope flows

Slope winds are usually referred with different names, depending on the place and geography. In general, the downslope movement of cold air is called a *katabatic* wind, while the upslope movement in daytime is termed *anabatic* wind. Other references to the katabatic winds are *gravitation* or *drainage* winds, although these terms are also used for down-valley currents.

The time and length scales of slope winds vary considerably. We can find large-scale katabatic winds in polar regions like the Antarctica or Greenland, where the snow or ice cover over long and uniform slopes (tens or hundreds of kilometres), generate downslope flows an order of magnitude stronger and deeper than those in middle latitudes. For such cases, the Coriolis acceleration plays a relevant role in the dynamics of a current than can last several weeks due to the endurance of stable conditions in polar regions during the winter season. These winds have been studied widely since they persistence and length scales are strong enough to affect the atmospheric general circulation at high latitudes (Parish

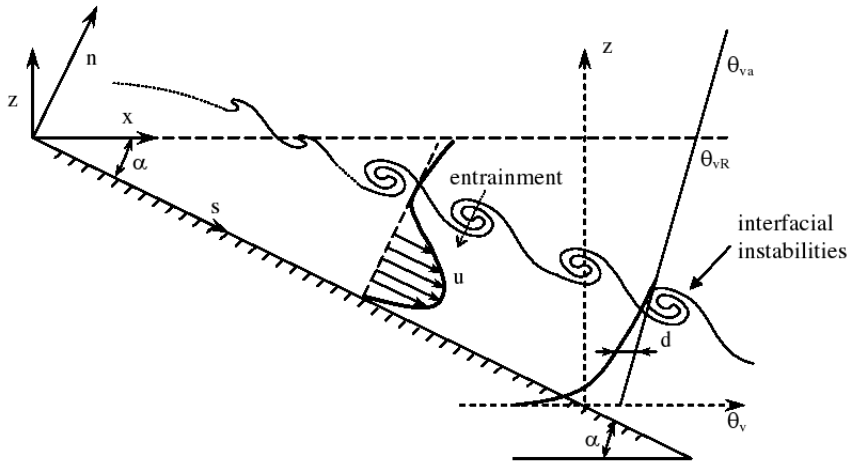

Figure 1.7: Sketch of a quasi-steady katabatic current on an idealised topography. Thin straight line θ_{va} represents the virtual potential temperature profile of the basic state. Bold thick line θ_{vR} corresponds to the virtual potential temperature profile of the katabatic wind, and d is the temperature deficit. Adapted from Princevac et al. (2008).

and Bromwich, 1991; Gallée and Pettré, 1998; Heinemann, 2002; Renfrew, 2004; Kavčič and Grisogono, 2007). For the rest of this work, the discussion is confined to katabatic flows occurring in middle latitudes, where nights are shorter and they usually develop over any sloping surface either of a valley sidewall or an isolated hill or mountain.

At night, the strongest air cooling occurs near the ground, producing the largest temperature gradient respect to the air at the same height but far from the surface influence. However, the maximum wind speed of the downslope current is formed above the ground because surface friction retards the flow at the lower levels. Consequently, the vertical wind profile takes the characteristic shape of a LLJ, with the peak of the wind speed normally within the temperature inversion. Katabatic winds have a typical thickness of 20–100 m, with maximum speeds of 1–6 m s^{-1} at normally 20–50 m above ground level (AGL) at their equilibrium steady-state. However, they are subject to local terrain and vegetation influences,

they are intermittent in time and may change over short distances (Whiteman, 1990).

Several investigators (Manins, 1992; Mahrt et al., 2001; Soler et al., 2002) have reported the presence of small-scale drainage winds particularly weak ($\sim$ 1 m s^{-1}), shallow (< 1–2 m) and non-turbulent that develop over gentle slopes. These winds have been referred sometimes as *skin flows* (Manins and Sawford, 1979a) and normally they are not considered like the rest of katabatic winds since do not seem to have the same properties (Zardi and Whiteman, 2011).

In order to describe properly the basic mechanisms of a katabatic wind, we rotate the set of equations (1.3)–(1.5) to a coordinate system oriented along (s) and perpendicular (n) to a slope of constant inclination angle α (Figure 1.7). In addition, the basic state is considered at rest, in hydrostatic equilibrium and horizontally homogeneous. Boussinesq approximation for shallow flows is applied and the flow is reduced to two dimensions, neglecting the effects in the cross-slope direction. Under such circumstances, the resulting s- and n-momentum equations, thermodynamic energy equation and the continuity equation are, respectively (Whiteman, 1990)

$$\frac{\partial u_s}{\partial t} + u_s\frac{\partial u_s}{\partial s} + w_n\frac{\partial u_s}{\partial n} = -\frac{1}{\rho_0}\frac{\partial \Delta p}{\partial s} + g\frac{\Delta\theta}{\theta_0}sin\alpha - \frac{\partial \overline{w_n' u_s'}}{\partial n} \tag{1.7}$$

$$\frac{\partial w_n}{\partial t} + u_s\frac{\partial w_n}{\partial s} + w_n\frac{\partial w_n}{\partial n} = -\frac{1}{\rho_0}\frac{\partial \Delta p}{\partial n} - g\frac{\Delta\theta}{\theta_0}cos\alpha \simeq 0 \tag{1.8}$$

$$\frac{\partial \theta}{\partial t} + u_s\frac{\partial \theta}{\partial s} + w_n\frac{\partial \theta}{\partial n} = -\frac{1}{\rho_0 C_p}\frac{\partial Q^*}{\partial n} - \frac{\partial \overline{w_n'\theta'}}{\partial n} \tag{1.9}$$

$$\frac{\partial u_s}{\partial s} + \frac{\partial w_n}{\partial n} = 0 \tag{1.10}$$

where u_s and w_n represent flows down and perpendicular to the slope, and $\Delta\theta = \theta_0 - \theta$ and $\Delta p = p - p_0$ consist in the thermal and pressure perturbations with respect to the basic state (p_0, θ_0). The ambient p_0 is determined from Equation 1.6. Besides, $\overline{w_n' u_s'}$ and $\overline{w_n'\theta'}$ are the turbulent momentum and sensible heat fluxes, respectively. The rest of variables have been defined in Section 1.3.1. Note that the set of equations (1.7)–(1.10) only includes the slope-normal turbulent fluxes and ignores the rest, consistently with the assumption of a shallow layer.

The potential temperature stratification is given by

$$\theta(n) = \theta_0(n) - \Delta\theta(s,n,t) = \theta_{r0} + \gamma z(n) - \Delta\theta(s,n,t) \tag{1.11}$$

where θ_{r0} is the value of θ_0 at a reference level and $\gamma = \partial\theta_0/\partial z$ is the ambient potential temperature gradient. The temperature perturbation $\Delta\theta$ is also usually known as *temperature deficit*.

Equation 1.8 assumes that accelerations perpendicular to the slope are negligible so that the slope flow is in hydrostatic balance normal to the slope, the so called *quasi-hydrostatic* approach (Mahrt, 1982; Haiden, 2003).

By rotating the system, the buoyancy force (which is parallel to the gravity acceleration) appears in the downslope momentum equation, represented by the second term on the right-hand side of Equation 1.7. This term is generated by the cooling of the adjacent air to the slope (Equation 1.9) and represents the driving force of downslope flows. On the right hand side, this acceleration is balanced by turbulent friction (third term) and by the pressure perturbation gradient along the slope (first term). On the left hand side, the acceleration of the flow is balanced by two advection terms that account for the intrusion of slower air into the flow.

Following the quasi-hydrostatic approximation, the pressure perturbation field Δp can be derived directly from the temperature perturbation field $\Delta\theta$ (Haiden, 2003). Thus, the first term of Equation 1.7 is only important when the temperature perturbation varies along the slope. In the case of cold air accumulating at the foot of the slope, temperature deficit increases downslope, leading to an adverse pressure perturbation gradient that can compensate for the buoyancy driving force (Zhong and Whiteman, 2008).

Equation 1.9 describes, on the left hand side, the cooling rate (first term) as a result of the advection (second term) and vertical entrainment (third term) of heat or cool by the mean wind and, on the right hand side, the radiative (first term) and turbulent (second term) sensible heat flux divergences.

Historically, the reduced set of equations (1.7)–(1.10) has been further simplified to solve it analytically. This method results in different kind of katabatic flow models depending on the assumptions done that give some hints about the relevant driving terms of the system. A first step consists in parametrising the turbulent fluxes in terms of mean flow variables.

Vertical models

Prandtl (1942) proposed a simple solution by considering a steady flow over a homogeneous slope and reducing Equation 1.7 only to the buoyancy and friction terms. For Equation 1.9, downslope temperature advection is balanced by heat diffusion. The resulted vertical profiles describe a temperature inversion

that strengthens close to the surface, with a maximum wind speed within the stable layer, reproducing the jet-like wind shape. Defant (1949) compared these analytical results with several observations, concluding that Prandtl's solution describes well the observations provided that the constant eddy diffusivities were adjusted accordingly. However, the lower part of the wind and temperature profiles were linear, with vertical gradients smoother than the experimental results. Grisogono and Oerlemans (2001a, 2002) show that vertical gradients can be more realistic by assuming diffusivity parameters that vary with height.

Prandtl analytical model is suitable to apply in polar regions, where steady flows over long and homogeneous slopes have been observed. For such cases, Kavčič and Grisogono (2007) extend this model by considering the Coriolis acceleration, which is very important for those katabatic flow scales.

Hydraulic flow models

Hydraulic models represent another type of analytical solutions obtained after averaging the terms of momentum and thermodynamic heat equations over the katabatic wind depth. These models consider the drainage flow as a single bulk layer that interacts with the overlying steady atmosphere, focusing on the layer-averaged quantities rather than on the vertical structure.

Fleagle (1950) studied the time evolution of a cold column over an inclined surface, whose work was extended by McNider (1982) by considering the air stratification. In their solutions, the drainage flow describes an oscillatory motion due to the buoyant disequilibrium between the adiabatic warming of the current as it moves down the slope and the diabatic cooling due to the downward sensible heat flux toward the underlying radiatively cooled surface. The oscillations predicted with such a simple model, with a periodicity between 15 and 90 minutes, have been observed recurrently (Doran and Horst, 1981; Van Gorsel et al., 2003; Princevac et al., 2008).

Further works applied the hydraulic model for steady flows to study the variation of the katabatic bulk quantities along the slope. This approach was started by Ball (1956) and Manins and Sawford (1979a,b). Latter authors solved the simplified model numerically to determine the role of turbulence at the top of the katabatic wind and the distribution of the drainage current along the slope depending on the angle inclination and ambient stratification. Mahrt (1982) categorised drainage flows depending on the relative magnitudes of the terms in the bulk downslope momentum equation.

Afterwards, some works have evaluated the terms of the equations from the hydraulic model with observations (Papadopoulos et al., 1997; Papadopoulos and

Helmis, 1999; Haiden and Whiteman, 2005) or with the outputs of a mesoscale model (Renfrew, 2004, for a katabatic wind simulated in the Antarctica).

Katabatic flows have also been studied by numerical modelling using large eddy simulations (LES) in an idealised context (Skyllingstad, 2004; Smith and Skyllingstad, 2005; Fedorovich and Shapiro, 2009; Largeron et al., 2010) or over more realistic complex terrain through mesoscale simulations (Savage et al., 2008, see Chapters 2 and 4).

1.3.3 Thermally driven winds in basins

When topography takes the form of a depression in the earth's surface, partially or fully surrounded by elevated land, the resulting configuration is defined as a basin. In this case, the diurnal thermally wind system lacks for valley winds since there is not a well defined channel. Thus, basins are characterised by slope winds and mountain-plain winds. At night, the valley wind is responsible for removing the air at the bottom of the valley, therefore its absence in small basins can lead to extreme cold minimum temperatures (Zängl, 2005b). As explained in Section 1.2.4, for large and wide basins, the ambient air can penetrate into the basin atmosphere. The buildup of a temperature inversion is then reduced to a shallow layer over the surface in which drainage flows develop.

1.4 The study of the thermally driven flows and nocturnal cooling

The scientific study of the thermally driven winds started in the 19th century but it was in the 1920s when the basic concepts were settle down. The observations compiled during those decades in the Alps led Wagner (1938) to the description of the still valid basic concepts of the wind regimes in major alpine valleys (Vergeiner and Dreiseitl, 1987). Hawkes (1947) reviewed the previous research works, mainly published in German and French, bringing this knowledge to the Anglo-Saxon scientific community for the first time. Similarly, Defant (1951) translated part of his findings in English, including the interrelationship between slope and valley winds systems with the well known figure of the four diurnal phases.

Katabatic winds had been also observed with meteorological instruments at the first part of the 20th century. An example is the earlier study of a katabatic flow

and its interaction with the buildup of a cold pool at the foot of the slope done by Heywood (1933) for a narrow valley in England. The interest to describe the basic mechanisms of katabatic winds led to develop analytical solutions. Jeffreys (1922) was the first one to provide a solution for the vertical profiles of a steady flow, similar to what Prandtl (1942) described 20 years later. Theoretical works were appearing in the following years (Fleagle, 1950; Ball, 1956) until late 1970s, when scientific community experienced a resurgence of interest in all kind of local winds (Vergeiner and Dreiseitl, 1987).

Progress in numerical computation allowed to solve the set of equations (1.7)–(1.10) numerically, taking new parametrisation from previous laboratory experiments (Ellison and Turner, 1959). This approach led to the construction of new hydraulic models for the katabatic winds (Manins and Sawford, 1979b; McNider, 1982; Fitzjarrald, 1984) that could be barely tested with the few experimental data available during those times, mainly confined to the wind field (Whiteman, 1990).

The resurgent interest aforementioned yielded to the proliferation of numerous field experiments focused in the study of the mountain wind system, like ASCOT program in west US (Clements et al., 1989) or MERKUR (Reiter et al., 1982) and DISKUS (Freytag, 1985) for the Alps. Main part of these experiments took place during short campaigns (1–2 weeks) with the attempt to investigate the wind circulations in simple topography under clear, fair weather conditions. Besides, the focus was centred in the mean variables rather than on turbulent fluctuations.

With these experimental data, conceptual and analytical models were developed during 1980s to understand key aspects of the valley dynamics. Vergeiner (1987) sought for basic relationships between topographic characteristics and the time response and strength of the valley flow, while Whiteman and McKee (1982) investigated the role of the energy budget and topography in the nocturnal cooling of the valley atmosphere, among other examples.

The progress done in the development of numerical weather models yielded to an incipient use of mesoscale simulations as a complementary tool to understand the observations (Fast et al., 1996). The combination of new experimental campaigns with mesoscale simulations increased the following years and the knowledge about characteristic mean flow structures of the valley and slope circulations and their corresponding thermodynamic structure was relatively well established by the end of 1990s, with a complete review available in Whiteman (2000).

The study of the atmospheric turbulence goes back to the beginning of 20th century with the attempts to understand turbulent mixing (Taylor and Green, 1937, among others). It is the time when Von Karman and Prandtl formulated the mixing length hypothesis for the direct application to the atmosphere. Later,

arrived the seminal works of Kolmogorov (1941) on spectral characteristics of the atmospheric turbulence and of Monin and Obukhov (1954) on similarity theory. Next decades, boundary layer meteorology was mainly concerned with flows over flat and homogeneous terrain, collecting experimental data to advance in the interpretation of the observations and test the theoretical insights done previously. The horizontally homogeneous assumption was a first step in order to reduce complexity in the problem and focus the main efforts in the study of the vertical structure of turbulence and its time evolution. This process culminated in the first experimental field campaigns that took place in the Great Plains of USA in 1953 (Lettau and Davidson, 1957) and in Australia in 1967 for the Wangara experiment (Clarke et al., 1971).

The first simulation was also devoted to deal with the horizontally homogeneous ABL evolution, carried out by Deardorff (1972), who first used a large-eddy simulation (LES). After that, a range of valuable contributions were done (see Nieuwstadt et al., 1993, for a review) to consolidate the modelling as a complementary tool to ameliorate the understanding of the observations. Similarly, laboratory experiments were also an alternative to improve the knowledge about ABL, with the seminal work of Willis and Deardoff (1974) to study the eddy structures within the CBL, assuming again horizontal homogeneity.

The study of the SBL regime with those new tools arrived almost one decade later since the turbulence characteristics under stable conditions make more difficult its treatment (see Section 1.1). LES simulations for this regime over flat and homogeneous terrain were firstly addressed by Mason and Derbyshire (1990), while Thoroddsen and Van Atta (1992) dealt with one of the first laboratory experiments. The nineties were also the scenario for the first attempts to perform LES simulations over non-uniform surfaces. Schumann (1990) reproduced a thermally driven flow over a sloping (but still homogeneous) surface in the convective regime, while Dörnbrack and Schumann (1993) studied the boundary layer development over smooth sinusoidal hills.

During those decades, observational instruments were largely improved and there was the need to take up again the performing of major experimental campaigns in the low and middle latitudes, with especial regard to the SBL regime, to take advantage of those new improvements. The SABLES 98 campaign (Cuxart et al., 2000) took place on the northern Spanish plateau in 1998 with the purpose to investigate different aspects of the boundary layer dynamics under stable conditions. One year later, it was followed by the CASES99 campaign (Poulos et al., 2002) in Kansas (US). In both cases, the field campaigns were mainly conceived as flat nocturnal boundary layer studies. However, it was necessary to consider terrain irregularities of the respective sites in order to understand much of the phenomena observed (Cuxart, 2008), like the arrival of density currents (Sun

et al., 2002) or the presence of drainage flows due to local slopes (Soler et al., 2002). These quasi-permanent LLJs of multiple origins generate gravity waves (Viana et al., 2010) or modulate the nocturnal temperature inversion (Sun et al., 2003), among other relevant aspects.

In addition to the specific field campaigns, observations of the SBL were supplemented by measurements made over a long period of time from high meteorological towers installed at different parts of the world, like in Boulder (US) or Cabauw (The Netherlands), or at the same place where the SABLES 98 campaign was held (Conangla and Cuxart, 2006).

At this point, it was clear that terrain heterogeneities and sloping topography, 70% of the Earth's land (Strobach, 1991), play a relevant role in the SBL development, claiming for a closer combination of the knowledge achieved by both mountain meteorology community and boundary layer meteorologists.

Moreover, the continuous progress with increased horizontal and vertical resolutions in numerical modelling at the beginning of the present century has yielded to mesoscale simulations able to capture the low-level currents developed within large basins (Zhong and Fast, 2003). These improvements have contributed to confirm hypothesis about the origin of the observed currents. Besides, new LES simulations performed under stable conditions allowed to study the vertical mixing through the wind maximum of a LLJ, which acts as a barrier with sporadic bursts of turbulence that shortly connects the air above and below this maximum (Cuxart and Jiménez, 2007). Pioneering LES simulations of katabatic winds over idealised slopes have been also addressed during these years, giving sounding information about their turbulence structure (Skyllingstad, 2004; Smith and Skyllingstad, 2005; Largeron et al., 2010).

Such proliferation of numerical models has not been matched with a corresponding increase in observational studies, more time- and source- consuming. An experimental benchmark to validate basic questions about surface heterogeneities or about downslope flows concerning the internal mechanisms (*i.e.* sensible heat and radiative flux divergences) or external influences (winds above the slope layer and ambient stability) had been unavailable (Zhong and Whiteman, 2008). Moreover, as soon as higher spatial resolutions have been reached with numerical models at all scales (from global climate to LES), the use of turbulence parametrisation developed under the framework of a flat and horizontally homogeneous terrain are called into question (Rotach and Zardi, 2007).

Therefore, in the last years new field campaigns have been designed to contribute to this historically lack of experimental data. The VTMX campaign (Doran et al., 2002) was conceived to study the vertical transport and mixing of atmospheric variables over complex terrain in the Salt Lake Valley, Utah (US). Part of the

MAP-Riviera project (Rotach et al., 2004) was devoted to the study of the ABL in complex terrain, with a special focus on the turbulence structure and test which properties designed for an ABL over flat and homogeneous terrain are still valid over highly complex terrain (Rotach and Zardi, 2007). The Energy Balance Experiment (EBEX) project (Oncley et al., 2007) or the Lindenberg Inhomogeneous Terrain-Fluxes between Atmosphere and Surface Study -LITFASS- (Beyrich and Mengelkamp, 2006) are examples of the efforts of the experimentalist community to address the effects of the terrain heterogeneity.

The complexity of real mountain valleys provides a challenge for numerical simulations. The spatial resolution of present models is not yet fine enough to reproduce all the small scale features of valley winds. Information about land cover, land usage and soil moisture are often approximate or incomplete. However, the smoothing of the terrain for large basins are not that far from reality provided the focus is stressed on the general behaviour of the thermally driven currents and the heterogeneous cooling. Moreover, the use of parametrisation for turbulence based on considerations over flat and homogeneous terrain is relatively acceptable considering such smoothed surfaces.

Model outputs must be carefully compared with available observations to make sure that simulations capture the relevant mechanisms. This is specially challenging under stable conditions, where the ABL evolution is strongly influenced by local features. Additional confidence is gained when comprehensive field observations are available for comparison. Therefore, an effort must be done in examining all the available experimental information to complement the simulation outputs.

1.5 Motivation and outline of thesis

Under this framework, the underlying research question that provides the motivation of this thesis can be formulated as "What is the nature of the nocturnal air circulations within a given topographical configuration under stable conditions?". To address this question we must examine how these flows originate, evolve and organise at a slope and basin scales, what is their spatial structure and what is their contribution to the SBL behaviour over complex terrain.

As stated in Chapter 2, thermally driven flows are locally generated and their characteristics therefore depend on the local features of an specific site. However, the analysis of these flows in different places can contribute to identify those features that are common to all of them and finally put the findings into a more

general context. This thesis seeks to contribute in such objective by analysing the thermal and wind structure of the SBL at different locations in middle latitudes.

The chapters in this thesis are -or will be- individually published in the reviewed literature as stand-alone papers. As such, some overlap occurs between this introduction, the chapters, and the general conclusions. Although a detailed description of the chosen landscapes and tools are present in the corresponding chapters, a brief summary is exposed here.

The landscapes evaluated correspond to four distinct topographical configurations with well defined hydrological basins of different scales.

The mountainous topography of the **island of Majorca** in the western Mediterranean defines three main basins at the coast. The terrain in the centre of the island is elevated, generating gentle slopes that face to the sea through these three major basins.

The **Duero basin**, a large basin located in the northern part of the Spanish plateau, is enclosed by high mountain ranges that isolate it from the ocean influence. The basin is wide, with a circular shape and relatively small topographical irregularities at the bottom.

The **Ebro valley**, located at the eastern border of the Duero basin, is a large valley with a triangular shape and a well-defined valley axis following the Ebro river (NW-SE). The main axis is channelised up-valley but it progressively widens in the down-valley direction. The widest part is blocked by a pre-coastal mountain range perpendicular to the valley axis, configuring a circular sub-basin at the eastern part of the valley (the Lleida basin). The pre-coastal mountain range, parallel to the Mediterranean coast, has a homogeneous slope that gently drops toward the center of the sub-basin. This configuration generally limits the influence of the Mediterranean sea to the sub-basin except in Summer, when the sea breeze manages to arrive at this area.

Finally, the **Meteor crater** consists in a small, enclosed basin located in the Colorado plateau, Arizona, with a length scale much smaller than the previous domains. This circular shaped crater is embedded into a large, flat and homogeneous 2% slope.

All these sites have been explored using different available observations, including objective-oriented measurement campaigns for the Ebro valley and Meteor crater areas. Besides, high-resolution mesoscale simulations have been performed for selected cases in Majorca and Duero basin sites. A list of these tools is exposed below:

1. **Mesoscale simulations.** The numerical model used is the Meso-NH (Lafore et al., 1998), a non-hydrostatic mesoscale atmospheric model of the French research community. It has been operated with a very fine vertical resolution to capture the details of the nocturnal low-level flows. Mesoscale simulations for single cases of study have been performed and verified against the observations, providing encouraging results. The characteristics of each simulation are deeply described in the corresponding chapters.

2. **Satellite imagery.** The land surface temperatures (LSTs) estimated from satellites are a useful tool to analyse the thermal spatial distribution and its temporal evolution at a basin scale. Under fair weather conditions, the presence of clouds is residual and satellites provide a unique two-dimensional field estimated from the observations. This information can be also used to verify mesoscale simulations, as explained in Jiménez et al. (2008).

   The spatial and temporal resolution of the images depend on the type of satellite, whether it is polar-orbiting or geostationary. The fields used come from (i) the MODerate resolution Imaging Spectroradiometer (MODIS, Salomonson et al., 1989), on board of the Terra and Aqua satellites, (ii) the Advanced Very High Resolution Radiometer (AVHRR) from the NOAA satellites (Kidwell, 1998), and (iii) the Visible and Infrared Spin Scan Radiometer (VISSR) from Meteosat-7 (Prata et al., 1995). Polar-orbiting satellites (Aqua, Terra and NOAA) provide about two images per night (low temporal resolution), but with a fine spatial resolution similar to mesoscale simulations (1 km^2). Meteosat-7 is a geostationary satellite and their images have a coarser spatial resolution of about 25 km^2 in middle latitudes, but with a higher temporal resolution (30 min).

3. **Automatic weather stations.** Regular automatic weather stations (AWS) from most of the official networks have measurements of wind direction and velocity at 10 m AGL (2 m for agrometeorological stations), and 1.5-m temperature, humidity, and atmospheric pressure. Wind speed is generally probed with regular cup anemometers and these sensors have a threshold value between 0.5 and 1.0 m s^{-1}. Under stable conditions, the wind at those measurement heights is usually weaker, providing values that are not trustworthy. The AWSs are usually irregularly distributed throughout a given site. Most of them are located in places subject to local irregularities like small valleys, summits or shorelines (for the case of Majorca). The information obtained is therefore not representative of a large area. In consequence, the estimation of either the nocturnal wind system or the spatial distribution of temperature is very difficult. Similarly, the point-to-point comparison against the mesoscale simulation outputs or satellite

imagery is not straightforward. However, their advantage is that AWSs are installed permanently to record data routinely and provide long time series. The statistical use of AWS data adds representativeness to the conclusions extracted from single case studies.

4. **CIBA 100-m mast.** The research centre for the lower atmosphere (CIBA) is located at the central part of the Duero basin and has quartered several experimental campaigns during last years, like SABLES 98 (Cuxart et al., 2000) or SABLES2006 (Yagüe et al., 2007). The centre is provided with a 100-m tower that was recording data continuously during 10 months (September 2002 – June 2003) with a variety of slow and rapid sensors. These data have been used to study statistically the observed LLJ (Conangla and Cuxart, 2006) and the SBL (Conangla et al., 2008). These results allowed Cuxart (2008) to propose a nocturnal basin-scale organisation to explain the observations.

5. **Lleida Basin Flow (LBF) experiments.** The flow at the eastern part of the Ebro valley (the Lleida basin) has studied with the installation of a new remote sensing device (the WindRASS by Scintec), together with short special observation periods, since 2009. The WindRASS is a system that estimates the temperature and wind vertical structure, among other ABL variables, up to 360 m AGL (see Chapter 7 for more details). This system is supplemented with one energy budget station (EBS) that provides all the individual terms of equations 1.1 and 1.2. In the Lleida basin there are 22 AWS separated with an average distance of 10 km and one of them is installed just aside the WindRASS and EBS. Two special observation periods were held during several days of July 2009 and 2010. During the first one, a meteorological mini-unmanned aerial vehicle (M^2AV, Van den Kroonenberg et al., 2008) was operated to perform several flights around the area under different regimes. The second period consisted in one day of continuous operation with a tethered balloon system. These two special periods allowed to compare the WindRASS estimations against the *in situ* measurements provided by the unmanned aircraft and the tethered balloon.

6. **METCRAX 2006.** A month-long meteorological field experiment was conducted in October 2006 in Meteor Crater, Arizona, focused on two research topics (Whiteman et al., 2008). First, the physical processes leading to the buildup and breakdown of temperature inversions in a small and enclosed basin, avoiding the complications introduced by more complex topography. A second objective was related with the atmospheric seiches, defined as air oscillations in the basin caused by wind disturbances at the basin

crest. Nonetheless, the complete data set provided by this experimental field campaign can be used to address a wide range of questions related with the SBL within small basins.

1.5.1 Outline of the thesis

Chapter 2 examines the nocturnal wind system at an island, basin and slope scales in Majorca. The interaction of the synoptic flow with the topography of the island and the rest of local winds are described by means of a mesoscale simulation carried out for a selected winter night. The model outputs are analysed to identify the structure of the flow in the Palma basin and the katabatic wind generated over the surrounding sloping terrain. The characteristics of the downslope current are studied according to the hydraulic model. The observations from the AWS network and NOAA imagery are used to confirm some of the results obtained by the simulation.

Chapter 3 addresses the same type of study for the Duero basin, focusing in the temporal and spatial heterogeneity of the surface cooling and the organisation of the flow at a basin scale. The thermal distribution is inspected through the satellite imagery and measurements of the meteorological network and the CIBA tower. An attempt to classify the large variety of local regimes developed throughout the basin under stable conditions is conducted using the vertical profiles of wind and temperature given by the mesoscale simulation.

This simulation generates a downslope current at the southern mountain range of the Duero basin which is analysed in detail in Chapter 4. In addition, the application of the hydraulic model to katabatic flows developed over real topography is assessed using the outputs of the mesoscale simulation. The terms of the bulk momentum and heat equations are computed to inspect the closure of the budget equations.

In Chapter 5, the reversal of the daytime upslope flow on the sidewall of the Meteor crater is inspected using all the available observations from the METCRAX 2006 field campaign. The analysis considers the time evolution of the surface radiation (Equation 1.1) and energy (Equation 1.2) budgets, and temperature, mean flow and turbulence structure over the slope. A wavelet analysis provides information about the scales involved in the flow transition.

The Ebro valley nocturnal circulations at a basin scale are addressed in the following chapters. A climatological study of the stable nights is described in Chapter 6. The analysis is carried out by filtering a 9-year-long time series gathered by the agrometerological station of Gimenells in the Lleida basin. The nighttime evolution of wind, humidity and temperature of the surface layer un-

der stable conditions is statistically described and the prevalent wind directions are related to the basin topography.

The conclusions from this early study are further extended in Chapter 7 after inspecting the results of the additional observations given by the LBF experiments. The characteristics of the observed LLJ are explored primarily by the WindRASS system and explained through examples of selected cases.

Finally, Chapter 8 provides a general overview of the results presented in the thesis, and discusses future research.

Chapter 2

Nocturnal meso-beta basin and katabatic flows on a midlatitude island

This chapter is based on
Cuxart, J., M. A. Jiménez, and D. Martínez, 2007: Nocturnal meso-beta basin and katabatic flows on a midlatitude island. *Mon. Wea. Rev.*, **135**, 918–932;
and
Martínez, D., and J. Cuxart, 2007: A gravity current study within the Palma de Mallorca basin. *Física de la Tierra*, **19**, 21–36.

Abstract

A mesoscale simulation for the island of Majorca in the Western Mediterranean Sea is used to study the nocturnal system of winds under weak synoptic pressure gradients. A very high vertical resolution is used in the first 500 meters above ground level to characterize with large detail the thin circulations close to ground, namely basin and katabatic flows. It is found that the island, the basin and the slope scales interact strongly, especially when a quasi-steady state is reached in the second part of the night. A high mountain range creates a high pressure area upwind where local winds can develop. Katabatic flows converge to the valleys, where they interact with a cold pool, which is advected slowly to sea

by the land-sea night-breeze effect combined with a topographic forcing. The katabatic flows experience small entrainment at the top and have well defined characteristics. The results are partially confirmed by the observations and some satellite images.

2.1 Introduction

The study of the atmospheric boundary layer normally assumes horizontal homogeneity. However, when a region is under slack synoptic-scale pressure gradients, the local meteorology is largely determined by the heterogeneities at the surface. The nighttime spatial structure and temporal evolution are far from stationary or homogeneous, especially in stably stratified conditions, and with light synoptic winds and clear skies the role of the topography becomes extremely important, say dominant (see, for instance, the VMTX campaign in the Salt Lake Valley, Doran et al., 2002); for example, cold pools in the center of the basins, out-valley circulations, slope flows or other kinds of low-level jets are present. All these features affect the local climate. To determine their spatial structure and temporal evolution is crucial to understand the air circulations within a basin.

The quasi-horizontal motions generated in this way transport air to locations that can be very distant from their sources, especially if they are combined with larger scale temperature gradients, such as a sea-land discontinuity or baroclinity at the scale of the basin (see Stull, 1988). At one particular point, for instance at a meteorological station, the first arrival of these currents may result in sudden changes in the wind speed and direction, changes in the surface cooling rate or turbulence bursts (Blumen, 1984).

This increase of understanding on how slope and basin flows behave and interact should be possible with objective-oriented measurement campaigns and ad-hoc numerical simulations that can ideally produce better theories and new parameterizations in models. The topographically induced flows are, obviously, locally generated, and their characteristics therefore are very location dependent. Observational and numerical studies in many different locations can contribute to discern what the main factors for each case are and seek the common features of them all. Our study aims to contribute to such effort, placing itself in respect previous efforts and checking against existing theories. Any findings can lead to practical applications on fields such as agrometeorology, road and

airborne transportation, energy consumption in housing or subjects related to biometeorology, including pollutant production and transport.

On complex terrain, it is necessary to analyze how the flows function at the scale of the slope and how they organize in a basin. After the pioneering study of (Prandtl, 1942) that analyzed the stationary vertical structure of a katabatic wind, these flows have been studied basically considering the bulk evolution of the drainage flow column, as in Fleagle (1950) or McNider (1982), who considered also the effect of the ambient stratification. Assuming steady-state, the theory can be extended to study the along-slope evolution as in Ball (1956) or Manins and Sawford (1979b). Those studies found analytical solutions from a balance of two or three dominant terms in the momentum and heat budget equations. Mahrt (1982) made a detailed scale analysis and a critical study of all the possible approximations. He provided a framework to study real katabatic flows, as in Heinemann (2002) or Renfrew (2004), that used it to investigate the dynamics of katabatic flows over Greenland and the Antarctica, respectively. Haiden and Whiteman (2005) applied it to a katabatic flow measured in mid-latitudes.

Valley wind dynamics have also been analyzed, although its study is more complex due to the different length and time scales involved. The valley or basin dynamics include thermally driven wind systems such as slope and valley winds, which have been studied for many years and the basic concepts were summarized by Defant (1951). A valley wind system can be modified by the presence of a regional pressure gradient (Whiteman and Doran, 1993), the formation of a cold pool (Banta et al., 2004), where drainage flows can play a very important role (Geiger, 1965), mechanical effects induced by the topography, etc (see Whiteman, 1990). In order to increase its understanding, several campaigns have taken place. For instance, the ASCOT program that was developed during the decade of 1980 with the aim to get more information regarding transport and diffusion in complex terrain (Clements et al., 1989); the MAP-Riviera project (Rotach et al., 2004) or the VTMX campaign (Doran et al., 2002) can also be mentioned as two more recent examples.

The observational study of the topographically generated flows at the scale of a basin is not straightforward. A practical complementary tool is mesoscale modeling. In this work, high-resolution mesoscale simulations are performed for the Island of Majorca and their characteristics are explored and checked using the available observations.

The island of Majorca (Figure 2.1) is the largest of the Balearic Islands archipelago in the Western Mediterranean Sea, 200 km offshore of the east coast of the Iberian Peninsula. It has a characteristic size of 100 km, a large mountain range at its northwestern side (Serra de Tramuntana), with an average height of 700 m above-

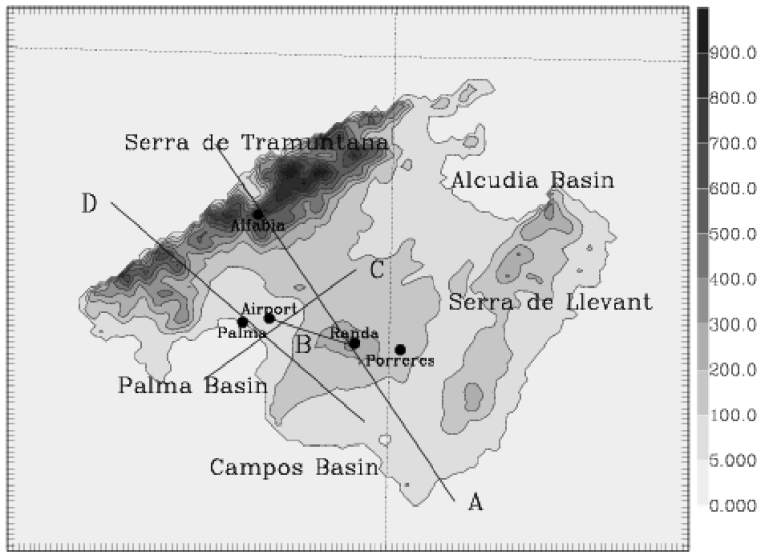

Figure 2.1: The inner domain (with a length size of 125 km × 100 km in the x and y directions, respectively) of the run corresponding to the island of Majorca, with the three well defined basins: Palma, Alcudia and Campos. Lines correspond to cross-sections in further figures and points to relevant locations

sea-level (ASL) and the central part has several peaks between 1000 and 1450 m. On the opposite side (SE) there is a discontinuous lower mountain range (Serra de Llevant), with an average height of 300 m, that perturbs much less the flow than the Serra de Tramuntana. The center of the island is relatively flat, although elevated about 200 m ASL and with a small central mountain (Randa, 500 m). This topographical configuration results in three main basins: the Palma basin at the SW part, the Campos basin at the SE, the Alcudia basin at the N, plus two coastal narrow basins between the mountain ranges and the sea at NW and E.

The island has a population of about 750000 inhabitants and more than 370000 live in the city of Palma de Majorca and its surroundings, located in the Palma basin. This basin has a characteristic size of 40 km and it is completely surrounded by mountain ranges and elevations that make it a semi-closed basin, except the wide bay at the southern part. In the center of the basin, at about 10

km N of the city, there is an installation where residuals are burnt that is upwind of the town when drainage flows occur. Within the basin, a international airport with very busy traffic is located east of the town. On the other hand, the inland is mostly agricultural and there is interest in a good characterization of the cold areas at night.

This work intends to describe the nocturnal circulations at the island, basin and slope scales. A general overview of the daytime part of the cycle was made by Ramis et al. (1990). Section 2.2 is devoted to the interaction of the island with the synoptic flow and the general system of local winds that develops inland. In section 2.3, the main characteristics of the flows in the Palma basin during nighttime are explored. In the eastern part of the Palma basin, a quasi bi-dimensional slope is found, with a drop of terrain height from an elevation of 300 m to the sea level in about 15 km. The simulation generates a katabatic flow that is analyzed in section 2.4 according to the proposals of Mahrt (1982) or the more recent work of Renfrew (2004). A summary of the results and a prospective for further work is given in section 2.5.

2.2 The interaction of the island with the general flow

To perform this study, the Meso-NH model of the French community has been used (Lafore et al., 1998). The model can be used in a large variety of configurations (from Large-Eddy simulations to synoptic scales). Its performance for several boundary layer regimes has been tested successfully (Cuxart et al., 2000) and the stable boundary layer has received special attention lately (Jiménez and Cuxart, 2005; Cuxart and Jiménez, 2007). These late works have shown that, in LES mode, an adequate prescription of the mesoscale forcing is necessary to perform successful simulations of the stable regime, and that these forcings are to be determined specifically for each location, taking into account the local and basin topography. Mesoscale modeling is an appropriate tool to estimate these forcings.

A case with a slack synoptic pressure gradient is chosen; the archipelago is very close to the center of a winter high pressure system, with the flow coming from the southeast (of about 4 m s^{-1} over the sea at 10 m ASL), thus normal to the main mountain range at the NW. This is a typical winter high-pressure situation with weak large-scale winds for this area. The skies were cloudless and the humidity was low (below 30%). The situation was steady at the synoptic scale over the complete simulation time. Two domains are chosen, the largest one with

a resolution of 5 km and the inner one of 1 km, covering only Majorca. The outer domain allows having a soft transition from the lateral boundary conditions provided by the European Centre of Medium-range Weather Forecasts (ECMWF) analyses to those of the inner domain. The resolution of 1 km is thought to be sufficient to capture most of the almost horizontal advective transport in the lower layers, fitting well with the resolution of the available physiographical data sets and avoiding the use of the computationally expensive three-dimensional turbulence scheme.

The simulation runs from 1200 UTC (12 local solar time) on January 5th, 1999 to the dawn of the next day, thus covering completely the 15-hour-long night. It has been run on the ECMWF supercomputers. In this work only plots of the inner domain will be shown, many of them at 0400 UTC, considered a time representative of the quasi-steady state situation of the second part of the night. The vertical resolution is very fine near the ground, to be able to capture all the details of the low level flows: close to 3 m in the surface layer, with a stretching factor that leads the resolution to about 7 m at 500 m ASL and to 600 m at the model top. Such a fine vertical resolution implies very short timesteps (below 2 s), especially at mountain slopes. Since such a simulation depends very much on the physiographical and the physics packages, its realism will depend very much on the good work of the schemes of turbulence (Cuxart et al., 2000), radiation (Morcrette, 1990) and soil-vegetation (Noilhan and Planton, 1989), together with a good representation of the terrain physiography as already discussed by Zhong and Fast (2003) using several mesoscale models. Here the Corine database (Heymann et al., 1994) is used, with a horizontal resolution of 1 km (Masson et al., 2003) (see Table 2.1).

The general flow in the area is from the SE. The streamlines at 0400 UTC show (Figure 2.2a), that the flow is not perturbed very much as it flows over the island at a height of 1000 m ASL. However at 100 m ASL (Figure 2.2b), the NW mountain range (Serra de Tramuntana) is clearly blocking and diverting the flow around it, with a bifurcation point near the centre of the island. The estimated Froude number ($Fr = \frac{U}{Nh}$, with N = 0.01 s^{-1}, U= 4 m s^{-1}, h = 800 m, average mountain height) is about 0.6, indicating that some of the air flows over the top of the range, while air at lower altitudes separates to flow around it (Figure 14.14, Stull, 1988). A low pressure area is found downwind of the main range, marked by an eddy, whereas upwind there is a mesobeta high pressure area (not shown). Therefore the center of the island is an area of low wind speeds and is able to develop local winds determined by the topographical configuration.

The exploration of the vertical cross section in the NW-SE direction (Figure 2.2d) indicates that the topographic obstacles perturb the flow for several hundreds of meters in the case of the Randa mountain, and for several thousands of meters in

Table 2.1: Summary of the setup of the run

Domains Inner domain Outer domain	2, two-way nested 125 km×100 km 480 km×320 km

Vertical resolution	near the ground: Δz = 3 m;
	at z = 500 m: Δz = 7 m;
	top of the domain: Δz = 600 m

Equation system	Durran (1989)
Lateral boundary conditions	Analysis from the ECMWF every 6 hours
Radiation scheme	Morcrette (1990)
Advection Scheme	Flux corrected second order centered
Turbulence Scheme	1-Dimensional TKE scheme: Cuxart et al. (2000) mixing length: Bougeault and Lacarrère (1989)
Soil Scheme	ISBA (Noilhan and Planton, 1989) cover types: CORINE (Heymann et al., 1994) z_0 (sea and inland waters): Charnock (1955) z_0 (artificial areas): Masson (2000)

the case of the Tramuntana range, developing stationary waves above them. This is in agreement with the potential temperature field (not shown). The same figure shows that the areas between the mountains have structures determined by the shape of the basins, with wind directions mainly determined by the mountain slopes, and vertical extension between 100 and 250 m above the ground.

The organization of these low-level structures is mainly found to be by topographical basins (Figure 2.2c). The streamlines at 10 m show that the air is flowing from the center of the island to the sea in the three main basins (Palma, Alcudia and Campos). The Llevant mountain range, despite of its modest vertical height, is able to produce land-to-sea winds strong enough to stop the progression inland of the general flow from the SE and is a key factor to shelter the center of the island and allow the development of local structures there. Within each basin, there is convergence in the center and maximum outland wind speeds flowing over the warmer sea where they become thermally unstable and finally lose identity.

This organization is also shown in Figure 2.3, where the values observed by the Automatic Weather Stations (AWS) are plotted over the modeled fields. The direction and the wind speed (Figures 2.3a and 2.3b) are well captured except in a sheltered station at the north of the island, showing that the main patterns of the circulations are correctly simulated. The existence of areas with very weak

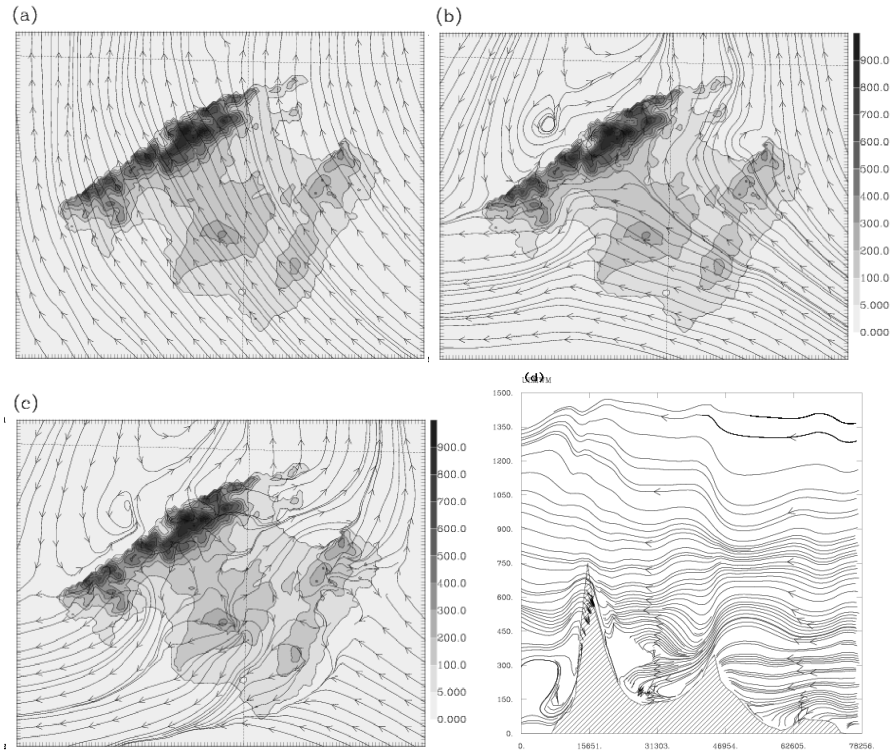

Figure 2.2: Stream lines at 0400 UTC at different heights: (a) 1000 m; (b) 100 m and (c) 10 m. (d) The vertical stream lines following line **A** in Figure 2.1

winds at 10 m is confirmed, although the number of inland stations is very low. The areas of lowest temperature are located in the center of the island where the wind is almost calm. These areas seem to act as sources of cold air that is drained following the topography to the center of the basins, flowing out to the sea (Figure 2.3c). However this description is probably conditioned by the mountain wave and eddy circulations described before, reinforcing the patterns in some areas (outland flows at the Palma and Alcudia basins) and inhibiting them in others (Llevant mountain range).

The 1.5 m-temperature field has spatial patterns similar to the ones shown by the NOAA image as the same as shown in Mira et al. (2006), their Figure 2. Nevertheless the modeled temperatures are somewhat warmer than the AWS observed ones. To evaluate if the time evolution is well captured, the observed

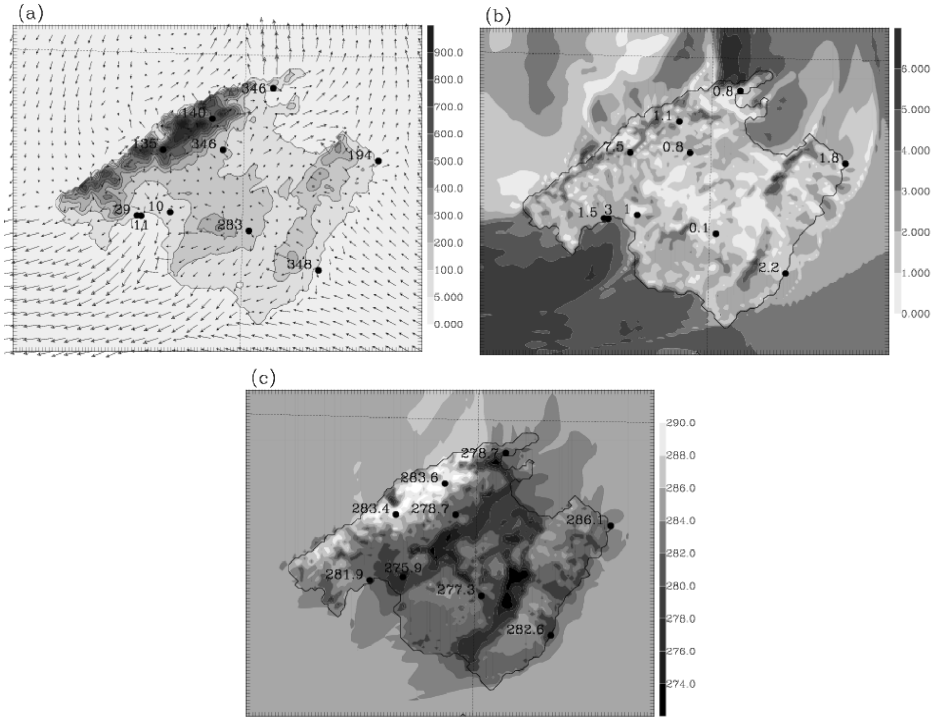

Figure 2.3: Horizontal cross sections at 0400 UTC for (a) wind direction (degrees) at 10 m, (b) wind speed (m s^{-1}) at 10 m and (c) potential temperature (K) at 1.5 m. The surface weather stations are indicated with a point with the observed value aside. In (a), only one arrow in every 3 grid points is drawn.

and modeled timeseries for some stations are compared (Figure 2.4). In Porreres, located at the east foothill of the Randa range in the flat central part of the island, the observations show almost calm wind for most part of the night. The AWS have an estimated threshold value of, at least, 0.5 m s^{-1}. The model generates winds larger for this location of about 1 m s^{-1}, with a good approximation to the wind direction. The temperature drop is larger in the observations. The very weak observed real wind allows the surface to cool radiatively practically without shear-generated turbulence present. Since the model has larger wind,

it has enhanced shear and mixing in the surface layer, therefore allowing for a less intense near-the-surface cooling. The model does not impose any minimum value on the wind speed or on the turbulence kinetic energy. Other reasons for the over-estimation of the low wind speeds might be that the model generates too active slope flows (see section 2.4) or that the used similarity theory is not apt for strongly stratified conditions (Pahlow et al., 1999). The same behavior is observed at the airport, inside a cold pool in the Palma basin, and will be discussed later.

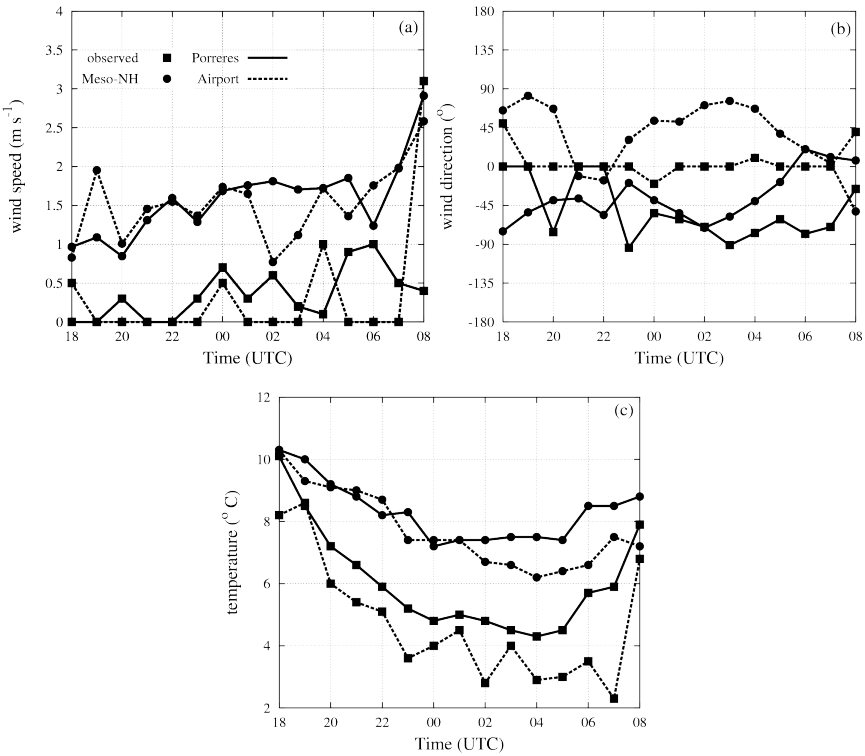

Figure 2.4: Modelled and observed time series for (a) wind speed (in m s^{-1}), (b) wind direction (in degrees where the north corresponds to 0°) and (c) temperature (in °C) at Porreres and the Airport (see the locations in Figure 2.1), corresponding to an inland and a coast sites, respectively.

2.3 Circulation in the mesobeta Palma basin

The Palma basin has the approximate shape of a semi-circle with a radius of approximately 20 km, opening to the sea at the SSW at the Palma bay. Three different types of terrain surround the almost flat central part of the basin, of about 10 km of radius. At the W and NW the very steep Tramuntana range is composed by a number of narrow valleys where the mountains top at about 1000 m and the bottom parts are at about 200 m ASL. Each valley has its own dynamics and generates outvalley flows during the nighttime (Whiteman, 1990) towards the center of the basin. The model smoothes these features and consequently the generated circulations, but the overall behavior is captured as the comparison of the wind with the observations shows.

At the N side of the basin, the Tramuntana range is more like a high wall dropping from 1100 to 250 m ASL in 4 km. The model topography has a resolution of 1 km, and underestimates the height of the range. At the E part, the basin is closed by a quasi bi-dimensional slope of a length of about 10 km that extends some 15 km inland. This slope has at the top in the central part the circular-shaped Randa mountain (500 m ASL). This slope is well represented by the model topography. Each of these three well defined structures generates katabatic winds that converge in the flat part of the basin.

The 1.5 m-temperature field at 0400 UTC (Figure 2.5b) has the minimum values in the center of the basin, right in the area where the airport is located. The AWS observed temperatures plotted on the figure show that the pattern is well captured. The evolution of the wind and temperature for the airport (Figure 2.4) indicates that, again, the model tends to slightly overestimate the wind in the central part of the basin. The modeled values are between 1 and 2 m s^{-1} compared to the observed values that are between calm and 1 m s^{-1}, a difference that can as well explain why the observed drop of temperature is 3 degrees larger than the modeled one.

The three-dimensional structure of the basin circulations can be described observing the vertical cross-sections NW-SE and NE-SW (following lines D and C in Figure 2.1, respectively) of the wind and the temperature drawn in Figure 2.6. Figure 2.6a shows two jets flowing out of the figure at a height of about 40 m AGL (indicated by white circles in the figure), the one on the left coming straight from the Tramuntana range at the north and the one at the right coming from the elevated part at the centre of the island. Both jets peak at about 6 m s^{-1} at their nose. Below the jets in the center of the basin, the air is much colder (Figure 2.6b) showing that it could be considered as a cold pool but not closed, since this air

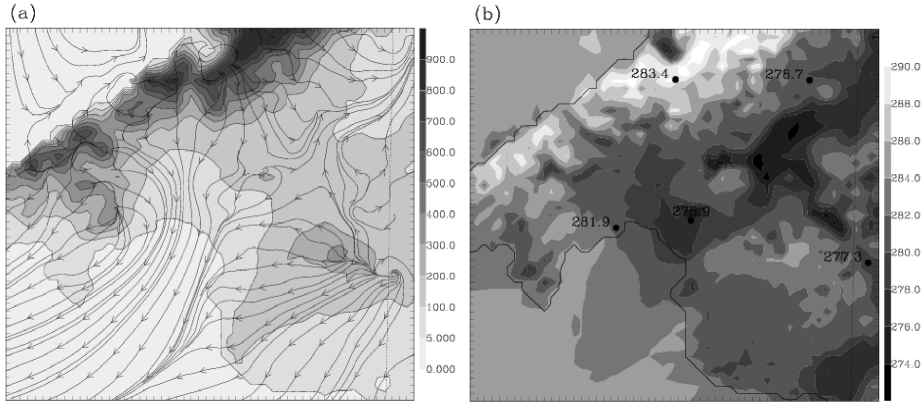

Figure 2.5: (a) Stream lines at 10 m and (b) potential temperature at 1.5 m at 0400 UTC in the Palma basin. Values of the surface weather stations are also shown in (b).

is advected to the sea. Above there is another maximum of the wind speed at 250 m ASL (market by an asterisk), blowing from the east and losing identity as it approaches the Tramuntana range. The vertical extension of the blocking area seems to reach 800 m ASL and above it the synoptic wind prevails.

The cross-section NE-SW shows a similar structure (Figures 2.6c and 2.6d). Here the out-basin jet blowing from the NE is cut longitudinally. Above the elevated central area, the temperature field shows the hint of a wave structure as the streamlines showed before, in an area of minimum wind speed (marked by a dark circle). Below that layer close to the ground, a wind maximum is generated that, with some oscillations is maintained until the jet reaches the sea (indicated by two asterisks). In the basin, the temperature is about 4 degrees colder than in the elevated area. No clear evidence of an elevated return current from the sea to inland is found, but over the center of the island there is divergence of the flow at 400 m ASL towards the basins of Palma and Alcudia, with slow eddies and alternances of positive and negative vertical velocities (not shown). Similar conclusions can be reached on the third side of the basin that will be discussed with more detail in the next section.

Summarizing, the flat part of the basin receives contributions from all the surrounding slopes. The W and NW parts seem to contribute as outvalley flows,

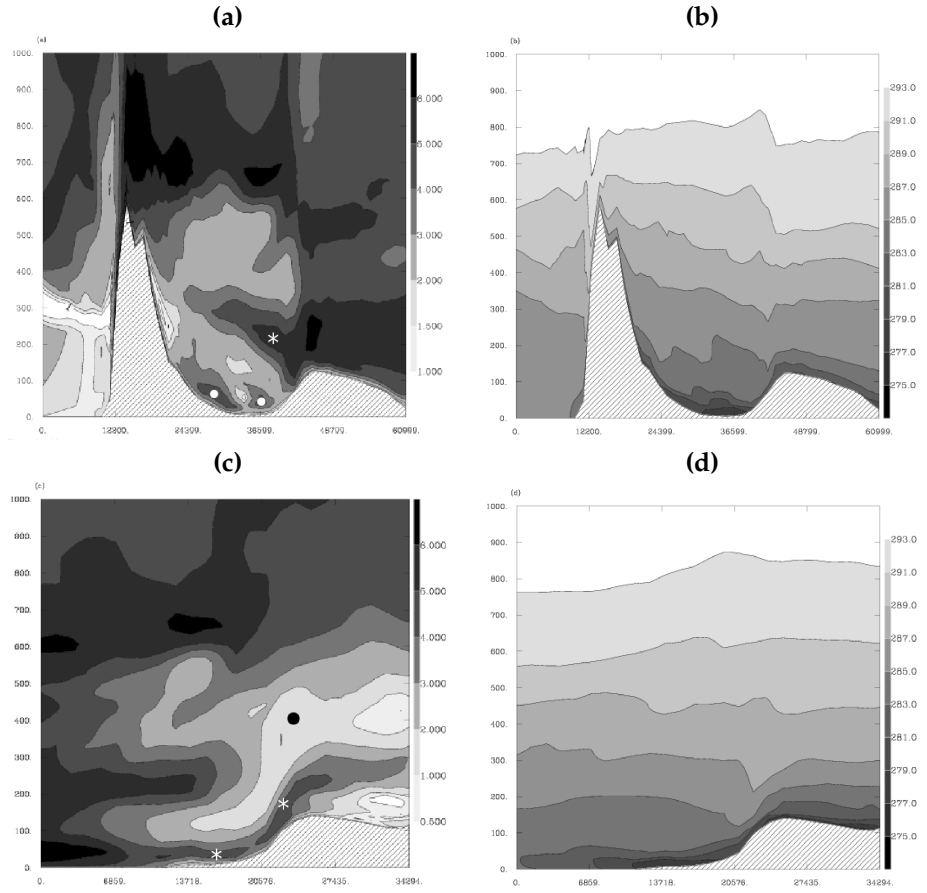

Figure 2.6: Vertical cross-section at 0400 UTC following line **D** in Figure 2.1 for the (a) wind speed (m s^{-1}) and (b) potential temperature (K). The same for (c) and (d) but following the line **C** in Figure 2.1. The vertical and horizontal dimensions are in meters. Symbols are locations explained in the text.

whereas the rest of the topography acts as a generator of katabatic flows. The ensemble of flows converge at the center of the basin, where the cold air accumulates and is impelled to the sea driven by the pressure gradient that results from the warmer air above the water in the Palma bay. It is interesting to note that two jets are formed that do not merge and flow outland independently. An open question is if these converging flows are creating a layered structure according to

their final potential temperature. Mahrt et al. (2001) found a similar behaviour at a very small scale in a gully during CASES-99. This will be further investigated in section 4.

2.4 Features of a katabatic flow over a gentle slope

As mentioned, the eastern part of the Palma basin is closed by a quasi bi-dimensional slope. The shape of the terrain shown in Figure 2.7 extends for several kilometers from the coast to the center of the island, without any valley structure of smaller scale. It has several changes of slope along the line from the mountain to the plane. The drop from the mountain to the center of the basin has, firstly, a steep part of 100 m in 1 km (a 10% slope), then 50 m in 4 km (a 1.25% slope) and finally the drop of 200 m in 8 km to the center of the basin (a 2.5% slope). The terrain is agricultural, with fields of olive, carob and almond trees and some small pine woods. At the end of the slope, the Palma international airport is found.

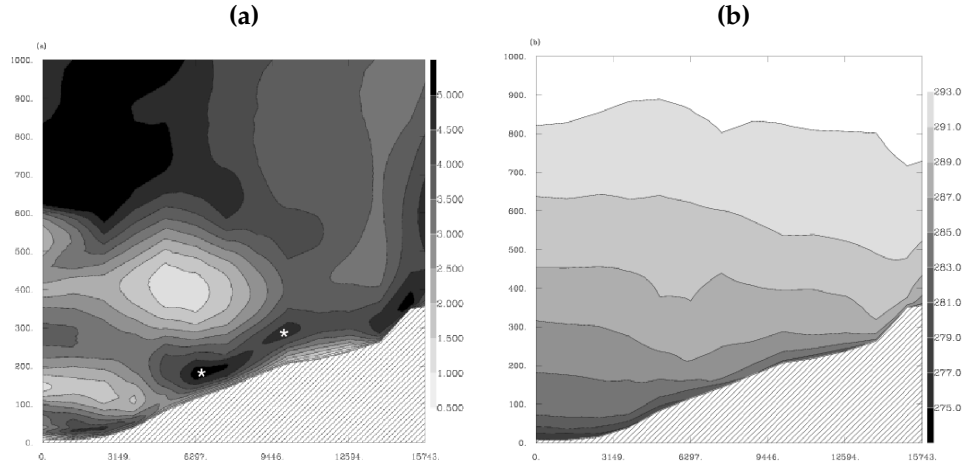

Figure 2.7: The same as Figure 2.6 but following the line **B** in Figure 2.1.

In Figure 2.7 the wind speed and potential temperature over the line Randa-airport (following line B in Figure 2.1) at 0400 UTC are shown. This line is parallel to the line of steepest slope. A maximum of wind is generated downslope of the Randa mountain. At the change of slope the jet nose is found at about 80 m above

the surface and when the slope becomes steeper, the wind accelerates again, with a maximum of about 5 m s^{-1} at about 50 m AGL (both features indicated with asterisks on the figure). When the downslope wind reaches the cold air in the basin it seems to split, with some air flowing close to the surface and the upper air above the cold pool. At this point it joins with the land-to-sea flow and changes direction. Renfrew (2004) found an elevated jet as the tail end of a part of the katabatic flow that rides over the cold air of the ice shelf. In the slope studied here, the temperature takes lower values at the parts where the slope is less steep. This structure would be in support of a layered structure of potential temperature over the valley, where each katabatic flow would contribute to air accumulation at his arriving level, except for the coldest air that would flow close to the surface.

Although this picture is quite stationary during the night, there is certain temporal variability point to point. For a given point located in the part with a 2.5% slope, the maximum of the wind can take values between 3 and 7 m s^{-1}, and its height oscillates between 20 and 100 m, being the more probable values around 40 m. The thermal stability -in average- below the jet nose is almost constant during the night at this point (about 3 K in 40 m), and is weaker above (1 K in 100 m) and oscillating (Figure 2.8).

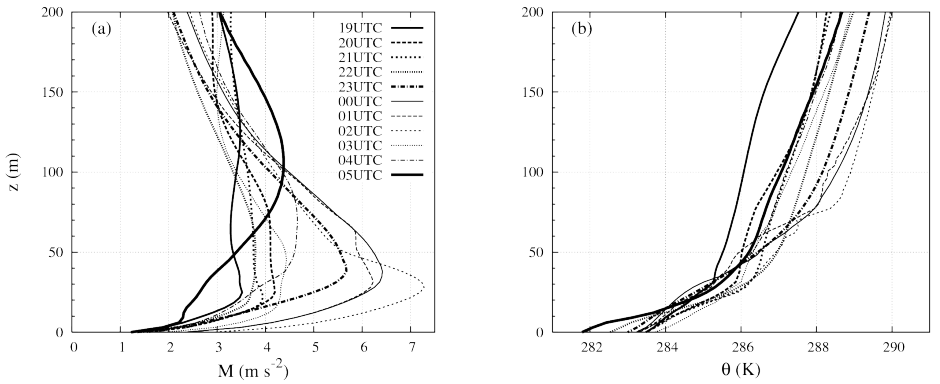

Figure 2.8: (a) Wind velocity (m s^{-1}) and (b) potential temperature (K) profiles every hour during the night at one point in km.9 (see Figure 2.9 for location).

In a rotated coordinate system, the momentum equation for a katabatic flow over a slope with a constant inclination angle α can be written as (Mahrt, 1982):

$$\frac{Du}{Dt} = -\frac{1}{\rho_0}\frac{\partial p}{\partial x} + g\frac{\triangle\theta}{\theta_0}sin\alpha + fv - \frac{\partial\overline{(w'u')}}{\partial z} \tag{2.1}$$

where shallow convection and "quasi-hydrostatic" approximations have been made, in which the hydrostatic equilibrium is present only for motion perpendicular to the ground (Mahrt, 1982; Haiden, 2003). The velocities u and w are referred to the rotated axes, tangent and normal to the slope, respectively.

Following Renfrew (2004), a two-layer model is assumed consisting of a katabatic layer as the lower one and a quiescent layer at higher level. A vertical integration of the momentum budget (2.1) from ground to katabatic-layer top (h_k), assuming that the temperature deficit and wind speed vanishes at the top of the layer and at surface, respectively, yields:

$$\begin{aligned}\frac{\partial u_k}{\partial t} &= -\left(u_k\frac{\partial u_k}{\partial x} + w_k\frac{u_h - u_k}{h_k}\right) + g\frac{\triangle\theta_k}{\theta_0}\alpha - \frac{gh_k}{\theta_0}\frac{\partial\triangle\theta_k}{\partial x} - \frac{g\triangle\theta_k}{\theta_0}\frac{\partial h_k}{\partial x} + fv_k \\ &- \frac{\overline{(w'u')}_h - \overline{(w'u')}_{sfc}}{h_k} = F_{adv} + F_b + F_{\triangle\theta_k} + F_h + F_{cor} + F_{div}\end{aligned} \tag{2.2}$$

where small angle slopes are considered ($sin\alpha \approx \alpha$, $cos\alpha \approx 1$). Here, u_k, w_k are katabatic-layer average velocities, u_h is the velocity at the top of the layer, θ_0 is a reference potential temperature and it is taken here as the value at the top of the layer, $\triangle\theta_k = \theta_0 - \theta_k$ is the katabatic-layer potential temperature deficit, g is the gravitational acceleration, f is the Coriolis parameter, and $\overline{(w'u')}_{sfc}$, $\overline{(w'u')}_h$ are the vertical turbulent u-momentum fluxes at the surface and at the top of the layer. The Lagrangian derivative has been expanded and the cross-slope variation of u_k has been neglected.

Equation (2.2) contains the different forcings involved in the momentum equation: F_{adv} refers to the total advection, F_b is the buoyancy term that, by definition, is supposed to be the source of the katabatic flow, $F_{\triangle\theta_k}$ and F_h are referred to as the thermal-wind terms (Mahrt, 1982), which are relevant if the layer depth and the katabatic potential temperature deficit vary along the slope. F_{cor} is related with the Coriolis force and F_{div} represents the divergence of turbulent vertical flux term and is related with the surface drag and the entrainment at the top.

To apply the former analysis to our case, a definition of the top of the katabatic layer is required. Due to the relative unsteadiness of the regime and its spatial

variability, here h_k is considered to be the height of temperature inversion related with the maximum wind generated by the katabatic flow.

In Figure 2.9 the time-averaged values along the slope, two hours after sunset (1900 to 2000 UTC) and towards the end of the night (0200 to 0400 UTC), are shown for the relevant parameters of the above formulation. Since the flow at the end of the slope (0 to 5 km in Figure 2.9) merges with the downvalley wind, it is probably not well represented by the theory used here.

The depth of the katabatic layer increases with time and potential temperature stays approximately constant with time, over the slope, whereas the lower layer cools around 3 K and its depth decreases at the foot. For the average velocities, u_k describes an oscillatory behavior along the slope (that becomes more relevant at the second period) and its maximum values match with potential temperature crests, that are well correlated with the changes of slope.

During the night, the maximum value of u_k located at the end of the slope moves 1 km downslope and the rest of the extreme values strengthen. Nevertheless, cross-slope velocity v_k changes significantly during the night except near the foothill, indicating that the slope wind turns with time. The slope-relative vertical wind component w_k (which is approximated to vertical component) alternates negative and positive values along the slope during second period (0200-0400 UTC). This behavior is consistent with the mass continuity principle in relation with the oscillatory distribution of u_k. In the convergence areas over the slope where horizontal velocity decreases, the vertical motion is positive, and vice versa. Banta et al. (2004) ran a simulation over the Great Salt Lake basin detecting bands of rising and sinking motions where the down-basin and canyon down-slope flows converged. Such vertical velocities were about 5 cm s^{-1}, the same order of magnitude as the velocities simulated here. The locations with a higher velocity also have high values of surface turbulence flux due to an increment of the wind shear close to the surface.

It is interesting to note that the momentum flux is, in general, one order of magnitude greater at the surface than at the top of the katabatic flow. This situation suggests that entrainment is not relevant and only surface friction can be considered, as for the flow described by Ball (1956). In Renfrew (2004), entrainment arose as important as surface drag because a quiescent upper layer leads to an important windshear at the top of the flow and the roughness length over ice is very low, therefore diminishing the difference between this two factors. For Manins and Sawford (1979b), the dominant retarding stress is the one related with the entrainment due to the interfacial mixing. However, in present study, the wind velocity is significant above the katabatic layer and it has the same direction than the slope flow. Therefore, less shear generation of turbulence is

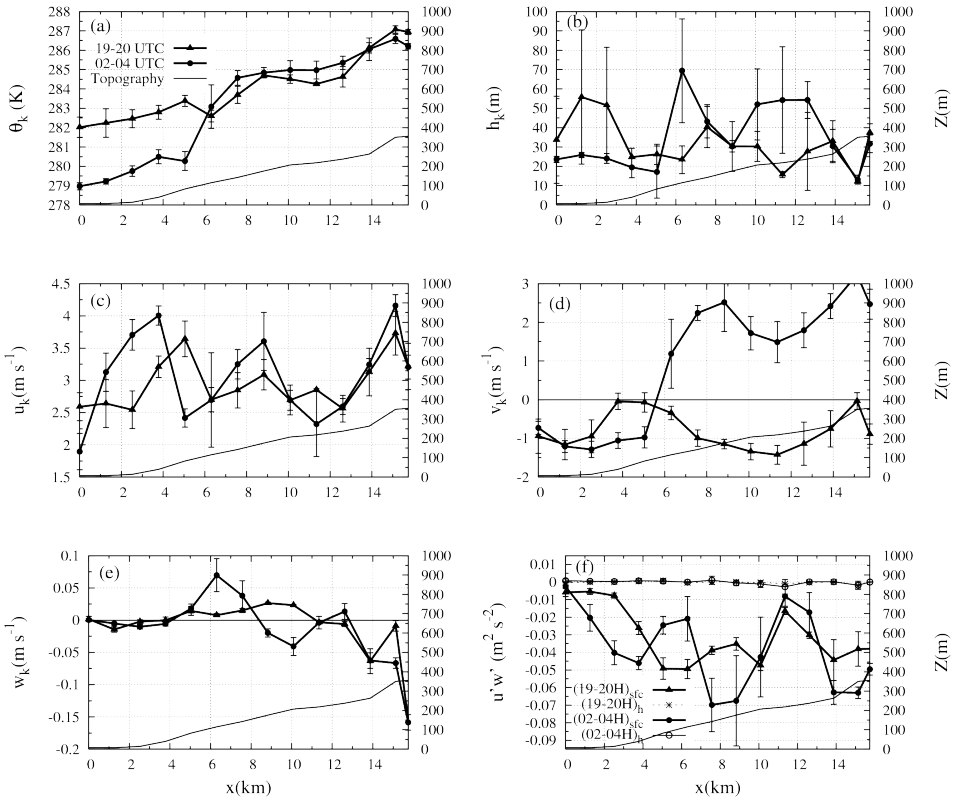

Figure 2.9: Mean parameters for the katabatic-layer along the slope following the line Randa-Airport in Figure 2.1. Time-averaged values and standard deviation are plotted for two different periods of the night: 1900-2000 UTC and 0200-0400 UTC. (a) Katabatic-layer mean potential temperature θ_k (K); (b) katabatic-layer height h_k (m); katabatic-layer mean velocities (m s^{-1}) in the (c) along-slope direction u_k and (d) cross-slope direction v_k; (e) slope relative vertical direction w_k; (f) kinematic momentum fluxes at the surface and at the katabatic-layer height ($m^2 s^{-2}$).

produced in respect to a quiescent layer above. This lack of mixing with the upper layers does not allow the katabatic air to get warmer or to lower its speed as much, probably resulting in very well defined cold and relatively fast flows. This issue requires more sounded investigation with the support of observations.

Several authors have studied how the presence of an ambient flow in the same direction as the katabatic wind affects its dynamics. Cornfeld (1938) observed that an aiding ambient flow could form an eddy on the lee side of a hill, able to scour the drainage wind near the hilltop or further down the slope. From this point to the plain, a calm zone is well developed. Differently, Hawkes (1947) argued that the effect is little due to the presence of a strong stability of katabatic flow. Finally, other authors (Coulter and Gudiksen, 1995), reported that a drainage flow increases its depth and velocity. Poulos et al. (2000) studied the interaction between a katabatic flow and the mountain waves generated by the ambient flow on the lee side of an idealized hill. It was found that the elimination of the drainage flow depends on the Froude number. An ambient flow with a high Fr value scours the katabatic wind, whereas a small Fr leads to a wind system where both phenomena are indistinguishable, enhancing the katabatic wind speed.

Figure 2.10 shows the streamlines over the Randa mountain at three different moments for the night. The wind direction is modified by the mountain, leading to a steady configuration that seems to strengthen with time. Wind speed increases near the mountain peak and close to the points where changes slope. The same pattern can be inferred from the field of potential temperature θ (not shown). Terrain-generated gravity waves are stationary relative to the ground surface (Nappo, 2002) like the oscillatory behavior detected in the present katabatic flow. The estimated Froude number for the ambient flow computed as in section 2.2 (with N = 0.04 s^{-1}, U= 4 m s^{-1}, but taking h = 300 m as the average Randa mountain height), is about 0.3. Following Poulos et al. (2000), this value leads to a situation where the downslope phase of the mountain wave couples with the katabatic flow, enhancing its speed. Furthermore, in these cases, the presence of a mountain wave flow induces a variability of the drainage flow, modifying the depth and speed of the jet, as shown in Figure 2.8. However, in present case, the angle slope is not constant, and its changes are well correlated to the variations of the wind speed downslope in points between 6-15 km. In consequence, the katabatic wind it is probably not only modified by the interaction with the mountain waves, but also by the changes of the slope, and perturbations are propagated upwards and are able to modulate the flow in the first thousands of meters above the ground. Up to what extend these motions are conditioning the overall behavior at the scale of the basin is a likely subject of a further study.

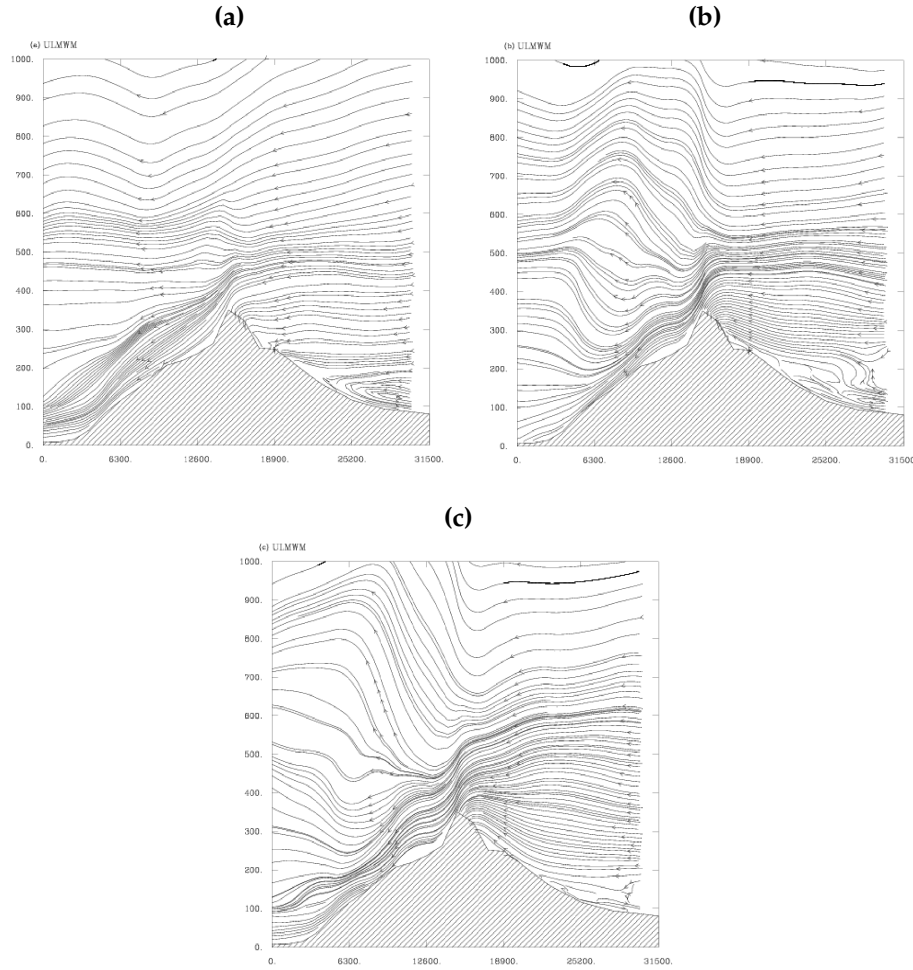

Figure 2.10: Vertical stream lines at the Randa mountain (Figure 2.1) following the direction of the synoptic wind at different times: (a) 1900 UTC, (b) 2300 UTC and (c) 0300 UTC.

Figure 2.11 illustrates the forcing terms of the downslope momentum budget from equation (2.2), as computed using the information of the mesoscale simulation along the problem slope. The buoyancy force F_b is balanced by momentum flux divergence F_{div}, specially at the beginning of the night, and the advection

term F_{adv}. The latter does not always slow the flow as it changes its sign along the slope. The thermal-wind terms $F_{\triangle\theta}$ and F_h are generally small and the Coriolis term F_{cor} is irrelevant due to the small spatial scale of the phenomena. Finally, F_{res} is the residual of equation (2.2) that also includes the Eulerian acceleration. Its sign is opposite to F_{adv} in almost every point, suggesting that the estimation of the total advection term is the main source of error. In order to improve the results, three-dimensional effects should be considered to represent the advection term.

These results are in agreement with Mahrt (1982), who showed that gravity flows can be generally approximated by a balance between buoyancy acceleration and downslope advection of weaker momentum or/and the turbulent transport term. Such flows coincide with a Froude number for the katabatic flow ($Fr = \frac{u_k^2}{(g\triangle\theta/\theta_0)h_k}$) greater than one, as in present case, where $Fr > 1$ along the slope (not shown), and the katabatic wind can be considered a shooting flow in terms of hydraulic theory.

The point located at the upper part of the longer slope (about km 11) has a very small contribution of all the forcing terms. From this point on, the buoyancy term grows downslope. It can be considered the origin of the buoyancy-driven flow. Another "singular" point is where the katabatic flow meets the downvalley flow in the second period (km 6). Here, the buoyancy force is not balanced by any forcing term, except for the residual, attributable to non 2D effects. The cross-slope average velocity v_k changes its sign and w_k is positive and significant. Also, the depth of the katabatic-layer is the largest of the slope and the vertically averaged potential temperature decreases 5 K, leading to important local gradients that increase the thermal wind terms ($F_{\triangle\theta}$ and F_h).

Mahrt (1982) presented a simple solution for downslope momentum equation (2.2) to cases where main terms are F_b, F_{div} and F_{adv}. Neglecting the rest of forcing terms and assuming constant h_k, downslope wind speed can be written as:

$$u_k = \left\{ {u_e}^2 \left[1 - exp\left(\frac{-x}{L_e}\right)\right] + {u_k}^2(0) exp\left(\frac{-x}{L_e}\right)\right\}^{1/2} \qquad (2.3)$$

$$u_e \equiv \left[\frac{h_k g \triangle\theta/\theta_0 sin\alpha}{(C_D + k)}\right]^{1/2} \quad L_e \equiv \frac{h_k}{C_D + k}$$

where $u_k(0)$ is the katabatic layer mean velocity at some arbitrary point on the slope; u_e is the solution for an equilibrium flow, a case where buoyancy acceleration only balances with turbulence term; and L_e is a length scale related with the distance needed for the flow to adjust to the equilibrium case. C_D and k are the drag and the entrainment or mixing coefficients, respectively, and here are

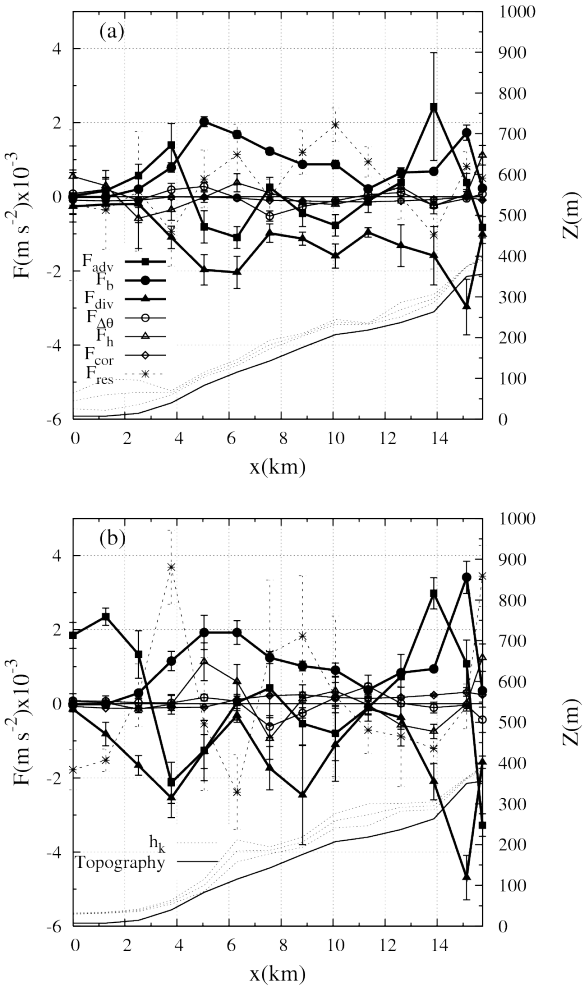

Figure 2.11: The same as Figure 2.9 but for the forcing terms from the downslope momentum equation (m s^{-2}) at (a) 1900-2000 UTC and (b) 0200-0400 UTC. The average katabatic layer height h_k and the standard deviation (m) are also plotted but relative to the topography line.

calculated through the vertical turbulent flux of momentum at the surface and at the top of the katabatic layer:

$$C_D = -\frac{\overline{(w'u')}_{sfc}}{{u_k}^2}; k = \frac{\overline{(w'u')}_h}{{u_k}^2}$$

Figure 2.12 illustrates the evolution of u_k along the slope for points where the buoyancy term is dominant (from the point located close to km 11, which is considered the origin of the katabatic wind, to km 4 in Figure 2.9). Therefore, $u_k(0)$ represents the vertically averaged velocity at the upper point of the area chosen. To apply the solution (2.3), it is necessary to assume that the parameters u_e and L_e are constant. A representative value for all the points has been estimated from the simulation for both time intervals analyzed (1900-2000 UTC and 0200-0400 UTC). Table 2.2 summarizes the values for the parameters needed to plot figure 2.12. The resulting length scale L_e is similar to the downslope length scale and, consequently, the katabatic flow cannot reach the equilibrium regime.

Table 2.2: Values used for the parameters present in analytical simple solution for downslope momentum equation in the case of a shooting flow.

	1900-2000 UTC	0200-0400 UTC
$C_D + k$	0.004	0.004
h_k	30 m	40 m
$\triangle\theta$	1 K	1.5 K
θ_0	283 K	283 K
$sin\alpha$	0.033	0.033
$u_k(0)$	2.83 m s^{-1}	2.30 m s^{-1}
u_e	2.93 m s^{-1}	4.14 m s^{-1}
L_e	7500 m	10000 m

The analytical simplified solution reproduces the tendency of the along-slope wind velocity from the simulation, which increases with the slope in both periods. The increasing of u_k is bigger during 0200-0400 UTC, but $u_k(0)$ is smaller. However, the solution (2.3) is very sensitive to changes in the parameters. For instance, arbitrary changes in the origin point $u_k(0)$ or in the estimation of h_k, may lead to a simplified solution with a different tilt, losing the similarity with the tendency from the simulation results. Since the oscillatory behavior of u_k is assumed to be related with terrain-generated gravity flows, the simplified solution cannot reproduce it. Besides, for the katabatic flow simulated, h_k is not constant and thermal wind terms are not smaller enough to be neglected in some specific points, specially during time interval 0200-0400 UTC.

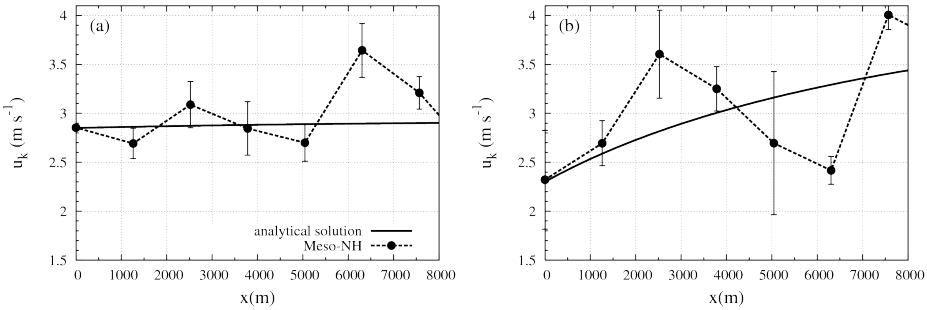

Figure 2.12: Solution for the downslope momentum equation (2.3) in the simple case of a *shooting flow* assuming constant h_k for points over slope where buoyancy term is dominant. X-axis indicates the downslope distance respect to the point in km.11 of Figure 2.9. Time-average wind speed u_k and standard deviation from simulation is also plotted. (a) 1900-2000 UTC and (b) 0200-0400 UTC.

In order to compare the katabatic flow simulated with real data, a method of validation for simulations implemented recently by Mira et al. (2006) has been applied. It consists of a comparison between the radiative surface temperature computed by the model with the estimated from NOAA IR imaginary. Since there are two NOAA images from the night of 5-6 January 1999 (1846 UTC and 0405 UTC), the radiative surface cooling rate has been calculated as:

$$\triangle T_{sfc} = T_{sfc}(t_2) - T_{sfc}(t_1) \tag{2.4}$$

Figure 2.13 shows the field $\triangle T_{sfc}$ along the slope obtained from the satellite images and from the model outputs 1900 UTC and 0400 UTC. There is good agreement between both cooling rates at the upper part of the slope, where a local maximum cooling is reproduced at the same point. It coincides with the minimum of katabatic-layer mean velocity u_k, in agreement with the conceptual scheme where, as the wind strength decreases, the surface turbulence becomes smaller and the lack of mixing leads to a decrease of radiative surface temperature.

The difference of 6 degrees observed at the airport (x = 0 km) might be explained by the formation of a shallow fog reported by the airport observers at the end of the night. The model cannot reproduce this phenomenon because condensation processes were not considered in this simulation.

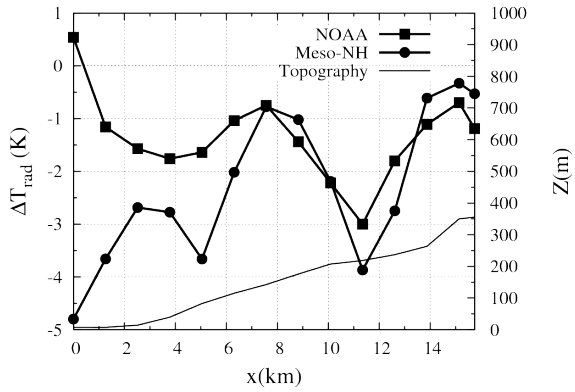

Figure 2.13: Surface cooling obtained from the model and the available NOAA satellite images computed with the model radiative temperatures at 1900 UTC and 0400 UTC, and the images at 1846 and 0405 UTC [$\Delta T = T_{rad}(0400UTC) - T_{rad}(1900UTC)$].

2.5 Conclusions

Despite its relatively small size, this mid-latitude island has a complicated flow pattern in the nighttime, mostly related to its topographical characteristics. When the synoptic wind is weak, the island becomes an area where locally generated winds prevail. The mesoscale simulation, performed at a very high vertical resolution, allows to inspect many details of the low level flows. It is found that the different relevant scales (island, basin and slope) generate flows that interact in a complex manner.

The Tramuntana mountain range allows the creation of a zone of very weak winds over the centre of the island, and outland flows at its sides. Inland, the calm wind areas in clear-sky conditions, allow for the development of slope flows and of cold pools in the valleys, that will interact as the night advances. The land-sea breeze effect, due to a relatively warm sea surrounding the island, introduces a component outland from the island. Once these features are set, at about 5 hour after the sunset, the patterns are almost stationary.

The katabatic flow studied here is along a gentle slope that has some changes in the slope angle downhill. These changes are well correlated with those in the wind speed and the potential temperature near the ground, determining their spatial distribution. The analysis of the terms of the momentum budget equation shows that the entrainment is not a relevant factor for this flow, that can be coupled with the flow above, especially with waves generated by the mountains. When this slope flow meets the cold pool air in the valley, it accumulates on the top of it, except for a thin cold layer that flows close to the surface. All these features should be further investigated through direct observational work.

Acknowledgements

The European Center for Medium-range Weather Forecasts (Reading, UK) is acknowledged for the access to its computing facilities, through the intermediation of the Spanish Met. Service (INM). Many thanks as well to the Centre National de Recherches Météorologiques (Toulouse, France) for their support in the use of the Meso-NH model, especially to Patrick Jabouille (deceased), Jeanine Payart and Isabelle Mallet. J.A. Guijarro (INM) is also acknowledged for the discusion and A. Luque and A. Mira from UIB for the processing of the NOAA satellite images. This work has been partially funded by the research project REN2003-09435/CLI of the Spanish Ministry of Research, and by a Special Project of the Governement of the Balearic Islands. Two anonymous reviewers have provided very useful comments that have contributed to the improvement of the paper.

Chapter 3

Heterogeneous nocturnal cooling in a large basin under very stable conditions

This chapter is based on Martínez, D., M. A. Jiménez, J. Cuxart, and L. Mahrt, 2010: Heterogeneous nocturnal cooling in a large basin under very stable conditions. *Bound.-Layer Meteorol.*, **137**, 97–113.

Abstract

Large basins with relatively wide floors experience heterogeneous nocturnal cooling due to the diversity of the topography and the land use within the basin. Near mountain ranges the drainage flows prevail, but in low areas, river valleys or embedded plateaux, the actual rates of cooling differ as does the behaviour of the local flows in the first few metres above the surface. In this study, the temporal and spatial heterogeneity of the surface cooling is inspected through the analysis of satellite radiative surface temperature, data from a meteorological network and a tall tower. The organisation of the flow within the basin is also studied by means of a high-resolution numerical mesoscale simulation. Although the basin cools almost as a unit, there exists a large diversity of local regimes. Vertical profiles from the mesoscale simulation are analysed and grouped according to their wind structure and stratification.

3.1 Introduction

Large river basins that are topographically confined have distinct local meteorological characteristics. A well-defined synoptic flow can cause specific patterns within the basin. Furthermore, heated upslope/upvalley daytime flows and nocturnal downslope/downvalley flows near the surface can co-exist with the general flow. Slope flows can be eliminated if the general flow is strong or the skies are overcast, but can predominate if the synoptic wind is weak and the skies are clear. Terrain heterogeneity generates patterns of temperature and circulation that are particular to each basin, having nocturnal drainage flows from the mountain ranges and surrounding gentle slopes towards the centre of the basin, and cold air pooling in local depressions or specific dynamics over elevated plateaux. The local thermal and wind profiles are therefore very different between these areas at night.

Some studies for large basins have reported several defining characteristics. Studies made for the USA intermountain western basin (Wolyn and McKee, 1989; Whiteman et al., 1999; Zhong et al., 2001) show that the air within the basin can be stably stratified from bottom to top (more than 1,000 m of depth) for several days if warm advection aloft prevails. Near the ground, a diurnal cycle is observed, with inversions stronger than 10 K over several hundred metres depth during the night, and neutrality or convection depending on the solar forcing and the situation aloft during the day. Zhong et al. (2004) inspected the wind and thermal patterns within the California's Central valley, driven by mesoscale thermal forcing due to the land-ocean thermal contrasts under fair weather conditions. The subsequent formation of a low-level jet at night interacts with the local-scale slope flows along the foothills. The sen- sitivity of the simulated low-level winds to the soil initialisation and large-scale atmospheric patterns are analysed in Michelson and Bao (2008).

The dynamics of quasi-ideal cold pools have been studied for small structures using observations, such as at Peter Sinks (Utah, Clements et al., 2003) or in elevated alpine basins (Zängl, 2005a,b). Clements et al. (2003) show that drainage flows are relevant in the first part of the night for the 1- km scale Peter Sinks basin, contributing to the initial pooling, but they disappear after the formation of the cold pool, which continue to intensify. Vosper and Brown (2008) study topographically induced cold pools with a two-dimensional (2D) numerical model and demonstrate that the results are very dependent on the wind velocity above the depression and sensitivity to cloudiness. In order to locate the areas of the

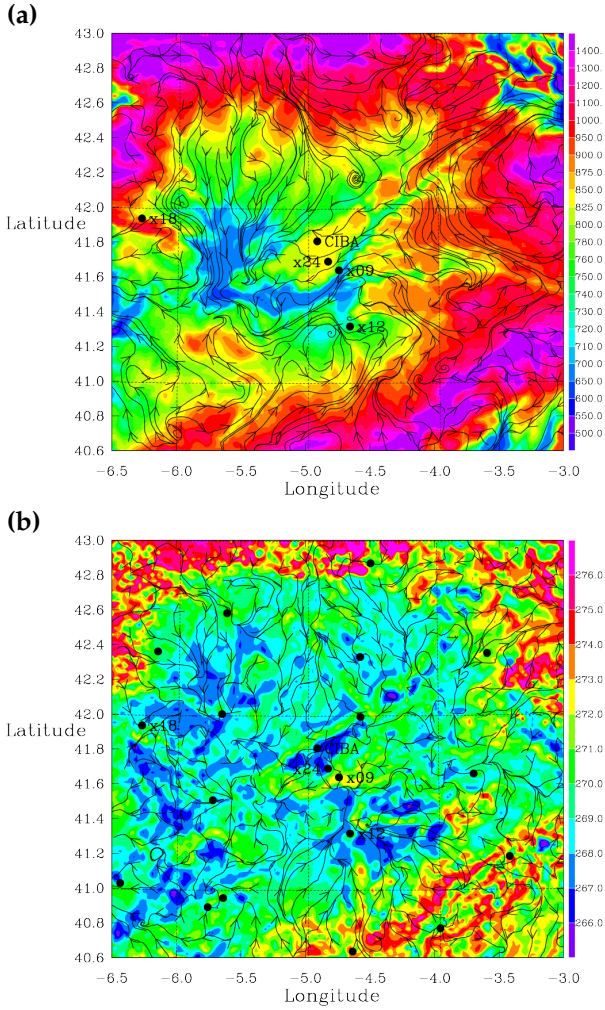

Figure 3.1: (a) Topography (in m) of the centre of the Duero basin and simulated streamlines at 50-m height at 0200 UTC. The locations of 4 automatic weather stations from AEMET are displayed in *dots*. The 100-m tower in the CIBA site is located in the Torozos Plateau, an elevated area in the centre of the basin. (b) 1.5-m temperature (in K) and streamlines at 0200 UTC. In both plots, the streamlines are plotted every 4 gridpoints (8 km).

landscape that are likely to be prone to cold-air pooling, Lundquist et al. (2008) developed an algorithm based on the local characteristics of the terrain.

The interaction of drainage flows and cold pools is investigated in Neff and King (1989) for a basin of intermediate size (De Beque, Colorado, USA, of 30-km radius), where the cold pool is formed and can extend to an open area outside the basin. The tributary valleys have drainage flows down their axes, which then often flow over the cold pool air above the valley floor. Sometimes the drainage flow is colder than the air in the cold pool and penetrates underneath. A similar pattern was found by Cuxart et al. (2007) for a numerical study of the Palma Basin on Majorca Island, which is of comparable dimension (20-km radius). There, the drainage flow from the Randa Mountain circulates over the cold pool except the very cold and thin skin flow that penetrates beneath the pool.

The current work seeks to understand the behaviour of the stably stratified boundary layer (SBL) within a wide basin. The Duero basin, in the north-west part of the Iberian Peninsula, covers 97,290 km^2 of which 78,952 km^2 are in the Spanish part (160 km of radius), a sub-area that is basically a closed basin connected to the Portugal part of the basin by a narrow pass. The airflow has been extensively studied during the last decade, using observations from SABLES 98 (Cuxart et al., 2000) and data gathered afterwards (Conangla et al., 2008; Viana et al., 2009) over an elevated plateau at the central part of the basin where the Research Centre for the Lower Atmosphere (CIBA) is located with a 100 m tower (Figure 3.1). The statistics of the wind data gathered at this site (Conangla and Cuxart, 2006) show that there must be a mesoscale forcing to explain the behaviour of the direction of the wind. Cuxart (2008), aided by the mesoscale simulations of Bravo et al. (2008), proposed a nocturnal basin-scale organisation to explain the observations. The details of a well-defined katabatic flow over the southern mountain range were analysed in Martínez and Cuxart (2009).

The main objective of our work is to study the behaviour of the basin-scale airflow close to the ground during nighttime conditions. A case study for a very stable night (14-15 January 2003) is explored using different available observations, described in Section 3.2. This night belongs to a 10-month period when the instruments on the CIBA tower functioned perfectly following calibration. The period has been analysed statistically (Conangla et al., 2008) and the case selected for this study has been previously modelled in Bravo et al. (2008). A description of the night is given in Section 3.3. The observed patterns are analysed using satellite imagery, which illustrate the within-basin heterogeneity, and are compared with results from a high-resolution mesoscale simulation, shown in Section 3.4. The within-basin heterogeneity of the near-surface air from the

mesoscale simulation is inspected in Section 3.5, where the geographical distribution of the different features is analysed. Conclusions are presented in Section 3.6.

3.2

Tools

This study uses the network of Automatic Weather Stations (AWS) of the Spanish Meteorological Service (AEMET), the NOAA and METEOSAT satellite imagery, and data from the CIBA site. In addition a high-resolution mesoscale simulation is verified against the observations.

Satellite Imagery

Meteosat-7 derived surface radiative temperatures are used (Prata et al., 1995), one every 30 min with a spatial resolution of about 25 km^2 per pixel in the area of interest. These images are corrected except for the removal of the water vapour effect, which implies that estimated values are 1-2 K lower than with the full correction (Coll et al., 1994). On nights with frost formation, as in the present case, the surface emissivity may vary overnight leading to additional errors in the radiative temperature structure. A NOAA image corresponding to 0200 UTC for the area is also used, which provides finer spatial resolution (about 1 km^2) that includes geometrical, navigation and water vapour corrections, as in Coll and Caselles (1997). The uses of these images are similar to that done in Jiménez et al. (2008).

Nineteen Automatic Weather Stations

The weather stations are irregularly distributed throughout the basin (Figure 3.1). They measure wind speed and direction at 10 m above ground level (a.g.l.) and temperature and humidity at 1.5 m a.g.l. We include one record every hour. For this very stable night with extremely weak winds, the wind sensors are often not working because their threshold is higher than 0.5 m s^{-1}.

CIBA 100-m Mast

This contains four Metek sonic anemometers with a sampling rate of 20 Hz (at levels 96.6, 49.6, 19.6, and 5.6 m), five cup anemometers made by Risoe National Laboratory of Denmark with a threshold of 0.5 m s^{-1} (at levels 98.6, 74.6, 34.6, 9.6, and 2.2 m) sampled five times per second; slow temperature sensors at 97.5, 35.5, 20.5, 10.5, 2.3 m and humidity sensors at 97, and 10 m. The 5-min averaged data and turbulence statistics are stored routinely.

Mesoscale Simulation

The Meso-NH model (Lafore et al., 1998) is operated using a single domain 640 x 500 km^2 with 2 km of horizontal resolution, and a very fine vertical resolution of 3 m near the surface, degrading gradually with height (for instance, a resolution of 5 m at 100 m a.g.l.). This configuration captures the main topographical features within the basin, allowing the dynamics to represent the advective motions generated and conditioned by the topography. The numerical simulation begins at 1200 UTC, 14 January and extends for 24 h, initialised using an analysis of the European Centre for Medium-Range Weather Forecasts (ECMWF), refreshing the lateral boundary conditions every 6 h. Since the synoptic forcing is very weak for this case, the physics of the model and the soil heterogeneity play a central role. These include the 1.5-order turbulence scheme (Cuxart et al., 2000), the Morcrette radiation scheme (Morcrette, 1990) and the Interaction Soil Biosphere Atmosphere (ISBA) soil-vegetation schema (Noilhan and Planton, 1989). Since clouds and fog were not observed during the night, the numerical simulation is made without the activation of the condensation scheme, although the surface scheme accounts for these condensation processes in the surface energy budget. The soil conditions are initialised using information from the ECMWF and the soil heterogeneity derives from the CORINE data base (Heymann et al., 1994). The water content from the ECMWF is integrated into the model in a way that prevents any water imbalance (Le Moigne, personal communication, 2010). The same set-up is described for another location in Jiménez et al. (2008).

3.3 Description of the night

The combined use of all available observational information and of the mesoscale simulation provides a good picture of the atmospheric dynamics within the

basin. The basin (taken here as the almost closed Spanish part of the Duero basin) has its bottom near 750 m above sea level (a.s.l.) and is surrounded by mountain ranges peaking at 2,500 m a.s.l. except for lower topography at the western edge (Figure 3.1a). The bottom part has some minor heterogeneities, such as elevated plateaux between the river valleys (height differences of about 100 m between plateau and river valley). The Pisuerga tributary is oriented from north-east to south-west and meets the Duero river (that runs primarily east-west) close to Valladolid (location x09 in the plots).

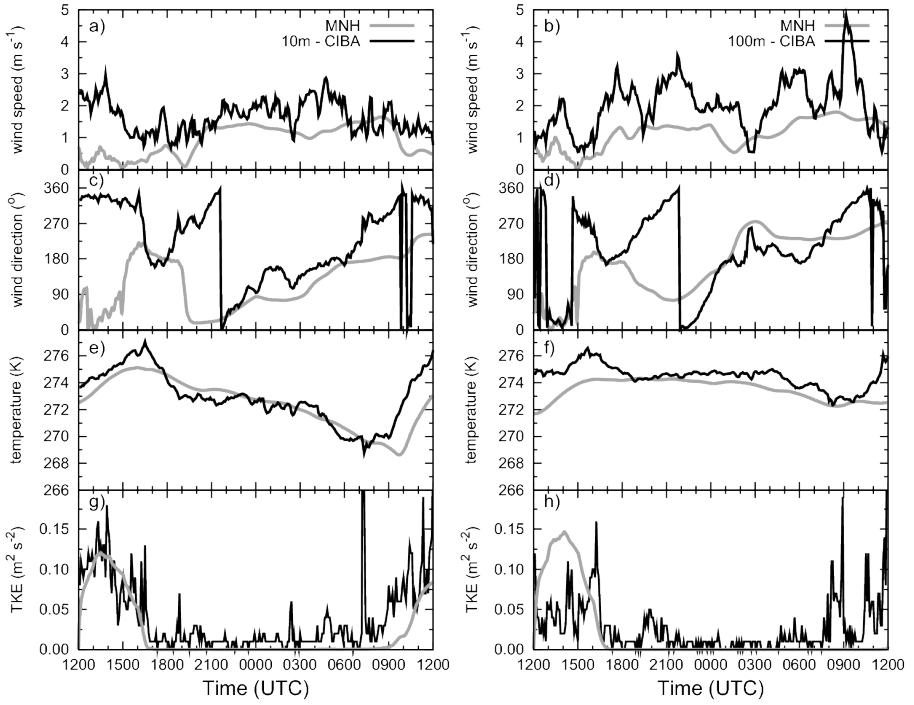

Figure 3.2: Time series measured by the CIBA tower compared to those obtained from mesoscale runs for (a) and (b) wind speed, (c) and (d) wind direction, (e) and (f) temperature and (g) and (h) TKE at (left) 10 m a.g.l. and (right) 100 m a.g.l. CIBA data correspond to 5-min averages whereas the model results correspond to outputs every 1 min.

The centre of the high pressure system lay over the basin, characterising the area with clear skies and a weak synoptic flow that lead to strong nocturnal cooling. The night-averaged value of the stability parameter z/L calculated from data at

the CIBA site is 2.5, where L is the Obukhov length and z is the height above the ground (5.6 m in this case). According to Figure 3.1 in Mahrt (1998), the stability parameter (z/L) corresponds to very stable conditions, as in the night analysed in Conangla et al. (2008). Their study found that 14% of the nocturnal periods at the CIBA site belonged to the very stable category.

The mesoscale simulation shows that this day is characterised by within-basin circulations that, at night, include drainage flows from the mountain ranges to the centre of the basin with wind maxima at heights of about 30-60 m a.g.l. These flows have longitudinal scales of several tens of km to about 100 km, and which are diverted by the local topography and can interact when they meet (see Figure 3.1a). They have different origins and only a small percentage can be classified as katabatic flows. Under very stable conditions, the likely presence of gravity waves (Terradellas et al., 2001) is restricted in the mesoscale simulation to those with a wavelength of the same order of the horizontal resolution.

Close to the ground, the very local terrain heterogeneities largely determine the variation of the meteorological variables, as illustrated by the satellite derived radiative surface temperatures and the observed and modelled 1.5-m temperatures (see Figure 3.1b for the latter case). The differences in the minimum temperature between the automatic weather stations are smaller than 4 K and the winds are very weak, usually below the threshold of the anemometers. In general the measurements near the ground seem to be disconnected from the stronger winds aloft, except in the areas where well-formed katabatic flows prevail. Air on the elevated plateaux and in cold pools or river valleys can be calm and cold.

To assess the model accuracy, results are compared to the CIBA values as shown in Figure 3.2. The observed wind at the beginning of the night veers at a faster rate (double) than an inertial oscillation, which is the behaviour in the numerical model, as reported for other cases (Cuxart, 2008). This difference may be related to factors such as thermal basin heterogeneity at the end of the daytime not well captured by the model. In the second part of the night (after 2200 UTC), a low-level jet is established below 100 m a.g.l. and the model compares more closely to the data, although the wind speed is slightly underestimated at the upper levels of the tower because the simulation does not capture properly the shape of the low-level jet.

The temperature between 10 and 100 m a.g.l. is well reproduced at the CIBA site, being almost constant at 100 m a.g.l. (940 m a.s.l.) during the night. Therefore, the difference between the 1.5-m temperature for the AWS and the 100-m tower temperature is a measure of the strength of the temperature inversion for different parts of the basin (Figure 3.3). The turbulent kinetic energy (TKE) is rel-

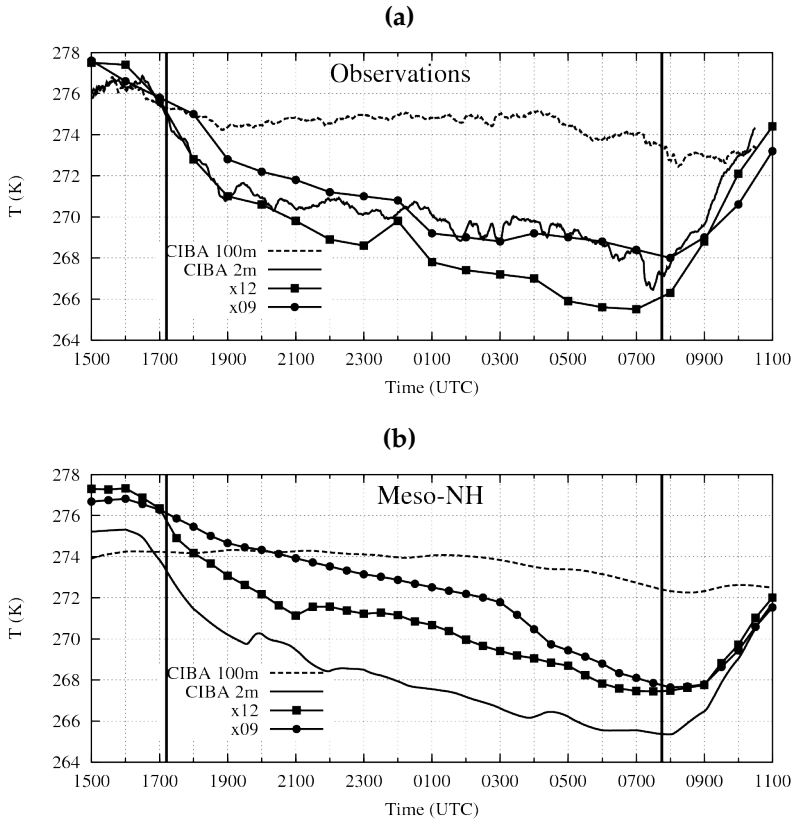

Figure 3.3: Time evolution of the temperature at the top of the tower and at 1.5 m a.g.l. for Olmedo (x12), Valladolid (x09) and the CIBA site (a) measured and (b) simulated. See Figure 3.1 for locations. Bold vertical lines indicate the sunrise and sunset times.

atively small in the daytime, corresponding to a very shallow winter convective boundary layer and the observed values at nighttime are very small and near zero in the model. The increase of the differences between the model and the observations through the night leads to simulated convection that is shallower and weaker than the observed convection the next morning. In the model, the increase in TKE is delayed approximately 2 h at 10 m a.g.l. and is non-existent at 100 m a.g.l. Figure 3.3 shows that the evolution of the CIBA and the AWS temperatures at 1.5 m a.g.l. differ from the model, with differences that are

not systematic, some places being colder and vice versa. At the points where the simulation generates a jet, the mixing of the air close to the surface leads to smaller cooling than the observations (not shown). This is the case for the grid point in the cold pool (x12) and in the river valley (x09). In contrast, at the CIBA site, the 1.5-m temperature fall is larger in the simulation due to the lack of turbulence generated in the model for this point. For that night, many observation locations reported the formation of frost. Therefore, the latent heat released by the frost formation may reduce the temperature decrease close to the surface (Whiteman et al., 2007).

Summarising, the model is able to generate a system of low-level flows organised at the basin scale, with katabatic winds on the gentle slopes between the mountain ranges and in the Duero river central valley. The model has a level of heterogeneity similar to the observations, but not precisely at the same locations. The evolution of the wind direction is well captured in the CIBA site after 2200 UTC but missing an earlier rapid veering, probably because of incomplete representation of the previous afternoon basin dynamics in the model. A quantitative estimation of the heterogeneity of the basin, as seen by the satellite images, the AWS and the model, is presented in the next section.

3.4 Spatial distribution and time evolution of surface temperature

To analyse the spatial variability and the temporal evolution of the temperature near the surface, we use 30-min values of radiative surface temperature for the complete basin, estimated from the Meteosat-7 images, and use hourly values of the 1.5-m temperature as measured by the AWS network. Temperatures at the surface and the 1.5-m level from the mesoscale simulation will also be analysed.

The two temperature fields are not directly comparable, especially in very stable conditions when large temperature gradients can exist in the first few metres above the ground and the surface energy budget depends strongly on the state of the surface (Jiménez et al., 2008). Surface temperature will mostly reflect the local energy budget in the layer adjacent to the ground, whereas the 1.5-m temperature may be influenced by larger scale atmospheric transport. Strong stratification near the ground may restrict the exchange of heat between the 1.5-m level and the surface.

The time-space variation of both temperatures are examined using a decomposition similar to that in Lundquist et al. (2008):

$$T_b(\mathbf{x}, t) = \overline{T}_b(\mathbf{x}) + \overline{\overline{T}}_b(t) + \widetilde{T}_b(\mathbf{x}, t) \tag{3.1}$$

where the brightness surface temperature $T_b(\mathbf{x}, t)$ is split into three terms,

(i) the mean nocturnal temperature $\overline{T}_b(\mathbf{x})$ is based on averaging all available values for each pixel or gridbox during the night (1730-0730 UTC), thus providing the average surface temperature pattern (this is a single two-dimensional field for the entire night). The spatial average of $\overline{T}_b(\mathbf{x})$ defines the mean nocturnal temperature;

(ii) the basin-averaged deviation of the temperature from the mean nocturnal temperature $\overline{\overline{T}}_b(t)$ reflects the general cooling of the basin during the night (this is a time series of one value for the whole basin);

(iii) the local spatial deviation $\widetilde{T}_b(\mathbf{x}, t)$ represents the additional information that is not explained by the previous two terms (it is a two-dimensional field).

The brightness surface temperature is analysed from the data provided by Meteosat-7 images and from the mesoscale simulation. The NOAA image at 0200 UTC with higher resolution provides similar patterns as Meteosat-7 for that hour. All the images are corrected, but Meteosat-7 provides a field that does not subtract the effect of water vapour and has a bias of about 1.5 K lower than the NOAA temperatures, for which this correction is performed. Since the model does not use a snow pack parameterisation, the simulation predicts different surface temperatures compared to the satellite observations for the snow-covered part of the south-western basin. The decomposition of the radiative surface temperature from the satellite data does not change significantly when the snow-covered areas are considered.

3.4.1 Mean nocturnal temperature, $\overline{T}_b(\mathbf{x})$

The nocturnal average $\overline{T}_b(\mathbf{x})$ for the basin (Figure 3.4a) computed from the satellite images shows the colder areas in blue. These areas are found over the mountain ranges and in certain parts of the centre of the basin, namely a small cold pool (x12), an area in the river valley (x09) and some locations on the elevated plateaux (such as the CIBA site). Warmer parts include the northern part

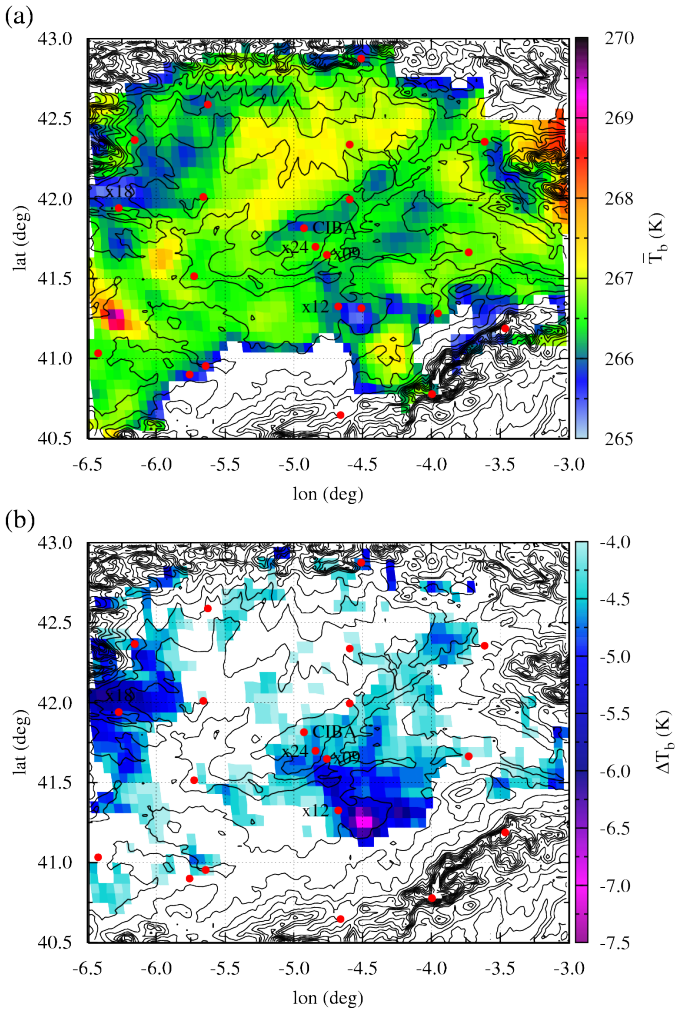

Figure 3.4: (a) Mean nocturnal temperature $\overline{T}_b(\mathbf{x})$ for the Duero basin derived from Meteosat-7 (without the snow area). (b) Total cooling from the beginning of the night (1730 UTC) to just before sunrise (0730 UTC). Only points with a total cooling equal or greater than 4 K are represented. In both plots, surface elevation contours are plotted every 100 m within the range 500 - 2,100 m a.s.l. The locations of the automatic weather stations from AEMET are displayed with dots.

of the basin and the south-east of x12, where well-defined katabatic flows persist and can be detected as a warmer signal in the satellite images (Bromwich, 1989).

The mesoscale simulation, which does not well capture the snow covered area in the south-west, shows absolute average values of about 1 K higher than the satellite temperature (not shown), which is in the range of the error caused by the non-removal of the water vapour effect (the NOAA image for 0200 UTC seems to confirm this). The simulation also generates the coldest areas over the elevated plateaux and, to a lesser degree, in the cold pools east of x12 and x18. The total spatial variability is of the same order, about 4 K, in both fields.

3.4.2 Basin-averaged deviation, $\overline{\overline{T}}_b(t)$

Figure 3.5a shows that the evolution of the averaged basin deviation from the mean nocturnal surface temperature can be fitted to a quadratic function:

$$\overline{\overline{T}}_b(t) = At^2 + Bt + C \tag{3.2}$$

where t represents the time in seconds after sunset. The linear term is an order of magnitude larger than the quadratic term. It is obvious that the model experiences a much larger surface temperature decrease during the night (about 7 K) than the temperature decrease observed by the satellite (about 3.5 K). Part of the difference comes from the different horizontal resolution of the fields, coarser for the satellite (Jiménez et al., 2008), and from the formation of frost within the basin. The accumulation of frost on the ground increases the surface emissivity during the night, leading to an observed fall of the radiative surface temperature on the order of 1 K smaller than the actual one. Another possibility is an inadequate representation of the surface energy budget in the model, which is forced to close point by point (the ground heat flux must equal the sum of the other fluxes and the land surface temperature is the temperature that fulfils this requirement). The observed energy balance can have large departures from the closure, and which may be due to the inadequacy of measurements or due to the local inhomogeneities. Finally, biases in the soil moisture derived from the original ECMWF fields may also have an effect on the surface temperature and moisture provided by the soil scheme, leading to an error in the representation of the ground heat flux.

In both cases, the cooling is more rapid in the first part of the night compared to the second part, indicating that a better fit is obtained through a quadratic adjustment. Whiteman et al. (2004) also found that the decrease of the surface

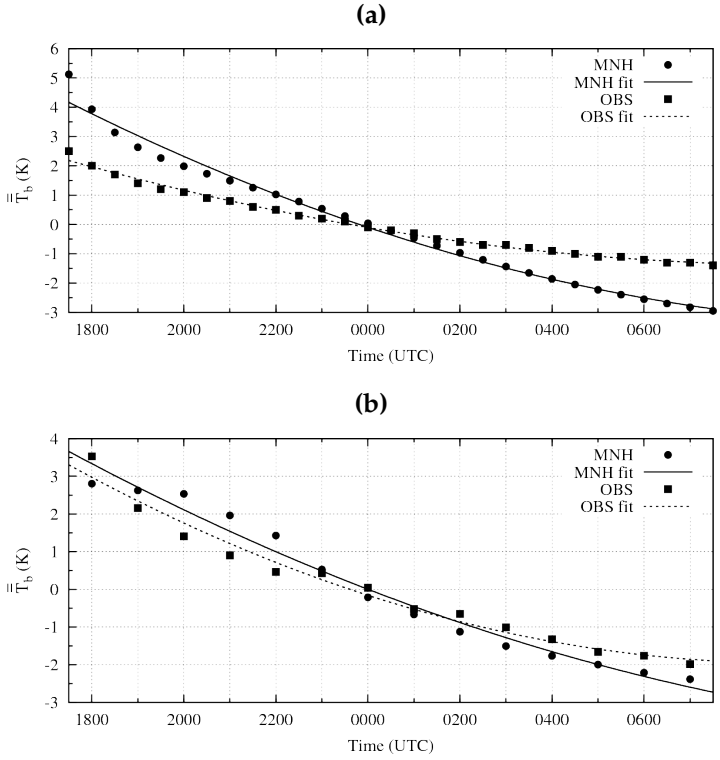

Figure 3.5: (a) Basin-averaged deviation of the radiative surface temperature from the mean nocturnal temperature $\overline{\overline{T}}_b(t)$ between sunset and sunrise from the mesoscale simulation and from the satellite data. (b) The same as (a), but for the 1.5-m temperature with the observations taken from the automatic weather stations.

temperature was more rapid during the first part of the night, represented in their case by an exponential function. They suggested that, under windless conditions, the longwave cooling of the surface is counteracted by the downward longwave radiation and the ground heat flux. As the surface temperature decreases with time, the net longwave radiation is asymptotically balanced by the ground heat flux, leading to smaller cooling of the surface during the second part of the night.

When the same curves are produced with the model 1.5-m temperature and the network of automatic weather stations (Figure 3.5b), the model temperature

decreases approximately 6 K and the observations decrease 5.5 K. This indicates that the model has similar cooling for the surface and 1.5-m levels. For the observations, after the rapid surface cooling just before sunset (not shown), the temperature decrease at the 1.5-m level exceeds the surface cooling, indicating that there may be issues still to address in the treatment of the image surface temperature.

3.4.3 Local spatial deviation, $\widetilde{T}_b(\mathbf{x}, t)$

The last term in Eq. 3.1 is shown in Figure 3.4b, which reveals the areas that have cooled more than 4 K between 1730 (beginning of the night) and 0730 UTC. This threshold represents a surface nocturnal cooling 0.5 K greater than the mean cooling of the basin, showing the area where the absolute cooling with respect to the temperature at sunset has been greater. The large cooling occupies an area at the centre of the basin, covering the elevated plateaux (the CIBA site and x24), the Duero and Pisuerga valleys (x09) and the cold pool close to station x12. Another cold area in the western part of the basin is found around station x18. The mesoscale simulation shows a pattern of the surface nocturnal cooling more constrained by the topography (not shown), with spatial detail that cannot be achieved by the satellite imagery. However, the areas with a larger total cooling include those revealed by Figure 3.4b, and which illustrates the heterogeneity of the surface cooling within a large basin.

3.5 Simulated within-basin flow heterogeneities

To inspect the heterogeneity of the wind and temperature fields in the area of interest, each column of the model fields for 0000 UTC within the domain (Figure 3.1) has been analysed. Although there are significant differences between the simulation and observations, it is not possible to account for the within-basin flow heteregeneity of the meteorological variables with the available experimental data. The wind speeds in the first 100 m a.g.l. have been examined to determine if there is a jet, defined as a maximum in the wind speed in this layer with a decrease in speed of at least 0.5 m s^{-1} above the height of the maximum. The analysis is restricted to the first 100 m because the wind maximum within the basin usually appears at heights between 30 and 60 m a.g.l. The strength of stratification near the ground has been estimated using the difference of potential

Table 3.1: Percentage of the cases (19,430 in total) for the classification of the points at 0000 UTC according to the wind maxima (up to 100 m) and the temperature gradient $\Delta\theta = \theta_{10.5m} - \theta_{1.5m}$). The jet category requires that the wind speed above the jet is, at least, 0.5 m s^{-1} smaller than in the jet height.

	$\Delta\theta < 0$ K	$0 \leq \Delta\theta < 2$ K	$2 \leq \Delta\theta < 4$ K	$\Delta\theta \geq 4$ K	Total
weak jet ($0.5 < wind_{max} \leq 2$ m s^{-1})	0.04	18.08	6.85	1.02	**25.99**
moderate jet ($2 < wind_{max} \leq 4$ m s^{-1})	0.02	21.98	2.17	0.25	**24.42**
strong jet ($wind_{max} > 4$ m s^{-1})	0.00	2.30	0.07	0.00	**2.37**
no jet-weak ($wind_{below100m} < 2$ m s^{-1})	0.08	12.10	8.32	2.05	**22.55**
no jet-moderate ($wind_{below100m} \geq 2$ m s^{-1})	0.12	20.45	3.29	0.81	**24.67**
total	**0.26**	**74.91**	**20.70**	**4.13**	**100.00**

temperatures between the levels at 10.5 and 1.5 m a.g.l., corresponding to the fourth and the first vertical levels of the simulation.

In Table 3.1, data are arbitrarily classified according to five categories for the wind and four categories for the stratification. The first three lines correspond to weak, moderate and strong jets, respectively, and the two last lines to grid points without a jet in the first 100 m a.g.l. The first column corresponds to unstable stratification, and the other three to sequentially increasing stable stratification. Every grid point is included into one of the resulting 20 categories.

Figure 3.6a describes the five wind categories for the selected area and Figure 3.6b describes the three stably stratified ones. Half of the points indicate a jet in the first 100 m a.g.l., almost all of them being weak ($u_{max} \leq 2$ m s^{-1}) or moderate (2 $< u_{max} \leq 4$ m s^{-1}). The strong ones ($u_{max} > 4$ m s^{-1}) represent only 2.4% of the total. The points without a jet have been separated into weak ($u_{max} < 2$ m s^{-1}) and moderate ($u_{max} \geq 2$ m s^{-1}) winds.

The strong jets occur for only a few selected areas within the basin that have a significantly larger local slope, the blue area at the south-east part of Figure 3.6a representing a well-defined downslope flow that was analysed in Martínez and Cuxart (2009). The moderate jets (green) occupy one-fourth of the analysed area, mostly on the slopes of the mountain ranges to the south and south-east of the basin. In contrast, the northern part of the basin with a smaller regional slope is mostly covered by weak jets (red) or weak winds (yellow). Most of the weak winds with no jet tend to be found over the river valleys and some over the

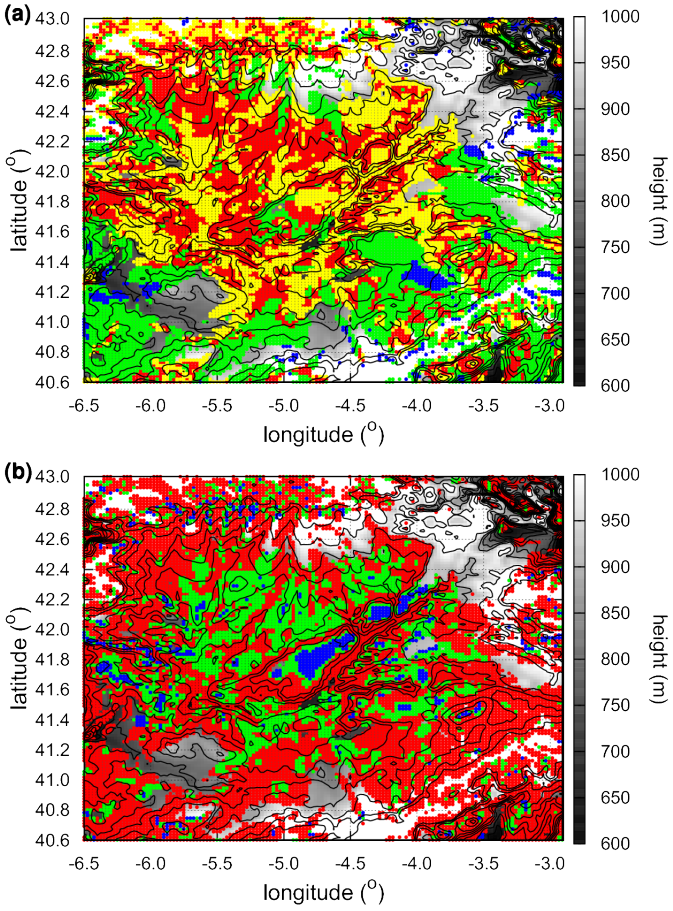

Figure 3.6: Location of the points corresponding to the categories in Table 3.1. (a) Classification according to the wind maxima up to 100 m a.g.l.: (red) weak jet, (green) moderate jet, (blue) strong jet and (yellow) no jet (when the wind speed up to 100 m is smaller than 2 m s^{-1}). The topography is plotted in grey scale for the range of 600-1,000 m a.s.l. (b) The same as in (a), but for the classification according to the strength of stratification in the surface layer: (red) weakly stratified, (green) moderately stratified and (blue) strongly stratified. In both plots, data classified as no jet-moderate in Table 3.1 are excluded.

elevated plateaux. The points without jets and the wind speed above 2 m s^{-1} in the first 100 m a.g.l. (non-coloured points in Figure 3.6a) are found basically at the higher mountain locations and outside the basin, and we will not consider them further.

Figure 3.6b plots the three stably stratified categories, after excluding the non-jet moderate cases. We also exclude the unstable cases, amounting to only 0.26% of the total area. Most of the area is covered by a weakly stratified surface layer (in red), located in the foothills and also in the river valleys. The moderately stratified points are found mostly at the centre of the basin (green), whereas the plateaux contain the strongest stratification (blue). About 80% of the points with a jet have a weakly stratified surface layer and only 2% have strong stratification, basically with weak jets. In contrast, the no-jet weak wind cases have more occurrences of moderate and strong surface-layer stratification (about 50%).

The average profiles of wind and temperature for the categories in Table 3.1 are shown in Figure 3.7a and b, respectively. Each wind profile is constructed by averaging all the occurrences of stably stratified categories (one profile for each of the first four lines in the Table 3.1). Figure 3.7a shows that, on average, the level of maximum speed above the surface increases as the jet strengthens. The standard deviations (not shown) for the three jet categories do not overlap. This statistical relationship is not described by any simple analytical model, such as the Prandtl model for katabatic flows (Grisogono and Oerlemans, 2001a). The jets that contribute to the average profiles have different origins and, as a result, these jets are unlikely to be described by such simple models. The stronger jets, which amount to only 2.4% of the total of the area, have an average value of 4.6 m s^{-1} above 40 m a.g.l. Within the basin, the weak jets, moderate jets, and weak wind no-jet cases each occupy about 1/3 of the area, the moderate ones with the jet maximum at about 25 m a.g.l. over the south-east, and the weak jet and no-jet points co-existing over the rest of the basin with very similar values of the wind speed and surface-layer stratification.

The points with different surface-layer stable stratification are drawn in Figure 3.7b, corresponding to the averages of columns 3, 4 and 5 of Table 3.1. The no-jet moderate winds, which lie outside the basin interior, are excluded. The weakly stratified case includes most of the jet points and about half of the weak non-jet points. It is seen that this average shows a weakly stable layer extending up to 25 m a.g.l. and a gradual transition to the upper levels. In contrast, the moderately and strongly stratified cases have a strong surface-based inversion of about 10 to 15 m a.g.l. (of 3 and 4.5 K respectively) and a sharp transition above.

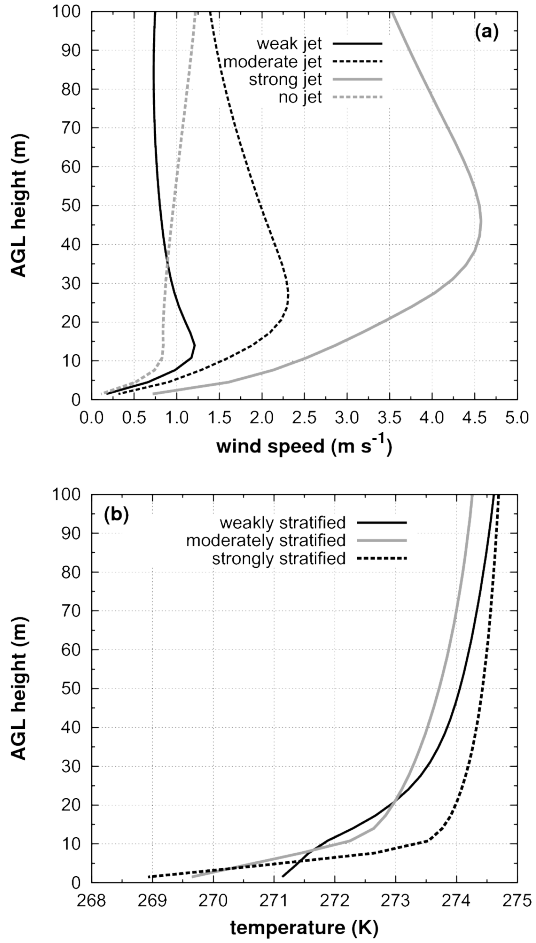

Figure 3.7: (a) Averaged wind speed profiles of the classified categories according to the wind maxima classification in Table 3.1. (b) Averaged temperature profiles for the categories in Table 3.1 based on the strength of stratification in the surface layer. In both plots, data classified as no jet-moderate in Table 3.1 are excluded.

The relative contribution of the radiative and turbulent terms to the temperature evolution is shown in Figure 3.8 for the profiles of Figure 3.7b, without considering the advection and latent heat flux terms. Figure 3.8 is given in a logarithmic

scale for height to emphasise the characteristics near the surface. The vertical divergence of the net radiation (Figure 3.8a) cools all the column with very similar integrated values for all the cases and -0.0004 K s^{-1} near the surface regardless of the stratification. The strongly stratified case (in 3.3% of the area, mostly with weak wind jet and no-jet cases) shows a layer of warming between the first and second atmospheric layers of the model, similarly to that reported by Savijärvi (2006) and Edwards (2009) for the SBL with weak winds close to the ground.

The vertical divergence of the turbulence flux shows large differences between the regimes, but they all are the dominant cooling mechanism in the surface layer and also warm the air closest to the surface, as in Gopalakrishnan et al. (1998). The turbulent heat-flux convergence warms the air below 3 m for the weakly stratified cases and can exceed the effect of the surface radiative cooling. The average heat-flux divergence for the moderately stratified case corresponds to warming only near the ground and is in equilibrium there with the radiation cooling. For the average strongly stratified case, the maximum of TKE occurs just above the layer of radiative warming.

3.6 Conclusions

This study, based on tall-tower observations, a surface meteorological network and satellite data, together with a mesoscale simulation, documents the large variability of nocturnal cooling within a large basin. The basin includes an isolated modest plateau near the centre, plus gentle slopes (angles of 0.003 rad) converging to the centre from the northern and southern mountain ranges.

The analysis of the evolution of the radiative surface temperature fields obtained from Meteosat-7 allows the characterisation of the terrain heterogeneity. The basin area-averaged surface temperature based on satellite data reduces by about 3.5 K between sunset and sunrise, with large within-basin variability. The surface temperature decrease during the same time period is double in the simulation (7 K). This difference is partially explained by the formation of frost during the night, since its effect increases the surface emissivity and leads to a satellite estimate smaller than the actual surface cooling. At 1.5-m height, the AWS network and the model provide similar nocturnal cooling, close to 6 K. The similar decrease of the temperature at the surface and at 1.5 m a.g.l. in the simulation, at the basin scale, indicates that the model efficiently couples the surface and the first computation level. In the areas where drainage flows prevail, turbulent mixing of the air close to the ground leads to less cooling compared

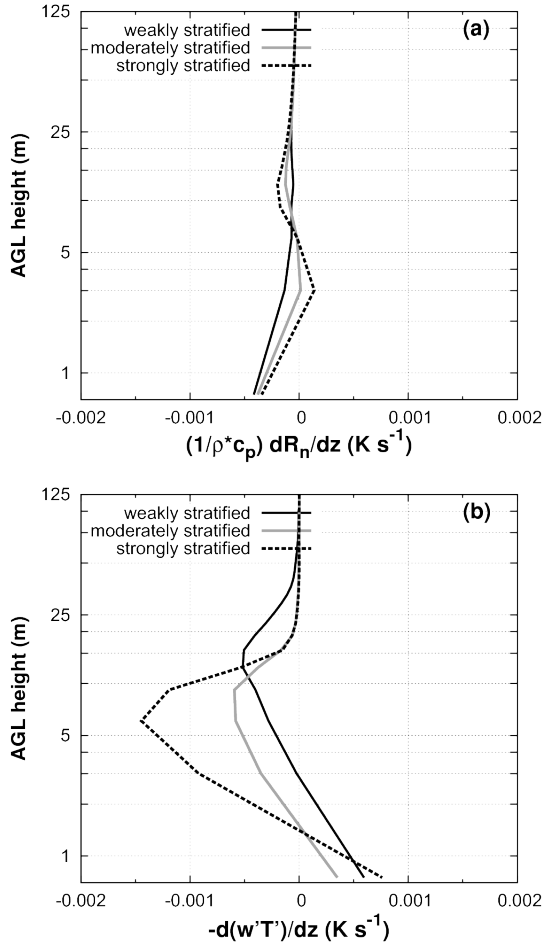

Figure 3.8: Averaged profiles of (a) radiative and (b) turbulent coolings for the categories in Table 3.1 based on the strength of stratification in the surface layer shown in Figure 3.7b.

to more stagnant areas. A time-space decomposition of the temperature field documents the time dependence of the coldest and warmest areas. It is important to note that cold air also collects on the elevated plateau in the centre of the basin, which is colder than the basin-averaged air.

The mesoscale simulation is not able to reproduce exactly the spatial distribution of warm and cold areas, although the amount of heterogeneity in the basin is well captured. The model results were used to explore the within-basin variability. More than half of the columns have a wind maximum in the lowest 100 m, usually with a maximum speed between 1 and 4 m s^{-1} and located below the 45-m level. The moderate jets dominate the airflow over the foothills and the weak jets dominate over gentle slopes, with no-jet weak winds occurring along the river valleys and over the plateaux. These jets have different origins and only a small percentage can be classified as katabatic flows and, therefore, cannot be analysed with the simple analytical models available in the literature. For the cases with jets, the stratification is weakly stable and the turbulence is the dominant cooling mechanism. For the strongly stratified cases near the surface, the turbulence flux convergence tends to warm partially the air and compensate for the effect of surface radiative cooling. Measurement of such turbulent flux convergence would require high quality flux measurements with fine vertical resolution.

Acknowledgements

ECMWF and AEMET are thanked for the access to computing time, AEMET also for the data from the AWS network, the University of Valladolid for the CIBA data, EUMETSAT and NOAA for the satellite images, and the Meso-NH team in Meteo France and Laboratoire d'AÃl'rologie for the technical support and maintenance of the modelling system. The University of the Balearic Islands (UIB) is thanked for providing the financial support for the visit of Dr. Mahrt to the Physics Department at the UIB. This work was partially funded through grants CGL2006-12474-C03, CGL2009-12797-C03 and BES-2007-16272 of the Spanish Government which include European Regional funds (FEDER). The authors are indebted to the three reviewers, who have helped to improve the manuscript substantially.

Chapter 4

Assessment of the hydraulic slope flow approach using a mesoscale model

This chapter is based on Martínez, D., and J. Cuxart, 2009: Assessment of the hydraulic slope flow approach using a mesoscale model. *Acta Geophys.*, **57**, 882–903.

Abstract

The simplified hydraulic two-layer model for a katabatic flow is analysed using the outputs from a high-resolution mesoscale simulation. A stably stratified night is simulated for the Duero basin, a complex terrain area located in the northern Spanish plateau, with large vertical and horizontal spatial resolution. Well-defined katabatic flows on the basin slopes are generated by the simulation, that are relatively stationary and quasi-bidimensional for some areas in the central part of the night.

The bulk quantities used in the two-layer approach as well as the different terms in the equations are computed from the three-dimensional information provided by the mesoscale simulation. This method allows to inspect how well the simplified approach represents the katabatic flow generated by the mesoscale model. The study shows that the hydraulic model allows for a comprehensive

analysis of the basic mechanisms of the slope flows but is not able to close the budget equations, since the residuals are large.

4.1 Introduction

The presence of the thermally driven flows is ubiquitous at the bottom end of the atmosphere whenever a stably stratified situation takes place over a topographically complex area. Cold air accumulates at the lower parts of the terrain (Clements et al., 2003), interacting with a hierarchy of low-level jets whose features depend on the spatial and time scales of the region analysed. Valley winds, slope flows and other kinds of gravity flows contribute to the formation of a wind pattern close to the surface that evolves to a steady situation as seen in Cuxart et al. (2007). The katabatic flow structure has important consequences for turbulent surface fluxes of momentum, heat, watervapour, among others, modifying their vertical transport. Thus, it is necessary to analyse their contribution since the thermally driven flows are usually misrepresented in numerical applications with a relatively low vertical resolution (tens of metres), such as weather or climate modeling. A better understanding would lead to the development of improved subgrid parameterizations for these applications (Haiden and Whiteman, 2005).

The gravity flows have been studied theoretically by reducing the problem to a set of equations that can be solved analytically. The classical Prandtl model predicts the stationary vertical structure at one point of the slope, while bulk hydraulic models predict the along-slope evolution of vertically integrated perturbation quantities. The latter approach has been developed by Ball (1956), Manins and Sawford (1979b) and Fitzjarrald (1984), among others. Mahrt (1982) focuses on the momentum equation, with a detailed scale analysis and a critical study of all the possible approximations, providing sounded information to decide which simplifications can be carried out and which are the dominant terms.

Other works have attempted to compare the predictions of the simplified models against observations (Manins and Sawford, 1979a; Kondo and Sato, 1988; Doran et al., 1990), with upsetting results. Most of the simplified models are developed assuming ideal conditions such as very large and homogenous slopes or a negligible ambient wind. Nevertheless, even observations from very planar slopes with a homogenous surface and a weak ambient wind differ from the theoretical predictions. Haiden and Whiteman (2005) revisit the bulk momentum and heat equations using measurements from a katabatic flow under such ideal conditions

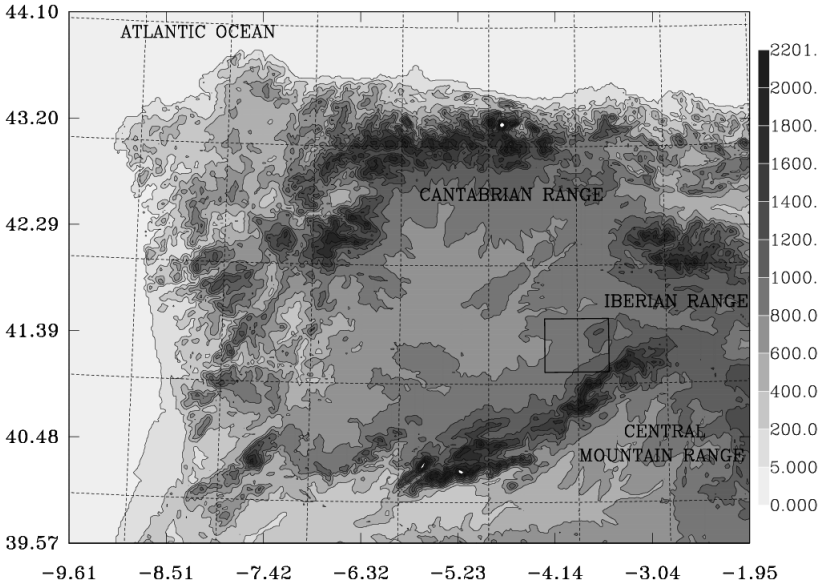

Figure 4.1: Domain of the run corresponding to the Duero basin, with the main mountain ranges that almost close the basin (altitude in m). The black square indicates the selected area for the katabatic wind study. Axes indicate geographical coordinates (in degrees)

during the VTMX campaign (Doran et al., 2002), in middle latitudes. They found that the cross-slope curvature is responsible of the observed deviations, specially under conditions of weaker stratification. Shapiro and Fedorovich (2007) analyse the effect of varying the surface cooling along the slope.

The hydraulic approach has also been used as a framework to study the features of the katabatic winds simulated by mesoscale models. Renfrew (2004) performs a three-dimensional (3D) simulation over the Antarctica, but still includes ideal effects like a topography uniform in the cross-slope direction or an initialization with a homogeneous atmosphere. Under these conditions, the author attributes the imbalances of the bulk momentum budget equation to the fact that the slope angle varies along the slope direction. Cuxart et al. (2007) use a mesoscale simulation to study the steady patterns of the nocturnal circulations over the island of Majorca, in the Western Mediterranean sea, in reasonable agreement

with the observations. The terms for the bulk budget equation of momentum are also calculated for a katabatic wind formed in the simulation. The authors attribute the imbalances to the misrepresentation of the advection due to the three-dimensional effects not included in the hydraulic theory.

These mesoscale simulations have been revealed to be enough realistic with respect to the behavior of the thermally-driven flows and the accumulation of the colder air (Jiménez et al., 2008), becoming a useful tool that complements the information of the observed katabatic winds (Savage et al., 2008; Zhong and Whiteman, 2008).

All the cited works, among others, coincide to point out that the hydraulic theory is a conceptual model that cannot be directly compared to the observations due to the simplifications made. Nevertheless, the framework is used to characterize the katabatic flows, even though the conditions are far from what is required to apply the theoretical framework. At this point, it is necessary to account what are the limits of the hydraulic model and how they assumptions can be applied to the observed or simulated flows.

In the present work, a high-resolution mesoscale simulation from a large basin in mid-latitudes is used to assess the validity of the hydraulic model under realistic conditions. The use of data from a mesoscale model instead of observations is preferred as it provides all the information required. With observations, on the contrary, it is common to be forced to estimate some expressions indirectly, adding uncertainty to the final results (Haiden and Whiteman, 2005).

The details of the mesoscale simulation are inspected in Section 4.2, focusing on a katabatic flow generated over the mountain slopes of the basin. The hydraulic theory for the momentum and heat equations is described in Section 4.3, and their basic parameters are defined and computed in Section 4.4. With these parameters derived from the three-dimensional information out of the model, the behavior of our flow problem is analysed in terms of the two-layer model in Section 4.5 and the goodness of the bulk momentum and temperature equations is checked in Section 4.6, looking for the residuals and their causes.

4.2 Description of the flow

The selected case corresponds to a strongly stratified night associated with the presence of a high-pressure system over the main part of the Iberian Peninsula during the night of 14-15 January 2003. As a result, a slack synoptic pressure

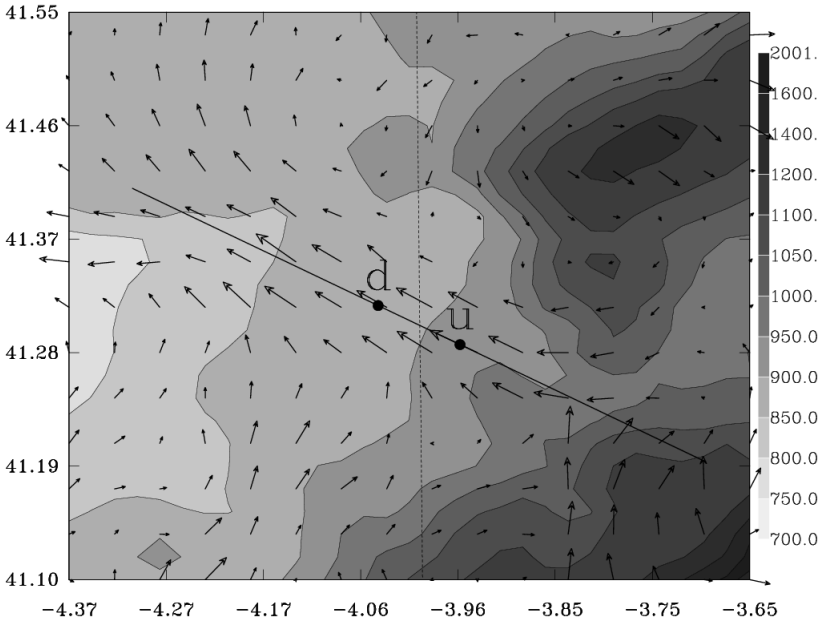

Figure 4.2: Area of the Duero basin selected to study the katabatic wind generated by the simulation (zoom of the square in Figure 4.1), with the topography in m as seen by the model and horizontal wind vectors at 40 m AGL at 0200 UTC. Solid line corresponds to the cross section analysed in further figures and dots refer to relevant points of the study. Axis labels in degrees.

gradient with clear skies and a strong radiation cooling on the surface was found in the Duero basin. This case has been used previously for an intercomparison between two state-of-the-art mesoscale models (Meso-NH and MM5) under stable conditions in Bravo et al. (2008).

The Meso-NH (Lafore et al., 1998) model has been run again for the present study with a finer horizontal resolution. Meso-NH is a nonhydrostatic, compressible model that utilizes a terrain-following coordinate system with a stretched vertical grid. The relevant parameterizations for this case are the turbulence (Cuxart et al., 2000), the radiation (Morcrette, 1990) and the soil vegetation (Noilhan and Planton, 1989) schemes.

The model domain covers the complete basin (Figure 4.1), with 320 x 250 points in the x and y directions, respectively, and a grid spacing of 2 km x 2 km. The vertical grid is stretched, with 85 levels that provide a resolution of 3 m close to the surface, 5 m at 100 m above ground level (AGL) and 700 m at the model top of about 9600 m AGL. This vertical resolution is high enough to capture the details of the low-level flows, as shown in Cuxart et al. (2007). Actually, all recent studies of the katabatic winds that use numerical models apply similar vertical resolutions: around 2.1 m close to the surface in Zhong and Whiteman (2008), 5 m in Renfrew (2004) or Smith and Skyllingstad (2005) or even larger, 20 m in Savage et al. (2008). All of them report katabatic flows with a maximum of the windspeed below 50 m AGL.

The simulation starts at 1200 UTC (12 local solar time) 14 January 2003 and is run for 24 hours. The rest of the features of the Meso-NH simulation are as described in Jiménez et al. (2008), where a very similar mesoscale simulation was applied over the Majorca island and verified against observations.

In the present case, the synoptic flow is very weak and comes from the southwest over the area of interest, allowing the thermally driven flows to develop 4 hours after the sunset (around 1700 UTC). In general, drainage winds blow from the top of the mountain ranges that surround the area (Cantabrian, Iberian and Central mountain ranges) towards the center of the almost closed basin. At the upper part of the slopes, gravity currents are diverted and converged depending on the curvature of the terrain in the cross-slope direction, as described in Haiden and Whiteman (2005). At the lower parts, the windspeed is reduced and katabatic winds lose their own features probably due to the accumulation of cold air at those parts of the basin. Zhong and Whiteman (2008) show how the buildup of the inversion of temperature at the valley contributes to the weakening or disappearing of the downslope flows. This interaction in the Duero basin will be analyzed in a further study. The surface wind pattern described here remains steady with a decrease of the windspeed until the sunrise destroys it completely (around 0800 UTC). For more details of the general dynamics within the basin, see Bravo et al. (2008) or Martínez et al. (2010).

In order to study a simulated katabatic flow as ideal as possible, the attention has been focused in a reduced area of 60 x 50 km^2 at the upper part of the Central mountain range slope, far away from the influence of the dynamics at the center of the basin (Figure 4.1). The drop of height is of 1000 m from the top of the mountain range to the center of the basin. The most regular part of this area is shown in Figure 4.2, with the terrain falling from 1100 to 820 m above sea level (ASL) in 45 km. Nevertheless, the presence of a hill and a gully perturbs the homogeneity of the terrain in the cross-slope direction and modifies the wind direction at the lower levels (Figure 4.2).

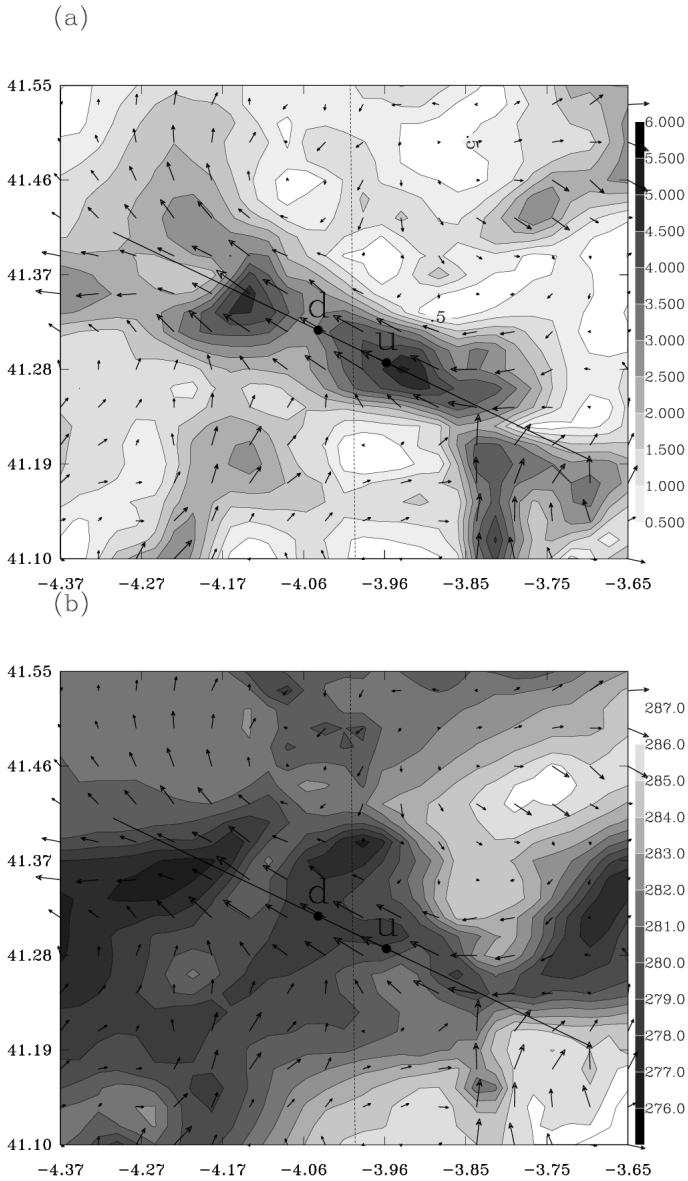

Figure 4.3: The same as in Figure 4.2 but for the (a) wind speed (m s^{-1}) and (b) potential temperature (K).

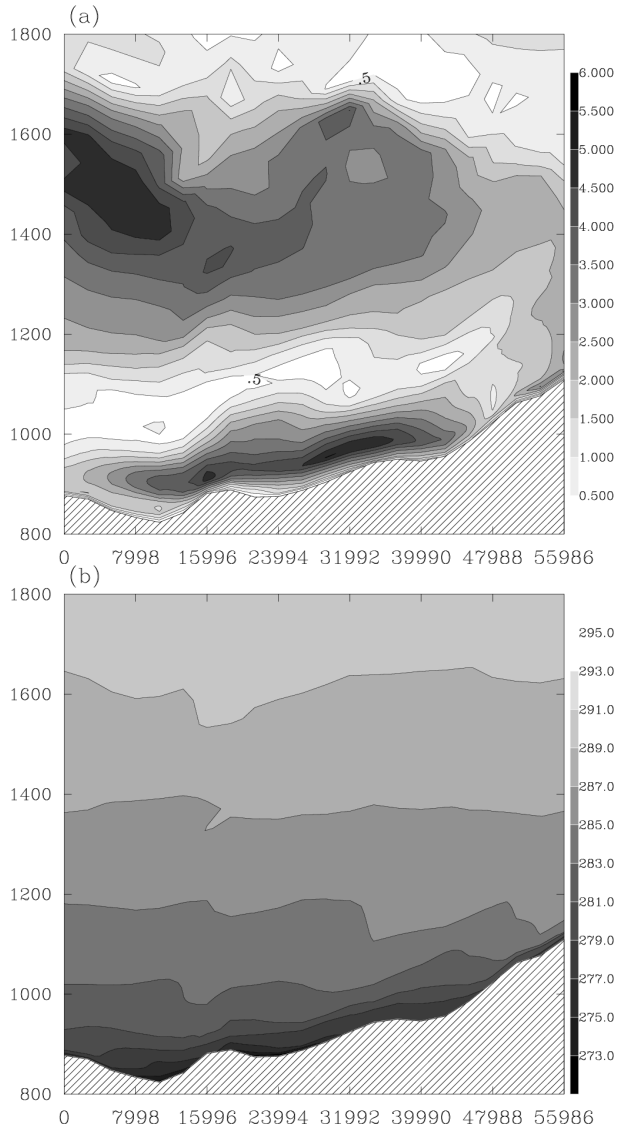

Figure 4.4: Vertical cross section at 0200 UTC following the line in Figure 4.2 for the (a) wind speed (m s^{-1}) and (b) potential temperature (K). Axis labels in meters.

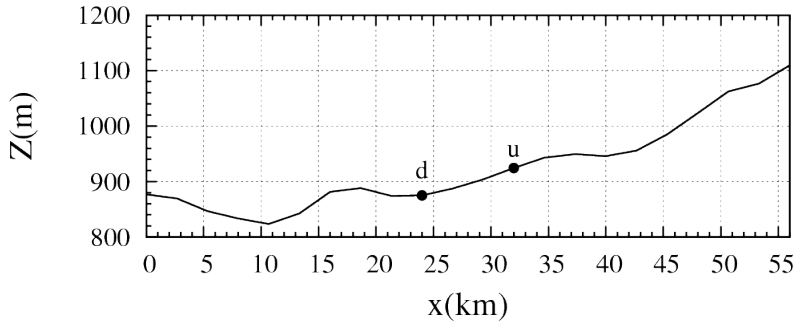

Figure 4.5: Topographic cross-section of the studied slope along the bold line in Figure 4.2, showing the location of the two points of interest.

When the gravity currents are well developed within the basin (after 2100 UTC), the surface wind in the area of interest turns to the southeast, following the downslope direction. The maximum windspeed is located over a reduced horizontal section of the terrain, where the slope is more homogeneous (Figure 4.3a). This pattern is steady during the first hours of the night, until 0300 UTC, when wind turns to southern directions and weakens rapidly. The air-temperature close to the surface decreases during the whole night because of the surface radiative cooling, with the minimum values at the lower and sheltered parts of the area (Figure 4.3b).

The vertical cross-sections along the slope show that the wind maximum is generated over the gentlest part of the slope, with values up to 6 ms^{-1} at 50 m AGL. This maximum weakens and its height increases as it advances downslope, and strengthens again at the rim of the lower gully (Figure 4.4a). Smith and Skyllingstad (2005) found that slopes with a concave shape have a stronger acceleration near the top of the slope which then transitions toward a slower and more elevated jet near the base. The same behavior seems to be reproduced in this mesoscale simulation. Above the katabatic wind, the wind speed is lower than 1 ms^{-1}, isolating the thermally driven flow from the influence of the air aloft.

There is a stratified layer close to the surface, with the potential temperature field parallel to the slope, that is even deeper over the gullies (Figure 4.4b). The tilt of the isothermals disappears at the inner part of the basin (left side of Figure 4.4b),

where the buildup of the temperature inversion takes place. Also in the vertical direction, the isothermals become horizontal approximately at 150-200 m AGL. This height gives an idea of the katabatic-layer depth.

At this part of the basin, a steady katabatic wind is formed over the most homogenous part of the slope, further away from the influence of the cold-air pooling at the center of the basin and with a very weak ambient wind. Under such conditions, although not completely ideal (the angle slope is not constant), it seems reasonable to apply the framework of the hydraulic theory. Thus, the rest of the text will focus on the part of the slope where these conditions are fulfilled, between points u and d (Figure 4.5).

4.3 The hydraulic slope flow approach

The hydraulic theory provides different sets of equations with regard to the equations and terms considered. In this section, the final budget equations are derived from a general frame of reference in order to clarify what are the simplifications carried out in the present study. The katabatic flow is finally described by bulk equations that reduce its vertical distribution to a single layer. In further sections, the terms from the derived budget equations are calculated using the data provided by the mesoscale model, with the aim to check the closure of these budgets.

In a two-dimensional, rotated and orthogonal coordinate system, with a basic state defined at rest, in hydrostatic equilibrium and horizontally homogeneous, and considering the Boussinesq approximation for shallow flows, the resulting set of equations governing the conservation of momentum (adding the effect of the Coriolis force), heat and mass can be written as (Manins and Sawford, 1979b):

$$\frac{\partial u_s}{\partial t} + u_s\frac{\partial u_s}{\partial s} + w_n\frac{\partial u_s}{\partial n} = -\frac{1}{\rho_0}\frac{\partial \Delta p}{\partial s} + g\frac{\Delta\theta}{\theta_0}sin\alpha + fv - \frac{\partial\overline{w'u'}}{\partial n} \quad (4.1)$$

$$\frac{\partial w_n}{\partial t} + u_s\frac{\partial w_n}{\partial s} + w_n\frac{\partial w_n}{\partial n} = -\frac{1}{\rho_0}\frac{\partial \Delta p}{\partial n} - g\frac{\Delta\theta}{\theta_0}cos\alpha \simeq 0 \quad (4.2)$$

$$\frac{\partial \Delta\theta}{\partial t} + u_s\frac{\partial \Delta\theta}{\partial s} + w_n\frac{\partial \Delta\theta}{\partial n} = \gamma(w_n cos\alpha - u_s sin\alpha) + \frac{1}{\rho_0 C_p}\frac{\partial R_n}{\partial n} + \frac{\partial\overline{w'\theta'}}{\partial n} \quad (4.3)$$

$$\frac{\partial u_s}{\partial s} + \frac{\partial w_n}{\partial n} = 0 \quad (4.4)$$

where α is the slope angle, the s and n axes follow the downslope and perpendicular directions, respectively, and u_s and w_n are the velocity components in the rotated system. Besides, $\Delta\theta = \theta_0 - \theta$ and $\Delta p = p - p_0$ refer to the time-average perturbation with respect to the basic state (θ_0, p_0), where $\Delta\theta$ is usually defined as the temperature deficit.

The conservation of heat (4.3) has been expressed in terms of the temperature deficit to keep the same variables in all the equations system. Thus, the advection of the potential temperature field is split in (i) the advection of the potential temperature perturbation and (ii) the advection of the basic state, where $\gamma = \partial\theta_0/\partial z$ is the vertical gradient of the basic state. Besides, the vertical divergences of the net radiation and the turbulent heat flux are also considered.

The quasi-hydrostatic approximation (Mahrt, 1982; Haiden, 2003) is applied in (4.2), which considers that the hydrostatic equilibrium of the perturbed flow is only present for motions perpendicular to the ground:

$$-\frac{1}{\rho_0}\frac{\partial \Delta p}{\partial n} = g\frac{\Delta\theta}{\theta_0}cos\alpha \tag{4.5}$$

This approximation is strictly applicable on the slopes with a length scale much larger than the depth of the katabatic flow. Since the simulated katabatic flow presents inhomogeneities along the slope, this assumption must be tested for the results given by the mesoscale model (see Section 4.6).

Renfrew (2004) proposed a simplified bulk momentum equation assuming a two-layer model with a katabatic layer as the lower one and a quiescent layer above, with the properties of the basic state, integrating equation (4.1) vertically from the ground ($n = 0$) to the katabatic-layer top ($n = h$). Moreover, the product of two bulk quantities is reduced to the bulk quantity of the product ($\widehat{\xi \cdot \phi} \rightarrow \widehat{\xi \cdot \phi}$). Expanding this simplification to the rest of the expressions (4.2)-(4.4), it is possible to get the complete set of bulk equations:

$$\frac{\partial}{\partial t}\left(\widehat{u_s}\right) + \widehat{u_s}\frac{\partial}{\partial s}\left(\widehat{u_s}\right) + \widehat{w_n}\left(\frac{u_h - \widehat{u_s}}{h}\right) =$$

$$-cos\alpha\frac{g}{\theta_0}\frac{\partial}{\partial s}\left(h\widehat{\triangle\theta}\right) + g\frac{\widehat{\triangle\theta}}{\theta_0}sin\alpha + f\widehat{v} - \frac{\overline{(w'u')}_h - \overline{(w'u')}_0}{h} \quad (4.6)$$

$$\frac{\partial}{\partial t}\left(\widehat{\triangle\theta}\right) + \widehat{u_s}\frac{\partial}{\partial s}\left(\widehat{\triangle\theta}\right) + \widehat{w_n}\left(\frac{\triangle\theta_h - \widehat{\triangle\theta}}{h}\right) =$$

$$\gamma\left(\widehat{w_n}cos\alpha - \widehat{u_s}sin\alpha\right) + \frac{1}{\rho_0 C_p}\frac{R_h - R_0}{h} + \frac{\overline{(w'\theta')}_h - \overline{(w'\theta')}_0}{h} \quad (4.7)$$

$$\frac{\partial}{\partial s}\left(\widehat{u_s}\right) + \left(\frac{w_h - \widehat{w_n}}{h}\right) = 0 \quad (4.8)$$

where $\widehat{\triangle\theta} = \theta_0 - \widehat{\theta}$ is the katabatic-layer potential temperature deficit, between the katabatic-layer ($\widehat{\theta}$) and the quiescent layer above (θ_0). Moreover, the vertically integrated variables $\widehat{\xi}$ are defined as:

$$\widehat{\xi} = \frac{1}{h}\int_0^h \xi(n)dn \quad (4.9)$$

and the subindexes ϕ_h and ϕ_0 refer to the values of variable ϕ at the levels $n = h$ and $n = 0$, respectively, except for the case of θ_0 that represents the potential temperature of the basic state.

The storage and advection terms are written on the lhs of the resulting budget equations for momentum (4.6) and deficit of potential temperature (4.7). In the first case (4.6), on the rhs are the thermal wind term (as expressed in Mahrt, 1982), the buoyancy forcing, considered the source of the katabatic wind, the Coriolis force and the turbulent stress divergence across the katabatic layer, which depends on the surface drag and the turbulent entrainment at the top of drainage flow. For the second case (4.7), there are the advection of the basic state temperature field as well as the longwave radiation and the turbulent heat flux divergences.

For the rest of the text, the forcing terms of the latter expressions will be referred *to* using the abbreviations:

$$U_{stor} + U_{adv} = U_{therm} + U_b + U_{cor} + U_{turb} \quad (4.10)$$

$$T_{stor} + T_{adv} = T_{backadv} + T_{rad} + T_{turb} \quad (4.11)$$

Most of the terms in (4.10) and (4.11) can be found in the above referenced works, where the authors define different budget equations depending on which simplification they want to apply. Manins and Sawford (1979b) deal with a steady case using all the terms presented here except the storage terms and the Coriolis force. Besides, Mahrt (1982) presented several simple solutions balancing a reduced number of terms depending on the results from the scale analysis. Analytical solutions were provided for the advective-gravity flow ($U_{adv} = U_b$), the equilibrium case ($U_b = -U_{turb}$) or the shooting regime ($U_b = U_{adv} - U_{turb}$). Moreover, Haiden and Whiteman (2005) applied the bulk momentum and heat budgets to experimental data by using the terms $U_{stor} + U_{adv} = U_{therm} + U_b + U_{turb}$ and $T_{stor} + T_{adv} = T_{backadv} + T_{turb}$. In all these works, the term U_{adv} is slightly different because the conservation of mass equation (4.4) is used to rewrite it in terms of a flux divergence. The simplification presented here (4.6) has been used in previous works (Renfrew, 2004; Cuxart et al., 2007), except that the storage term was not considered and the thermal wind term was split in two contributions depending on which parameter (the deficit or the height of the katabatic layer) varies along the slope.

4.4 Application of the simplified model

The hydraulic theory just described represents the simplest version of the bulk momentum and heat equations found in the literature. The katabatic wind generated by the mesoscale simulation is developed under conditions that can be reasonably assumed by the hydraulic simplification, *i.e.*, a weak ambient wind aloft or being further away from the influence of the buildup of the inversion of temperature. Thus, the model outputs from the simulated gravity current will be used to compute the bulk quantities of the expressions (4.6)–(4.8). The degree of closure of these budget equations will provide information about the capacity of the simplified hydraulic model to describe a more complex problem, such as the simulated katabatic flows by mesoscale models, that include the effects of many other phenomena.

Before applying the two-layer hydraulic model, it is necessary to define the katabatic-layer height. Mahrt (1982) defines the top of the drainage flow layer as the level where the pressure perturbation, related with the presence of the katabatic flow, vanishes ($\triangle p(h) = 0$). At this level, using the expression (4.5), also the deficit is negligible $\triangle\theta = 0$, allowing us to consider the katabatic-layer top as the height of the temperature inversion.

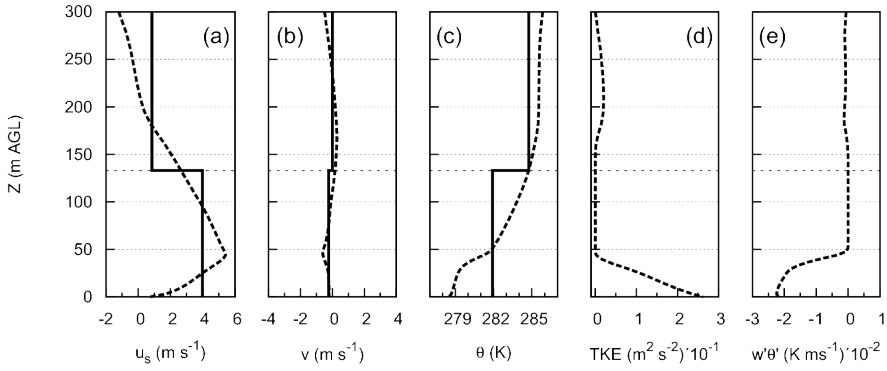

Figure 4.6: Vertical profiles for (a) along slope velocity (m s^{-1}), (b) cross-slope velocity (m s^{-1}), (c) potential temperature (K), (d) TKE (m^2 s^{-2}) and (e) kinematic flux of latent heat (K m s^{-1}) for the output of the mesoscale model (dashed line) and the result after applying the hydraulic approach (bold line) for point *u* (Figure 4.5) at 0000 UTC.

The vertical profiles of the mesoscale simulation vary significantly during the whole night, implying a change of the katabatic-layer depth. These variations yield to additional terms in the budget equations that mask the more general and steadier features of the katabatic flow. Thus, a constant h is defined at every point of the slope using the time-averaged profiles of θ from the period 2130-0230 UTC, when the katabatic wind is almost steady.

To locate the top of the katabatic-layer, we adopt the method of Renfrew (2004) that locates this height by searching the first level where the vertical gradient of θ falls below 0.025 K m^{-1}. The heights obtained cover a range from 86.5 to 125.4 m AGL, with the lowest values at the lower part of the slope. The terms of the budget equations that are divided by h reduce their contribution as h increases. Nevertheless, neither the bulk parametres nor their time-evolution present significant differences in the range of the computed h. Since the vertical integration is insensitive to the exact choice of h if it is above the temperature inversion (Haiden and Whiteman, 2005), the highest h was applied to the rest of the points along the slope (h=125.4 m AGL). Similarly, different values of the threshold on the temperature gradient have been tested, providing a range of variable heights that did not change the conclusions this study.

Once the katabatic layer height is found, the idealized hydraulic model can be applied to the mesoscale simulation outputs (Figure 4.6). The defined h

splits the SBL in two layers, the katabatic-layer close to the ground and a quasi-quiescent layer above. All the needed katabatic bulk variables are computed by integrating them from the surface to the top of the katabatic layer h (4.9). Besides, the potential temperature of the basic-state is considered vertically constant and equal to the temperature simulated at the top $\theta_0 = \theta(h)$ (Renfrew, 2004), yielding a negligible deficit at this level $\triangle\theta_h = 0$. Finally, the bulk along slope velocity of the upper layer u_h is computed integrating it vertically from the height of the katabatic layer h to the level where the vertical wind shear is minimum.

Figure 4.6 gives an idea of the simplification carried out by the hydraulic approach with respect to the three-dimensional flow. Here, it is interesting to point out how the two-layer model neglects the differences of the wind shear below and aloft the maximum of the wind. Respect to the potential temperature, the simplified model considers a well mixed layer within the katabatic wind, locating a very strong and unrealistic inversion of temperature at the top of the layer. The effect of these simplifications to the data from the mesoscale simulation is analyzed in the next sections.

4.5 The katabatic wind as seen by the two-layer approach

The hydraulic two-layer model has been applied to the slope segment located between the points u and d from Figure 4.5, where the simulated drainage wind flows in the downslope direction. In Figure 4.7, the 1-minute time-evolution of the relevant bulk parameters is shown for the period 1800-0600 UTC for the two points, which are the most interesting since they present different behavior. The points in between show a smooth transition from the upper u to the lower d location.

The bulk velocity component along the slope shows three different episodes at night, with a quasi-steady-state of 5 hours during the central part of the time period and significant positive and negative accelerations before and afterwards, respectively (Figure 4.7a). The quasi-steady period of $\widehat{u_s}$ (2130-0230 UTC) has been used to define the katabatic layer depth, especially because the bulk cross-slope component $\widehat{v}$ is small compared to $\widehat{u_s}$ (Figure 4.7b), that makes it a good estimation of the conditions of the simplified hydraulic model.

The bulk slope-relative vertical wind component $\widehat{w_n}$ (which is approximated to the vertical wind component due to the small angle α) is two orders of magnitude smaller than the downslope velocity $\widehat{u_s}$ (Figure 4.7c), being positive at point d during the whole night and negative at point u until midnight, when it

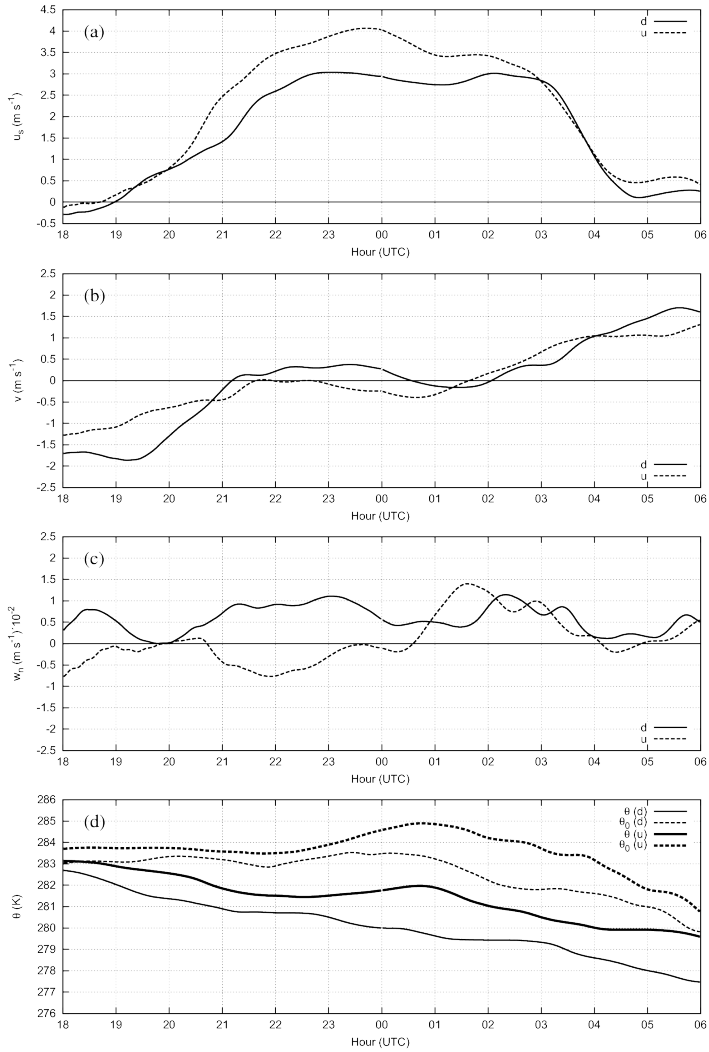

Figure 4.7: Time evolution of the bulk parameters for the nocturnal period 1800-0600 UTC using a steady katabatic layer depth of 125.4 m AGL for the two points indicated in Figure 4.5. Katabatic-layer velocities (m s^{-1}) in the (a) along slope direction, (b) cross-slope direction and (c) slope-relative vertical direction and (d) potential temperature (K) of both the katabatic-layer θ and the upper layer θ_0.

turns positive probably due to a mixing process during an episode of elevated turbulence (not shown). The cold air accumulated at the lower part of the slope displaces the katabatic current upwards, yielding to positive values of $\widehat{\overline{w_n}}$ at point d.

The katabatic layer potential temperature $\widehat{\theta}$ decreases during the whole night in both points (Figure 4.7d) but faster at the lower parts of the slope, where the windspeed is lower. This general cooling presents several interruptions, turning to heating episodes in the case of point u (*i.e.*, 2200-0100 UTC) due to the higher values of the surface turbulent fluxes (Figure 4.8b). For the ambient potential temperature, θ_0 remains constant or even increases during the first part of the night due to the elevated turbulence, which appears intermittently and above the maximum of the windspeed for the case of d. Afterwards, as long as the turbulence disappears, θ_0 decreases with a constant rate.

In point d, there is a strong temperature inversion (8 K in 50 m) due to the accumulation of cold air that inhibits any sustained turbulent activity, leading to a decoupling between the katabatic flow and the surface layer. On the contrary, the persistent surface turbulence in u drives to a well-mixed vertical profile of θ within the surface layer, causing a smaller cooling rate of the bulk potential temperature at the upper part of the slope.

Turbulent fluxes at the top of the katabatic layer as seen by the mesoscale simulation are very small compared to the surface fluxes, specially at the upper part of the slope (Figure 4.8). Thus, it can be concluded that the dominant retarding stress for the simulated katabatic wind is the surface drag, as in the katabatic wind described by Ball (1956). However, the elevated turbulence, which appears intermittently, can mix warmer air from above and heat the upper part of the katabatic layer, increasing mainly the value of θ_0 (Figure 4.7d). Since the air close to the surface is constantly cooling during the whole night, the temperature deficit $\widehat{\triangle\theta}$ increases during these intermittent episodes. In Manins and Sawford (1979b), the entrainment was found to be the responsible of heating the complete layer of the katabatic flow due to the interfacial mixing, diminishing the magnitude of $\widehat{u_s}$ and $\widehat{\triangle\theta}$. The katabatic flow simulated here shows how an elevated mixing episode does not retard the flow and, due to the definition of the katabatic-layer deficit, increases the difference between the temperatures of the katabatic layer and the quiescent layer above.

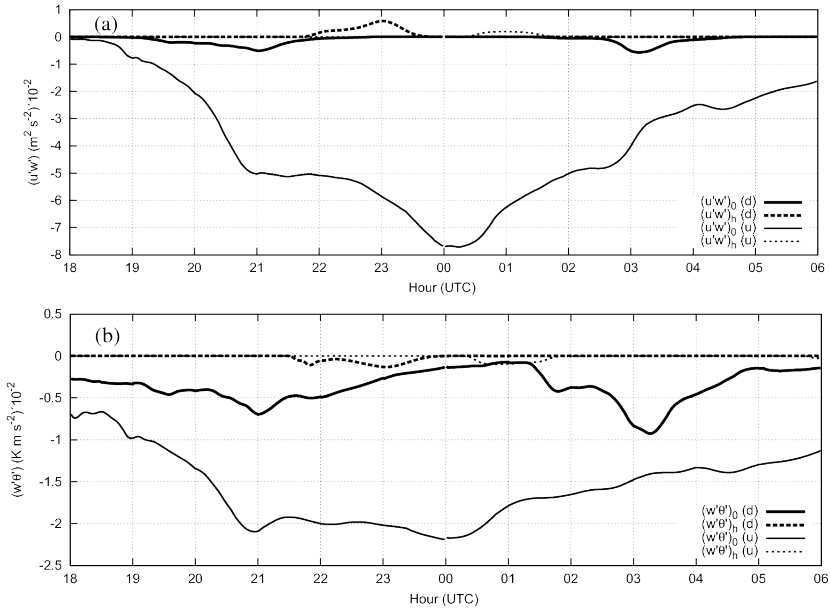

Figure 4.8: The same as in Figure 4.7 but for the kinematic fluxes of (a) momentum (m^2 s^{-2}) and (b) latent heat (K m s^{-1}) at the surface and at the katabatic layer height.

4.6

Analysis of the closure of the two-layer budget equations

Figure 4.9 shows the time-evolution of the forcing terms of the downslope momentum (4.6) and heat (4.7) for the two points of the analysis.

For the momentum budget equation, the forcing terms are balanced in u during the quasi-steady period (Figure 4.9a). In general, U_b and U_{turb} are the more constant and larger terms of the budget, with similar values but opposite sign and U_{cor} is very small because of the reduced spatial scale. U_{adv} is always positive due to the decrease of $\widehat{u_s}$ along the slope, changing significantly its value with time. U_{stor} is relevant before and after the quasi-steady transition, balancing U_{adv} at the beginning, and being replaced by U_{therm} during the quasi-steady period. When $\widehat{u_s}$ decelerates (Figure 4.7a), U_{turb} cannot compensate the rest of the terms

(U_b, U_{adv} and U_{stor}) and the budget equation has strong imbalances. For point d, U_{turb} is very small due to the weak surface turbulence and thus cannot balance U_b (Figure 4.9b). Although the deficit is larger at this point, U_b is smaller because the slope angle decreases at this part of the cross-section. During the quasi-steady period, the decrease of $\widehat{u_s}$ along the slope is stronger at the lower points, leading to an increase of U_{adv} that cannot be balanced by any other term (U_{therm} and U_{stor}).

This behavior suggests that the two-layer model approach, in terms of the downslope momentum budget, can describe a certain period of the katabatic currents at the upper parts of the slope, far from the accumulation of cold air at the lower layers. At these points, the presence of the cold air pushes the drainage flow upwards, forcing it to reduce its downslope velocity that leads to a large increase of U_{adv}. The presence of a strong inversion of temperature reduces the turbulence and, thus, U_{turb} cannot balance the increment of U_{adv}.

Concerning the heat budget equation, the advection terms (specially T_{adv}) are larger than T_{stor} or T_{turb} which, for the case of point d, is very small due to the weak turbulence (Figure 4.9). Besides, T_{rad} is also very small for the whole slope and does not play any role in the budget equation, showing that the radiative flux divergence can be neglected (Haiden and Whiteman, 2005).

The budgets do not close during the quasi-steady period of the simulated katabatic flow, being the upper point u the closest to balance and only for the momentum budget equation. The hydraulic model assumes that katabatic layer variables can be related to each other through a simple system of equations, without the need of knowing their vertical profiles. Since strong imbalances are found and the mesoscale model outputs are the result of the fully 3-D equations, the vertical reduction to bulk quantities should be revised. This is particularly true for the heat budget, where the parameterized terms would lead to a heating of the katabatic layer (reduction of the deficit) instead of the layer cooling produced by the mesoscale model.

In order to shed some light on the bulk simplifications carried out, the bulk versions of the quasi-hydrostatic balance and the conservation of mass (4.8) have been checked. For the first case, the forcing terms are smaller than the terms from the downslope budget equation (4.6) (not shown), confirming that the quasi-hydrostatic approximation is still valid. For the case of the conservation of mass, it is only accomplished for point u and during the quasi-steady period (Figure 4.10a). At the lower point d, the residual of the budget is large during the main part of the night. The term $\partial\widehat{u_s}/\partial s$ is imbalanced during the first part of the steady-period, when U_{adv} takes large and also imbalanced values. The presence of large residuals in the two-dimensional bulk conservation of mass suggests that the two-layer approach cannot be reduced to a two-dimensional

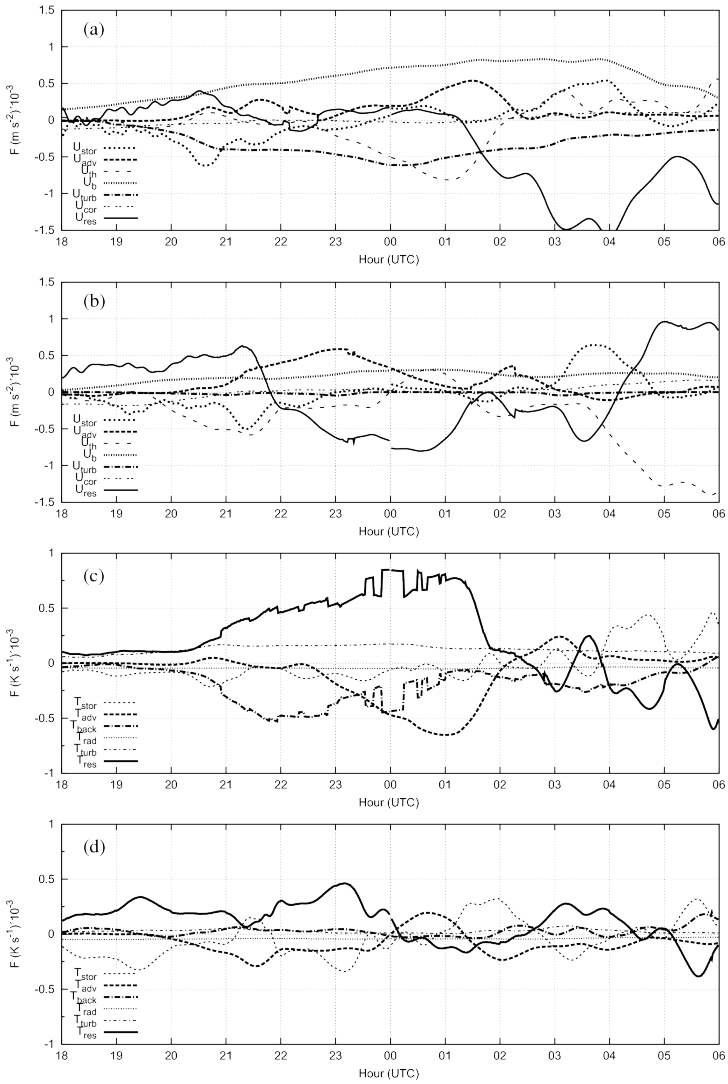

Figure 4.9: The same as in Figure 4.7 but for the forcing terms of the budget bulk equations for momentum (m s^{-2}) at the points (a) *u* and (b) *d* and heat (K s^{-1}) at the points (c) *u* and (d) *d* in Figure 4.5. U_{res} and T_{res} represent the residual terms of the momentum and heat budget equations, respectively.

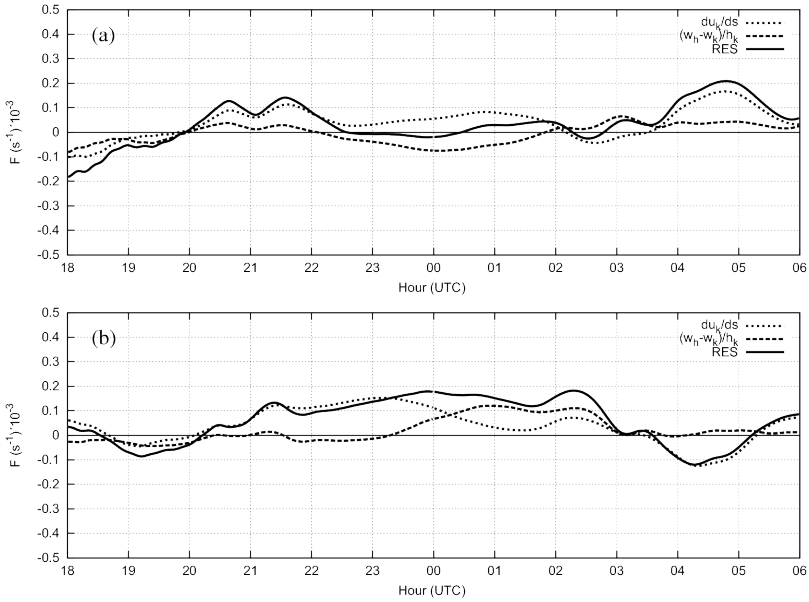

Figure 4.10: The same as in Figure 4.9 but for the conservation of mass bulk equation (s^{-1}) at the points (a) u and (b) d in Figure 4.5. *RES* represents the residual term of the budget equation.

problem due to the importance of the cross-slope effects, as suggested by Haiden and Whiteman (2005).

4.7 Conclusions

A mesoscale simulation over complex terrain under stable conditions is used to inspect if the hydraulic approach is able to describe adequately a simple but realistic katabatic wind, allowing to analyze the main driven mechanisms. The selected gravity current is quasi-bidimensional and quasi-steady during 5 hours of the night, when the two-layer model approach is applied.

The bulk parameterization shows that the katabatic wind decelerates as the deficit increases along the slope due to the accumulation of cold air at the lower parts, which pushes the katabatic wind upwards. Besides, the turbulence is only continuous and significant at the surface and, during most of the time, is the only mechanism responsible of retarding the flow at the upper part of the slope. On the contrary, the elevated turbulence is intermittent and weak and cannot retard the katabatic wind but increases the temperature deficit.

Although the bulk approach seems to reflect the features of the simulated katabatic wind by a mesoscale model during the quasi-steady period, the budget equations give large imbalances, specially for heat. The imbalances can be explained by effects that are not present in the two-layer model, like the presence of cold air at the lower end of the slope or three dimensional effects that also cause imbalances for the bulk conservation of mass. In the case of the heat budget equation, the radiative divergence term does not play any significant role, although extra terms may be computed in order to explain the constant cooling of the layer.

Finally, despite of the fact that these mesoscale simulations provide a good agreement with the observations (Jiménez et al., 2008), it is necessary to compare the results with more accurate observations from objective-oriented experimental campaigns (like VTMX) to check whether the mechanism observed in the simulation also takes place in the field, specially for the turbulence behavior across the maximum of wind.

Acknowledgements

This work has been possible thanks to the funding of the research project CGL2006-12474-C03-01 and the grant FPI BES-2007-16272 of the Spanish Government. ECMWF and AEMET are thanked for the access to computing time as is the Meso-NH team in Meteo France and Laboratoire d'Aérologie for its support. Dr. Dave Fitzjarrald is acknowledged for valuable comments. The manuscript has been enriched by the suggestions of Dra. Maria Antònia Jiménez as well as the comments of two anonymous reviewers.

Chapter 5

The upslope-dowslope flow transition on a basin sidewall

This chapter is based on Martínez, D., C. D. Whiteman, S. Hoch, M. Lehner, and J. Cuxart, 2011: The upslope-dowslope flow transition on a basin sidewall. To be submitted to *J. Appl. Meteor. Climatol.*

Abstract

The late afternoon upslope-downslope flow transition on the west inner sidewall of Arizona's Meteor Crater, visualized by photographs of smoke dispersion, is investigated for 20 October 2006, using surface radiative and energy budget data and mean and turbulent flow profiles from three towers, two at different distances up the slope and one on the basin floor. The bowl-shaped crater allows the development of the evening transition flow with minimal influence from larger scale motions from outside and avoiding the upvalley-downvalley flow interactions typical of valleys. The slow downslope propagation of the shadow from the west rim causes a change in the surface radiation budget and the consequent loss of heat from the shallow atmospheric layer above the western slope when the sun still heats the crater floor and the east inner sidewall. The onset of the katabatic flow is visualized by the dispersion of the smoke, with the onset occurring at the same time at the two slope towers. It arrives later at the crater floor, cooling the air and contributing to the stabilization of a shallow but strong inversion layer on the crater floor. A wavelet analysis indicates that the

initial upslope current is driven by crater-size scales, while the later downslope flow is influenced by the thermal gradient between opposing sidewalls generated by their different cooling rates during the evening transition.

5.1 Introduction

The reversal of daytime upslope and up-valley flows in valleys and the associated buildup of nighttime temperature inversions take place during a period in late afternoon and evening called the *evening transition period*. The evening transition period is initiated by the upslope-downslope flow transition on valley sidewalls, as driven by the reversal of the sensible heat flux on the sidewalls as shadows propagate across the terrain (Whiteman et al., 1989). While the general features of the upslope-downslope transition are known, there have been no comprehensive studies of this transition during which coincident measurements were made of the surface radiation budget, the surface energy budget, and temperature, mean flow and turbulence structure over the slope. Such measurements, however, were made as part of the Meteor Crater Experiment (METCRAX) of October 2006 (Whiteman et al., 2008).

During the evening transition of 20 October 2006, the slope flow reversal on the west inner sidewall was visualized by time lapse movies of smoke dispersion from three smoke grenades that were ignited consecutively at a site in the middle of the sidewall (Figure 5.5). The processes producing the upslope-downslope flow transition and the sequence of events are the subject of the present paper.

The following section describes previous research on the evening transition, while the description of the METCRAX sites and data are introduced in Section 5.3. General characteristics of the case study are given in Section 5.4 and the features of the observed flow transition are presented in Section 5.5. Finally, discussion and conclusions are presented in Sections 5.6 and 5.7, respectively.

5.2 Background

Drainage flows develop during stable conditions over most land surfaces, even over those with very small slope angles, under clear skies and weak synoptic flows. They have been studied in many different locations, including Antarctica

Figure 5.1: Aerial photograph of Meteor Crater from southeast. (@John S. Shelton, used with permission).

(Renfrew, 2004) and Greenland (Heinemann, 2002), as well as in different topographies of middle latitudes (Haiden and Whiteman, 2005; Cuxart et al., 2007; Papadopoulos et al., 1997, and others). Drainage flows have been addressed analytically by simplifying the set of equations that describe the flows (Prandtl, 1942; Fleagle, 1950; McNider, 1982), or numerically (Manins and Sawford, 1979b). Others have compared the simple solutions with experimental results (Mahrt, 1982; Haiden and Whiteman, 2005) or against mesoscale simulations of real cases (Martínez and Cuxart, 2009). For a complete review see Zardi and Whiteman (2011).

The onset of katabatic flow during the evening transition has been addressed through observations on relatively homogeneous and gentle slopes. In the absence of any opposing motion, the downslope flow develops gradually with the formation of a temperature inversion through surface cooling (Papadopoulos and Helmis, 1999). When a planar slope is oriented towards east, a shadow starts to cover the surface from the upper part of the slope where the air first becomes stably stratified. In these cases, the drainage flow begins at the upper shaded part of the slope. Its subsequent arrival farther downslope occurs in the

form of a propagating gravity current (Papadopoulos and Helmis, 1999; Mahrt et al., 2010). At a given point on the lower slope, the arrival of the gravity current is characterized by a sudden shift in wind direction and a temperature drop (Simpson, 1999).

In contrast, when there is an opposing flow (either an anabatic current or a larger scale flow), the local surface cooling generates the buoyancy conditions that lead to the onset of a gravity current once the opposing flow disappears. Mahrt and Larsen (1982) found that an opposing larger scale flow delayed the onset of a drainage current for several hours. It then appeared in the form of a gravity current with a thick frontal bulge. Sometimes, the gravity current arrival occurs only with a sudden wind shift, while the temperature decreases gradually (Monti et al., 2002) or simply increases the cooling rate (Mahrt et al., 2010).

Beginning with an existing anabatic current, Hunt et al. (2003) developed a simplified theoretical model to describe the upslope to downslope transition over a gentle slope. The transition occurs via the formation of a stagnant frontal region (see their figure 3) at a certain distance upslope. This distance depends on the initial buoyancy, the cooling time scale of the surface layer and the former upslope velocity. Results from a laboratory experiment supported the theoretical predictions, which also state that the front migrates down the slope in the form of a gravity current. Monti et al. (2002) and Brazel et al. (2005) used guidance from the simplified model to analyze their wind transitions, while Mahrt et al. (2010) reports that a period of weak winds and variable directions occurs following the cessation of the upslope flow before the katabatic current begins.

The flow transition for slopes on valley sidewalls is necessarily embedded in a more general circulation pattern characterized by slope and valley winds close to the ground and their corresponding compensating return motions in the upper part of the atmosphere (Whiteman, 2000). As an example, see the results from an LES simulation of a complete diurnal cycle of the thermally driven circulation over an idealized valley performed by Catalano and Cenedese (2010). During the day, the upslope wind is modulated by its interaction with the convective boundary layer (CBL) evolution within the valley atmosphere (Serafin and Zardi, 2010) and the establishment of closed slope flow circulations within this layer (Reuten et al., 2005). At night, the downslope current either is affected by the growth of a cold pool at the base of the slope (Cuxart et al., 2007; Zhong and Whiteman, 2008) in the case of an enclosed basin, or interacts with the downvalley current (Whiteman et al., 1989).

In enclosed basins of a size similar to the Meteor Crater, the onset of drainage flows is produced after the reversal of the sensible heat flux (Whiteman et al., 1989). The slope currents can be generated locally, persisting until the growth of

the cold pool eliminates the temperature differences between the air close to the sidewall and the air at the same level over the center of the basin (Clements et al., 2003) or can be generated by an inflow of colder air into the basin (Fast et al., 1996; Whiteman et al., 2010). Drainage currents contribute to the cooling in the center of the basin (Fast et al., 1996) but their relevant role is more related to the sensible heat flux production over the sidewalls, cooling the basin atmosphere during the evening transition (Whiteman et al., 1996).

5.3 Meteor Crater topography and meteorological data

Arizona's Meteor Crater (Figure 5.1), 40 km east of Flagstaff, Arizona, was produced by the impact of an approximately 50-m-diameter meteorite about 50,000 years ago (Kring, 2007). The idealized, bowl-shaped basin is 170 m in depth and has a diameter of 1.2 km, with an unbroken rim that extends 30-60 m above the surrounding arid uniform plain that slopes gently upward to the southwest of the crater. The soil inside the crater becomes increasingly rockier with distance up the alluvium on the sidewalls and is sparsely covered with grasses and small bushes.

The meteorological equipment and accuracies, measurement locations and other details of the METCRAX experimental program were summarized by Whiteman et al. (2008). Here, a brief overview of the measurements used in the present article is provided. The primary data come from an array of 5 10-m micrometeorological flux towers located on a west-east cross section inside the crater (Figure 5.2). They were installed near the center of the crater floor (FLR) and on the lower west (WL), upper west (WU), lower east (EL) and upper east (EU) sidewalls. The measurement equipment on the flux towers is listed in Table 5.1. Data from the sonic anemometers and the UV absorption hygrometer were rotated into a wind-following coordinate system using the method of Wilczak et al. (2001). All components of the surface radiation budget were individually measured at these sites over a surface parallel to the local slope (see Hoch and Whiteman, 2010, for more details). In addition, a 10-m tripod was located at the highest point on the crater rim (RIM) measuring averaged meteorological data.

Three tethersondes were operated simultaneously along the same cross section on the west sidewall (TS-W), floor (TS-C) and east sidewall (TS-E). They provided vertical profiles of the mean meteorological variables within the depth of the crater atmosphere at approximately 30-min time intervals during 7 Intensive Observational Periods (IOPs). Additionally, for the present case study (IOP 4)

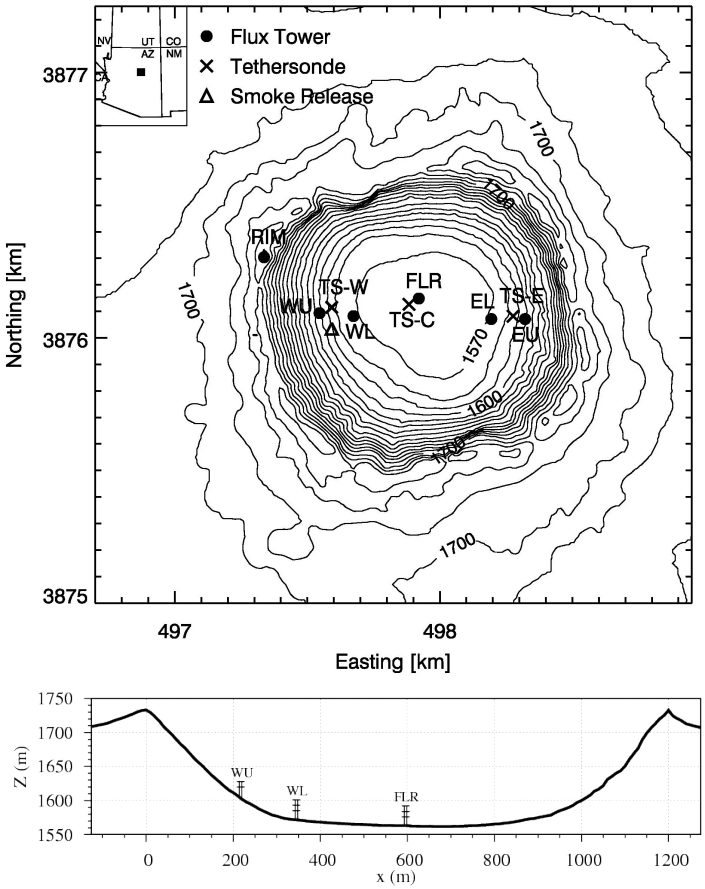

Figure 5.2: (a) Universal Transverse Mercator zone 12S map of Meteor Crater and its surroundings. Location of the instrumentation in the crater with a 10-m altitude contour. Flux tower locations are indicated by filled circles and labeled WU (west upper), WL (west lower), FLR (crater floor), EL (east lower), EU (east upper) and RIM. Tethered balloon sounding locations are indicated with an X as TS-W (west), TS-C (central) and TS-E (east). The three smoke grenades were released at the point indicated with a triangle. (b) Topographic cross section of the crater showing the locations of WU, WL and FLR.

Table 5.1: Meteorological measurement equipment at the ISFF towers. A GPS at each tower was used to synchronize sampling times and data logger clocks.

Instrumentation	Sampling interval	Averaging interval	Heights (m) WU, EU	Heights (m) WL, EL	Heights (m) FLR
sonic anemometers	20 Hz	30 s, 5 min	0.5, 1.5, 3.0, 5.0	0.5, 1.5, 3.0, 5.0, 8.5	0.5, 2.0, 5.0, 8.5
UV absorption hygrometer	20 Hz	30 s, 5 min	3.0	3.0	3.0
hygrothermometers	1 Hz	1 min	0.5, 1.5, 3.0, 5.0	0.5, 1.5, 3.0, 5.0, 8.5	0.5, 2.0, 5.0, 8.5
soil radiation thermometer	1 Hz	1 min			
barometer	1 Hz	1 min	2.0	2.0	2.0
slope-parallel 4-component radiometers	0.2 Hz	1 min	2.0	2.0	2.0
soil temperature, soil properties, soil heat flux, soil moisture	0.2 Hz	5 min	-0.005	-0.005	-0.005

the slope flow reversal on the west sidewall was visualized by time lapse movies of smoke dispersion from a site 50 m south of WU (Figure 5.2).

5.4 Case study of 20 October 2006

The afternoon and evening transition period of 20 October 2006 were characterized by clear, undisturbed meteorological conditions. Clear skies and light and variable winds persisted until the arrival of a cold front at approximately 2100 mountain standard time (MST). The cold front, associated with a trough over the US central plains, moved southeastward across the Colorado Plateau.

Yao and Zhong (2009) consider the night of 20-21 October 2006 as a case where the inner basin atmosphere is decoupled from the ambient flows aloft. They also found that nighttime wind speeds over the surrounding plain need to be less than 5 m s^{-1} to allow the decoupling. Considering the measurements at the rim to be representative of the air above the crater, this condition is fulfilled until astronomical sunset at 1732 MST (not shown). After that, the wind speed

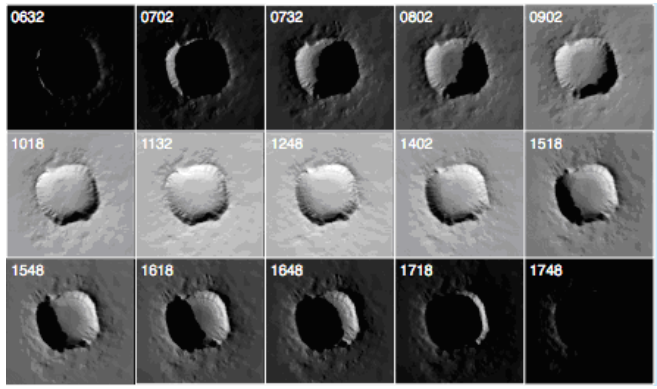

Figure 5.3: Modeled propagation of shadows and extraterrestrial insolation across the Meteor Crater on October 15 at different times of day (MST). Shades of gray are radiation intensity, with black indicating 0 and white indicating 1364 W m^{-2}.

increased above the 5 m s^{-1} threshold and shifted to the west as the cold front approached.

The evening transition within the crater basin is strongly affected by the propagation of shadows cast by the crater rim, which blocks incoming shortwave radiation well before astronomical sunset. Figure 5.3 shows the modeled propagation of shadows for selected times during the evening transition of 15 October. The inner southwest sidewall of the crater is the first area covered by shadow. Similarly, the northeast inner sidewall is the area of the crater that receives the largest amount of irradiance during the evening transition. This configuration establishes a horizontal gradient of irradiance following a northeast-southwest orientation. This gradient may contribute to the dynamics within the crater. As the sun sets, the shadow moves northeastward down the west sidewall and across the floor of the crater. Local sunset arrives 160, 130, 75, 55 and 40 minutes before astronomical sunset at the WU, WL, FLR, EL and EU sites, respectively (Hoch and Whiteman, 2010).

The effects on the crater atmosphere of the shadow propagation and time evolution of the wind aloft can be analyzed through vertical profiles from the three tethersondes collected during the evening transition (Figure 5.4). Raw data have been filtered to avoid the inherent noise associated with these measurements.

The time evolution of the potential temperature profiles shows the development of a stable layer at the lower elevations within the crater, starting at the western

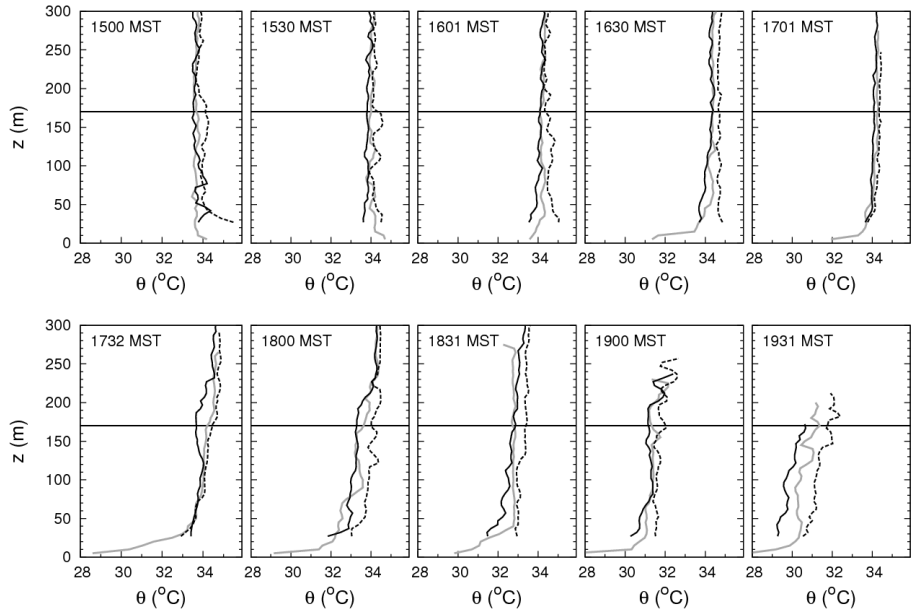

Figure 5.4: Tethered balloon potential temperature soundings from the western sidewall (black solid), crater floor (gray solid) and eastern sidewall (black dashed) from 1500 to 1931 MST. Sounding times are given in the legend. Potential temperature is smoothed with a weight function depending on the inverse of the distance. The horizontal bold line indicates the mean crater rim level.

side of the crater, as wind speed continuously decreases within the crater atmosphere due to the decoupling with the ambient flow aloft (not shown). At 1600 MST, when the shadow covers almost half of the crater, the stability has built up at the crater floor and over the west sidewall, while the potential temperature profile over the eastern part remains super-adiabatic. Temperature differences develop across the crater, with a temperature difference of about 0.5 K in the upper crater atmosphere between the west and east tethersonde sites. At 1701 MST, when the shadow covers almost all the crater, the temperature profile differences are minimized. A strong inversion of 5 K in the first 50 m is formed over the crater floor by the time of astronomical sunset at 1732 MST. From this time on, the wind aloft veers to the west and increases in speed as the cold front approaches. An increase in speed is seen above the east inner sidewall, as turbulent eddies mix the air downward here (Yao and Zhong, 2009). The wind speed

increase aloft does not affect the western part, however, presumably because it is dynamically sheltered by the upwind rim which blocks the wind blowing from the west. This situation leads to a faster cooling of the western part of the crater during this period.

An upslope-downslope flow transition took place between 1500 and 1600 MST on the western sidewall during the buildup of the crater stable layer. This transition will be analyzed in the following sections.

5.5 The upslope-downslope flow transition

5.5.1 Smoke dispersion

Three 3-min-duration smoke grenades were ignited at a site on the west sidewall at 1510, 1530 and 1550 MST as the shadows propagated down the slope (Clements et al., 2007). Time-lapse photographs recorded the dispersion of the plumes generated by the smoke releases. Figure 5.5 shows one picture representative of each smoke release.

The first ignition occurred when the shadow edge (the terminator) had passed WU. Upslope easterly winds were still present over the shadowed slope, with big eddies that were able to transport the smoke up to the rim (Figure 5.5a).

The second release was made just after the terminator passed WL. At this time, the slope flow intermittently reversed from downslope to upslope and from upslope to downslope (Figure 5.5b). The downslope flow confined the smoke plume to the ground, while it was dispersed vertically by the enhanced turbulence when the flow turned upslope.

The third ignition took place when the shadow covered the entire west sidewall, as shown in Figure 5.3. At this time, the smoke plume propagated downslope in a shallow layer whose depth increased along the slope (Figure 5.5c). The time-lapse movie showed that the flow was disturbed occasionally by turbulent episodes that sporadically dispersed the smoke plume vertically, reaching a height of tens of meters above ground level (AGL). When the smoke plume was observed from the east sidewall (Figure 5.5d), this perspective revealed that the downslope current blew from the southwest, with the smoke flowing between the two west slope towers with a depth similar to the height of the WL tower. The smoke arrived to the center of the crater detached from the surface (not shown), where the sunlight still heated the ground but with a weak convection

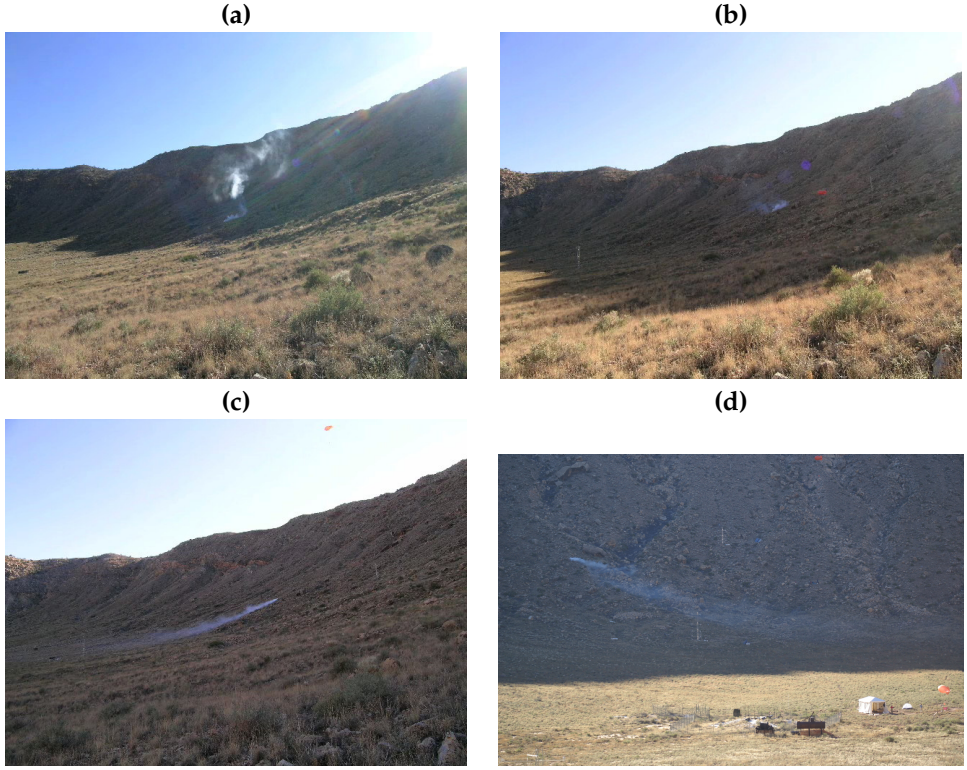

Figure 5.5: Photographs of the dispersion of smoke from 3-minute-duration releases on the west slope of Meteor Crater started at (a) 1510, (b) 1530, and (c) 1550 MST on 20 October 2006, as photographed from a point on the crater floor northeast of the smoke release. (d) The same as in (c) but photograph taken from the foot of the east sidewall. The WU and WL towers can be seen in the photos. A red tethered balloon is visible in (b) and (c).

that was not able to disperse the smoke upwards, probably due to the increasing stability of the atmosphere over the crater floor (Figure 5.4).

5.5.2 Results from the meteorological towers

Figure 5.6 shows data from the WU and WL sites averaged over 5-min intervals during the upslope-downslope flow transition visualized by the smoke releases.

The 30-min delay in shadow arrival between the two west sidewall sites leads to different surface conditions during the transition period.

Net radiation changes sign abruptly with the passage of the terminator due to the large shortwave radiation drop (Figure 5.6a and 5.6b). This drop of net radiation is larger at WL since global radiation is larger when the shadow arrives at this site due to its gentler slope angle (Hoch and Whiteman, 2010). The sudden lack of shortwave energy input that had warmed the surface results in a rapid decrease in the temperature. This is indicated by the immediate decrease in the magnitude of the outgoing longwave flux. This decrease in the longwave outgoing magnitude and in the surface temperature is larger at WL than at WU, corresponding to the relative magnitudes in the change in shortwave available energy. This is consistent with De Wekker and Whiteman's (2006) finding that cooling rates are larger on the lower parts of basin sidewalls where net radiation losses are somewhat higher than on steeper upper sidewalls.

Figures 5.6c and 5.6d show the response of the other components of the surface energy balance to the sudden decrease in net radiation. The sign convention used in this thesis is that fluxes directed toward the surface, whether from the atmosphere or soil, are positive. The sensible heat flux at 3 m AGL reverses approximately 15 minutes after terminator passage at both sites, while the latent heat flux remains negative during the whole evening transition, indicating sustained evaporation. Large differences can be seen in the evolution of the ground heat fluxes at the different sites. At WL the ground heat flux shows a strong reaction to the change in net radiation at approximately the same time as sensible heat flux. At WU, however, the ground heat flux reverses well before local sunset, growing only from 0 to 25 W m^{-2} between 1400 and 1800 MST, while the ground heat flux at WU changes from -85 to +30 W m^{-2}. Local irregularities of the terrain and dispersed bushes could shade the ground effectively before local sunset at WU, where a steeper slope leads to longer shadows. This effect, together with differences in the soil thermal characteristics with distance up the alluvium on the sidewalls, could be an explanation for the differences between the west slope sites. Further, the ground heat flux was measured at a certain depth within the soil, and is corrected using soil temperature measurements above the ground heat flux plate. Different depths of the flux plates and soil temperature observations may lead to a smoothing of the sudden changes in the ground heat flux. The measured imbalance of the surface energy budget (see additional information on this feature, which is seen in many measurement programs, by Oncley et al., 2007) is very large, especially immediately after local sunset. The slow response of sensible and ground heat fluxes contributes to the reduction of this large imbalance afterward.

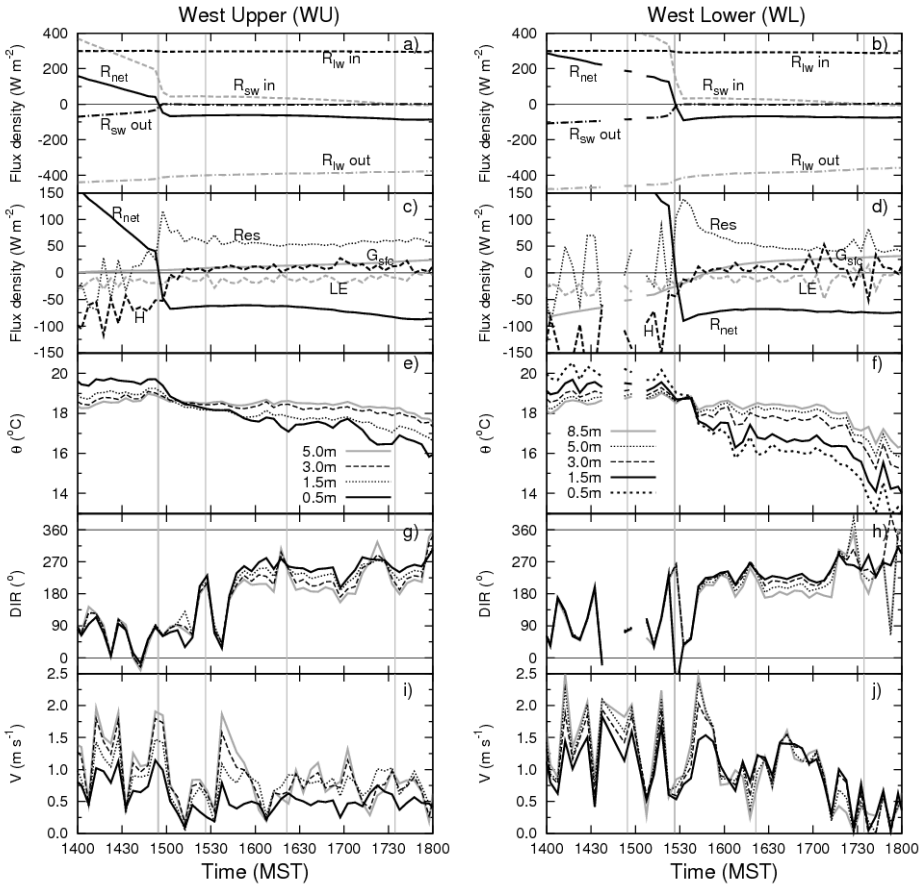

Figure 5.6: Meteorograms from the WU (left) and WL (right) towers for the evening transition period of 20 October 2006. (a-b) Radiation budget components, (c-d) surface energy budget components, including net radiation R_{net}, surface heat flux G_{sfc}, sensible heat flux H, latent heat flux LE, and energy balance residual $Res + R_{net} + G_{sfc} + H + LE = 0$, (e-f) potential temperature, (g-h) wind speed and (i-j) wind direction at different levels of the towers. Data are from 5-min averages. Vertical lines indicate the times of local sunset at, from left to right, WU, WL, FLR and EU, and at astronomical sunset (extreme right).

Figures 5.6e and 5.6f show the local potential temperature, defined here for simplicity by means of the adiabatic lapse rate ($\Gamma_D \approx 0.0098 Km^{-1}$), $\theta = T + \Gamma_D \delta z$, where δz represents the relative elevation above the crater floor. The near-surface air temperature decreases following the passage of the terminator, as it is strongly influenced by the ground surface temperature. Similarly to the drop in surface temperature, the air temperature drop at WL at local sunset is larger than at WU. The near-surface cooling of air stabilizes the surface layer, and results in the reversal of sensible heat flux (Figures 5.6c and 5.6d).

Wind direction evolves simultaneously at both sites (Figures 5.6g and 5.6h) and mirrors the evolution of the observed smoke plumes. The wind shifts from the easterly upslope direction observed with the 1510 MST smoke release into a southwesterly downslope direction by the time of the third smoke release. Wind directions were variable from 1515 to 1545 MST during the release of the second smoke grenade. By 1550 MST a steady downslope current was established that persisted for the next two hours, although with two mixing episodes and with wind speeds significantly lower than for the upslope regime (Figures 5.6i and 5.6j). The downslope current presents a layered structure with a westerly to southwesterly direction close to the surface, progressively turning into a southerly direction with height. This wind direction shear is largest for WU.

To compare the flow evolution among sites, Figure 5.7 shows the 30-sec averaged wind speeds and directions for the WU and WL (3 m AGL) and FLR (2m AGL) towers, together with the local 1-min averaged potential temperature at two different heights for each tower.

At 1538 MST, the wind direction at WL shows the onset of a downslope current (gray arrow in Figure 5.7b). The wind suddenly turns into 180° and then gradually changes to a southwesterly direction over the next 10 minutes (1550 MST). The same evolution is seen at WU with a delay of two minutes. With the downslope regime established, the wind direction remains more or less steady until 1710 MST with a similar evolution at both west sidewall sites.

At WU the temperature close to the surface (1.5 m AGL) decreases quickly in the first 20 minutes after local sunset (1454 MST). The temperature at 5 m AGL, however, remains similar to that recorded at RIM. This indicates that the buildup of the stability layer is formed by surface cooling and is confined to the first 5 meters AGL. At WL, the buildup of stability and a sudden drop of temperature in the whole column coincide with the final onset of the downslope current (1538 MST). Before this event, there is another significant drop in air temperature when the flow suddenly changes into a downslope direction for nearly 8 minutes (around 1525 MST). With the final onset of the downslope

current, the temperatures at 5 m AGL at WU and WL drop below the temperature at RIM, indicating the formation of a weak inversion within the western side of the crater. These temperatures remain approximately steady until 1710 MST when the buildup of the cold pool within the basin leads to a decrease of both temperature and wind speed that is larger at WL (Figure 5.6), anticipating the end of the downslope regime.

At FLR, the air temperature starts to decrease with the arrival of air from the west sidewall (dashed arrow in Figure 5.7b), 10 minutes after the onset of the downslope current at WL and about 30 minutes before local sunset. This effect would be the explanation for the temperature inversion recorded by the tethersondes at lower levels in the center of the crater at 1601 MST (Figure 5.4) and shows the importance of the contribution of the katabatic flow to the cooling of the lower atmosphere over the basin center. However, the largest temperature drop occurs after the arrival of the terminator at FLR (1622 MST). The surface cooling associated with the shadow passage produces a buildup of atmospheric stability close to the surface. Nevertheless, a weak downslope current is able to continue to reach the FLR site (Figure 5.7a).

5.5.3 Evolution as seen by the wavelet transform

A wavelet analysis of the kinetic energy as measured by the sonic anemometers on the towers was performed to identify the relevant scales of motion (or, equivalently, time scales) during the evening transition. The wavelet transform method is able to separate the contributions of different frequencies to the kinetic energy and reduces the contamination by frequencies outside the desired interval (Cuxart et al., 2002). In this study, the Morlet wavelet with a base frequency ($w_0 = 6$) has been applied to 20-Hz wind components and virtual temperature time series.

Figure 5.8 shows the wavelet transform of the kinetic energy time series recorded at 5 m at WU for illustrative purposes. The same has been done for WL and FLR. At all sites, the scales that contribute to the kinetic energy are reduced with the onset of the drainage flow, decreasing from scales up to 25 minutes to scales below 10-15 minutes. The former time scales can be related to the crater size (for instance, assuming a horizontal velocity scale of 1 m s^{-1}, the resulting larger length scale is 1500 m, which leads to circular eddies with a diameter of 500 m). During the downslope regime (1540-1710 MST), there is a gap between the turbulent scales (up to 5 minutes) and the larger scales centered around 12 minutes (Figure 5.8). Similarly, the later time scales can be related to lengths of 600-900 m, half the size of the crater. At FLR, the gap is not present (not shown),

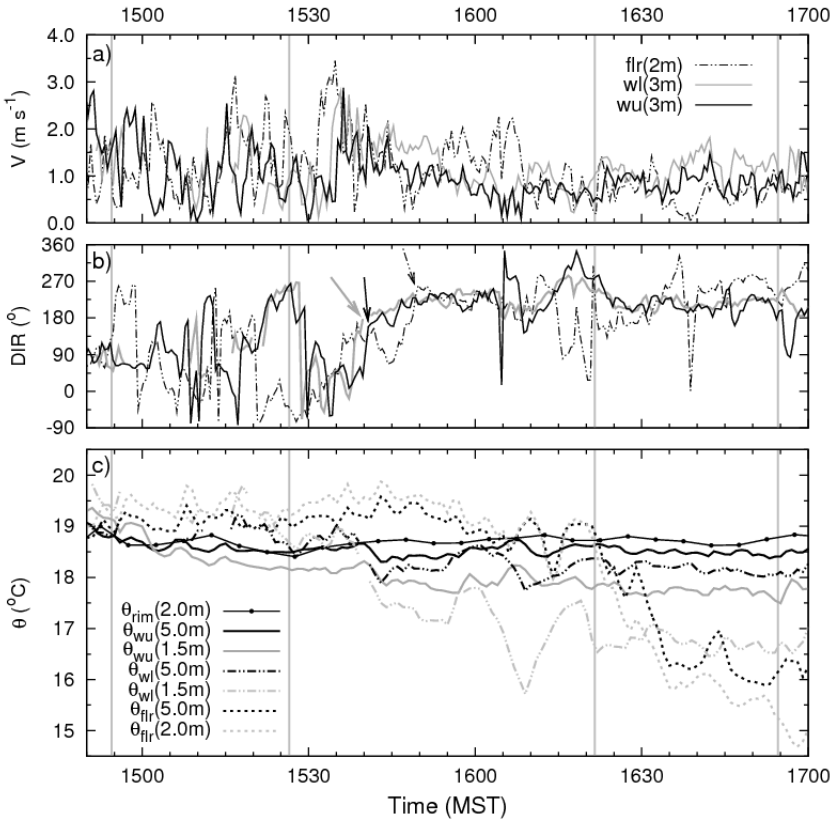

Figure 5.7: Time evolution of (a) wind speed, (b) wind direction and (c) local potential temperature for the WU, WL and FLR sites. Wind and temperature data correspond to 30-sec and 1-min averages, respectively. In (c), the 5-min averaged local potential temperature measured at the rim is shown for comparison. Vertical lines indicate the times of local sunset at, from left to right, WU, WL, FLR and EU. In (b), arrows indicate the arrival of the gravity current at WL (bold gray), WU (bold black) and FLR (dashed).

probably because the center of the crater floor is influenced by phenomena of a wider range of scales generated at other parts of the basin.

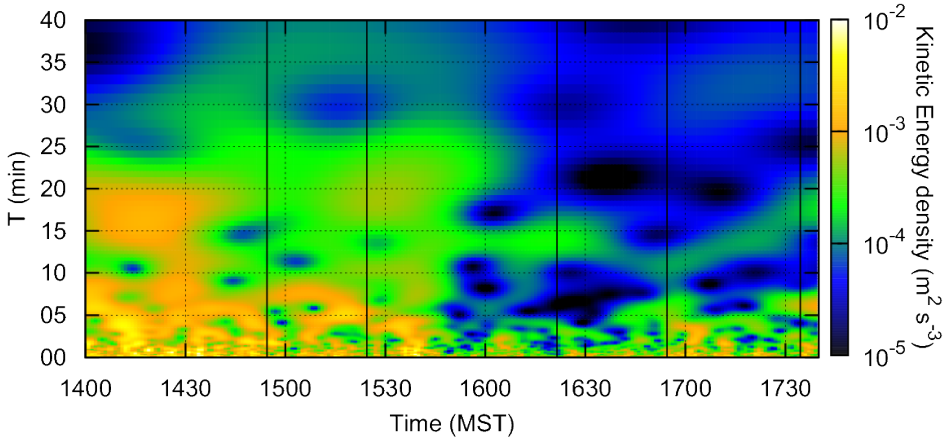

Figure 5.8: Time evolution of kinetic energy per unit period at 5-m height computed from the wavelet transform of the wind components at WU. Vertical lines as in Figure 5.6.

To sum up these results for the three towers, the energy has been integrated between two periods, (i) the turbulent periods (0-5 min) and (ii) larger-scale periods (5-40 min). The time evolution of both contributions (Figure 5.9) shows clearly the two regimes present during the evening transition. During the upslope regime (up to 1538 MST), all the scales at least duplicate their value in comparison with the downslope regime (1540-1710 MST). The kinetic energy is also largest at higher levels (not shown) since, in general, the eddy sizes are larger as the measurement level gets farther from the surface. For all sites, the change of regime is preceded by an enhanced peak of small-scale or Turbulent KE (TKE). The contribution of TKE to total kinetic energy even exceeds that of the larger scale contributions at WU and WL. This peak coincides with a sudden increase of wind speed (1532-1537 MST, Figure 5.7a) and occurs at nearly the same time at all three sites and at EL (not shown), indicating that the event occurs throughout practically the entire crater. Moreover, this energy enhancement takes place at all periods up to 25 minutes, suggesting that the event has a crater scale. With

the establishment of the downslope flows the contribution of the larger scales progressively decreases until reaching values similar to those for TKE.

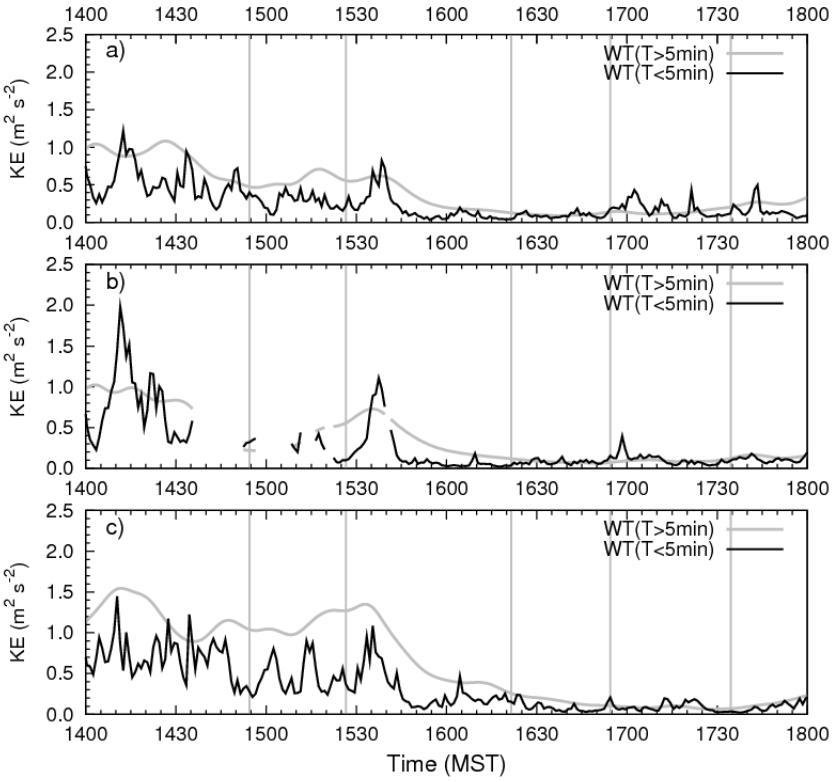

Figure 5.9: Time evolution of the contribution to kinetic energy (KE) at 5-m height of small periods (up to 5 minutes), and of larger periods for the (a) WU, (b) WL and (c) FLR sites. The scale contribution has been computed from the wavelet transform of the wind components (see text for more details). Contributions of periods below 5 minutes are considered representative of turbulence scales. Vertical lines as in Figure 5.6.

5.6 Discussion

The upslope-downslope flow transition at the inner west sidewall of the crater is related to the propagation of the shadow cast by the west rim, which descends the slope as the sun gets lower in the sky in late afternoon. The ground surface cools rapidly after the arrival of the shadow edge. The sensible heat flux close to the ground diminishes and then changes sign, leading to a downward heat flux that cools the atmosphere above the slope and leading to the buildup of a surface-based temperature inversion above the slope. Neither the downward sensible heat flux nor the observed ground heat flux are large enough to compensate for the negative net radiation, which leads to the large imbalances in the measured surface energy budget (Figures 5.6c and 5.6d).

Parts of the energy imbalance can be related to sensible heat and radiative flux divergences between the ground and heights where these fluxes were recorded, 3 and 2 m AGL, respectively (Oncley et al., 2007). Using the turbulent heat fluxes computed from the sonic anemometers at 0.5 and 3.0 m AGL and accounting for humidity effects (Kaimal and Gaynor, 1991), we estimate an upper bound error of 6 W m^{-2} for the heat flux divergence. Direct measurements of radiative flux divergence at FLR (Hoch and Whiteman, 2007) between 0.5 and 2 m AGL showed small values within ±1 W m^{-3} between 1500 and 1700 MST. The ground heat flux is generally underestimated since it is measured within the soil and corrected by means of soil temperature measurements above the ground heat flux plate (Oncley et al., 2007). An estimation of the error made in the present case is 15 – 30 W m^{-2}. The sum of all these effects accounts, at maximum, for 80% of the residual. The rest of the energy imbalance may be attributed to advective effects caused by the slope current.

Figure 5.10 shows the observed along-slope and cross-slope bulk momentum and buoyancy deficit of the slope current given by

$$UH = \int_0^h u dn \tag{5.1}$$

$$VH = \int_0^h v dn \tag{5.2}$$

$$\triangle \Theta H = g \int_0^h \frac{\triangle \theta}{\theta_0} dn \tag{5.3}$$

where the upper limit of integration h (= 5 m) is the highest level with measurements at the WU tower. Here, the temperature perturbation is defined as $\triangle\theta = \theta_0 - \theta$ so it becomes a positive quantity for a denser fluid and buoyancy drives the current downslope. Since the main part of the temperature inversion is constrained within the first 5 m AGL (see previous section), for simplicity, the potential temperature of the undisturbed background field θ_0 is approximated here as the value at 5 m AGL for each tower. The evolution of these variables is shown in Figure 5.10 for WU and WL during the evening transition. The u and v components follow the local downslope (s) and cross-slope (y) directions, deviated 10° and 38° from the geographical coordinates at WU and WL, respectively. The vertical velocity is perpendicular (n) to the underlying surface.

The defined bulk quantities are an extension of the model proposed by Manins and Sawford (1979b) with the shape factors reduced to unity. The along slope momentum flux UH and cross-slope momentum flux VH reflect the evolution of the flow within the layer measured by the west slope towers, which is affected by a bulk buoyancy deficit $\triangle\Theta H$. However, these variables only describe the lowest 5 m of the flow. Anabatic flows have a depth larger than the tower heights (Serafin and Zardi, 2010; Catalano and Cenedese, 2010), as seen by the smoke plume released by the first grenade, which was sporadically dispersed upwards to the rim level. For the downslope regime, the depth of the current is also uncertain, since a jet-like structure is not seen within the measurement levels of the towers.

The upslope regime is characterized by variable but mainly negative values of UH (upslope) at both towers and includes the transition period (1505-1540 MST), defined here as the time interval between a rapid increase of the buoyancy deficit at WU, which turns positive, and the final onset of the downslope current. The buoyancy deficit keeps growing at both sites and becomes positive at WL with the onset of the downslope flow, when both along slope momentum fluxes reverse their signs. After a period with large values, the momentum fluxes reach a steady state between 1555 and 1710 MST. During this period, VH gets very small at WL, but still takes positive values at WU, since the downslope current follows a direction close to the aspect angle of the local slope at WL. The buoyancy deficit grows at a faster rate at WL, reaching values larger than at WU due to the formation of a stronger temperature inversion at the lower part of the sidewall. In both cases, the buoyancy deficit stops growing after local sunset at FLR.

Figure 5.10 shows that the buoyancy deficit tends to push the air downslope at the upper sidewall, where the shadow arrives first, while the convective regime is still present at the lower sidewall. Nevertheless, once the flow is established - nearly simultaneously at both sites - the downslope momentum flux is greater

at the lower sidewall than at the upper sidewall. This scenario has not been considered in the previous works on evening transitions over slopes (Hunt et al., 2003; Papadopoulos and Helmis, 1999) or within valleys (Catalano and Cenedese, 2010).

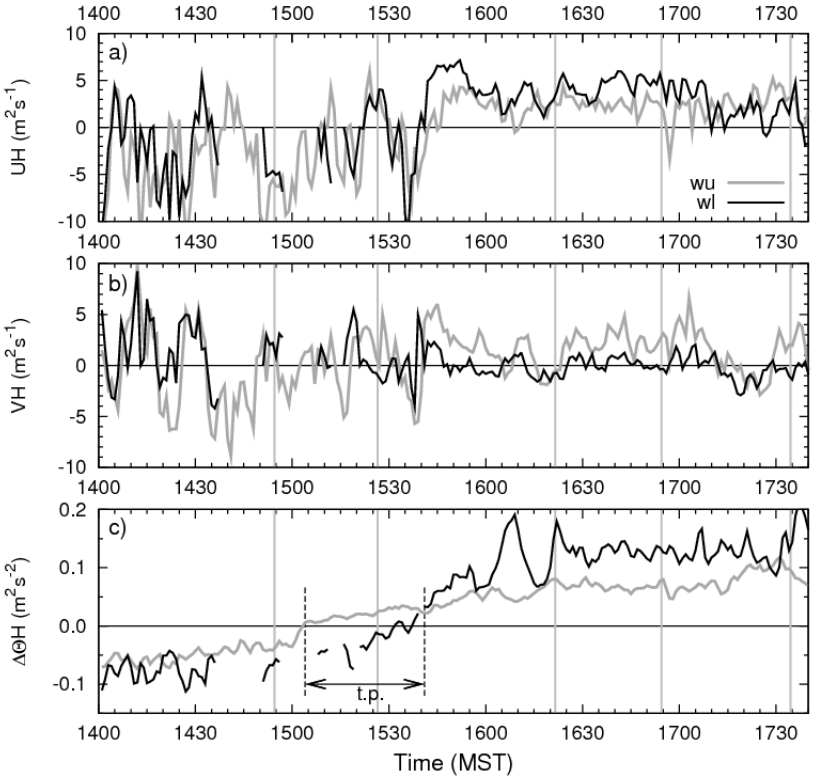

Figure 5.10: Time evolution of the bulk (a) along-slope momentum flux (negative values indicate upslope flow), (b) cross-slope momentum flux and (c) buoyancy deficit for WU and WL sites during the upslope-downslope flow transition. Gray vertical lines as in Figure 5.6. In (c), bold arrow indicates the transition period (t.p.). See text for reference.

Hunt et al. (2003) analyze the flow transition considering that the cutoff of heating occurs at the same time over the slope and valley. In this context, the airflow still moves upslope due to its significant mean momentum. Papadopoulos and

Helmis (1999) describe the formation of the downslope current without the presence of a previous upslope current, while Catalano and Cenedese (2010) perform a simulation where the sensible heat flux reverses first at the valley floor and then over the slope. In the present study, the interaction between the buildup of the stably stratified layer over the west sidewall and the convective regime at the crater floor and east sidewall are key to understanding the evening transition.

The presence of the upslope current over the sidewall leads to strong turbulence close to the ground (Figure 5.9), contributing to a large heat exchange at the surface and cooling of the surface layer during the *transition period* on the upper sidewall. This cooling process, however, is mostly balanced by the advection of warmer air coming from the valley floor carried by the anabatic or upslope current.

Considering the temperature tendency equation

$$\frac{\partial \theta}{\partial t} + \overrightarrow{v}\overrightarrow{\nabla}\theta = -\frac{1}{\rho_0 C_p}\frac{\partial R_n}{\partial z} - \frac{\partial \overline{w'\theta'}}{\partial z} \tag{5.4}$$

with the vertical flux divergences of net radiation (R_n) and sensible heat flux ($\overline{w'\theta'}$), it is possible to estimate the contribution of advection. The layer between 0.5 m and 5 m at WU was cooled -3.5 K h^{-1} during the *transition period* due to turbulent heat flux divergence. However, the total cooling of the layer during this period was -0.6 K h^{-1}. Thus, the advective term should be 2.9 K h^{-1} to balance Equation (5.4). Assuming a scale velocity of 1 m s^{-1}, there should be a gradient of 0.1 K between WU and WL. The advection term is probably larger, since we have not accounted for the contribution of the radiative term, also very important in the cooling process during the evening transition (Sun et al., 2003). In any case, these estimates are compatible with temperature differences between WU and WL, as shown in Figure 5.7.

To assess which forcings contribute to the evolution of *UH* and *VH*, the along-slope and cross-slope momentum equations over the sidewall (using the Boussinesq approximation) can be written

$$\frac{\partial u}{\partial t} + \overrightarrow{v}\overrightarrow{\nabla}u = -\frac{1}{\rho_0}\frac{\partial \triangle p}{\partial s} - g\frac{\triangle\theta}{\theta_0}sin\alpha + \frac{\partial \tau_u}{\partial n} \tag{5.5}$$

$$\frac{\partial v}{\partial t} + \overrightarrow{v}\overrightarrow{\nabla}v = -\frac{1}{\rho_0}\frac{\partial \triangle p}{\partial y} + \frac{\partial \tau_v}{\partial n} \tag{5.6}$$

where the evolution of the downslope momentum and the advection in (5.5) is related to the perturbation pressure gradient force, the along-slope buoyancy force, where α represents the slope angle, and the shear stress τ_u. The cross-slope momentum equation (5.6) does not include the buoyancy force, since the y direction is perpendicular to this force. The time derivative of the curves in Figures 5.10a and 5.10b represent the bulk version of the first term on the lhs of Equations (5.5) and (5.6).

During the convective regime, the wavelet transform analysis shows the presence of time scales related to the crater size, connecting the upslope current with larger circulations driven by the convection. Under this situation, the anabatic current probably draws in flow from higher-level air, forming a recirculating flow typical of alpine-like valleys. Thus, the advective and pressure gradient terms also contribute to the evolution of UH and VH. Although the description of the circulation patterns within the crater during the daylight period is out of the scope of the present work, it is worthy to note here that it is extremely complex, as tethered balloon soundings suggest (not shown). The crater configuration, with radial symmetry, yields to horizontal circular patterns at certain crater heights close to the sidewalls that add complexity to the vertical circulations described by idealized simulations like those of Catalano and Cenedese (2010).

During the *transition period*, a diabatic cooling process starts at WU, forming a surface temperature inversion. During this stage, the atmosphere experiences rapid changes over the upper west sidewall, with the buoyancy force changing its sign and giving a downslope contribution. In this transient situation, the pressure perturbation field probably takes either sign, compensating or contributing to the buoyancy forcing. Advective terms are responsible for compensating these previous forces, as the air still blows upslope.

The convective regime ceases abruptly with a large energetic event, which is spread everywhere at all crater scales (Figure 5.9). This is followed by the arrival of a downslope current from the south (note the positive value in VH) at WL and, two minutes later, WU and progressively veers towards a downslope direction. At both towers, the arrival of the downslope flow coincides with a sudden shift of wind direction and a drop in air temperature (Figure 5.7), suggesting that the current takes the form of a gravity current, coming from the cold area located at the southwestern sidewall.

Once the large scales from the convective regime disappear at this part of the crater, buoyancy force drives the air over the sidewall in a downslope direction. The air follows the terrain slope close to the surface, but it is deviated towards a southwesterly direction with height (Figures 5.6g and 5.6h). At a crater scale, the SW-NE axis is the direction of the largest thermal gradient between opposing

sidewalls, due to the differential heating rates during the evening transition (Figure 5.3). Haiden and Whiteman (2005) and Mahrt et al. (2001) note that katabatic flows follow topographic gradients of a larger scale at higher levels. Similarly, in the present case, the drainage current would be sensitive to the thermal gradient at the crater scale for increasing heights (Lehner et al., 2011). Above the tower measurements, where the buoyancy deficit is small, this effect is still present and may be responsible for the lack of a jet-like profile within the tower layer. At WU, the difference between the aspect angle and the temperature gradient direction at the crater scale is larger than at WL, producing a stronger wind direction shear. In the cross-slope momentum equation (5.6), the pressure perturbation term is responsible for this deviation. For the along-slope direction (5.5), however, the pressure gradient term probably becomes smaller, since the basin temperature inversion is not yet formed (Zhong and Whiteman, 2008).

An estimation of the terms of Equation (5.5) for the steady period of downslope flow (1555-1710 MST) show that buoyancy and friction terms compensate the advection terms, resembling the features of a shooting flow, as classified by Mahrt (1982). The along-slope pressure gradient term is small, as well as the residual of the momentum budget.

5.7 Conclusions

The crater basin evening transition is strongly influenced by the propagation of shadows, which induce the development of a stable layer over the west sidewall while the sun still heats the surface over the eastern part of the crater. This situation leads to temperature differences within the crater atmosphere between the opposing sidewalls and to the upslope-downslope flow transition over the west sidewall. This flow transition was observed during the late afternoon of 20 October 2006 with three smoke releases over the west sidewall.

The downslope propagation of a shadow cast from the western rim of the crater leads to a sudden drop of net radiation as the terminator passes. Radiative cooling of the ground causes the near-surface air temperature to decrease and reverses the turbulent sensible heat flux in the near-surface air layer. A measured imbalance in the surface energy budget at this time is apparently caused primarily by uncertainty in the ground heat flux measurements and advection of warmer air by the upslope/downslope current.

The cooling process at the upper part of the sidewall is driven by flux divergences of the sensible heat and net radiation, but is partially counteracted by the warm advection produced by the anabatic current.

Results from a wavelet transform suggest that the evening transition is driven by motions with a range of scales up to crater size, probably connected with closed circulation patterns similar to those usually found in alpine valleys. The progressive buildup of stability over the west sidewall leads to the formation of a positive buoyancy force which, after storing enough potential energy, is able to counteract these circulation patterns. The sudden change in the local dynamics would release a peak of energy at all scales throughout the crater, which is detected by the sonic anemometers right before the onset of the downslope current.

The downslope regime arrives from the south in the form of a gravity current at both west slope towers, veering to a southwest direction 10 minutes later. It is characterized by a stable layer carrying cold air from the southwest sidewall. Wind direction also shows a layering effect, following the surface at lower levels, but blowing in the direction of the largest thermal gradient between opposing sides of the crater at higher levels. The wind direction shear produces turbulence close to the ground, enhancing the surface heat exchange. The scale of this motion is also reflected in the wavelet transform results, giving a maximum contribution from time scales around 12 minutes.

The downslope current arrives at the center of the crater floor 10 minutes after its onset over the west sidewall, cooling the area before local sunset. However, the formation of a strong surface temperature inversion follows the arrival of the shadow. The downslope current reaches a steady regime for approximately two hours, completing the buildup of the cold pool on the crater floor.

An analysis of the forcings involved in the evening transition suggests that the growth of the buoyancy force at the upper part of the slope is counteracted by the advection of the anabatic current. Once the drainage current is established, the pressure perturbation directs the downslope flow toward the warmer sidewall.

Acknowledgements

This paper, started while the first author was a visiting scientist at the University of Utah, was supported by a travel grant from the fellowship BES-2007-16272 of the research project CGL2006-12474-C03-01 from the Spanish government. Contributions by the co-authors were supported by National Science Foundation grant ATM-0444205 (CDW and ML), by Army Research Office grant 52734-

EV (SWH), and by a DOC-fFORTE fellowship from the Austrian Academy of Sciences (ML). We thank the Barringer Crater Company (D. Barringer, Pres.) and Meteor Crater Enterprises, Inc. (B. Andes, Pres.) for crater access, and those listed in the acknowledgments section of Whiteman et al.'s (2008) article for their help with the field program and data processing. Chad Kahler is thanked for assistance with Figure 5.3.

Chapter 6

Conditioned climatology for stably stratified nights in the Lleida area

This chapter is based on Martínez, D, J. Cuxart, and J. Cunillera, 2008: Conditioned climatology for stably stratified nights in the Lleida area. *Tethys*, **5**, 13–24.

Abstract

Nights with clear skies and weak winds are common in the western Mediterranean area when pressure gradients are weak, usually associated with anticyclones that have their center over southwestern Europe. In such conditions, local factors predominate and nights are calm, with possible intense cooling in valleys and plains. Fog, dew or frost could appear. This study analyzes, through the application of some selection filters, the characteristics of stable nights during the period of 1997-2005 in the agrometeorological station of Gimenells, located in the eastern half of the Ebro basin. It shows the typical evolution of wind, humidity and temperature in stable conditions, identifying its principal directions and relating them to the topography of the Ebro basin.

6.1

Introduction

The Ebro basin is an approximately triangular shaped valley, oriented on the NW/SE axis, ca. 400 km long, closed in by some important mountain ranges (the Pyrenees and Cantabrian Mountains to the north, Iberian System to the west and south and Pre-coastal Catalan Range to the East). The outflow to the sea goes through narrow gorges that communicate the Lleida area with the coastal area, and for this reason the basin could be considered, in a primary approximation, a closed valley (Figure 6.1). The valley has a slope to the SE following its main axis, and the lateral slopes converge to the center from the Pyrenees, the Iberian System and the Catalan Pre-coastal Range, configuring a bucket where the lower areas are located between Zaragoza and Lleida, with the lowest and widest area close to Lleida.

This topographic configuration makes the climatology in the Ebro basin different from the surrounding areas. Winds blowing from the west usually arrive dry after crossing the several ranges located in the interior of the Iberian Peninsula and are channelled following the valley axis. Winds from the north and south must go around the Pyrenees and also take the direction of the valley. In the case of winds blowing from the north, a mesoscale low pressure area is generated downwind and the channelled wind is locally called *Cerç* or *Mestral* (Masson and Bougeault, 1996). In synoptic anticyclonic conditions with a weak pressure gradient on the area, winds are weak in wide areas of the basin, often generated at slopes during the night, converging in the valleys and plains, with areas of cold air accumulation where fog and frost can occur. Some examples of similar dynamics have been documented in other places, such as the Mesa Creek Valley in the state of Colorado (Gudiksen et al., 1992) or the Hudson River Valley (Fitzjarrald and Lala, 1989).

As the central valley and the Lleida region are areas mainly dedicated to agrarian production with some important population centers, it is important to have a good knowledge of climatic behavior on stable nights, which could create some significant problems for the population (due to fog formation or little dispersion of atmospheric pollution) or for the agriculture (due to frost formation). It is especially important to study the temperature behavior in such situations, since important falls in this variable could entail intense frosts (Snyder and de Melo Abreu, 2005). Previous studies have dealt with the risk of frosts in the Ebro basin (Hernandez Navarro, 1995) or have elaborated a general climatology for Lleida city (Sousa, 1987). However, as far as the authors know, there is still no climatic study conditioned to stable nights in the area, nor have they found it

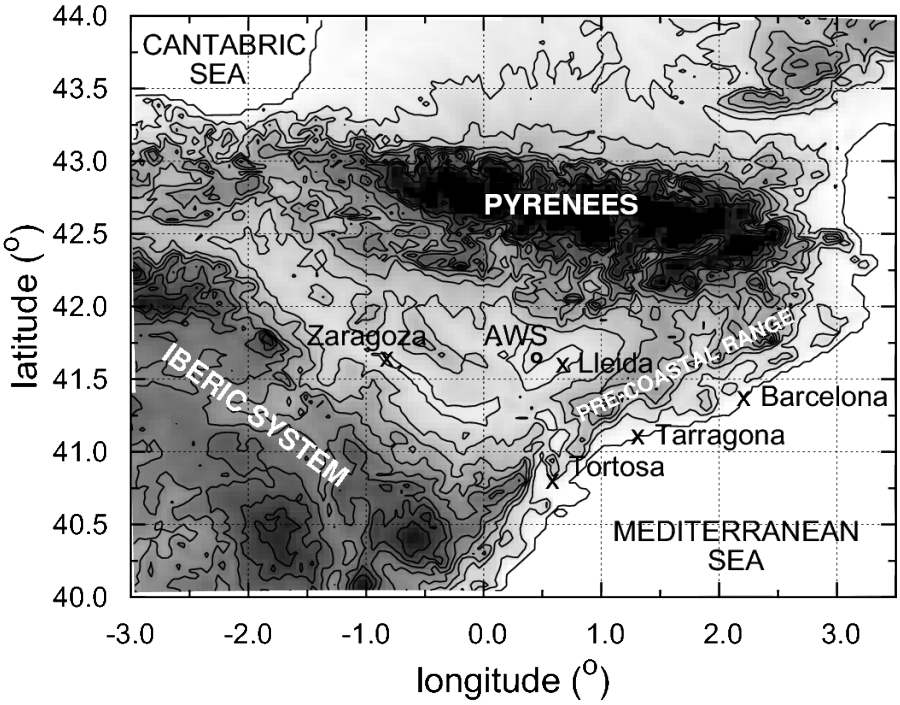

Figure 6.1: Location of the Gimenells AWS in the Ebro basin.

for any other place.

The study of the climate of an area is usually done by using statistical parameters of the principal meteorological variables. The characterization of some episodes is done according to the method of case studies, and it often combines the analysis of observations (*in situ* and remote) and simulations with mesoscale models (Cuxart et al., 2007). While climatology describes the average behavior of the weather in a certain area and gives information about the variability of the studied series, the case studies describe situations which can appear regularly (as it is the case of anticyclones when local effects predominate) or sporadically.

A case study does not have, in principle, statistical representativity. To be considered representative, it is first necessary to study the climatology of the area of interest conditioned to the situation to be studied, and check if the selected

case behaves consistently with the correspondent conditioned climatology. This study aims to characterize stable nights in the Ebro basin, more precisely in the Lleida area, in order to, in subsequent studies, evaluate if a determined case study is representative of the behavior indicated by the climatology.

Accordingly, it is necessary to develop a study methodology of climatic series conditioned to the existence of particular meteorological situations. To be specific, those that are favorable to the development of local circulations are typically related to weak pressure gradients in an area. This will allow studying the characteristics of stable nights from a statistical point of view.

In the absence of relevant synoptic gradients, the heterogeneity of the surface (due to topography or to the uses of the soil) favors the appearance of phenomena such as drainage flows, valley winds, breezes or cold pool growth (Whiteman, 1990) that strongly condition meteorological measurements and make possible the appearance of significant differences between stations which are close to each other (Cuxart et al., 2007).

In Section 6.2 the environment of the weather station chosen for this study is described. The station is located in the Segrià (the region around Lleida), in a relatively homogeneous area (regarding crops and topography) and far away from any important population centers. There is as well climatic information from the main Lleida station, located in the same area. A 9-year series of hourly data will be studied, described in Section 6.3, only for the stable nights with weak wind, no clouds or fog, as they are the most favorable to the development of local circulations and at a hydrographic basin scale.

In Section 6.4, three factors to filter the series are defined using the information provided only by the station, based on insolation, relative humidity and wind speed. After that, in Section 6.5, the filtered series are analyzed, the physical significance of the results in both local dynamics and basin terms is discussed, and the validity of the methodology is evaluated. Finally, in Section 6.6 the most relevant conclusions are given. In the future, it is expected to test this methodology simultaneously in several stations in the same basin.

6.2 Climatology and location

The automatic weather station (AWS) of Gimenells (0.394°E, 41.656°N) is located 248 m above sea level (ASL), on the western side of the Lleida area. From a physiographic point of view, the station is on a plateau located between the

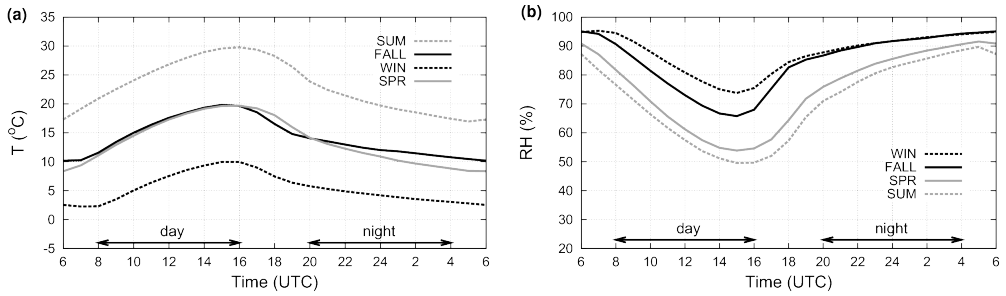

Figure 6.2: (a) Daily cycle of the average temperature (°C) and (b) relative humidity (%) for all four seasons calculated from the time series registered in the Gimenells AWS in the period 1997-2005.

rivers Cinca and Segre, in the eastern part of the Ebro basin, with the Pyrenees to the north and the Pre-coastal Range to the east (Figure 6.1). The basin stretches to the west with several tributaries of the Ebro river coming from the Pyrenees (the Cinca and the Gàllego, among others), the river Jalón being the main tributary from the right side, which brings water from the Iberian System.

The station is located 20 km to the west of Lleida (which is 155 m ASL) and 25 km to the north of where the Ebro and its tributaries Cinca and Segre meet at 128 m ASL. The area is locally plain, but it is on a basin slope oriented from north to south and from east to west with a very weak slope. The Central Pyrenees are in the north, with peaks higher than 3000 m ASL, together with the pre-Pyrenees, a group of mountains located between the main rivers (Segre, les Nogueres, Éssera and Cinca) that are oriented from west to east, the closest ones of which are the Montsec (1677 m ASL, 50 km to the Northeast) and the Serra Llarga (509 m ASL, 25 km to the north). The layout of these mountains favors katabatic flows to be mainly channeled along the river valleys.

The Pre-coastal Range borders the basin on its eastern and southeastern edges to the Ebro River. To the east, the maximum elevations of the different ranges are between 700 and 900 m ASL, with a very gentle slope, without any important obstacles to the west, passing Cervera and Tàrrega (548 and 373 m ASL respectively) to the Pla d'Urgell (ca. 250 m ASL average). To the southeast, the mountains lose elevation, from the highest ones (Prades and Montsant, that are ca. 1200 m ASL in height), to those on the border of the plain, which are approximately 500-600 m ASL in height. On the southern side of the Ebro, the Iberian Mountains present a complex relief with heights ca. 400 m ASL when

passing by the Ebro, that increase until 1470 m ASL over Ports de Beseit, at a distance of 100 km.

It is to be expected that this topographic distribution highly conditions the climatology of the studied area, as it has already been observed in a numerical study of air circulations in Mallorca Island in similar meteorological circumstances (Cuxart et al., 2007). The drainage flows generated in the mountains located in the area between the east and south do not encounter any significant orographic obstacle and, in principle, can arrive well developed over the Lleida area.

The entire region is characterized by an intense agrarian activity. Next to the station there is an experimental crop area (42 ha of fruit trees, cereals and fodders) and, in the surrounding areas, there are fields of cereal, vegetables and fruit trees. To the northeast there are irrigation lands (corn, alfalfa) and at 4 km to the northeast, the wine-growing region of Raimat (2245 ha).

From a climatic point of view, the Lleida area is one of the driest in Catalonia, with a pronounced continental climate. In the Lleida station of the *Agencia Estatal de Meteorología* (AEMET) (Spanish meteorology agency), according to their website*, for the period of 1971-2000, the average precipitation was 369 mm per year, with maximum values in spring and fall, with an average yearly temperature of 14.7°C and a yearly thermal range of 20°C (the difference between the average temperature of the warmest and the coldest months). These are characteristics of a continental Mediterranean dry climate (Martín-Vide, 2005). There are 46 days with rainfall over 1 mm, 53 days of fog (37 between November and January) and 37 days of frost. Fog could be persistent in the area during winter anticyclones, remaining over the area 24 hours a day. Average maximum temperatures are over 30°C in summer and the average minimum is 1°C in winter. The extreme values in Lleida were 41.2°C on July 30th 1983 and -14.2°C on January 8th 1985.

6.3 Characteristics of the temporal series

The station of Gimenells belongs to the *Xarxa d'Estacions Meteorològiques Automàtiques* (XEMA) (Automatic Weather Stations Network), of the *Servei Meteorològic de Catalunya* (SMC) (Meteorological Service of Catalonia) and it is located in the municipality of Gimenells and el Pla de la Font, about 600 m away of the

*http://www.aemet.es/en/elclima/datosclimatologicos/valoresclimatologicos?l=9771C\&k=cat

town of Gimenells. The *Departament d'Agricultura, Ramaderia i Pesca* (DARP) (Department of agriculture, farming and fishing) of the Catalan government set up this installation on December 1st 1996 for agrometeorological purposes. It measures (i) the temperature at 1.5 m above ground level (AGL), (ii) wind speed and direction at 2.0 m AGL, (iii) relative humidity at 1.5 m AGL, (iv) global solar radiation and (v) precipitation.

Until March 2005, temperature and relative humidity data were taken with a sampling frequency of 10 minutes whereas samples in the fields of wind, rainfall and solar radiation were taken every second. The hourly data saved were the scalar average of the sample values for one hour. From April 2005, the data (not considering rainfall) is taken with a sampling frequency of one per second in order to calculate minute averages (in the case of wind speed and direction these are vectorial averages, according to the normative UNE500520). In this work, hourly averages for the period 1997-2005 have been used (taken from the minute averages for the interval April-December 2005).

For the studied time interval, the quality control of SMC was based on filling in the blanks of the series by using a linear interpolation when there is a period of one or two hours. In all other cases, the series is left untouched. Throughout these nine years of data compilation there have been blanks concentrated in two periods: (i) from 08 UTC on August 6th 1999 to 00 UTC on September 4th of the same year and (ii) from 04 UTC to 10 UTC on June 8th 2003. As the number of missing data represents less than 1% of the total, these points in the series are not considered in the following analysis.

Figure 6.2 shows the daily cycle of the average temperature and relative humidity for all four seasons, taken from the temporal series of 9 years. Related to temperature, transition seasons (fall and spring) have very similar evolution and values. The average amplitude is ca. 10°C and night temperatures are slightly lower in spring, when there is less fog and night cooling can be more intense at the end of the night. Winter has the smaller daily thermal amplitude (ca. 7°C) and the minimum absolute night cooling, even if temperatures are clearly below the other seasons, while summer is the season with a wider daily thermal amplitude 13°C). Relative humidity also shows a very clear daily cycle for all seasons. Values shortly after midday show that spring and summer have values below the average (60%) while in fall and winter values are about 10 to 25% higher. During the night, all seasons register very high values of relative humidity due to strong superficial radiative cooling.

Figure 6.3 shows the distribution of wind speed frequencies during 9 years of data for each season. To distinguish the relevant directions during day and night, calculations have been made for the periods 08 - 16 UTC and 20 - 04 UTC,

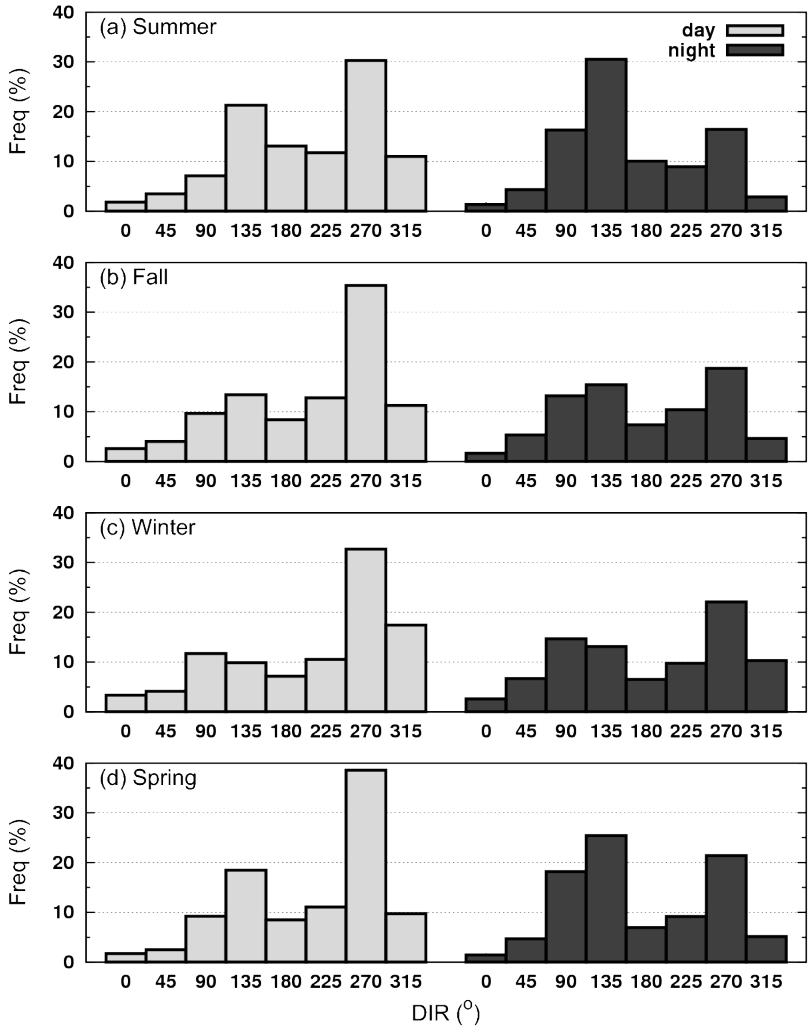

Figure 6.3: Frequency distribution (%) of wind direction (°) for the seasons of (a) summer, (b) fall, (c) winter, and (d) spring, calculated from the time series registered in the Gimenells AWS in the period 1997-2005. The day corresponds to the hourly data obtained from the period 08 - 16 UTC and the night, from the period 20 - 04 UTC (see Figure 6.2).

respectively, therefore avoiding the influence of the variation in the time of sunrise and sunset along the year. During the day, wind from the W predominates in all seasons. The explanation is that this is an area with general winds from the W and so these are predominant if there is no anticyclone.

On the other hand, by night there is a approximately bimodal distribution, with maximum from the W and E/SE. The first ones could also be related to general circulation; while the second ones could be produced by the generation of drainage flows from mountains located in these directions and relatively nearby. However, it must be noted that wind from the N and NE is rare in this AWS, despite the presence of the Pyrenees and Montsec mountains in these directions, and everything seems to indicate that this is a phenomenon linked to the peculiarities of the circulation in the area (the channelling of these low-level winds by the Segre and Cinca valleys, as observed in other complex basins (Gudiksen et al., 1992).

6.4 Selection of stable nights

It is very difficult to distinguish the specific climatic characteristics of stable nights, based on the general climatology of an AWS, which are strongly conditioned by local circulation. In order to make a more accurate analysis, the current study has developed a method to select stable nights from the series based on the variables measured at the station.

The goal is to detect the nights of the series with clear skies and a weak synoptic pressure gradient. Unfortunately, the Gimenells AWS has no net radiation sensor (which could indicate if there is strong cooling and therefore clear skies) that allows identifying the nights that have these characteristics. There is also no pressure sensor, even if this measure itself does not allow the estimation of the gradient (stationary pressures could have strong winds associated). However, and despite the difficulties, it has been decided to build a simple selection method from the information obtained from the analyzed AWS in order to generalize it to other stations. In this study, the specifically defined parameters to extract the

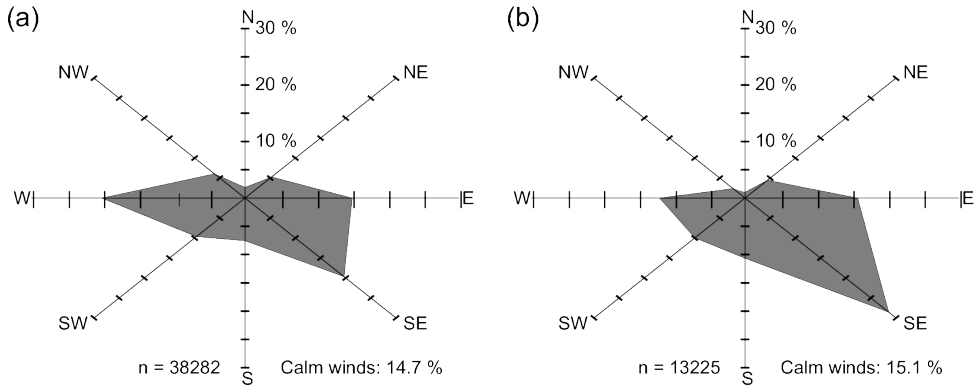

Figure 6.4: Wind rose for all (a) nights, and (b) stable nights according to the criteria defined in the text (Expression 6.4). Winds are considered calm when the wind speed has an hourly average inferior to 0.2 m s^{-1}. *n* indicates the number of data used for each diagram.

nights of interest are:

$$Q_d = \frac{Q_t - Q_e}{Q_t} \tag{6.1}$$

$$HUM = \frac{HR_d - HR_s}{HR_d} \tag{6.2}$$

$$\overline{V_n} = \frac{1}{N}\sum_{N} v_i \tag{6.3}$$

The first (Q_d) is named *insolation deficit index*, where Q_t and Q_e represent the theoretically and measured average daily insolation, respectively. It calculates the difference between measured solar radiation and the radiation that theoretically arrives to the top of the atmosphere at the same latitude and day of the year. Therefore, besides the dimming effect of the bulk of the atmosphere, the other reason for this difference is the cloudiness during the day. Actually, on a cloudy day, the value of Q_d will be higher than on a sunny day. With this index it is assumed that the cloudiness during daylight time is similar to that produced during the following night. This parameter allows ruling out the days with cloudiness of a synoptic origin, associated to fronts or disruptions and that, due to the temporal scale of the phenomenon, does often affect the following night as

well. However, there are situations in which Q_d could discriminate cloudy days of strictly daily evolution (cumulus) typical of good weather and followed by a stable night. This condition has been considered when defining the threshold value of this parameter.

HUM is the *index of the humidity cycle*. It uses average relative humidity (HR_d) and average relative humidity measured only during daylight (HR_s). It depends on the daily cycle of relative humidity. If this is important, the average relative humidity during daylight hours would be lower than daily relative humidity, therefore producing a HUM value higher than if the relative humidity is relatively constant throughout the day. Large daily cycles of temperature and humidity involve great contrasts between day and night, a situation often found in stable conditions. Relative humidity has been used instead of temperature because one of the aims of this study is to analyze the evolution of this variable on stable nights. Therefore, it was decided not to use it as a discriminating factor.

On the other hand, HUM discards atmospheric situations with meteorological phenomena of a temporal scale that are longer than a day (dry advections, for instance), as well as situations of persistent fog throughout the day. As indicated in Section 6.2, persistent fog is a winter phenomenon that is frequent in the area, which significantly disturbs the balance of energy on the surface as it changes the quantity of net radiation that reaches the surface; those cases were discarded in the current study.

Finally, $\overline{V_n}$ is the *average speed of night wind*, where v_i represents wind speed at the i-hour of the night. It is used to discard the nights with an important synoptic or mesoscalar pressure gradient, which can be translated into a moderate wind close to the surface.

Stable nights are considered to be those that comply of the following inequalities:

$$Q_d \leq 0.4; \quad HUM \geq 0.07; \quad \overline{V_n} \leq 2\ ms^{-1} \tag{6.4}$$

All the nights with an average wind speed below 2 m s^{-1}, preceded by a day with little cloudiness and dry in relation to the night will be selected.

The threshold values are selected as follows. On the one hand, the limit of Q_d considers those days when measured average global radiation represents at least, 60% of what theoretically arrives to the top of the atmosphere. On an clear sunny day, Q_d value is greater than 0.2, while when a front passes, Q_d exceeds 0.6.

The fixed threshold for HUM is small because this is a parameter that has values between 0.00 and 0.20 for the vast majority of nights. For instance, HUM value is lower than 0.09 on a day that has had the same daily oscillation as the average

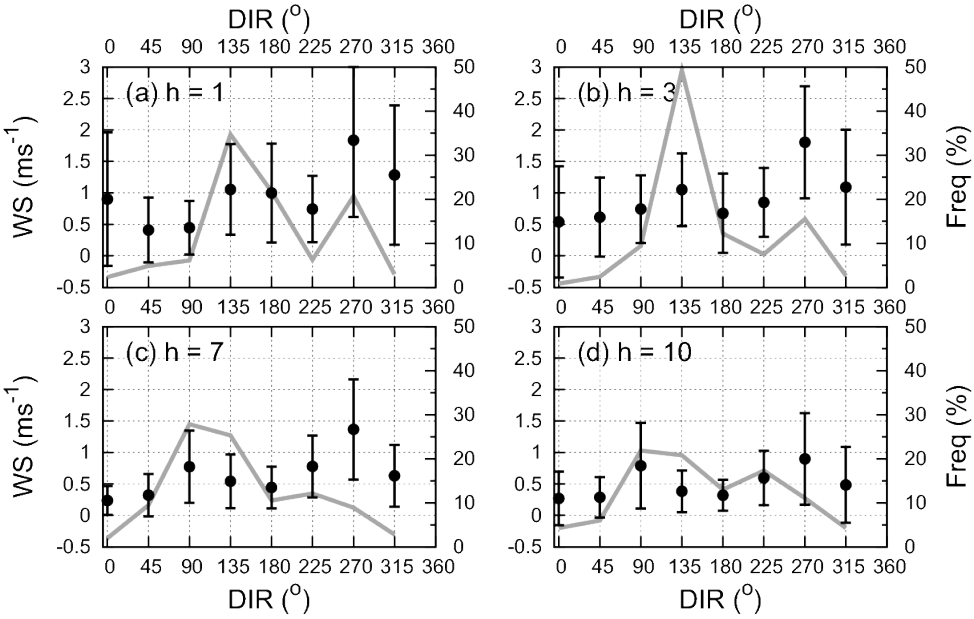

Figure 6.5: Average wind speed (m s^{-1}) regarding the direction (°) (black) and frequencies distribution (%) of the wind direction (gray) for the (a) first, (b) third, (c) seventh and (d) tenth night hours. The night hours refer to the number of hours from the last registered data before sunset. Error bars indicate the standard deviation of the group of individual results that contribute to the wind average value.

represented in summer (Figure 6.2). Therefore, the selected value includes cases with a daily oscillation of, at least, the average obtained during that season. The restriction imposed on the average speed of the night wind is based on previous experimental studies. During the experimental campaign of SABLES 98 (Cuxart et al., 2000), that took place on the Duero basin, stable situations had wind speeds below 2 m s^{-1} close to the ground. Actually, Conangla and Cuxart (2006) impose a similar criterion for the selection of nights with a maximum of well-defined wind at low-level jet. Among other restrictions, wind average every 30 minutes at 2.2 m AGL should be lower than 2 m s^{-1}. In that study, all selected nights corresponded to synoptic situations defined by a strong anticyclone with its center next to the Iberian Peninsula. In the current study, this condition is less

Table 6.1: Number of stable nights in the 9 year series for each season (left) and percentages regarding the total number of nights of the time series (center) and regarding the season (right).

	n. of stable nights	% over the total	% over season total
WINTER	125	10.3	15.5
SPRING	380	31.3	45.9
SUMMER	447	36.8	54.8
FALL	262	21.6	32.2
Total number	1214	100	37.3

rigidly applied, as it is the average of the hourly wind measured along the night, which has to be under the established value limit.

When applying this filter, 1214 stable nights are obtained out of a total of 3253. Table 6.1 shows the number of cases according to the season, summer being the one with a higher absolute number of nights that fulfill the required conditions (and there is nearly one month of the summer of 1999 missing in the series). The following is spring, over fall, when fog is more frequent and its likeliness is lower in winter, as in these months there are frontal passages combined with anticyclones that generate persistent fog. The percentages elaborated for each season show that approximately half of the nights in the summer and spring fit the given definition of stable nights, while these proportions decline to 32% and 16% in fall and winter, respectively.

6.5 Study of the selected nights

6.5.1 Wind roses and nightly evolution

Figure 6.4 compares the wind roses of the total number of nights and of the subgroup of selected nights. The general rose shows three predominant directions (W, E and SE with ca. 20% each) and a little represented sector (NE and NW with ca. 5% and N with 2%). The rose, during stable nights, has its main sector to the SE (28%) and the E (15%), W frequency descends to 12% and N

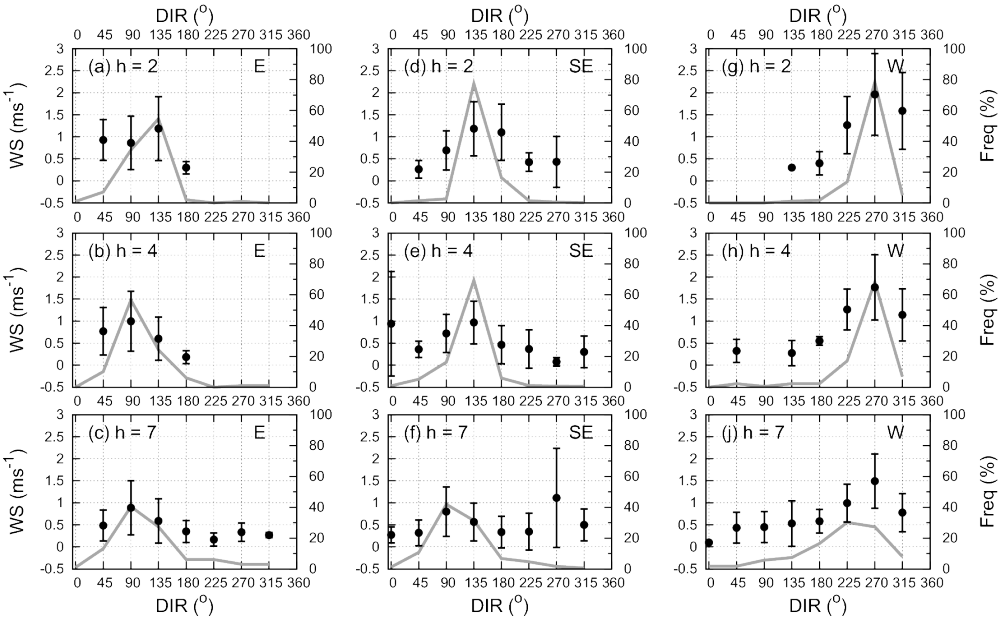

Figure 6.6: Same as Figure 6.5 but with stable nights gathered in three different subgroups, according to wind direction during the third night hour (Figure 6.5b): (i) E (left column), (ii) SE (central column) and (iii) W (right column) for (a, d, g) second, (b, e, h) fourth and (c, f, j) seventh night hours.

sector is still rare. It can be observed that the proportion of calms* is similar in both roses (15%), which indicates that there are situations of weak wind that do not fulfill the required criteria. Nights with persistent fog could be an example. Moreover, assuming that the cloudiness of the day will remain during the night, it is possible to have cloudy nights after a cloudy day, which would also explain the persistence of the proportion of calm nights.

The diminishing of west winds on stable nights is the result of filtering situations of west winds with associated cloudiness and cases of strong Cerç winds. The predominance of SE winds indicates a probable influence of high mountains located in that direction (Prades, Montsant) and winds from the E could indicate slope winds from the Segarra plateau. Instead, drainage flows from sector N, which could come from the Pyrenees or Montsec, do not arrive to the weather

*It is considered calm when the hourly average of the wind speed is lower than 0.2 m s^{-1}.

station in significant quantities, possibly because they descend channeled by the nearby valleys of Segre and Cinca, as indicated in the climatologies of the stations located next to the Segre River (available at www.meteo.cat). It must be noted that recent numeric studies (Cuxart et al. (2007) for Mallorca, Bravo et al. (2008) for the Duero basin) indicate that nocturnal drainage flows are organized and interact, and this could explain circulations that seem apparently counterintuitive.

In order to inspect the evolution of the wind direction frequency distribution during the night, attention will be focused on four significant moments (Figure 6.5): (i) beginning of the night, (ii) change of tendency, (iii) late night and (iv) end of the night. In the first hour SE predominates, with high percentages of S and W. In the third hour, the SE predominance has increased (it gets to its maximum value during the night) and S and W descend to relatively low values that will be maintained during the whole night, while the E component is increased in the final hours of the night as SE decreases gradually, until it is exceeded in the seventh hour. Calm winds are more frequent at the end of the longest nights, between the end of fall and beginning of spring (not shown). The amount of data decreases after the seventh hour due to the shorter length of the night in summertime.

Trying to make a reading of these statistics in a physical code is risky. One could think that at the first hour there could be either (i) winds from the W of one type (weak west winds), or (ii) a local winds linked to weak pressure gradients that favor winds from the S and the SE that turn to the E during the night, linked to the topography of this part of the basin. Actually, when analyzing on an hourly basis, it is evident that the night distribution is bimodal, there is more frequency of SE or E at all hours, with W/SW being the second most frequent with winds that usually have twice the strength as in the first case (Figure 6.5).

To evaluate this hypothesis, three subgroups were chosen out of all the nights selected, defined according to the predominant direction in the third hour after sunset (Figure 6.5b): W (15.5%), SE (49.3%) or E (9.3%). This instant was selected because the time of the night when there is the maximum data concentration in a specific direction (SE). By doing a similar analysis to this one for all nights, but paying attention to the instants immediately prior and after the hour chosen to divide the three subgroups, one could see that the evolutions of E and SE are very similar, and the case of E could be considered as one of the cases that have changed faster than the others (Figure 6.6a - 6.6f). Both of them show the SE component in the first hours of the night turning to E between 4 and 6 hours after sunset.

Instead, nights with wind from the W three hours after sunset keep this

direction as predominant during the rest of the night with a gradual diminishing of speed as the night goes on (Figure 6.6g - 6.6j).

6.5.2 Temperature, speed and humidity evolution

Figure 6.7 shows the evolution of some variables for each subgroup above defined, giving the curve that links average values and standard hourly deviations. The subgroups from E and SE have similar behaviors, which suggests a similar origin for both cases (drainage flows). It can be observed that the evolution of the direction is very different depending on wind direction during the third night hour. There are fewer differences at the end of the night, when the wind speed is smaller in both cases. In fact, the average speed is nearly double on the nights when the wind blows from the W than when it blows from E/SE.

Thermal evolution shows similar coolings in all three cases during the first five hours. Since this moment, if the winds regime is W, the air gets cooler than if it blows from the E/SE. It is still not clear if this difference is due to the different nature of the phenomena that intervene in each of the mentioned regimes. The cooling per hours is more intense in the first part of the night (2°C h^{-1} at the beginning and 1.5°C h^{-1} thereafter) and gets stable in the second part with values of 0.5°C h^{-1} in the case of drainage and slightly higher for west winds (0.7°C h^{-1}). Snyder and de Melo Abreu (2005) highlight that those nights with frost risk have similar behaviour, with very intense coolings around sunset (that could reach 10°C h^{-1} in some cases) and smoother at the end of the night (1°C h^{-1}). Regarding relative humidity, west winds start at the beginning of the night with values an average of 10% lower than when the wind blows from E/SE. However, in all cases, relative humidity is increased during the night with the diminishing of temperatures reaching an average values of 90%, which generates dew and mist or fog at the end of the night.

Figure 6.8 shows, on the other hand, the same variables (except wind direction) for all selected nights grouped by seasons. The most remarkable thing in this figure is that there are no qualitative differences between the evolution during the different seasons. The curves are almost parallel to each other, and the only difference is their length, due to the variation in the number of night hours depending on the season. In all of them, the wind speed decreases in the middle of the night, humidity increases to values close to saturation and cooling eight hours after sunset is 6 to 7 degrees with similar error bars. Hourly cooling also follows the same pattern, with intense cooling during the first hour of the night (2°C h^{-1}), moderate between the third and the seventh (between 1.5 and 1°C h^{-1}) and gentle in the last period (lower than 1°C h^{-1}). This perseverance in

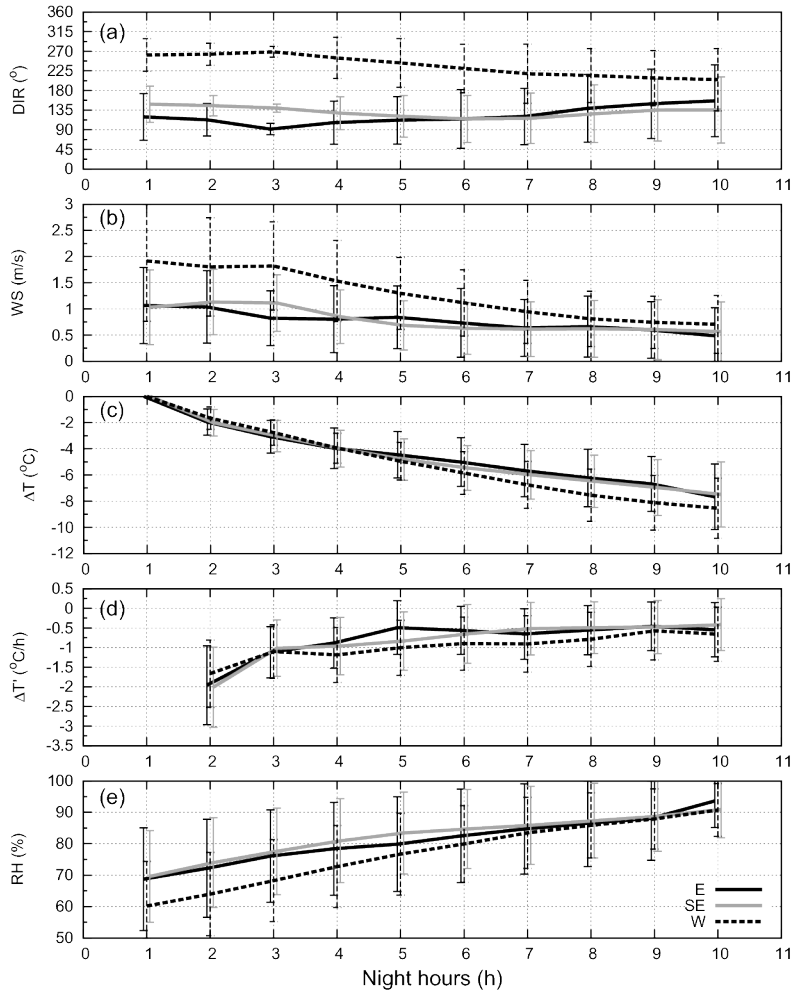

Figure 6.7: Temporal evolution of the average of wind (a) direction (°) and (b) speed (m s^{-1}), (c) cooling (°C), (d) cooling hourly rate (°C h^{-1}) and (e) relative humidity (%) for all three subgroups of stable nights defined in Figure 6.6. The bars indicate standard deviation. The abscissa axis corresponds to the hour of the night (defined in Figure 6.5).

the behavior of the main meteorological variables allows for the predefinition of a night evolution pattern for the Gimenells AWS, regardless of the season.

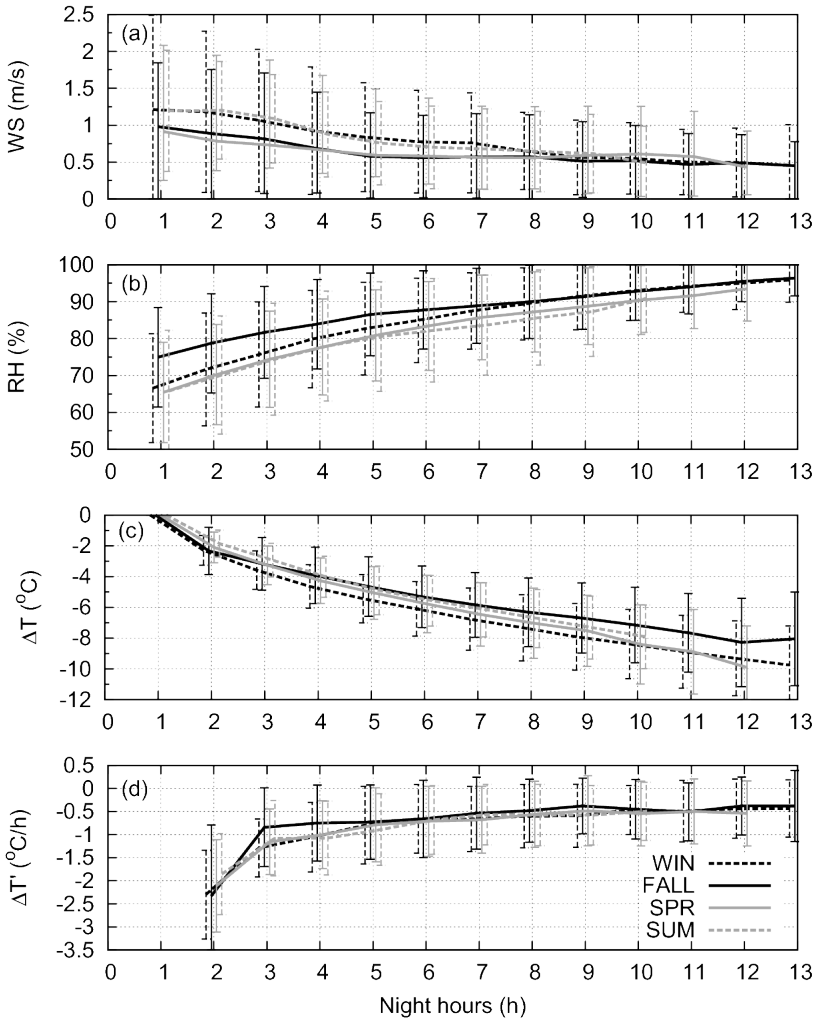

Figure 6.8: The same as Figure 6.7 for the variables (a) wind speed (m s^{-1}), (b) relative humidity (%), (c) cooling (°C) and (d) hourly cooling rate (°C h^{-1}) for all four seasons: winter (WIN), spring (SPR), fall (FALL) and summer (SUM) for all selected nights.

6.6 Conclusions

With the objective of characterizing the average behavior of the meteorological variables of the Gimenells AWS, conditioned to some specific characteristics on calm nights with weak wind, three parameters have been defined. These parameters made it possible to extract nights of interest just by using the data registered in the station for the years 1997-2005. Insolation, relative humidity and wind speed were used as discriminative variables, leaving aside temperature as its behavior is of special interest during stable nights.

The chosen parameters seek out nights that correspond to days with a well defined daily cycle and weak winds on the station (until to 2 m s^{-1} a 2 m AGL). The filters selected 37.3% of the nights in the 9 years series, which indicates a first estimation of the frequency of this kind of weather in the Lleida area (clear nights with weak or calm winds and no fog). They occur mainly in the summer and spring, as in the fall and winter this situation normally generates fog and the nights are not selected. As fog is a protective factor against steep temperature drops, clear and calm nights are the most likely to cause frosts. In the Gimenells AWS these nights represent up to 16% of all nights in the winter and a 46% of the spring nights, which is the most critical season for agriculture.

The study of the wind shows that there are two kinds of preferential regimes in the selected station. The first and more usual one seems to be related with drainage flows that are first generated in the SE, in the ranges of Prades and Montsant and arrive later on from the E from the Segarra plateau. The second in frequency is a regime of weak west winds, which maintain their direction during the whole night. Winds from the north sector do not arrive well defined to the station and this could be due to its channeling through the valleys of Segre and Cinca that, as they are power in respect to the station, would be under the drainages described above. In any case, the observed winds always tend to decrease during the night.

The temperature drop follows a unique pattern for all regimes and stations. Cooling during the four hours after sunset is ca. 4°C, while during the first eight nightly hours the temperature descends ca. 8°C in the case of west winds, and 6.5 °C when there are drainage flows. In all cases, there is a strong hourly cooling (2°C h^{-1}) in the first hour after sunset, which declines gradually as the night draws on. These results make it possible to estimate the minimum temperature regarding the measured temperature just after sunset and the winds regime.

To confirm what the study indicates, other observatories in the area must be explored, especially those with longer climatic series, to see if there are any

congruent conclusions, as well as to carry out studies with a numeric and experimental character that confirm the hypothesis developed here.

Acknowledgements

This work has been possible thanks to the funding of the research project CGL2006-12474 and the grant FPI BES-2007-16272, from the MEC. The manuscript has been enriched by the suggestions of Dra. Maria Antònia Jiménez and some calculations done by Felipe Molinos. We would also like to acknowledge the collaboration of Tomeu Clapés in the design of Figure 6.1 and the comments of Mr. Miquel Perpinyà i Romeu, from the SMC, about data quality control, as well as the comments of two anonymous reviewers.

Chapter 7

Meso-beta basin flows in the eastern Ebro river basin

This chapter is based on Cuxart, J., J. Cunillera, M. A. Jiménez, D. Martínez, F. Molinos, and J. L. Palau, 2011: Study of mesobeta basin flows by remote sensing. Submitted to *Bound.-Layer Meteorol.*

Abstract

If no well-defined synoptic gradients exist on a basin, flows can develop at a variety of scales, the main generators of circulations being spatial thermal differences. These dynamics are studied for the Eastern Ebro basin, at the northeast part of the Iberian Peninsula, almost isolated from the surrounding areas by mountain ranges. The main tool for the study is the new RASS-Sodar by Scintec, the WindRASS, that emits radio waves in three directions with a range up to 360 m above the ground.

One year of operation shows that low-level jets are found routinely, their maximum being at a height under 500 m above ground level. The jets blow from constant direction during several hours over the whole observed column, with fast transitions between these periods. They allow for efficient heat transport at the basin scale and are good producers of vertical mixing due to the strong wind shear. In summer the irrigated plain has larger thermal contrast with the

dry slopes and the winds are stronger than in winter, when katabatic flows can develop at night and usually radiation fogs appear that may last for days.

7.1 Introduction

In the development of parametrisation of processes within the atmospheric boundary layer (ABL), terrain homogeneity has been usually invoked, with the aim to reduce the number of factors involved. However, studies developed in the last years show that it is not possible to comprehend the behaviour of ABL on one site without taking into account the surrounding heterogeneity.

Recent campaigns have repeatedly shown that the nocturnal ABL, in the absence of synoptic forcings, can have a large variety of flows that still have to be fully characterised (Cuxart et al., 2000; Poulos et al., 2002), whereas in the daytime ABL focus has been put on small scale heterogeneities (Beyrich and Mengelkamp, 2006; Oncley et al., 2007).

In the nocturnal ABL over land, low-level jets (LLJ) are observed routinely (Conangla and Cuxart, 2006; Baas et al., 2009), but very few of them are generated by inertial oscillations, even in the Great American Plains (Banta et al., 2002). Their presence can influence the value of the surface fluxes (Grisogono and Oerlemans, 2001b; Martínez et al., 2010), since they can generate elevated turbulence by wind shear that is able to reach the surface layer regardless of the local state of the ground (Cuxart and Jiménez, 2007).

These jets can be explicitly resolved by the models if they have enough horizontal and vertical resolution to reproduce them and if the factors generating them are well represented. Unfortunately, numerical weather prediction models usually do not fulfil these requirements and the effects of these circulations are underestimated or overlooked. Missing them in the models may partly explain why they lack turbulence mixing in very stable conditions that can lead to unrealistic surface runaway cooling (Viterbo et al., 1999).

The origin of these low level flows over land may be linked to terrain heterogeneity. Basins are formed by slopes of varying angle and vegetation together with relatively complex bottom areas. The usual case of a steep upper slope followed by a gentler slope can generate a rapid acceleration on the upper slope followed by a transition to a slower evolving structure characterised by an elevated jet over the lower slope (Smith and Skyllingstad, 2005). Differential cooling along the slope generates accelerations and vertical motions associated with low-level

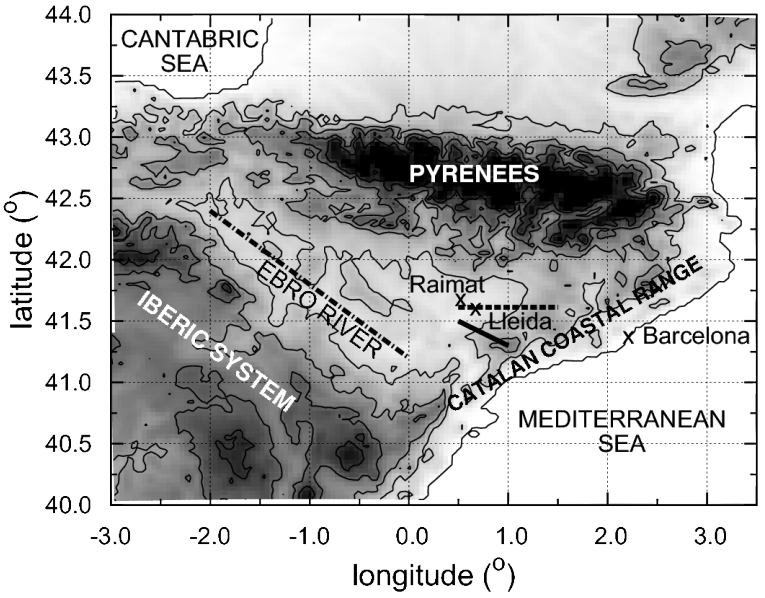

Figure 7.1: Topography of the Ebro Valley indicating the main rivers and mountain ranges together with the location of Raimat, Lleida and Barcelona. Surface elevation contours are plotted every 400 m and the colours vary linearly, indicating 0 m in white and 2000 m in black above sea level.

convergence (Shapiro and Fedorovich, 2007). Some of these effects are found in high-resolution mesoscale simulations (Cuxart et al., 2007; Jiménez et al., 2008).

In the bottom areas, the terrain depressions are prone to the formation of cold air pools where the air decouples of the flow above and larger radiative cooling takes place, with significant amounts of dew deposition (Whiteman et al., 2009). Their persistence is directly related to the strength of the flow above and the amount of radiative loss to space (Vosper and Brown, 2008). If the basin is large enough, mesoscale temperature differences can arise due to different types of surface that may generate baroclinic circulations (Taylor et al., 2007), whose strength may be proportional to the temperature gradients.

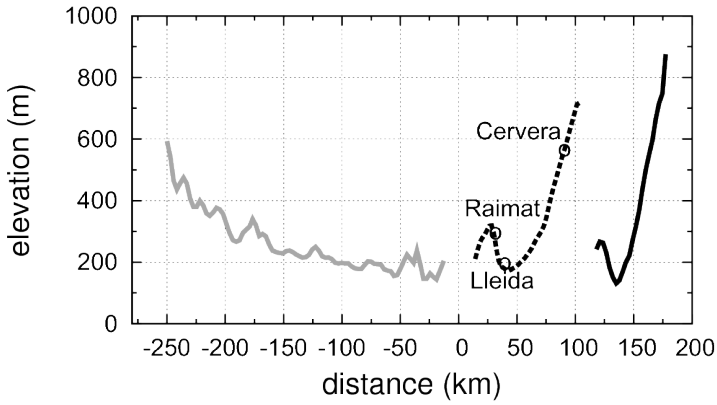

Figure 7.2: Slopes converging to the Raimat site following the Ebro river (gray solid), the eastern slope (black dashed) and the south-eastern slope (black solid). Zero in the x-axis indicates 0.2°E. Black solid line has been displaced eastwards 100 km for clarity.

The installation in July 2009 of a new remote sensing device made by Scintec, the WindRASS, in Raimat near the city of Lleida in the Eastern Ebro valley at the North-East part of the Iberian Peninsula, gives the opportunity to characterise these flows as the device is operating continuously. It provides profiles of virtual temperature, speed and direction of the wind and vertical velocity and its standard deviation. The novelty of this device makes necessary that its performance is checked against complementary information.

The basin of the Ebro river is a triangular-shaped valley in the North-Eastern Iberian Peninsula (Figure 7.1). Its main axis (North-West/South-East) is about 400 km long and the basis along the Catalan Coastal Range extends about 250 km. It is practically closed since the river reaches its delta through narrow gorges. In the Eastern part, the drainage currents from the Pyrenees flow along the channelled valleys of the tributary rivers and the local flows are basically determined by the slopes from the mountain ranges limiting the basin at the East and Southeast.

This area is in the zone of general westerlies, but the mountain ranges of the Iberian Peninsula make that most of the frontal passages precipitate before reach-

ing the Ebro basin, which is one of the driest areas of the region (400 mm per year). However, the tops of the immediate surrounding ranges (especially the Pyrenees) have significantly higher precipitation, which allows extensive irrigation in the plain from the large rivers originating there. This results in a moist green flat valley enclosed by semiarid mountain slopes that generate large thermal differences between the plain and its surroundings. Most of the irrigated area is in the Eastern Ebro basin, being more patchy at the western part. The location of the WindRASS is in the bottom of the valley where the slopes coming from the East and the West meet (Figure 7.2).

The area has 15 % of days with fog, mostly in winter and the clear sky nights with weak winds represent 37.3% of the cases. The later are mostly from East-Southeast (18%), locally generated and with night temperature drops concentrated at the first part of the night, smaller than the westerly cases (9.5%) that have continuous cooling of the air during the whole night (Martínez et al., 2008). Figure 7.3 shows the averaged temperature and wind evolutions for the three regimes for Raimat. The local easterly flows are warmer since they predominate in good weather conditions, whereas the westerlies are linked to the general circulation between fall and spring and fog is basically a winter phenomenon.

7.2 Observational tools

The location where the experimental measurements take place is nearby the Automatic Weather Station (AWS) of Raimat (41°41′N, 0°34′E), close to Lleida town, in a terrain belonging to the Codorniu wine company, where there is an extensive culture of vines over a surface of 22.45 km^2. The property is surrounded by extensive irrigated lands with other cultures, mostly alfalfa, cereals, fruit trees and sweetcorn. The station is located over a terrace open to all directions at the West of the Segre river, after the ending of the eastern slope. The automatic weather station is supplemented with an Energy Budget Station (EBS) that provides heat, moisture and momentum flux at 2 m, plus the four components of the radiation budget and ground heat flux, soil temperature and water contents. The WindRASS (described in the next section) is installed just alongside. This configuration (automatic weather station, WindRASS and energy budget station) has been operating in Raimat since July 1st, 2009. In the area there are 22 automatic weather stations with an average distance between them of about 10 km. All these equipments belong to the Catalan Meteorological Service (SMC).

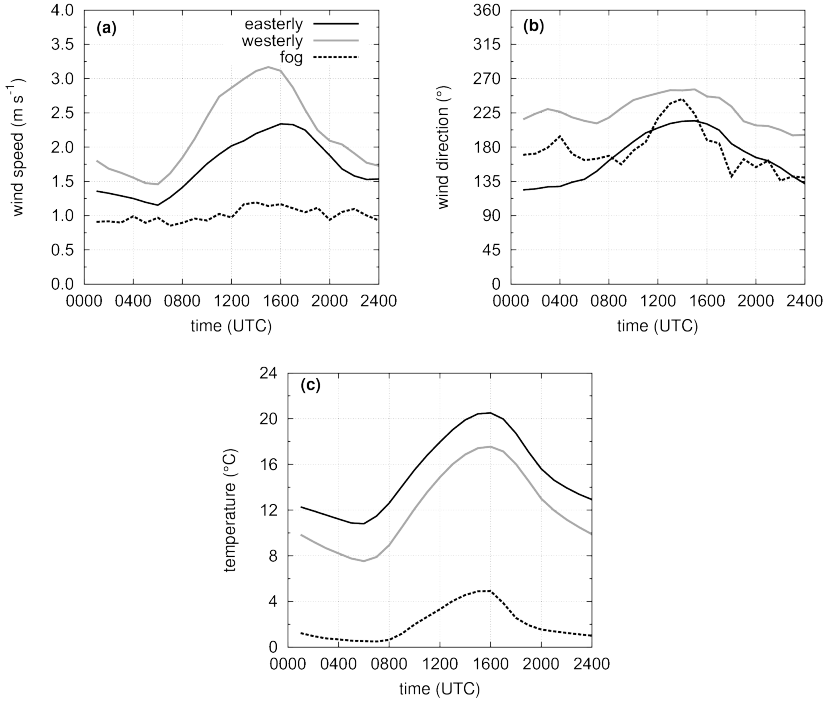

Figure 7.3: Statistical behavior in the Raimat automatic weather station of (a) wind speed, (b) wind direction and (c) temperature for clear skies and weak wind nights in the easterly and westerly cases in the period 1998-2007 and for 46 fog cases between 2005 and 2009.

A first special observation period was held during the first two weeks of July 2009, when some flights were made with an instrumented remote-controlled Meteorological Mini Unmanned Aerial Vehicle (M2AV, Figure 7.4a, Spießet al., 2007; Van den Kroonenberg et al., 2008). It has a wing span of 2 m, its total weight is 6 kg and it is navigated by GPS, an onboard barometer and an Inertial Measuring Unit (IMU) to determine its inertial speed and the attitude (Euler angles). The endurance is near 60 minutes and the typical speed is between 21 and 24 m s^{-1}, allowing a total flying path of 60 to 70 km. Wind speeds below 12 m s^{-1} and heights below 800 m a.g.l. are recommended for safe operation.

The wind vector is determined at 40 Hz with a 5-hole pitot tube. Accuracies and resolutions for fast wind are 0.5 and 0.05 m s^{-1} whereas for fast temperature the

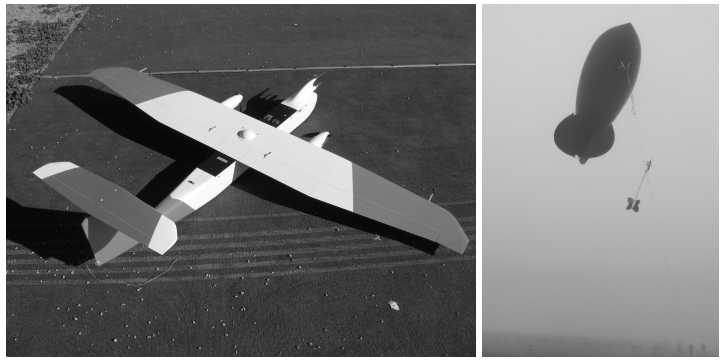

Figure 7.4: (a) M2AV Carolo and (b) Vaisala's Tethersonde and balloon.

accuracy is low (5 K) but the resolution high (less than 0.05 K). This measure is supplemented with a more accurate but slower temperature and humidity sensor. Flights are made on horizontal planes to comply with the requirement of small Euler angles, pursing straight lines long enough to gather a sufficient amount of data to compute significant statistics. The flights were made under different meteorological conditions, including early daytime convective conditions, and daytime and nighttime well-established low-level jets, at an area 1 km to the West of the WindRASS column, outside of the vineyards.

The second special observation period was between noon of July 13th 2010 to 1000 UTC of the next day, with a tethered balloon system, for a day with similar conditions to one year before, when local circulations prevailed. The 3 m^3 Vaisala tethered balloon was equipped with a TTS111 tetherprobe and a 1000 m long tether (Figure 7.4b). It continuously provided vertical profiles of temperature, humidity, pressure and wind speed and direction. Unfortunately, the UAV was not available at this time and direct comparison with the tetherprobe is not possible.

The accuracies of the sensors of the tetherprobe are shown in Table 7.1 and are similar to the UAV, except for the wind speed which is higher. Commonly, the balloon reached altitudes between 450 to 800 m depending on the wind speed aloft. Time series of all parameters are retrieved at about 1 s resolution. Between 0000 and 0200 UTC the balloon could not be lifted because the LLJ had speeds

Figure 7.5: The WindRASS installed in Raimat since July 1st, 2009.

above 12 m s^{-1} which did not allow its operation. The advantages and limitations of the tethered balloon can be found in Moriarty (1993).

7.3 Scintec's WindRASS

The WindRASS (WR) is a new product by Scintec (Figure 7.5) and the installation described here is one of its first scientific uses. This device emits sound waves by a MFAS sodar plus electromagnetic radio waves using two pairs of emitter-receiver antennas. The 1290 MHz electromagnetic radio waves are emitted in five directions: vertical, North, East, South and West. The density variations generated by the sound waves are used by the electromagnetic waves for interaction. The radio waves emitted by one antenna are dispersed in contact with the acoustic ones and captured by a second antenna.

It differs from conventional RASS, for which radio-acoustic sounding is used for temperature measurements only, since here acoustic and electro-magnetic beams can be emitted in vertical and tilted directions. The electromagnetic waves are backscattered at the acoustic waves and the 3 kHz Doppler shift of the reflected radio signal is analysed. The later together with the time travel of the pulse allow to calculate a profile of the speed of sound and from there infer wind and temperature, whereas the length of the pulse determines the spatial resolution.

In this site, the device has been configured to work at a vertical resolution of 10 m and a vertical range from 40 to 360 m to produce vertical profiles every 10 minutes. In the post-processing stage time averages of shorter or larger length can be generated. The range of operation and nominal accuracy of temperature are -50°C to 60 °C and 0.2°C respectively, and for the wind speed 0 to 12 m s^{-1} and 0.5 m s^{-1}, with an estimated accuracy in wind direction of 15°. Its operation is possible in absence of atmospheric turbulence (therefore in clear calm nights) and it is apt for working in foggy or rainy conditions.

The turbulence kinetic energy (TKE) provided by the device is estimated as 1.5 time the standard deviation of the vertical velocity, implying isotropic turbulence, because this measure is trustful since it is directly measured with a vertical beam, whereas the horizontal wind component variances are derived from tilted beams at low tilt angles. The projection factor increases errors and those tilted beam variances also contain contributions of the vertical component which need to be subtracted to obtain the pure horizontal variances. In consequence it is less convenient to use these horizontal wind variances to compute TKE as the half-sum of the three variances as it would seem natural.

Another significant feature of the device is that the profiles obtained usually lose statistical significance as the height increases, because less echoes reach the antennas from the upper part of the height range. Sometimes it is so low (especially with wind speeds above 10 m s^{-1}) that no data are generated. This implies that, when averages of profiles are produced, the values of the upper part are not fully trustful, especially in presence of LLJs. Therefore WindRASS statistics have to be used with caution and comparison with other data sources is compulsory.

In July 2009, nine M2AV selected flights -with 5 or 6 levels each- yield 43 point to point comparisons after neglecting those where the WindRASS had no data. In July 2010, twenty-five tethered balloon soundings filtered to provide vertical profiles with a resolution of 10 m generate 420 point to point comparisons. The statistics of both comparisons are given in Table 7.1. The accuracies stated by the builder are within the limits given by the differences with the balloon probe and the UAV.

Table 7.1: Statistics of the comparison between WindRASS (WR) and UAV (July 2009) and tethered balloon sonde (S) (July 2010). Mean Error (ME), Standard Deviation of the Difference (SDD) and estimated Accuracies (Acc) are indicated.

	ME ± SDD (S-WR)	ME ± SDD (UAV-WR)	Acc S	Acc WR	Acc UAV
Virtual Temperature (K)	(0.7 ± 0.7)	(-0.04 ± 0.78)	0.5	0.2	0.6
Wind Speed (m s^{-1})	(0.5 ± 1.6)	(0.6 ± 1.6)	0.1	1	1
Wind Direction (°)	(24 ± 11)	(16 ± 27)	10	15	15

Figure 7.6a shows the average and the standard deviation of the WindRASS wind profiles for the night 7 to 8 July 2009 and for the last two hours for the virtual temperature. The situation is very steady in direction and there is an increase of the wind speed with height. The UAV flight from 0428 UTC to 0506 UTC confirms the main features but does not show at the moment of the flight a jet below 360 m, which may indicate that the statistics are biased in the upper part. The temperature compare well in value and in vertical gradient, with the largest difference at the upper levels as well.

Figure 7.6b shows the WindRASS average and standard deviation for the period 0240 to 0610 UTC of the night 13 to 14 July 2010, when the flow was sustained from the East in a night with local winds. The same statistics out of seven tether soundings are also shown. The quantitative comparison is difficult, also because of the limitations of the tether sounding, but some qualitative features can be discussed. The balloon indicates clearly the presence of a LLJ with maximum values between 80 and 150 m, whereas the WindRASS average tends to loosen this structure in the upper part of its range. Instead the profiles of wind direction and virtual temperature are very similar with some shift in value. The more remarkable features are the constancy of wind direction with height and the good correspondence between the vertical thermal gradients, particularly the unstable layer between 50 and 100 m (above the surface inversion seen by the balloon probe) probably related to the strong sheared layer below the wind maximum.

As supplementary information, the WindRASS has functioned without significant problems in the presence of fog, even when the cloud deck was deeper than the column sampled by the device. The establishment of the fog, the increase in height of the top inversion, the well defined winds above the cloud and the weakness of the in-deck winds and the existence of episodic turbulence are features also reproduced by numerical simulations, which compare well with the automatic weather station network (Cuxart and Jiménez, 2011).

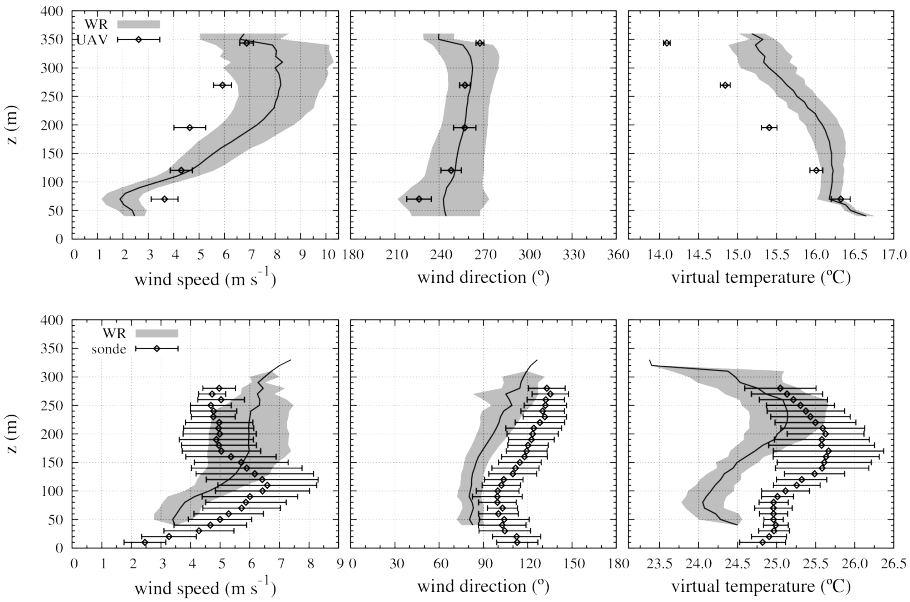

Figure 7.6: (a) WindRASS night averages and standard deviation for the night 7/8 July 2009 for the wind speed (left) and wind direction (center). The virtual temperature corresponds to the last two hours before sunrise. Diamonds and bars correspond to the average and standard deviation of an UAV flight just before sunrise. (b) The same as (a) but the three graphs correspond to the period 0240 to 0610 UTC of 13/14 July 2010. Diamonds and bars correspond to the average and standard deviation of seven tether soundings during the same time interval.

7.4 Within-basin boundary-layer flows

7.4.1 Weak westerly flows: case WEST (7/8 July 2009)

Winds of North-West component are forced along the valley by the topographical barriers of the Pyrenees and the Iberic System, with a flow of varying intensity depending on the synoptic pressure gradient. In the cases of our interest, the pressure gradients and the winds are weak to moderate along the valley. These are the cases closer to the more classical textbook nocturnal ABL, since the

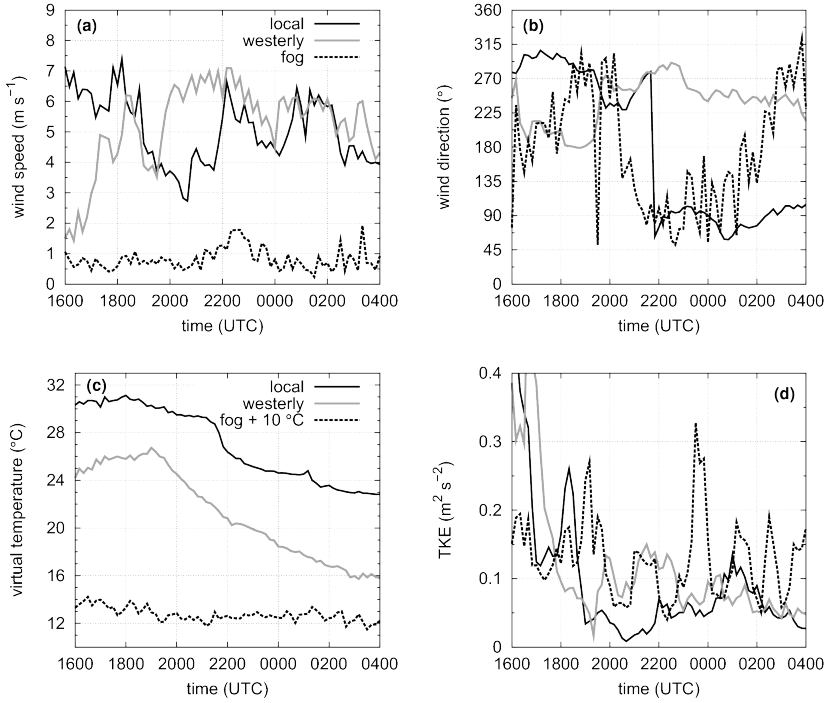

Figure 7.7: Evolution of the vertically integrated profiles for three typical nights of (a) wind speed, (b) wind direction, (c) virtual temperature and (d) estimation of the TKE from 1600 UTC to 0400 UTC. (EAST) 5-6 July 2009, (WEST) 7-8 July 2009 and (FOG) 11-12 December 2009. For the fog case, the virtual temperature is increased 10 °C to clarify the plot.

air mass progresses over a cooler ground and can yield substantial temperature drops during the night. No local flows other than modification by the topography seem to exist, probably because the continuous renewal of air in western flow does not allow the air to get in equilibrium with the underlying surface and prevents the buildup of significant spatial thermal differences. A statistical study of the WindRASS profiles will probably shed light on this point in the future.

A night of the first special observation period (7 to 8 July 2009) is chosen as a good example of this regime. The WindRASS average profiles for the whole night given in Figure 7.6a have been already discussed in the previous section.

The time-height evolution profiles vary very gradually during night and are not shown. Instead, in Figure 7.7 are plotted the evolutions of the vertically averaged values (for a column up to 360 m of depth) of virtual temperature, speed and direction of wind and TKE. The wind speed is sustained around 6 m s^{-1}, above this value before midnight and below it afterwards, with the wind blowing from the West all night. The column-averaged temperature drops about 5 K, very similar to the climatological drop for automatic weather station data at 2 m, indicating that the surface cooling is easily transferred upwards. The regime is weakly turbulent with TKE above 0.1 m^2 s^{-2} before midnight and above 0.05 m^2 s^{-2} afterwards. The time series appear to have relatively smooth evolutions.

7.4.2 Thermal within-basin flows: case EAST (5/6 July 2009)

When there are no well-defined synoptic pressure gradients on the area, winds develop because there are locally generated thermal differences due to the variety of surface conditions. A theoretical development about these circulations can be found in Dalu et al. (1996). A main factor in this basin is the presence of the moist plain located alongside the dry slopes to the East.

The largest heat capacity of the upper wet soil allows morning heating and evening cooling to take place on the plain at a much lower pace than over the slope, therefore amplifying the classical plain-slope diurnal circulation, following the conceptual model provided by the Bjerknes theorem of circulation. This would be a frequent situation between March and October when there is a high pressure system over the area. The sensitivity of the ABL to the soil moisture changes has been shown for the Sahel by Taylor et al. (2007), where flights in the convective ABL above areas where showers had fallen previously where up to the 3 K cooler than those where the surface was drier.

To provide evidence of this phenomenon, we use Land Surface Temperatures (LSTs) obtained from the MODIS (MODerate resolution Imaging Spectroradiometer, Salomonson et al., 1989) instrument aboard the Terra and Aqua satellites, using the slip-window method Coll et al. (2005). Figure 7.8 illustrates the LST fields, corresponding to 1300 and 2200 UTC, just before the strong diurnal and nocturnal circulations start (white areas mean no LST data). The differences between the warm and cool areas are of the order of 8 K both by day and night, meaning that the diurnal cycle in the dry slope is 16 K larger than in the irrigated plain. Images at night are patchy because high clouds related to late afternoon convection to the West are pushed over the area of interest by upper atmosphere winds.

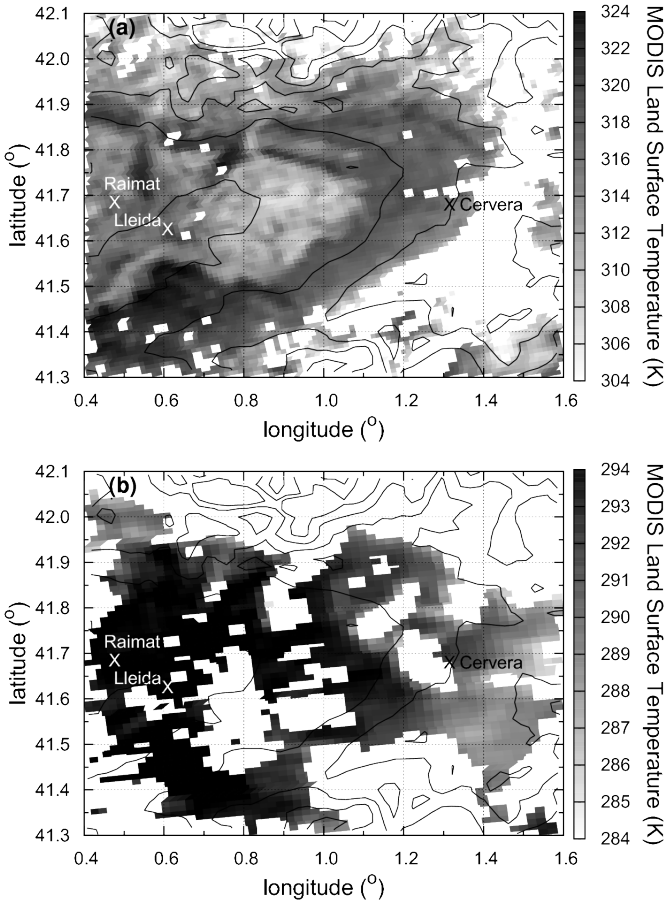

Figure 7.8: Land Surface Temperature provided by MODIS during 5th July 2009 at (a) 1300 UTC and (b) 2200 UTC. The location of Raimat, Lleida and Cervera are indicated and the surface elevation contours are plotted every 200 m. White areas indicate no data.

The data gathered at Raimat point in favour of the just described mechanism. The time series for the 5-6 July in Figure 7.7 show that the wind from the West in the afternoon weakens close to sunset, and a jet from the East is established two hours after sunset. The height-time evolution plots (Figure 7.9) indicate winds close to 10 m s^{-1} in the afternoon and during the central part of the

night with directions consistent with the above rationale, and a sharp transition between regimes. This transition at 2200 UTC also has a strong change of the vertical velocity, with strong negative velocities followed by ascents during the following half hour (averaged column values of -0.6 and 0.2 m s^{-1} before and after the transition). This behaviour would be comparable to the arrival of a deep gravity current and advection of similar conditions afterwards continues progressively weakening. A similar event is described for the Sahel in Bain et al. (2010).

The jet stays in place all night, although it weakens from 0200 UTC on, probably because the thermal forcing progressively diminishes, but the effect of some synoptic forcing cannot be excluded since the high pressure system has a very weak easterly component on the area. The presence of the jet allows the turbulence to be relatively active during the night, preventing the formation of strong surface-rooted inversions. Data from the EBS (not shown) indicate that cooling is carried out by radiation and evaporation whereas the ground heat flux and the turbulent mixing of sensible heat flux warm the air layer close to the ground.

The application of the Bjerknes theorem of circulation C -keeping only the solenoidal term- to an area where there is a discontinuity (like a transition dry-irrigated terrain) is expressed as (Holton, 1972, Chapter 4)

$$\frac{dC}{dt} = -\oint RTd(ln\, p) \tag{7.1}$$

which, integrated along a circuit that goes from the dry terrain over the slopes to the moist plain a distance L following an isobar p_0, is raised to a height h at T_m constant, way back at about p_0 - 100 hPa and close the circuit vertically at a constant T_d, yields for the average tangential velocity $V=C/(2(L+h))$, with the typical values for our area of interest (h = 500 m, L = 50 km, T_m -T_d = 8 K, p_0 = 1000 hPa, p_1 = 900 hPa)

$$\frac{dV}{dt} = \frac{R\, ln(p_0/p_1)}{2(h+L)}(T_m - T_d) \tag{7.2}$$

The resulting acceleration (2 * 10^{-3} m s^{-2}), in steady conditions, would take about 5000 s to develop a velocity of 10 m s^{-1} from calm conditions, which is comparable to what is observed by the WindRASS and the satellite images.

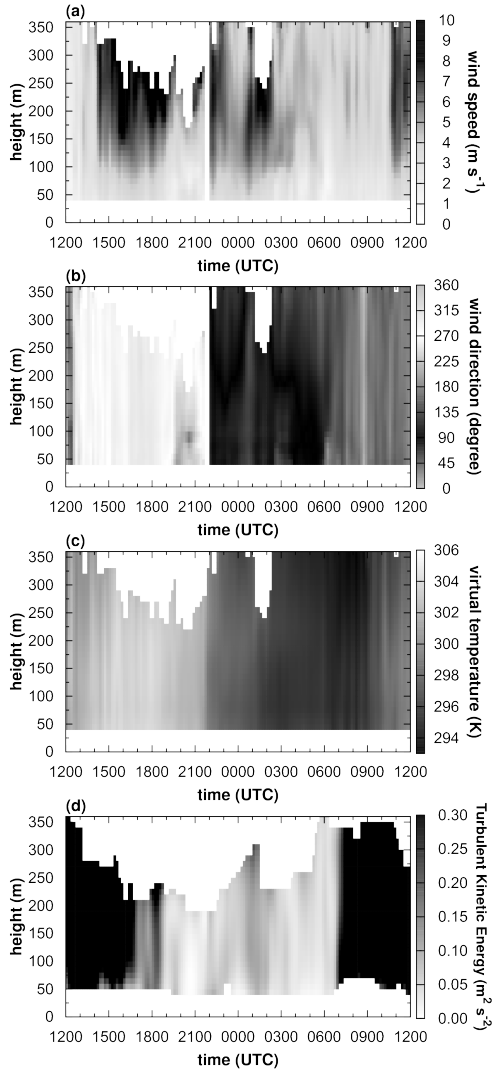

Figure 7.9: Temporal evolution of the WindRASS profiles of (a) wind speed, (b) wind direction, (c) virtual temperature and (d) estimation of the TKE for the night 5/6 July 2009, with local circulations.

7.4.3 Winter circulation and radiation Fog: case FOG (9/13 December 2009)

Similar synoptic patterns in the winter produce a different evolution. On one hand, there is no irrigation during this season and the soil response to the radiation forcings is closer between the plain and the slopes than in the summertime, with lesser thermal differences between both areas and weaker jets. On the other hand, long nights allow the establishment of radiation fog, usually after one first clear night when the high-pressure system establishes on the area. The clear nights allow the development of katabatic flows and cold pools. Once the fog established, the basin dynamics change drastically. The fog part of this case is extensively studied using all the available data (WindRASS included) and a high resolution numerical simulation in Cuxart and Jiménez (2011).

The case from 9-13 December 2009 illustrates this evolution. The night 9-10 is the first under a high-pressure system. The WindRASS and the automatic weather station network indicate that the evolution of the wind direction is very similar to the summertime one (not shown, West before sunset, switching to East in the evening), but the values of the wind are much weaker (around 3 m s^{-1}) and the wind maximum is located at a lower height (at about 150 m a.g.l.). The automatic weather station in the area indicate that the wind direction at night follows the local slope, therefore allowing us to expect katabatic winds.

The temperature evolution of three weather stations is shown in Figure 7.10a, one at the edge of the fog layer (Cervera) and the other two well inside - Poal and Raimat, where the WindRASS is. It indicates how the situation gradually evolves from a diurnal cycle with clear skies to the disappearance of the diurnal cycle due to persistent fog. The night 9-10 is clear and the drop of temperature at the automatic weather station ends with the sunrise, about 0730 UTC. On the contrary, the night 10 to 11 sees the establishment of fog at around midnight, when the temperature starts to increase - humidity is close to 100 % and there are human reports of fog that night in the area. The subsequent evolution of the temperature indicates that the diurnal cycle is cut except at the station at the edge, which is over the slopes and it is only some of the time under fog. The area covered by fog is displayed in Figure 7.10b and coincides with all the bottom part of the basin, about 20000 km^2.

The WindRASS observations (Figures 7.6 and 7.10a) are able to capture these features. The device indicates very weak wind and absence of diurnal cycle in the whole column, with intermittent turbulence (stronger than for the local and westerly cases), probably by radiative and evaporative cooling at the fog top. The evolution of the temperature in the WindRASS at 40 and 250 m shows how the fog progresses upwards and takes almost 6 hours to develop between these

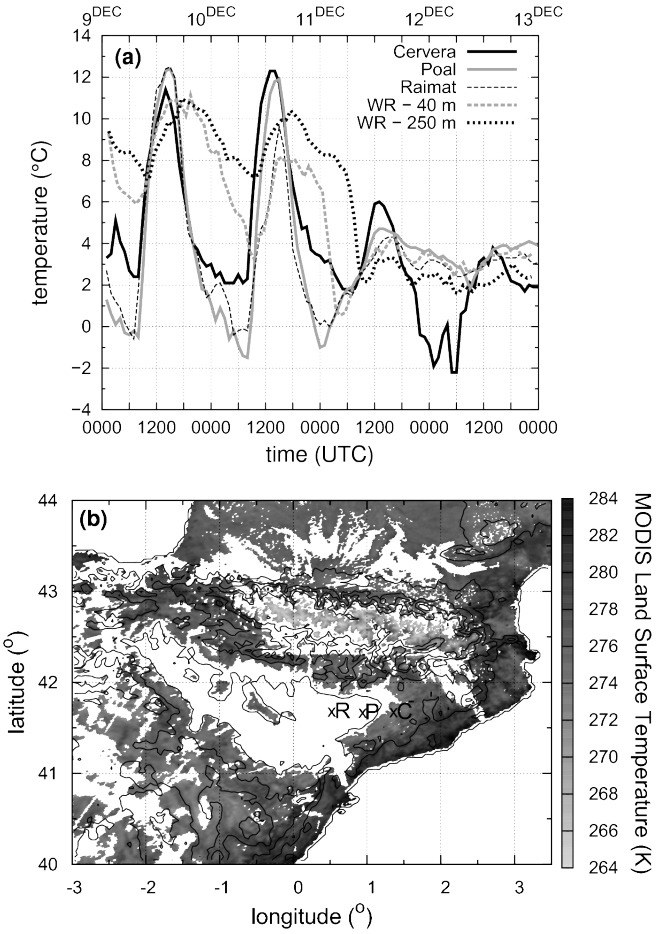

Figure 7.10: (a) Temperature evolution for three automatic weather stations in the area during a winter clear skies night followed by a persistent fog event (from 9 to 13 December 2009). Evolution of temperature at 40 and 250 m above ground for the WindRASS are also included. (b) Land Surface Temperature derived from MODIS for the Ebro basin indicating (in white) the area covered by fog and the three locations (R: Raimat, P: El Poal, C: Cervera) during 11th December 2009 at 2140 UTC. The surface elevation contours are plotted every 400 m.

two levels. This moderate intermittent turbulence when the fog is set contrasts with the absence of any significant turbulence during the stable night before the fog was established. This is an ABL regime practically decoupled from the rest of the basin, with a well mixed thermodynamic structure and that is usually taken away only by the arrival of a new airmass.

7.5 Summary

The study for a practically closed basin with a well defined slope at its eastern end and an irrigated bottom plain has allowed us to investigate the within-basin dynamics when the ABL processes are predominant. The majority of this time is linked to a high-pressure system over the area, driven by well defined plain-slope circulation between spring and early autumn, and by katabatic flows and oftentimes thick persistent fogs in the wintertime. The rest of the ABL-driven regimes are linked to weak westerlies, associated with the largest nocturnal temperature drops.

Spring to early autumn within-basin thermal flows are driven by the conjunction of the well-known difference of heating between the plain and the slopes, but reinforced in this case by the irrigation in the plain, that allows that the temperature gradients become larger than for dry zones and circulations stronger. Night-time downslope jets at a height near 200 m above the level of the basin bottom are found routinely. These structures are moderately turbulent and do not allow the establishment of strong ground-rooted temperature inversions over the basin.

In the winter time, the plain is not irrigated and the thermal contrast between plain and slope is very small. Katabatic flows develop downslope but, very often, radiation fog is formed soon after over the whole basin bottom. The dynamics in the cloud layer are decoupled from the upper circulation, although the layer is well mixed by turbulence at the cloud top by radiative and evaporative cooling and wind shear. There is little hint of the diurnal cycle although the sun usually manages to reach the ground around noon.

These mesobeta scale circulations seem to be climatological features of the area and have to be taken into account in the description of moderately complex terrain. The present cases have been mostly studied using observational information, namely the automatic weather station network in the area and the Scintec WindRASS in Raimat belonging to SMC, together with information from satellite imagery. The WindRASS has shown very good performance in all the types of weather and all the comparisons made with airborne and captive balloon

data show qualitative good agreement, but further quantitative comparisons are necessary.

Acknowledgements

Mr. Armando Álvarez is acknowledged by his continuous local support. Damià Gomila, Hugo García and Margalida Riutort for their participation in the operation of M2AV. José Ignacio Roselló for his guidance in the operation of the tethered balloon. Francesc Torrens, manager of the Finca Montserrat property in Raimat, for his willingness to let us operate there. Antonio Gázquez (SMC) for his general support and Niels Thiermann (Scintec) for the technical support.

Work funded by SMC together with grants of the Spanish Government CGL2009-12797-C03-01 and BES-2007-16272 for UIB and CGL2007-65359/CLI and CSD2007-00067-CONSOLIDER-INGENIO-2010 for CEAM.

Data from MODIS are distributed by the Land Processes Distributed Active Archieve Center (LPDAAC), located at the U.S. Geological Survey (USGS) Earth Resources Observation and Science (EROS) Center (lpdaac.usgs.gov).

Chapter 8

General Conclusions

This thesis has explored the low-level currents generated under stable conditions over complex terrain. Inhomogeneities in the topography forces a spatial distribution of the temperature at the surface and in overlying air, producing coherent structures like gravity currents and valley winds. Major efforts have been put therefore on the role of topography in the generation and organisation of local currents at a basin scale, looking to the interactions among them and with larger scale flows as well as to the thermal patterns generated over land.

The study has been made for four mid-latitude domains, three in the western Mediterranean area, and one in the North American Colorado plateau. These areas consist in well defined hydrological basins, where mesoscale organisation takes place and determines the evolution of the stably stratified boundary layer (SBL). The dynamics of the local currents have been analysed at multiple scales, identifying the related topographic features and the largest scales that must be considered for every site.

For the island of Majorca and the Duero basin studies, mesoscale simulations with a high spatial resolution have been performed for some selected winter nights. The model outputs have provided a first approach about the wind and temperature patterns developed under stably stratified conditions. These results have been validated against all the available observations provided by satellite imagery, the automatic weather stations (AWS) network and, for the Duero basin case, the CIBA tower (see Section 1.5).

The dynamics in the Ebro valley and the Meteor crater, on the contrary, have been addressed primarily using experimental data. The METCRAX 2006 experiment provided a suitable dataset to address the slope flow evening transition in the crater sidewall. In the case of the Ebro basin, an effort to extract all the avail-

able information from the observations was done. The resulting preliminary conclusions were further explored by *ad hoc* measurement campaigns under the framework of Lleida Basin Flow (LBF) experiments.

SBL evolution

The evening transition is characterised by an initial rapid evolution of the boundary layer variables around sunset (the so called early evening transition), when the air close to the ground adjusts to the progressively cooled surface. The fast decay of the temperature is a common feature for both simulations and observations and it is found at multiple scales. The statistical study of an AWS for stable nights shows the largest cooling rate during the first hour after sunset and a progressive decrease for the rest of the night (Chapter 6). A similar behaviour is detected when the basin averaged surface and 1.5-m air temperature are analysed (Chapter 3). During the early evening transition, the time evolution of mean quantities depends on the local features (Section 1.2.3), generating horizontal differences of temperature and humidity throughout the basin. These patterns have been clearly observed by satellite images and confirmed by mesoscale simulations (Jiménez et al., 2008, Chapter 3).

Low-level currents start to develop after sunset due to the heterogeneous distribution of temperature, initialising a period in which the flow organises at multiple levels. Katabatic winds form over the slopes, merging with larger scale currents at the foot of the slopes. This process lasts several hours until a steady wind pattern for the whole basin is set for the second part of the night. During the stationary phase, the low-level winds progressively weaken until sunrise.

During the whole night, the SBL is subject to transient periods that can be related to a specific topographic feature. For instance, sudden changes in the wind direction and speed can be attributed to the arrival of a drainage current to the site.

Cold air accumulates in stagnant areas that are sheltered by elevated surrounding topography, allowing for the buildup of a temperature inversion. The topographical configuration protects the cold-air pools from the influence of the low-level currents, while the strong stability makes difficult the air mixing with the warmer layer aloft. Thus, these areas are prone to develop very low temperatures by the end of the night, contributing to the thermal heterogeneity pattern throughout the zone (Chapter 3). Due to the stagnation of air, they are also responsible for pollution and fog formation, specially in winter (Chapter 7).

Wide flat areas not topographically sheltered are subject to a strong radiative surface cooling generating also a large thermally stable layer close to the ground.

Such cooling is strong enough to compensate for eventual warming episodes through air mixing generated by the presence of drainage currents. This is the case for the elevated plateau in the centre of the Duero basin, where the surface temperature is lower than the basin-averaged one (Chapter 3).

Basin scale

In Majorca (Chapter 2) the flow is organised at different scales. In the case of weak ambient flow, it interacts with the island topography, generating a high pressure area over land. Next, drainage currents are developed over slopes and within valleys, converging to the centre of the three main basins of the island. Colder air accumulates over the low-lying areas of the basin floors, where the air temperature decreases at a faster rate due to the radiative cooling of the underlying surface. This air is finally expelled into the sea due to the horizontal thermal gradients between the sea and basin atmospheres. The resulting dynamics depicts a complex nocturnal wind system that couples the land-sea breeze with the slope and basin currents.

For the Duero case (Chapter 3), the mesoscale simulation shows the generation of drainage currents over mountain sidewalls, flowing downslope to the basin floor. These flows travel long distances and can reach the centre of the basin several hours after sunset, alternating their arrival at the CIBA site from different directions (Cuxart, 2008; Viana et al., 2010). To reach the tower, drainage winds must overcome the river depression that surrounds the plateau where the CIBA site is installed. Low-level currents may be ubiquitous during the steady state period and take the form of a low-level jet (LLJ) with a maximum wind speed below 100 m AGL over the 50% of the basin area. The presence of jets generates mechanical turbulence close to the ground, arising as the driven cooling mechanism at the lower layers.

The study of the Ebro valley (Chapters 6 and 7), of a similar scale than the Duero one but with a different shape, has led to identify two different large topographic regions: the main valley axis and the quasi-enclosed, wide sub-basin at the eastern part (the Lleida basin). Under stable conditions, the influence of each of these topographies depends on the regional-scale pressure configuration. With the presence of a high pressure area over the site, circulations driven by local surrounding topography appear and the largest length scale to be considered is the eastern sub-basin scale. That is the plain plus the wide, homogeneous and gentle slope located at the east. The slope-plain circulation organises the flow and local irregularities modulate the currents at lower levels. However, when the synoptic pressure gradient leads to weak westerly winds, the air is channelised along the

main valley axis, overcoming local circulations and organising the flow at the whole Ebro basin scale. These two different wind patterns deduced from the analysis of a single AWS (Chapter 6) and the WindRass measurements (Chapter 7) have been confirmed afterwards by mesoscale simulations (not shown in the present thesis) and by extending the analysis of the single weather station to the rest of the network (Cuxart et al., 2009).

The case of the meteor crater in Arizona (Chapter 5) differs from the rest of the studied sites because of its smaller scale and less complexity. For this basin, the relevant largest length scale is the crater size, conditioning the evening transition. However, it is common to find air intrusions into the crater due to the development or a large-scale katabatic current over the flat and homogeneous tilted surface that surrounds the enclosed basin (Whiteman et al., 2010; Savage et al., 2008).

Slope scale

Mesoscale simulations have also been used to analyse in detail the main characteristics of two particular katabatic flows generated in Majorca (Chapter 2) and Duero basin (Chapter 4). Although both topographic configurations are different, it is possible to extract some common conclusions.

In both cases, the katabatic flow is subject to external influences since it is embedded in the mesoscale wind system described above. Therefore, they develop smoothly after sunset and reach a steady state during the second part of the night. Other particular influences for the Majorca case are the cold air accumulation at the end of the slope and the land-sea breeze circulation, perpendicular to the downslope axis. In the Duero basin, although the selected slope is far enough from the influence of the basin dynamics at the centre, it contains local irregularities like cross-slope gullies and small hills.

Changes in the slope inclination have an effect on their vertical structure, locating the maximum of the wind speed closer to the ground at the steeper parts of the slope. The case in Majorca shows a relation between several katabatic layer variables. The points along the slope with lower velocities deal to lower temperatures and smaller surface turbulent fluxes probably caused by a decrease in the wind shear. This relationship is not observed in the Duero case since a shallow cold layer with a strong temperature inversion builds up within the small gullies present along the slope. In these regions, turbulence is inhibited close to the surface and the katabatic wind is displaced upwards, overflowing the cold air layer with relevant wind speeds.

The distinct scales of the mountains that held the studied katabatic flows lead to different interactions between the drainage current and the ambient wind. In Majorca, the mountain hill displaces the ambient flow upwards, generating gravity waves at the lee side of the hill, where the katabatic wind is developed. These waves give to the katabatic flow an oscillatory behaviour along the slope. On the contrary, the mountain range in the Duero basin is much higher, sheltering the katabatic layer from the ambient wind influence. This configuration may be an explanation for the different time evolution of the air temperature close to the sloping surfaces. In Majorca, it remains constant at the upper part of the slope, while in the Duero slope the air is cooled continuously throughout the night. For the first case, the denser air that flows downslope has to be continuously replaced by the ambient air and the sloping surface would not have enough time to progressively cool the overlying air. In the Duero situation, the air over the slope is replaced by low-level upwind air that has been also in contact with the underlying surface at upper elevations.

Another common feature for both cases is the lack of entrainment at the upper part of the katabatic layer. Turbulence, when present, seems to appear only at the surface. Contrarily, turbulent fluxes at the upper levels are sporadic and very weak. From the simulations, then, the exchange of heat and mass through the katabatic layer plays a secondary role. Even during the elevated turbulence episodes, the air is only mixed at the upper part, warming the entrainment zone but not the whole katabatic layer. This effect would enhance the buoyancy force since the temperature deficit between the katabatic current and the ambient air increases (Chapter 4). Experimental evidences are needed in order to confirm the simulation results.

The application of the hydraulic two-layer model to reproduce the katabatic wind dynamics in the form of a bulk layer is subject to several drawbacks. First, the budget momentum and heat equations do not close in their bulk version. In Chapter 4, it is speculated that the main reason is the reduction of the katabatic wind to a two dimensional problem. Over real topography, three-dimensional effects have to be considered in order to close the equation budgets. Secondly, the interaction of the katabatic flow with larger phenomena alters the prognostic equations of the hydraulic model (Chapter 2).

The behaviour of the downslope current over the sidewall of an enclosed small basin can differ significantly of the previous two cases. In the Meteor Crater (Chapter 5), the studied katabatic flow on the west sidewall starts well before the astronomical sunset, as soon as the terrain becomes shaded by the crater rim. The onset of the downslope current can be very fast, with a reverse from upslope to downslope flow occurring in less than one hour, with a transition period characterised by intermittent changes back to upslope directions before

becoming steady. Since the development of the gravity current takes place within a context where convective motions are still present in the sunny part of the crater, a similar evening transition could be expected in those sheltered places where shadow arrives first. Like in the Meteor crater, downslope currents may not start until larger scale flows lose energy as a consequence of the extinction of the surface sensible heat.

Suggestions for further work

Under stable conditions, numerical simulations strongly depend on the parametrisations implemented in the model, like radiation, surface or turbulence schemes. For instance, difficulties to adequately treat the surface layer might produce incorrect representations of the real physical processes.

Complementary information, then, is provided by satellite images by means of the derived land surface temperature (LST). This two-dimensional field can be directly compared with the simulation output to check the reliability of the simulation. However, such comparison present also difficulties since surface temperatures depend on the surface energy budget which, in turn, depends on many factors (water content in soil, albedo, surface heterogeneity, see Chapter 1). Most of these elements are parametrised in the model. For the case of the physiographic fields like soil uses, surface water content or vegetation index, climatological values are used despite that surface conditions for a single night can be far away from their climatological fields.

From the perspective of improving mesoscale simulation results, specific efforts should be focused in the surface parametrisation. One first step could be changing the climatological values by observed daily fields and inspect the sensitivity of the runs to these changes.

The observations from the satellite imagery are also subject of important errors. For instance, the estimated LST is sensitive to changes in the emissivity overnight (very important in case of frost formation) or to the water vapour content in the atmosphere (for the Meteosat images). These problems were exposed as possible causes for the discrepancies observed in the temporal evolution of the basin-averaged surface temperature between the Meteosat-7 and simulation results (Chapter 3). Further comparisons with the Meteosat Second Generation (MSG) satellites, with significant improvements in the LST estimations and temporal resolution, are expected to clarify which are the reasons for the differences shown in Figure 3.5a.

Similarly, the use of satellite images can be put forward in order to get more information. Attempts to relate the surface temperature field with the wind

close to the surface have to be addressed systematically, in the line started in Chapter 2, where the oscillatory signal of wind speed was matched with surface cooling rates. This technique was first proposed by Bromwich (1989) who used a warm signature on winter thermal infrared NOAA images to detect the presence of katabatic flows in polar regions.

The statistical study of long time series from a single AWS presented in Chapter 6 provided robustness to the characterisation of the flow close to the surface in the eastern part of the Ebro basin, despite of the documented limitations in the wind measurements. Such analysis has been preliminary extended to the rest of the AWS network and further research is contemplated by applying the analysis cluster and empirical orthogonal function (EOF) techniques, with the objective to climatically characterised the nocturnal wind system of the basin (Kaufmann and Weber, 1998).

In addition, the progressive substitution of the classical wind cup anemometers for the 2D sonic anemometers in the AWS networks will improve the information of the surface wind field. Sonic anemometers have a minimum threshold of the measurable wind much lower than the former sensors and are able to probe the light winds close to the surface under stable conditions.

The use of the meteorological unmanned aerial vehicle M^2AV during the LBF experiment has shown us that it is a suitable device for the study of the NBL regime for several reasons. First, under these atmospheric conditions, wind speed is usually below the maximum values recommended for its operation. Second, the size of the eddies for stable conditions are smaller than for the CBL regime, requiring shorter straight legs for the flight pattern in order to compute adequate statistics with the airborne data. Finally, most of the relevant phenomena occur within the first 300 m above ground, a layer very difficult to cover by a manned aircraft.

Data recorded by the M^2AV is still pending to be fully analysed but their *in situ* measurements of the current at different levels -including above the wind maximum of the LLJ- have provided unique information from these flows, usually with a depth larger than the height of the actual tower measurements. With this dataset, turbulence structure above the maximum jet can be explored.

Open questions

The classification of the vertical wind profiles done for the simulation outputs in the Duero basin (Chapter 3) has shown a statistical relationship between the height and the strength of the maximum wind speed, although a theoretical explanation is not yet available. Related to this issue, simulated katabatic currents

have the maximum of the wind speed normally below 50 m AGL, while for most of the observed LLJs in the CIBA site (Duero basin) this height is between 50 and 100 m. The LBF experiments show that this maximum is even higher for the Ebro basin flow. With these experimental results, it is compulsory to wonder whether there is a relationship between the depth of a low-level current and the scale of the topographical configuration that originates it.

In the observations exposed in this thesis, the wind speed diminishes throughout the night as the temperature cooling rate also decreases. These results coincide with most of the observations done all around the world. Temperature advection driven by horizontal motions may reduce thermal differences within the basin, reducing the baroclinity and, in consequence, the driving force of the low-level currents. This hypothesis should be checked in the following years.

For the two mesoscale simulations described, the organisation of the flow within a basin takes several hours until the system of winds reaches a steady state. An interesting question arises about the existence of a time scale related with the organisation of this mesoscale flow and whether this time scale is related with the largest length scale of the topographic configuration.

Finally, the amount of moisture, energy and momentum in a selected location advected by low-level currents in a basin would be interesting to determine defining specific experiments. This type of estimations could be carried out by computing their horizontal fluxes.

Chapter 9

List of publications

Publications related to this thesis:

- Martínez, D., C. D. Whiteman, S. Hoch, M. Lehner, and J. Cuxart, 2011: The upslope-dowslope flow transition on a basin sidewall. To be submitted to *J. Appl. Meteor. Climatol.*
- Cuxart, J., J. Cunillera, M. A. Jiménez, D. Martínez, F. Molinos, and J. L. Palau, 2011: Study of mesobeta basin flows by remote sensing. Submitted to *Bound.-Layer Meteorol.*
- Martínez, D., M. A. Jiménez, J. Cuxart, and L. Mahrt, 2010: Heterogeneous nocturnal cooling in a large basin under very stable conditions. *Bound.-Layer Meteorol.*, **137**, 97–113.
- Martínez, D., and J. Cuxart, 2009: Assessment of the hydraulic slope flow approach using a mesoscale model. *Acta Geophys.*, **57**, 882–903.
- Martínez, D, J. Cuxart, and J. Cunillera, 2008: Conditioned climatology for stably stratified nights in the Lleida area. *Tethys*, **5**, 13–24.
- Cuxart, J., M. A. Jiménez, and D. Martínez, 2007: Nocturnal meso-beta basin and katabatic flows on a midlatitude island. *Mon. Wea. Rev.*, **135**, 918–932.
- Martínez, D., and J. Cuxart, 2007: A gravity current study within the Palma de Mallorca basin. *Física de la Tierra*, **19**, 21–36.
- Jiménez, M. A., J. Cuxart, A. Mira, and D. Martínez, 2006: Local nocturnal circulations in the island of Majorca: mesoscale modelling and verification. *Tethys*, **3**, 67–73.

CHAPTER 9. LIST OF PUBLICATIONS

Publications in proceedings:

- Martínez, D., J. Cuxart, and M. A. Jiménez, 2006: Katabatic wind over gentle slope on the Majorca island. *17th Symposium on Boundary Layers and Turbulence*, 22–27 May, San Diego.

List of Tables

2.1 Summary of the setup of the run 41

2.2 Values used for the parameters present in analytical simple solution for downslope momentum equation in the case of a shooting flow. 57

3.1 Percentage of the cases for the classification of the points at 0000 UTC according to the wind maxima (up to 100 m) and the temperature gradient $\Delta\theta = \theta_{10.5m} - \theta_{1.5m}$). 76

5.1 Meteorological measurement equipment at the ISFF towers. . . . 111

6.1 Number of stable nights in the 9 year series for each season (left) and percentages regarding the total number of nights of the time series (center) and regarding the season (right). 143

7.1 Statistics of the comparison between WindRASS and UAV (July 2009) and tethered balloon sonde (July 2010). 160

List of Figures

1.1 Schematic illustration of the surface radiation and energy budgets for a flat and homogeneous surface. 5

1.2 Relationship between energy storage in a volume ΔQ_s and (a) vertical flux convergence, (b) vertical flux divergence and (c) horizontal flux divergence. 8

1.3 Vertical temperature profiles in a small and large basin. 11

1.4 Diurnal mountain wind system in (a) daytime and (b) nighttime. 14

1.5 Diurnal cycle of the ABL in a valley considering valley and mountain-plain circulations. 16

1.6 Illustration of the thermal forcing of valley-plain pressure gradients leading to the development of an along-valley wind system. 17

1.7 Sketch of a quasi-steady katabatic current on an idealised topography. 20

2.1 The island of Majorca, with the three well defined basins: Palma, Alcudia and Campos. 38

2.2 Stream lines at 0400 UTC at different heights: (a) 1000 m; (b) 100 m and (c) 10 m. (d) The vertical stream lines following line **A** in Figure 2.1 42

2.3 Horizontal cross sections at 0400 UTC for (a) wind direction (degrees) at 10 m, (b) wind speed (m s^{-1}) at 10 m and (c) potential temperature (K) at 1.5 m. 43

2.4 Modelled and observed time series for (a) wind speed, (b) wind direction and (c) temperature at an inland and a coast sites 44

2.5 (a) Stream lines at 10 m and (b) potential temperature at 1.5 m at 0400 UTC in the Palma basin. Values of the surface weather stations are also shown in (b). 46

2.6 Vertical cross-section at 0400 UTC following line **D** in Figure 2.1 for the (a) wind speed (m s^{-1}) and (b) potential temperature (K). The same for (c) and (d) but following the line **C** in Figure 2.1. . . 47

2.7 The same as Figure 2.6 but following the line **B** in Figure 2.1. . . . 48

2.8 (a) Wind velocity (m s^{-1}) and (b) potential temperature (K) profiles every hour during the night at one point in km.9 (see Figure 2.9 for location). 49

2.9 Mean parameters for the katabatic-layer along the slope following the line Randa-Airport in Figure 2.1 for two different periods of the night: 1900-2000 UTC and 0200-0400 UTC. 52

2.10 Vertical stream lines at the Randa mountain (Figure 2.1) following the direction of the synoptic wind at different times: (a) 1900 UTC, (b) 2300 UTC and (c) 0300 UTC. 54

2.11 The same as Figure 2.9 but for the forcing terms from the downslope momentum equation (m s^{-2}) at (a) 1900-2000 UTC and (b) 0200-0400 UTC. 56

2.12 Solution for the downslope momentum equation (2.3) in the simple case of a *shooting flow* assuming constant h_k for points over slope where buoyancy term is dominant. 58

2.13 Surface cooling obtained from the model and the available NOAA satellite images computed with the model radiative temperatures at 1900 UTC and 0400 UTC, and the images at 1846 and 0405 UTC [$\Delta T = T_{rad}(0400UTC) - T_{rad}(1900UTC)$]. 59

3.1 (a) Topography (in m) of the centre of the Duero basin and simulated streamlines at 50-m height at 0200 UTC. The locations of 4 automatic weather stations from AEMET and the 100-m tower in the CIBA are displayed. (b) 1.5-m temperature (in K) and streamlines at 0200 UTC. 63

3.2 Time series measured by the CIBA tower compared to those obtained from mesoscale runs for (a) and (b) wind speed, (c) and (d) wind direction, (e) and (f) temperature and (g) and (h) TKE at (left) 10 m a.g.l. and (right) 100 m a.g.l. 67

3.3 Time evolution of the temperature at the top of the tower and at 1.5 m a.g.l. for Olmedo (x12), Valladolid (x09) and the CIBA site (a) measured and (b) simulated. See Figure 3.1 for locations. Bold vertical lines indicate the sunrise and sunset times. 69

3.4 (a) Mean nocturnal temperature $\overline{T}_b(\mathbf{x})$ for the Duero basin derived from Meteosat-7 (without the snow area). (b) Total cooling from the beginning of the night (1730 UTC) to just before sunrise (0730 UTC). 72

3.5 (a) Basin-averaged deviation of the radiative surface temperature from the mean nocturnal temperature $\overline{\overline{T}}_b(t)$ between sunset and sunrise from the mesoscale simulation and from the satellite data. (b) The same as (a), but for the 1.5-m temperature with the observations taken from the automatic weather stations. 74

3.6 Location of the points corresponding to the categories in Table 3.1. (a) Classification according to the wind maxima up to 100 m a.g.l. (b) The same as in (a), but for the classification according to the strength of stratification in the surface layer. 77

3.7 (a) Averaged wind speed profiles of the classified categories according to the wind maxima classification in Table 3.1. (b) Averaged temperature profiles for the categories in Table 3.1 based on the strength of stratification in the surface layer. 79

3.8 Averaged profiles of (a) radiative and (b) turbulent coolings for the categories in Table 3.1 based on the strength of stratification in the surface layer shown in Figure 3.7b. 81

4.1 Domain of the run corresponding to the Duero basin, indicating the selected area for the katabatic wind study. 85

4.2 Area of the Duero basin selected to study the katabatic wind generated by the simulation (zoom of the square in Figure 4.1), with the topography in m as seen by the model and horizontal wind vectors at 40 m AGL at 0200 UTC. 87

4.3 The same as in Figure 4.2 but for the (a) wind speed (m s^{-1}) and (b) potential temperature (K). 89

4.4 Vertical cross section at 0200 UTC following the line in Figure 4.2 for the (a) wind speed (m s^{-1}) and (b) potential temperature (K). . 90

4.5 Topographic cross-section of the studied slope along the bold line in Figure 4.2, showing the location of the two points of interest. . 91

4.6 Vertical profiles for (a) along slope velocity (m s^{-1}), (b) cross-slope velocity (m s^{-1}), (c) potential temperature (K), (d) TKE (m^2 s^{-2}) and (e) kinematic flux of latent heat (K m s^{-1}) for the output of the mesoscale model (dashed line) and the result after applying the hydraulic approach (bold line) for point u (Figure 4.5) at 0000 UTC. 96

4.7 Time evolution of the bulk parameters for the nocturnal period 1800-0600 UTC using a steady katabatic layer depth of 125.4 m AGL for the two points indicated in Figure 4.5. Katabatic-layer velocities (m s^{-1}) in the (a) along slope direction, (b) cross-slope direction and (c) slope-relative vertical direction and (d) potential temperature (K) of both the katabatic-layer θ and the upper layer θ_0. 98

4.8 The same as in Figure 4.7 but for the kinematic fluxes of (a) momentum (m^2 s^{-2}) and (b) latent heat (K m s^{-1}) at the surface and at the katabatic layer height. 100

4.9 The same as in Figure 4.7 but for the forcing terms of the budget bulk equations for momentum (m s^{-2}) at the points (a) u and (b) d and heat (K s^{-1}) at the points (c) u and (d) d in Figure 4.5. 102

4.10 The same as in Figure 4.9 but for the conservation of mass bulk equation (s^{-1}) at the points (a) u and (b) d in Figure 4.5. 103

5.1 Aerial photograph of Meteor Crater from southeast. (@John S. Shelton, used with permission). 107

5.2 (a) Universal Transverse Mercator zone 12S map of Meteor Crater and its surroundings. (b) Topographic cross section of the crater showing the locations of WU, WL and FLR. 110

5.3 Modeled propagation of shadows and extraterrestrial insolation across the Meteor Crater on October 15 at different times of day (MST). Shades of gray are radiation intensity, with black indicating 0 and white indicating 1364 W m^{-2}. 112

5.4 Tethered balloon potential temperature soundings from the western sidewall (black solid), crater floor (gray solid) and eastern sidewall (black dashed) from 1500 to 1931 MST. 113

5.5 Photographs of the dispersion of smoke from 3-minute-duration releases on the west slope of Meteor Crater started at (a) 1510, (b) 1530, and (c) 1550 MST on 20 October 2006, as photographed from a point on the crater floor northeast of the smoke release. (d) The same as in (c) but photograph taken from the foot of the east sidewall. The WU and WL towers can be seen in the photos. . . . 115

5.6 Meteorograms from the WU (left) and WL (right) towers for the evening transition period of 20 October 2006. (a-b) Radiation budget components, (c-d) surface energy budget components, (e-f) potential temperature, (g-h) wind speed and (i-j) wind direction at different levels of the towers. 117

5.7 Time evolution of (a) wind speed, (b) wind direction and (c) local potential temperature for the WU, WL and FLR sites. Wind and temperature data correspond to 30-sec and 1-min averages, respectively. 120

5.8 Time evolution of kinetic energy per unit period at 5-m height computed from the wavelet transform of the wind components at WU. 121

5.9 Time evolution of the contribution to kinetic energy (KE) at 5-m height of small periods (up to 5 minutes), and of larger periods for the (a) WU, (b) WL and (c) FLR sites. 122

5.10 Time evolution of the bulk (a) along-slope momentum flux (negative values indicate upslope flow), (b) cross-slope momentum flux and (c) buoyancy deficit for WU and WL sites during the upslope-downslope flow transition. 125

6.1 Location of the Gimenells AWS in the Ebro basin. 133

6.2 (a) Daily cycle of the average temperature (°C) and (b) relative humidity (%) for all four seasons calculated from the time series registered in the Gimenells AWS in the period 1997-2005. 135

6.3 Frequency distribution (%) of wind direction (°) for the seasons of (a) summer, (b) fall, (c) winter, and (d) spring, calculated from the time series registered in the Gimenells AWS in the period 1997-2005. 138

6.4 Wind rose for all (a) nights, and (b) stable nights according to the criteria defined in the text (Expression 6.4). 140

6.5 Average wind speed (m s^{-1}) regarding the direction (°) (black) and frequencies distribution (%) of the wind direction (gray) for the (a) first, (b) third, (c) seventh and (d) tenth night hours. 142

6.6 Same as Figure 6.5 but with stable nights gathered in three different subgroups, according to wind direction during the third night hour (Figure 6.5b): (i) E (left column), (ii) SE (central column) and (iii) W (right column) for (a, d, g) second, (b, e, h) fourth and (c, f, j) seventh night hours. 144

6.7 Temporal evolution of the average of wind (a) direction (°) and (b) speed (m s^{-1}), (c) cooling (°C), (d) cooling hourly rate (°C h^{-1}) and (e) relative humidity (%) for all three subgroups of stable nights defined in Figure 6.6. 147

6.8 The same as Figure 6.7 for the variables (a) wind speed (m s^{-1}), (b) relative humidity (%), (c) cooling (°C) and (d) hourly cooling rate (°C h^{-1}) for all four seasons: winter (WIN), spring (SPR), fall (FALL) and summer (SUM) for all selected nights. 148

7.1 Topography of the Ebro Valley with the location of Raimat, Lleida and Barcelona. 153

7.2 Slopes converging to the Raimat site following different slopes. . 154

7.3 Statistical behavior in the Raimat automatic weather station of (a) wind speed, (b) wind direction and (c) temperature for clear skies and weak wind nights in the easterly and westerly cases in the period 1998-2007 and for 46 fog cases between 2005 and 2009. . . 156

7.4 (a) M2AV Carolo and (b) Vaisala's Tethersonde and balloon. . . . 157

7.5 The WindRASS installed in Raimat since July 1st, 2009. 158

7.6 WindRASS night averaged profiles compared against an UAV flight and seven tether soundings. 161

7.7 Evolution of the vertically integrated profiles for three typical nights of (a) wind speed, (b) wind direction, (c) virtual temperature and (d) estimation of the TKE from 1600 UTC to 0400 UTC. . 162

7.8 Land Surface Temperature provided by MODIS during 5th July 2009 at (a) 1300 UTC and (b) 2200 UTC. 164

7.9 Temporal evolution of the WindRASS profiles of (a) wind speed, (b) wind direction, (c) virtual temperature and (d) estimation of the TKE for the night 5/6 July 2009. 166

7.10 (a) Temperature evolution for three automatic weather stations in the area and for the WindRass at 40 and 250 m above ground during a winter clear skies night followed by a persistent fog event (from 9 to 13 December 2009). (b) Land Surface Temperature derived from MODIS for the Ebro basin indicating the area covered by fog at 2140 UTC. 168

Bibliography

Acevedo, O. C., and D. R. Fitzjarrald, 2001: The early evening surface-layer transition: Temporal and spatial variability. *J. Atmos. Sci.*, **58**, 2650–2667.

André, J. C., and L. Mahrt, 1982: The nocturnal surface inversion and influence of clear-air radiative cooling. *J. Atmos. Sci.*, **39**, 864–878.

Baas, P., F. C. Bosveld, H. K. Baltink, and A. A. M. Holtslag, 2009: A climatology of nocturnal low-level jets at Cabauw. *J. Appl. Meteor. Climatol.*, **48**, 1627–1642.

Bain, C. L., D. J. Parker, C. M. Taylor, L. Kergoat, and F. Guichard, 2010: Observations of the nocturnal boundary layer associated with the west African Monsoon. *Mon. Wea. Rev.*, **138**, 3142–3156.

Ball, F. K., 1956: The theory of strong katabatic winds. *Aust. J. Phys.*, **9**, 373–386.

Banta, R. M., L. S. Darby, J. D. Fast, J. O. Pinto, C. D. Whiteman, W. J. Shaw, and B. W. Orr, 2004: Nocturnal low-level jet in a mountain basin complex. Part I: Evolution and effects on local flows. *J. Appl. Meteor.*, **43**, 1348–1365.

Banta, R. M., R. K. Newsom, J. K. Lundquist, Y. L. Pichugina, R. L. Coulter, and L. Mahrt, 2002: Nocturnal low-level jet characteristics over kansas during CASES-99. *Bound.-Layer Meteorol.*, **105**, 221–252.

Barry, R. G., 2008: *Mountain weather and climate*. Cambridge University Press, New York, 506 pp, 3rd edition.

Belušić, D., and L. Mahrt, 2008: Estimation of length scales from mesoscale networks. *Tellus A*, **60**, 706–715.

Beyrich, F., and H.-T. Mengelkamp, 2006: Evaporation over a heterogeneous land surface. *Bound.-Layer Meteorol.*, **121**, 5–32.

Blackadar, A. K., 1957: Boundary layer wind maxima and their significance for the growth of nocturnal inversions. *Bull. Amer. Met. Soc.*, **38**, 283–290.

Blumen, W., 1984: An observational study of instability and turbulence in nighttime drainage winds. *Bound.-Layer Meteorol.*, **28**, 245–269.

Bodine, D., P. M. Klein, S. C. Arms, and A. Shapiro, 2009: Variability of surface air temperature over gently sloped terrain. *J. Appl. Meteor. Climatol.*, **48**, 1117–1141.

Bougeault, P., and P. Lacarrère, 1989: Parameterization of orography-induced turbulence in a mesobeta scale model. *Mon. Wea. Rev.*, **117**, 1872–1890.

Bravo, M., T. Mira, M. R. Soler, and J. Cuxart, 2008: Intercomparison and evaluation of MM5 and Meso-NH mesoscale models in the stable boundary layer. *Bound.-Layer Meteorol.*, **128**, 77–101.

Brazel, A. J., H. J. S. Fernando, J. C. R. Hunt, N. Selover, B. C. Hedquist, and E. Pardyjak, 2005: Evening transition observations in Phoenix, Arizona. *J. Appl. Meteor.*, **44**, 99–112.

Bromwich, D. H., 1989: Satellite analyses of antarctic katabatic wind behavior. *Bull. Amer. Met. Soc.*, **70**, 738–749.

Catalano, F., and A. Cenedese, 2010: High-resolution numerical modeling of thermally driven slope winds in a valley with strong capping. *J. Appl. Meteor. Climatol.*, **49**, 1859–1880.

Charnock, H., 1955: Wind stress in a water surface. *Quart. J. Roy. Meteor. Soc.*, **81**, 639–640.

Clarke, R. H., A. J. Dyer, R. R. Brook, D. G. Reid, and A. J. Troup, 1971: The Wangara experiment: Boundary-layer data. Technical Report 19, Div. Meteorol. Phys., CSIRO, Aspendale, Australia.

Clements, C. B., C. D. Whiteman, and J. D. Horel, 2003: Cold-air-pool structure and evolution in a mountain basin. *J. Appl. Meteor.*, **42**, 752–768.

Clements, C. B., W. Yao, S. Zhong, C. D. Whiteman, and T. Horst, 2007: Slope flows observed during METCRAX. *29th International Conference on Alpine Meteorology (ICAM)*, Chambéry, France.

Clements, W., J. A. Archuleta, and P. H. Gudiksen, 1989: Experimental design of the 1984 ASCOT field experiment. *J. Appl. Meteor.*, **28**, 405–413.

Coll, C., and V. Caselles, 1997: A split-window algorithm for land surface temperature from advanced very high resolution radiometer data: Validation and algorithm comparison. *J. Geophys. Res.*, **102**, 697–713.

Coll, C., V. Caselles, J. M. Galve, E. Valor, R. Niclòs, J. M. Sánchez, and R. Rivas, 2005: Ground measurements for the validation of land surface temperatures derived from AATSR and MODIS data. *Remote Sens. Environ.*, **97**, 288–300.

Coll, C., V. Caselles, J. Sobrino, and E. Valor, 1994: On the atmospheric dependence of the split-window equation for land surface temperature. *Int. J. Rem. Sens.*, **15**, 105–122.

Conangla, L., and J. Cuxart, 2006: On the turbulence in the upper part of the low-level jet: An experimental and numerical study. *Bound.-Layer Meteorol.*, **118**, 379–400.

Conangla, L., J. Cuxart, and M. R. Soler, 2008: Characterisation of the nocturnal boundary layer at a site in northern Spain. *Bound.-Layer Meteorol.*, **128**, 255–276.

Cornfeld, C., 1938: Katabatic winds and the prevention of frost damage. *Quart. J. Roy. Meteor. Soc.*, **64**, 553–584.

Coulter, R., and P. Gudiksen, 1995: The dependence of canyon winds and surface cooling and external forcing in Colorado's Front Range. *J. Appl. Meteor.*, **34**, 1419–1429.

Cuxart, J., 2008: Nocturnal basin low-level jets: An integrated study. *Acta Geophys.*, **56**, 100–113.

Cuxart, J., P. Bougeault, and J.-L. Redelsperger, 2000: A turbulence scheme allowing for mesoscale and large-eddy simulations. *Quart. J. Roy. Meteor. Soc.*, **126**, 1–30.

Cuxart, J., A. A. M. Holtslag, R. J. Beare, E. Bazile, A. Beljaars, L. Conangla, M. Ek, F. Freedman, R. Hamdi, A. Kerstein, A. Kitagawa, G. Lenderink, D. Lewellen, J. Mailhot, T. Mauritsen, V. Perov, G. Schayes, G.-J. Steeneveld, G. Svensson, P. Taylor, W. Weng, S. Wunsch, and K.-M. Xu, 2006: Single-column model intercomparison for a stably stratified atmospheric boundary layer. *Bound.-Layer Meteorol.*, **118**, 273–303.

Cuxart, J., and M. A. Jiménez, 2007: Mixing processes in a nocturnal low-level jet: An LES study. *J. Atmos. Sci.*, **64**, 1666–1679.

Cuxart, J., and M. A. Jiménez, 2011: A high-resolution mesoscale simulation of a long-lasting basin fog. *Pure. Appl. Geophys.*, Submitted.

Cuxart, J., M. A. Jiménez, and D. Martínez, 2007: Nocturnal meso-beta and katabatic flows on a midlatitude island. *Mon. Wea. Rev.*, **135**, 918–932.

Cuxart, J., F. Molinos, D. Martínez, M. A. Jiménez, and J. Cunillera, 2009: Conditioned climatology of the stably stratified nights in the Ebro basin. *30th International Conference on Alpine Meteorology ICAM*, Rastatt, Germany.

Cuxart, J., G. Morales, E. Terradellas, and C. Yagüe, 2002: Study of coherent structures and estimation of the pressure transport terms for the nocturnal stable boundary layer. *Bound.-Layer Meteorol.*, **105**, 305–328.

Cuxart, J., C. Yagüe, G. Morales, E. Terradellas, J. Orbe, J. Calvo, A. Fernandez, M. R. Soler, C. Infante, P. Buenestado, A. Espinalt, H. E. Joergensen, J. M. Rees, J. Vilà, J. M. Redondo, I. R. Cantalapiedra, and L. Conangla, 2000: Stable Atmospheric Boundary-Layer Experiment in Spain (SABLES 98): A report. *Bound.-Layer Meteorol.*, **96**, 337–370.

Dalu, G. A., R. A. Piellke, M. Baldi, and X. Zeng, 1996: Heat and momentum fluxes induced by thermal inhomogeneities with and without large-scale flow. *J. Atmos. Sci.*, **53**, 3286–3302.

Davidson, B., and P. K. Rao, 1963: Experimental studies of the valley-plain wind. *Int. J. Air Water Pollut.*, **7**, 907–923.

De Wekker, S. F. J., and C. D. Whiteman, 2006: On the time scale of nocturnal boundary layer cooling in valleys and basins and over plains. *J. Appl. Meteor.*, **45**, 813–820.

Deardorff, J. W., 1972: Parameterization of the planetary boundary layer for use in general circulation models. *J. Atmos. Sci.*, **100**, 93–106.

Defant, F., 1949: Zur theorie der Hangwinde, nebst bemerkungsen zur theorie der Berg- und Talwinde. *Arch. Meteor. Geophys. Biokl.*, **A1**, 421–450.

Defant, F., 1951: Local winds. *Compendium of Meteorology*, T. M. Malone, Ed. Amer. Meteor. Soc., 655-672.

Doran, J., and T. W. Horst, 1981: Velocity and temperature oscillations in drainage winds. *J. Appl. Meteor.*, **20**, 227–232.

Doran, J., T. W. Horst, and C. D. Whiteman, 1990: The development and structure of nocturnal slope winds in a simple valley. *Bound.-Layer Meteorol.*, **52**, 41–68.

Doran, J. C., J. D. Fast, and J. Horel, 2002: The VTMX 2000 campaign. *Bull. Amer. Met. Soc.*, **83**, 537–551.

Dörnbrack, A., and U. Schumann, 1993: Numerical simulation of turbulent convective flow over wavy terrain. *Bound.-Layer Meteorol.*, **65**, 323–355.

Durran, D., 1989: Improving the anelastic approximation. *J. Atmos. Sci.*, **46**, 1453–1461.

Edwards, J., 2009: Radiative processes in the stable boundary layer: Part II. The development of the nocturnal boundary layer. *Bound.-Layer Meteorol.*, **131**, 127–146.

Egger, J., 1990: Thermally forced flows: Theory. *Atmospheric processes over complex terrain, Meteor. Monogr.*, W. Blumen, Ed., volume 23. Amer. Meteor. Soc., 43-58.

Ellison, T. H., and J. S. Turner, 1959: Turbulent entrainment in stratified flows. *J. Fluid Mech.*, **6**, 423–448.

Fast, J., S. Zhong, and C. D. Whiteman, 1996: Boundary layer evolution within a canyonland basin. Part II. Numerical simulations of nocturnal flows and heat budgets. *J. Appl. Meteor.*, **35**, 2162–2178.

Fedorovich, E., and A. Shapiro, 2009: Structure of numerically simulated katabatic and anabatic flows along steep slopes. *Acta Geophys.*, **57**, 981–1010.

Fitzjarrald, D. R., 1984: Katabatic wind in opposing flow. *J. Atmos. Sci.*, **41**, 1143–1158.

Fitzjarrald, D. R., and G. G. Lala, 1989: Hudson valley fog environment. *J. Appl. Meteor.*, **28**, 1303–1328.

Fleagle, R. G., 1950: A theory of air drainage. *J. Meteor.*, **7**, 227–232.

Freytag, C., 1985: MERKUR-results: Aspects of the temperature field and the energy budget in a large alpine valley during mountain and valley wind. *Beitr. Phys. Atm.*, **58**, 458–476.

Gallée, H., and P. Pettré, 1998: Dynamical constraints on katabatic wind cessation in Adélie land, Antarctica. *J. Atmos. Sci.*, **55**, 1755–1770.

Garratt, J. R., 1992: *The atmospheric boundary layer*. Cambridge University Press, Cambridge, 316 pp.

Geiger, R., 1965: *The climate near the ground*. Rev. ed. Harvard University Press, Cambridge, 611 pp. Translated by Scriptia Technica, Inc., from the German 4th ed.

Gopalakrishnan, S., S. Maithili, R. McNider, and M. Singh, 1998: Study of radiative and turbulent processes in the stable boundary layer under weak wind conditions. *J. Atmos. Sci.*, **55**, 954–960.

Grisogono, B., and J. Oerlemans, 2001a: Katabatic flow: Analytic solution for gradually varying eddy diffusivities. *J. Atmos. Sci.*, **58**, 3349–3354.

Grisogono, B., and J. Oerlemans, 2001b: A theory for the estimation of surface fluxes in simple katabatic flows. *Quart. J. Roy. Meteor. Soc.*, **127**, 2725–2739.

Grisogono, B., and J. Oerlemans, 2002: Justifying the WKB approximation in pure katabatic flows. *Tellus*, **54A**, 453–462.

Gudiksen, P. H., J. M. J. Leone, C. W. King, D. Ruffieux, and W. D. Neff, 1992: Measurements and modelling of the effects of ambient meteorology on nocturnal drainage flows. *J. Appl. Meteor.*, **31**, 1023–1032.

Gustavsson, T., M. Karlsson, J. Bogren, and S. Lindqvist, 1998: Development of temperature patterns during clear nights. *J. Appl. Meteor.*, **37**, 559–571.

Ha, K.-J., and L. Mahrt, 2003: Radiative and turbulent fluxes in the nocturnal boundary layer. *Tellus*, **55A**, 317–327.

Haiden, T., 2003: On the pressure field in the slope wind layer. Notes and correspondence. *J. Atmos. Sci.*, **60**, 1632–1635.

Haiden, T., and C. D. Whiteman, 2005: Katabatic flow mechanims on a low-angle slope. *J. Appl. Meteor.*, **44**, 113–126.

Hawkes, H. B., 1947: *Mountain and valley winds with special reference to the diurnal mountain winds of the Great Salt Lake Region*. PhD thesis, Ohio State University, 312 pp.

Heinemann, G., 2002: Modelling and observations of the katabatic flow dynamics over Greenland. *Tellus*, **54A**, 542–554.

Hernandez Navarro, M. L., 1995: *El riesgo de helada en las plantaciones de frutales. El valle medio del Ebro*. Institución Fernando el Católico, Zaragoza, 237 pp.

Heymann, Y., C. Steenmans, G. Croissille, and M. Bossard, 1994: Corine land cover- Technical Guide. *Office for Official Publications of the European Communities*.

Heywood, G. S. P., 1933: Katabatic winds in a valley. *Quart. J. Roy. Meteor. Soc.*, **59**, 47–58.

Hoch, S. W., and C. D. Whiteman, 2007: Observations of radiative flux divergence and vertical temperature structure evolution. *24th General Assembly, Intern. Union Geodesy Geophys.*, Perugia, Italy.

Hoch, S. W., and C. D. Whiteman, 2010: Topographic effects on the surface radiation balance in and around Arizona's Meteor Crater. *J. Appl. Meteor. Climatol.*, **49**, 1114–1128.

Holton, J. R., 1972: *An introduction to dynamic meteorology*. Academic Press, New York, 319 pp.

Hunt, J. C. R., H. J. S. Fernando, and M. Princevac, 2003: Unsteady thermally driven flows on gentle slopes. *J. Atmos. Sci.*, **60**, 2169–2182.

Jeffreys, H., 1922: On the dynamics of wind. *Quart. J. Roy. Meteor. Soc.*, **48**, 29–48.

Jiménez, M. A., and J. Cuxart, 2005: Large-eddy simulations of the stable boundary layer using the standard Kolmogorov theory: Range of applicability. *Bound.-Layer Meteorol.*, **115**, 241–261.

Jiménez, M. A., A. Mira, C. J., A. Luque, S. Alonso, and J. A. Guijarro, 2008: Verification of a clear-sky mesoscale simulation using satellite-derived surface temperatures. *Mon. Wea. Rev.*, **136**, 5148–5161.

Kaimal, J. C., and J. E. Gaynor, 1991: Another look to sonic thermometry. *Bound.-Layer Meteorol.*, **56**, 401–410.

Kaufmann, P., and R. O. Weber, 1998: Directional correlation coefficient for channeled flow and application to wind data over complex terrain. *J. Atmos. Oceanic. Technol.*, **15**, 89–97.

Kavčič, I., and B. Grisogono, 2007: Katabatic flow with Coriolis effect and gradually varying eddy diffusivity. *Bound.-Layer Meteorol.*, **125**, 377–387.

Kidwell, K. B., 1998: NOAA polar orbiter data user's guide (TIROS-N, NOAA-6, NOAA-7, NOAA-8, NOAA-9, NOAA-10, NOAA-11, NOAA-12, NOAA-13, and NOAA-14). Technical report, NOAA. [Available online at http://www2.ncdc.noaa.gov/docs/podug/index.htm.].

Kolmogorov, A. N., 1941: Dissipation of energy in a locally isotropic turbulence. *Doklady Akad. Nauk SSSR*, **32**, 141–147.

Kondo, J., and T. Sato, 1988: A simple model of drainage flow on a slope. *Bound.-Layer Meteorol.*, **43**, 103–123.

Kring, D. A., 2007: *Guidebook to the geology of Barringer meteorite crater, Arizona (aka Meteor Crater)*. LPI Contribution 1355, Lunar and Planetary Institute, Houston, TX, 150 pp.

Lafore, J. P., J. Stein, N. Asencio, P. Bougeault, V. Ducrocq, J. Duron, C. Fisher, P. Héreil, P. Mascart, J. P. Pinty, J.-L. Redelsperger, E. Richard, and J. Vilá-Guerau de Arellano, 1998: The Meso-NH atmospheric simulation system. Part I: Adiabatic formulation and control simulation. *Ann. Geophys.*, **16**, 90–109.

Largeron, Y., C. Staquet, and C. Chemel, 2010: Turbulent mixing in a katabatic wind under stable conditions. *Meteorol. Z.*, **19**, 467–480.

Lehner, M., C. D. Whiteman, and S. W. Hoch, 2011: Diurnal cycle of thermally driven cross-basin winds in Arizona's Meteor Crater. *J. Appl. Meteor. Climatol.*, **50**, 729–744.

Lettau, H. H., and B. Davidson, 1957: *Exploring the atmosphere's first mile*. Pergamon Press, UK, 578 pp.

Lundquist, J. D., N. Pepin, and C. Rochford, 2008: Automated algorithm for mapping regions of cold-air pooling in complex terrain. *J. Geophys. Res.*, **113**, D22107.

Mahrt, L., 1982: Momentum balance of gravity flows. *J. Atmos. Sci.*, **39**, 2701–2711.

Mahrt, L., 1998: Nocturnal boundary-layer regimes. *Bound.-Layer Meteorol.*, **88**, 255–278.

Mahrt, L., 1999: Stratified atmospheric boundary layers. *Bound.-Layer Meteorol.*, **90**, 375–396.

Mahrt, L., 2008: Mesoscale wind direction shifts in the stable boundary-layer. *Tellus A*, **60**, 700–705.

Mahrt, L., and S. Larsen, 1982: Small scale drainage flow. *Tellus*, **34**, 579–587.

Mahrt, L., S. Richardson, N. Seaman, and D. Stauffer, 2010: Non-stationary drainage flows and motions in the cold pool. *Tellus A*, **62**, 698–705.

Mahrt, L., D. Vickers, R. Nakamura, M. R. Soler, J. L. Sun, S. Burns, and D. H. Lenschow, 2001: Shallow drainage flows. *Bound.-Layer Meteorol.*, **101**, 243–260.

Manins, P. C., 1992: Vertical fluxes in katabatic flows. *Bound.-Layer Meteorol.*, **60**, 169–178.

Manins, P. C., and B. L. Sawford, 1979a: Katabatic winds: a field case study. *Quart. J. Roy. Meteor. Soc.*, **105**, 1011–1025.

Manins, P. C., and B. L. Sawford, 1979b: A model of katabatic winds. *J. Atmos. Sci.*, **36**, 619–630.

Martín-Vide, J., 2005: Factors geogràfics, regionalització climàtica i tendències de les sèries climàtiques a Catalunya. *Informe sobre el canvi climàtic a Catalunya*, J. E. Llebot, Ed. Institut d'Estudis Catalans, Barcelona, 81-111.

Martínez, D., and J. Cuxart, 2009: Assesment of the hydraulic slope flow approach using a mesoscale model. *Acta Geophys.*, **57**, 882–903.

Martínez, D., J. Cuxart, and J. Cunillera, 2008: Conditioned climatology for stably stratified nights in the Lleida area. *Tethys*, **5**, 13–24.

Martínez, D., M. A. Jiménez, J. Cuxart, and L. Mahrt, 2010: Heterogeneous nocturnal cooling in a large basin under very stable conditions. *Bound.-Layer Meteorol.*, **137**, 97–113.

Mason, P. J., and S. H. Derbyshire, 1990: Large-eddy simulation of the stably-stratified atmospheric boundary layer. *Bound.-Layer Meteorol.*, **53**, 117–162.

Masson, V., 2000: A physically based scheme for the urban energy budget in atmospheric models. *Bound.-Layer Meteorol.*, **94**, 357–397.

Masson, V., and P. Bougeault, 1996: Numerical simulation of a low-level wind created by complex orography: a Cierzo case study. *Mon. Wea. Rev.*, **124**, 701–715.

Masson, V., J.-L. Champeaux, F. Chauvin, C. Meriguet, and R. Lacaze, 2003: A Gobal database of land surface parameters at 1-km resolution in meteorological and climate models. *J. Climate*, **16**, 1261–1282.

McKee, T. B., and R. D. O'Neal, 1989: The role of valley geometry and energy budget in the formation of nocturnal valley winds. *J. Appl. Meteor.*, **28**, 445–456.

McNider, R. T., 1982: A note on velocity fluctuations in drainage flows. *J. Atmos. Sci.*, **39**, 1658–1660.

Michelson, S., and J. Bao, 2008: Sensitivity of low-level winds simulated by the WRF model in California's Central valley to uncertainties in the large-scale forcing and soil initialization. *J. Appl. Meteor. Climatol.*, **47**, 3131–3149.

Mira, A., J. Cuxart, A. Luque, and J. Guijarro, 2006: Mesoscale basin flows in the nocturnal boundary layer: modelling and verification. *Proceedings of the 17th Symposium on Boundary Layers and Turbulence*, San Diego, CA.

Monin, A. S., and A. M. Obukhov, 1954: Basic laws of turbulence mixing in the atmosphere near the ground. *Tr. Akad. Nauk. SSSR Geofiz. Ins.*, **46**, 2311–2330.

Monti, P., H. J. S. Fernando, M. Princevac, W. C. Chan, T. A. Kowalewski, and E. R. Pardyjak, 2002: Observations of flow and turbulence in the nocturnal boundary layer over a slope. *J. Atmos. Sci.*, **59**, 2513–2534.

Morcrette, J.-J., 1990: Impact of changes to the radiation transfer parameterizations plus cloud optical properties in the ECMWF model. *Mon. Wea. Rev.*, **118**, 847–873.

Moriarty, W. W., 1993: An improved calibration for tethered balloon wind measurements. *Bound.-Layer Meteorol.*, **63**, 183–196.

Nappo, C. J., 2002: *An introduction to atmospheric gravity waves*. Academic Press, San Diego, 276 pp.

Neff, W., and C. King, 1989: The accumulation and pooling of drainage flows in a large basin. *J. Appl. Meteor.*, **28**, 518–529.

Nieuwstadt, F. T. M., P. J. Mason, C.-H. Moeng, and U. Schumann, 1993: Large-eddy simulation of the convective boundary layer: A comparison of four computer codes. *Turbulent shear flows 8*, F. Durst, R. Friedrich, F. W. Schmidt, and B. E. Launder, Eds. Springer-Verlag, Berlin, 343-367.

Noilhan, J., and S. Planton, 1989: A simple parameterization of land surface processes for meteorological models. *Mon. Wea. Rev.*, **117**, 536–549.

Oke, T. R., 1987: *Boundary layer climates*. Routledge, London, 435 pp, 2nd edition.

Oncley, S. P., T. Foken, R. Vogt, W. Kohsiek, H. DeBruin, C. Bernhofer, A. Christen, E. Gorsel, D. Grantz, C. Feigenwinter, I. Lehner, C. Liebethal, H. Liu, M. Mauder, A. Pitacco, L. Ribeiro, T. Weidinger, and Coauthors, 2007: The Energy Balance Experiment EBEX-2000. Part I: Overview and energy balance. *Bound.-Layer Meteorol.*, **123**, 1–28.

Pahlow, M., M. Parlange, and F. Porté-Agel, 1999: On Monin-Obukhov similarity in the stable atmospheric boundary layer. *Bound.-Layer Meteorol.*, **99**, 225–248.

Papadopoulos, K. H., and C. G. Helmis, 1999: Evening and morning transition of katabatic flows. *Bound.-Layer Meteorol.*, **92**, 195–227.

Papadopoulos, K. H., C. G. Helmis, A. T. Soilemes, J. Kalogiros, P. G. Papageorgas, and D. N. Asimakopoulos, 1997: The structure of katabatic flows down a simple slope. *Quart. J. Roy. Meteor. Soc.*, **123**, 1581–1601.

Parish, T. R., and D. H. Bromwich, 1991: Continental-scale simulation of the antarctic katabatic wind regime. *J. Climate*, **4**, 135–146.

Poulos, G. S., W. Blumen, D. C. Fritts, J. K. Lundquist, J. Sun, S. P. Burns, C. Nappo, R. Banta, R. Newsom, J. Cuxart, E. Terradellas, B. Balsley, and M. Jensen, 2002: Cases-99: A comprehensive investigation of the stable nocturnal boundary layer. *Bull. Amer. Met. Soc.*, **83**, 555–581.

Poulos, G. S., T. B. Bossert, T. B. McKee, and R. A. Pielke, 2000: The interaction of katabatic flow and mountain waves. Part I: Observations and idealized simulations. *J. Atmos. Sci.*, **57**, 1919–1936.

Prandtl, L., 1942: *Fürer durch die Strömungslehre*. Vieweg und Sohn, Braunschweig, 382 pp.

Prata, A. J., V. Caselles, C. Coll, J. A. Sobrino, and C. Otllé, 1995: Thermal remote sensing of land surface temperature from satellites: current status and future prospects. *Rem. Sens. Environ.*, **12**, 175–224.

Princevac, M., J. C. R. Hunt, and H. J. S. Fernando, 2008: Quasi-steady katabatic winds on slopes in wide valleys: Hydraulic theory and observations. *J. Atmos. Sci.*, **65**, 253–273.

Ramis, C., A. Jansa, and S. Alonso, 1990: Sea breeze in Mallorca - A numerical study. *Meteor. Atmos. Phys.*, **42**, 249–258.

Reiter, R., H. Müller, R. Sladkovic, and K. Munzert, 1982: Aerologische Untersuchungen des tagesperiodischen Windsystems im Inntal während MERKUR. [Aerological investigations of diurnal wind systems in the Inn Valley during MERKUR]. *Meteor. Rundsch.*, **37**, 176–190.

Renfrew, I. A., 2004: The dynamics of idealized katabatic flow over a moderate slope and ice shelf. *Quart. J. Roy. Meteor. Soc.*, **130**, 1023–1045.

Reuten, C., D. G. Steyn, K. B. Strawbridge, and P. Bovis, 2005: Observations of the relation between upslope flows and the convective boundary layer in steep terrain. *Bound.-Layer Meteorol.*, **116**, 37–61.

Rotach, M. W., P. Calanca, G. Giovanni, J. Gurtz, D. G. Steyn, R. Vogt, M. Andretta, A. Christen, C. Stanislaw, R. Connolly, S. F. J. De Wekker, S. Galmarini, E. N. Kadygrov, V. Kadygrov, E. Miller, B. Neininger, M. Rucker, E. Van Gorsel, H. Weber, A. Weiss, and M. Zappa, 2004: Turbulence structure and exchange processes in an alpine valley: The Riviera project. *Bull. Amer. Met. Soc.*, **85**, 1367–1385.

Rotach, M. W., and D. Zardi, 2007: On the boundary-layer structure over highly complex terrain: Key findings from MAP. *Quart. J. Roy. Meteor. Soc.*, **133**, 937–948.

Salomonson, V., W. Bames, W. Maymon, H. Montgomery, and H. Ostrow, 1989: MODIS: advanced facility instrument for studies of the Earth as a system. *IEEE Trans. Geosci. Remote Sens.*, **27**, 145–153.

Savage, L. C. I., S. Zhong, W. Yao, W. J. O. Brown, T. W. Horst, and C. D. Whiteman, 2008: An observational and numerical study of a regional-scale downslope flow in northern Arizona. *J. Geophys. Res.*, **113**, D14114.

Savijärvi, H., 2006: Radiative and turbulent heating rates in the clear-air boundary layer. *Quart. J. Roy. Meteor. Soc.*, **132**, 147–161.

Schumann, U., 1990: Large-eddy simulation of the up-slope boundary layer. *Quart. J. Roy. Meteor. Soc.*, **116**, 637–670.

Serafin, S., and D. Zardi, 2010: Structure of the atmospheric boundary layer in the vicinity of a developing upslope flow system: A numerical model study. *J. Atmos. Sci.*, **67**, 1171–1185.

Shapiro, A., and E. Fedorovich, 2007: Katabatic flows along a differentially cooled sloping surface. *J. Fluid. Mech.*, **571**, 149–175.

Simpson, J. E., 1999: *Gravity currents in the environment and the laboratory*. Cambridge University Press, Cambridge, 259 pp, 2nd edition.

Skyllingstad, E. D., 2004: Large-eddy simulation of katabatic flows. *Bound.-Layer Meteorol.*, **106**, 217–243.

Smith, C. M., and E. D. Skyllingstad, 2005: Numerical simulation of a katabatic flor with changing slope angle. *Mon. Wea. Rev.*, **133**, 3065–3080.

Snyder, R., and J. de Melo Abreu, 2005: *Frost protection: fundamentals, practice and economics*. Service Series 10, FAO, Roma. Environment and natural resources, Vol. 1, 240 pp.

Soler, M. R., C. Infante, P. Buenestado, and L. Mahrt, 2002: Observations of nocturnal drainage flow in a shallow gully. *Bound.-Layer Meteorol.*, **105**, 253–273.

Sousa, R., 1987: *Notas para una climatología en Lérida*. K-26, Instituto Nacional de Meteorología, Madrid.

Spieß, T., J. Bange, M. Buschmann, and P. Vörsmann, 2007: First application of the meteorological Mini-UAV 'M^{2}AV'. *Meteorol. Z.*, **16**, 159–169.

Strobach, K., 1991: *Unser Planet Erde: Unsprung und Dynamik*. Gebr. Borntrager, Berlin.

Stull, R. B., 1988: *An introduction to boundary layer meteorology*. Kluwer Academic Publishers, Dordretch, 666 pp.

Sun, J., S. P. Burns, A. C. Delany, Oncley, T. W. Horst, and D. H. Lenschow, 2003: Heat balance in the nocturnal boundary layer during CASES-99. *J. Appl. Meteor.*, **42**, 1649–1666.

Sun, J., S. P. Burns, D. H. Lenschow, R. Banta, R. Newson, R. Coulter, S. Frasier, T. Ince, C. Nappo, J. Cuxart, W. Blumen, X. Lee, and X.-Z. Hu, 2002: Intermittent turbulence associated with a density current passage in the stable boundary layer. *Bound.-Layer Meteorol.*, **105**, 199–219.

Taylor, C. M., D. J. Parker, and P. P. Harris, 2007: An observational case study of mesoscale atmospheric circulations induced by soil moisture. *Geophys. Res. Lett.*, **34**, L15801.

Taylor, G. I., and A. K. Green, 1937: Mechanism of the production of small eddies from large ones. *Proc. R. Soc. London*, **A158**, 499–521.

Terradellas, E., G. Morales, J. Cuxart, and C. Yagüe, 2001: Wavelet methods: Application to the study of the stable atmospheric boundary layer under non-stationary conditions. *Dyn. Atmos. Oceans*, **34**, 225–244.

Thompson, B. W., 1986: Small-scale katabatics and cold hollows. *Weather*, **41**, 146–153.

Thoroddsen, S. T., and C. W. Van Atta, 1992: Exponential tails and skewness of density-gradient probability density functions in stably stratified turbulence. *J. Fluid. Mech.*, **244**, 547–566.

Van den Kroonenberg, A. C., T. Martin, M. Buschmann, J. Bange, and P. Vörsmann, 2008: Measuring the wind vector using the autonomous mini aerial vehicle M^{2}AV. *J. Atmos. Oceanic. Technol.*, **25**, 1969–1982.

Van Gorsel, E. R., R. Vogt, A. Christen, and M. W. Rotach, 2003: Low frequency temperature and velocity oscillations in katabatic winds. *ICAM/MAP conference proceedings*, Brig, Switzerland.

Vergeiner, I., 1987: An elementary valley wind model. *Meteor. Atmos. Phys.*, **36**, 255–263.

Vergeiner, I., and E. Dreiseitl, 1987: Valley winds and slope winds – Observations and elementary thoughts. *Meteor. Atmos. Physics*, **36**, 264–286.

Viana, S., E. Terradellas, and C. Yagüe, 2010: Analysis of gravity waves generated at the top of a drainage flow. *J. Atmos. Sci.*, **67**, 3949–3966.

Viana, S., C. Yagüe, and G. Maqueda, 2009: Propagation and effects of a mesoscale gravity wave over a weakly-stratified nocturnal boundary layer during the SABLES2006 field campaign. *Bound.-Layer Meteorol.*, **133**, 165–188.

Viterbo, P., A. Beljaars, J.-F. Mahfouf, and J. Teixeira, 1999: The representation of soil moisture freezing and its impact on the stable boundary layer. *Quart. J. Roy. Meteor. Soc.*, **125**, 2401–2426.

Vosper, S. B., and A. R. Brown, 2008: Numerical simulations of sheltering in valleys: The formation of nighttime cold-air pools. *Bound.-Layer Meteorol.*, **127**, 429–448.

Wagner, A., 1938: Theorie und Beobachtung der periodischen Gebirgswinde. [Theory and observation of periodic mountain winds]. *Gerlands Beitr. Geophys.*, **52**, 408–449, [English translation: Whiteman, C. D., and E. Dreiseitl, 1984: Alpine meteorology: Translations of classic contributions by A. Wagner, E. Ekhart and F. Defant. PNL-5141 ASCOT-84-3. Pacific Northwest Laboratory, Richland, Washington, 121 pp].

Whiteman, C. D., 1990: Observations of thermally developed wind systems in mountainous terrain. *Atmospheric processes over complex terrain, Meteor. Monogr.*, W. Blumen, Ed., volume 23. Amer. Meteor. Soc., 5-42.

Whiteman, C. D., 2000: *Mountain meteorology: fundamentals and applications*. Oxford University Press, New York, 355 pp.

Whiteman, C. D., K. J. Allwine, L. J. Fritschen, M. M. Orgill, and J. R. Simpson, 1989: Deep valley radiation and surface energy budget microclimates. Part II: Energy budget. *J. Appl. Meteor.*, **28**, 427–437.

Whiteman, C. D., X. Bian, and S. Zhong, 1999: Wintertime evolution of the temperature inversion in the Colorado plateau basin. *J. Appl. Meteor.*, **38**, 1103–1117.

Whiteman, C. D., S. F. L. De Wekker, and T. Haiden, 2007: Effect of dewfall and frostfall on nighttime cooling in a small, closed basin. *J. Appl. Meteor. Climatol.*, **46**, 3–13.

Whiteman, C. D., and J. C. Doran, 1993: The relationship between overlying synoptic-scale flows and winds within valley. *J. Appl. Meteor.*, **32**, 1669–1682.

Whiteman, C. D., T. Haiden, B. Pospichal, S. Eisenbach, and R. Steinacker, 2004: Minimum temperatures, diurnal temperature ranges, and temperature inversions in limestone sinkholes of different sizes and shapes. *J. Appl. Meteor.*, **43**, 1224–1236.

Whiteman, C. D., S. Hoch, and G. Poulos, 2009: Evening temperature rises on valley floors and slopes: Their causes and their relationship to the thermally driven wind systems. *J. Appl. Meteor. Climatol.*, **48**, 776–788.

Whiteman, C. D., S. W. Hoch, M. Lehner, and T. Haiden, 2010: Nocturnal cold air intrusions into Arizona's Meteor Crater: Observational evidence and conceptual model. *J. Appl. Meteor. Climatol.*, **49**, 1894–1905.

Whiteman, C. D., and T. B. McKee, 1982: Breakup of temperature inversions in deep mountain calleys: Part II. Thermodynamic model. *J. Appl. Meteor.*, **21**, 290–302.

Whiteman, C. D., T. B. McKee, and J. C. Doran, 1996: Boundary layer evolution within a canyonland basin. Part I. Mass, heat, and moisture budgets from observations. *J. Appl. Meteor.*, **35**, 2145–2161.

Whiteman, C. D., A. Muschinski, S. Zhong, D. Fritts, S. W. Hoch, M. Hahnenberger, W. Yao, V. Hohreiter, M. Behn, Y. Cheon, C. B. Clements, T. W. Horst, W. O. J. Brown, and S. P. Oncley, 2008: METCRAX 2006 – Meteorological experiments in Arizona's Meteor Crater. *Bull. Amer. Met. Soc.*, **89**, 1665–1680.

Whiteman, C. D., S. Zhong, W. J. Shaw, J. M. Hubbe, X. Bian, and J. Mittelstadt, 2001: Cold pools in the Columbia basin. *Wea. Forecasting*, **16**, 432–447.

Wilczak, J. M., S. P. Oncley, and S. A. Stage, 2001: Sonic anemometer tilt correction algorithms. *Bound.-Layer Meteorol.*, **99**, 127–150.

Willis, G. E., and J. W. Deardoff, 1974: A laboratory model of the unstable planetary boundary layer. *J. Atmos. Sci.*, **31**, 1297–1307.

Wolyn, P. G., and T. B. McKee, 1989: Deep stable layers in the intermountain western United States. *Mon. Wea. Rev.*, **117**, 461–472.

Yagüe, C., S. Viana, G. Maqueda, M. F. Lazcano, G. Morales, and J. M. Rees, 2007: A study on the nocturnal atmospheric boundary layer: SABLES2006. *Física de la Tierra*, **19**, 37–53.

Yao, W., and S. Zhong, 2009: Nocturnal temperature inversions in a small, enclosed basin and their relationship to ambient atmospheric conditions. *Meteorol. Atmos. Phys.*, **103**, 195–210.

Yoshino, M. M., 1984: Thermal belt and cold air drainage on the mountain slope and cold air lake in the basin at quiet clear night. *Geophys. J.*, **8**, 235–250.

Zängl, G., 2005a: Dynamical aspects of wintertime cold-air pools in an alpine valley system. *Mon. Wea. Rev.*, **133**, 2721–2740.

Zängl, G., 2005b: Formation of extreme cold-air pools in elevated sinkholes: An idealized numerical process study. *Mon. Wea. Rev.*, **133**, 925–941.

Zardi, D., and C. D. Whiteman, 2011: Diurnal mountain wind systems. *Mountain weather research and forecasting*, F. K. Chow, S. F. J. DeWekker, and B. Snyder, Eds. Amer. Meteor. Soc. Submitted.

Zhong, S., and J. D. Fast, 2003: An evaluation of MM5, RAMS, and Meso Eta at sub-kilometer resolution using VTMX field campaign data in the Salt Lake valley. *Mon. Wea. Rev.*, **131**, 1301–1322.

Zhong, S., and C. D. Whiteman, 2008: Downslope flows on a low-angle slope and their interactions with valley inversions. Part II: Numerical modeling. *J. Appl. Meteor. Climatol.*, **47**, 2039–2057.

Zhong, S., C. D. Whiteman, and X. Bian, 2004: Diurnal evolution of three-dimensional wind and temperature structure in California's Central valley. *J. Appl. Meteor.*, **43**, 1679–1699.

Zhong, S., C. D. Whiteman, X. Bian, W. J. Shaw, and J. M. Hubble, 2001: Meteorological processes affecting the evolution of a wintertime cold air pool in the Columbia basin. *Mon. Wea. Rev.*, **129**, 2600–2613.